Thermodynamic Modeling and Thermoeconomic Optimization of Integrated Trigeneration Plants Using Organic Rankine Cycles

by

Fahad A. Al-Sulaiman

A thesis
presented to the University of Waterloo
in fulfilment of the
thesis requirement for the degree of
Doctor of Philosophy
in
Mechanical Engineering

Waterloo, Ontario, Canada, 2010

Author's Declaration

I hereby declare that I am the sole author of this thesis. This is a true copy of the thesis, including any required final revisions, as accepted by my examiners.

I understand that my thesis may be made electronically available to the public.

Abstract

In this study, the feasibility of using an organic Rankine cycle (ORC) in trigeneration plants is examined through thermodynamic modeling and thermoeconomic optimization. Three novel trigeneration systems are considered. Each one of these systems consists of an ORC, a heating-process heat exchanger, and a single-effect absorption chiller. The three systems are distinguished by the source of the heat input to the ORC. The systems considered are SOFC-trigeneration, biomass- trigeneration, and solar-trigeneration systems. For each system four cases are considered: electrical-power, cooling-cogeneration, heating-cogeneration, and trigeneration cases. Comprehensive thermodynamic analysis on each system is carried out. Furthermore, thermoeconomic optimization is conducted. The objective of the thermoeconomic optimization is to minimize the cost per exergy unit of the trigeneration product. The results of the thermoeconomic optimization are used to compare the three systems through thermodynamic and thermoeconomic analyses. This study illustrates key output parameters to assess the trigeneration systems considered. These parameters are energy efficiency, exergy efficiency, net electrical power, electrical to cooling ratio, and electrical to heating ratio. Moreover, exergy destruction modeling is conducted to identify and quantify the major sources of exergy destruction in the systems considered. In addition, an environmental impact assessment is conducted to quantify the amount of CO_2 emissions in the systems considered. Furthermore, this study examines both the cost rate and cost per exergy unit of the electrical power and other trigeneration products.

This study reveals that there is a considerable efficiency improvement when trigeneration is used, as compared to only electrical power production. In addition, the emissions of CO_2 per MWh of trigeneration are significantly lower than that

of electrical power. It was shown that the exergy destruction rates of the ORC evaporators for the three systems are quite high. Therefore, it is important to consider using more efficient ORC evaporators in trigeneration plants. In addition, this study reveals that the SOFC-trigeneration system has the highest electrical energy efficiency while the biomass-trigeneration system and the solar mode of the solar-trigeneration system have the highest trigeneration energy efficiencies. In contrast, the SOFC-trigeneration system has the highest exergy efficiency for both electrical and trigeneration cases. Furthermore, the thermoeconomic optimization shows that the solar-trigeneration system has the lowest cost per exergy unit. Meanwhile the solar-trigeneration system has zero CO_2 emissions and depends on a free renewable energy source. Therefore, it can be concluded that the solar-trigeneration system has the best thermoeconomic performance among the three systems considered.

Acknowledgments

All praise and glory to ALLAH, the God, the creator, the almighty who gave me the spirit, strength, patience, and health to accomplish this work.

I acknowledge, with deep gratitude and appreciation, the careful guidance and encouragement given to me by my PhD thesis co-supervisors, Prof. Feridun Hamdullahpur and Prof. Ibrahim Dincer. They have not only taken a keen interest in the work by patiently giving constructive comments, in spite of their very busy schedule, but also worked closely with me through every step of this work. I am especially thankful and grateful to my thesis committee members – Prof. Z. Chen, Prof. A. Fung, Prof. X. Li, and Prof. F.-S. Lien – for their useful comments on the research work conducted and their review of the thesis.

I would like to thank my colleagues, especially C.O. Colpan, for his valuable comments throughout my PhD work. I would also like to thank my colleagues Siamak Farhad and A. Abuadala for their help. I acknowledge King Fahd University of Petroleum and Minerals, Dhahran, Saudi Arabia for sponsoring my PhD work. In addition, I would like to acknowledge all of my family members – especially my parents, my wife, and my brother Khaled – for their appreciation, encouragement, and prayers.

Table of Contents

List of Figures

List of Tables

List of Symbols

a	:	Extent of steam reforming reaction for methane, mole/s
A	:	Active surface area, cm^2
A_{ap}	:	Aperture area, m^2
A_c	:	Area of the receiver cover, m^2
A_r	:	Area of the receiver, m^2
b	:	Extent of water gas shift reaction, mole/s
c	:	Extent of electrochemical reaction, mole/s, cell, or
	:	cost per unit of exergy, $/GJ
$\dot{C}_{chiller,1}$	:	Cost rate at the inlet of the SEAC (evaporator), $/h
$\dot{C}_{chiller,2}$	:	Cost rate at the exit of the SEAC (evaporator), $/h
C	:	Constant or heat capacity, kW/K
C_p	:	Specific heat, kJ/kg-K
Col_n	:	Total number of collectors per single row
Col_r	:	Total number of solar collectors rows
$\dot{C}$	:	Cost rate of the respective stream, $/hour
D	:	Diameter, m
COP	:	Coefficient of performance
D_{aeff}	:	Effective gaseous diffusivity through the anode, cm^2/s

D_{ceff}	:	Effective gaseous diffusivity through the cathode, cm^2/s
e	:	Specific energy, kJ/kg
E	:	Energy, kJ
$\dot{E}$	:	Energy rate, kW
ex	:	Specific exergy, kJ/kg
Ex	:	Exergy, kJ
$\dot{E}x$	:	Exergy rate, kW
F	:	Faraday constant, C
F_R	:	Heat removal factor
F_1	:	Collector efficiency factor
G	:	Change in specific molar Gibbs free energy, J/mole
G_b	:	Solar radiation, W/m^2
h	:	Specific enthalpy, kJ/kg
$\dot{H}$	:	Enthalpy rate, kW
h_c	:	Convection heat coefficient, kW/m^2-K
h_r	:	Radiation heat coefficient, kW/m^2-K
I	:	Current, A
j	:	Current density, A/cm^2
j_{as}	:	Anode-limiting current density, A/cm^2
j_{cs}	:	Cathode-limiting current density, A/cm^2
j_{oa}	:	Exchange current density of anode, A/cm^2
j_{oc}	:	Exchange current density of cathode, A/cm^2
k	:	Thermal conductivity, W/m
K	:	Equilibrium constant
L	:	Thickness of an SOFC layer, cm
HHV	:	Higher heating value, kJ/kg

LHV	:	Lower heating value, kJ/kg
$LMTD$	:	Log mean temperature difference, K
m	:	Mass, kg
M_w	:	Moisture content in the biomass fuel, % wt, dry basis
Nus	:	Nusselt number
P	:	Pressure, kPa
Q	:	Heat, kJ
$\dot{Q}$	:	Heat rate, kW
R	:	Universal gas constant, J/mol-K
$r_{el,h}$	:	Electrical to heating energy ratio
$r_{el,c}$	:	Electrical to cooling energy ratio
s	:	Specific entropy, kJ/kg-K or heat exchanger
S	:	Entropy, kJ/K or absorbed radiation by the receiver, W/m^2
$\dot{S}$	:	Entropy rate, kW/K
T	:	Temperature, C^o or K
U_f	:	Fuel utilization ratio
U_{O2}	:	Air (oxidant) utilization ratio
UA	:	Overall heat coefficient and area, kW/K
U_L	:	Overall heat loss coefficient of the solar collector, kW/m^2-K
U_o	:	Heat loss coefficient between the ambient and receiver of the solar collector, kW/m^2-K
v	:	Velocity, m/s
V	:	Voltage, V
w	:	Collector width, m
$\dot{W}$	:	Power, kW
$\dot{W}_{FC}$	:	Power of the fuel cell (W)

x	:	Molar concentration
z	:	Distance, m

Greek letters

Δt	:	Change in time in second
Δt_h	:	Change in time in hour
ϵ	:	Effectiveness
ϵ_{cv}	:	Emittance of the receiver cover
η	:	Energy efficiency
η_{ex}	:	Exergy efficiency
ω	:	Moisture content factor
σ	:	Stefan-Boltzmann constant, kW/m^2-K^4
ρ	:	Density, kg/m^3 or electrical resistivity of fuel
	:	cell components, ohm-cm

Subscripts

0	:	Atmospheric conditions
a	:	Anode, absorber, or ambient
ac	:	AC current, actual
act	:	Activation
BM	:	Biomass-trigeneration system
$b1$	:	Blower 1
$b2$	:	Blower 2
c	:	Cathode or receiver cover

$chst$	:	Charging hot storage tank
$conc$	:	Concentration
$cond$	:	Condenser
cog, c	:	Cooling cogeneration
cog, h	:	Heating cogeneration
cst	:	Cold storage tank
cv	:	Control volume
$dhst$	:	Discharging hot storage tank
d	:	Desorber, destruction
e	:	Electrolyte, exit
eq	:	Equilibrium
ev	:	Evaporator
ex	:	Exergy
f	:	Fuel
FC	:	Fuel cell
g	:	Generator
h	:	Heating
H	:	High reservoir temperature
HEx	:	Heat exchanger
hp	:	Heating process
hst	:	hot storage tank
i	:	Inlet
int	:	Interconnect
$inverter$	:	DC to AC inverter
is	:	Isentropic
L	:	Low reservoir temperature

l, cst	:	Lost of heat from the cold storage tank
l, hst	:	Lost of heat from the hot storage tank
m	:	Motor
o	:	Organic
oe	:	ORC evaporator
ohm	:	Ohmic
op	:	ORC pump
ot	:	ORC turbine
N	:	Nernst
p	:	Product
r	:	Reactant or receiver
R	:	Refrigerator
rev	:	Reversible
So	:	Solar-trigeneration system
so	:	Solar mode of the solar-trigeneration system
$SOFC$	:	SOFC-trigeneration system
sol, p	:	Pump of the solar system
$so - st$	:	Solar and storage mode of the solar-trigeneration system
sp	:	Solution pump
st	:	Storage mode of the solar-trigeneration system
$st1, p$	:	First pump in the thermal storage system
$st2, p$	:	Second pump in the thermal storage system
wgs	:	Water gas shift reaction
wp	:	Water pump
tri	:	Trigeneration
u	:	Useful

Superscripts

$\bar{}$	:	Molar base
$\dot{}$	:	Rate of a component
0	:	At standard pressure
CH	:	Chemical exergy
PH	:	Physical exergy

Acronyms

GHG	:	Greenhouse gas
LiBr	:	Lithium-bromide
PTSC	:	Parabolic trough solar collectors
ORC	:	Organic Rankine cycle
SEAC	:	Singe-effect absorption chiller
SOFC	:	Solid oxide fuel cell

Chapter 1

Introduction and Background

1.1 Background

Availability of sources and global warming are the two main concerns for the sustainability of energy production in the future. The demand for energy has been on a steady rise despite the limited availability of non-renewable fuel resources. For example, the world energy consumption is expected to increase by around 40% between 2006 and 2030 [1], while a dramatic increase in greenhouse gas emissions is also foreseen. For instance, from 1990 to 2007, CO_2 equivalent emissions increased 17% in the USA [2]. Therefore, finding more efficient energy systems is more crucial now than at any time since the beginning of the industrial revolution. The efficiency of conventional power plants that are based on single prime movers is usually less than 39%. Thus, most of the energy is lost as waste heat. Integrating cooling and heating subsystems in a conventional plant could increase the plant efficiency significantly where the CHP efficiency could reach 80% [3, 4].

Trigeneration usually refers to the simultaneous production of cooling, heating, and power based on a single energy source. It is also known as combined cooling, heating and power (CCHP). Sometimes combined heating and power (CHP) refers to trigeneration.

That is, if the heat produced from CHP is used for cooling, as well as heating, the plant is called a trigeneration plant. CHP could refer to a cogeneration plant if it produces only heat and power.

In a trigeneration plant, the waste energy from a generation unit, such as a gas turbine, is used to drive both the heating and cooling systems. Therefore, the use of a trigeneration plant results in an improvement of the overall thermal efficiency and a reduction of the contamination to the environment. The degree of improvement of the plant is sensitive to the performance of each unit in the trigeneration plant and the approach of integrating the units of the plant.

Trigeneration plants are usually used as decentralized plants in order to keep the cooling and heating demands at the needed temperatures. In other words, they are used as decentralized plants since the production of the heating and cooling of the trigeneration plants requires insulation to keep the cooling and/or heating production in a valuable benefit. Therefore, the trigeneration plants are usually located close to the end user. The cooling equipment of the trigeneration plants could include a*b*sorption chillers, a*d*sorption chillers, and/or reversible heat pumps.

As the literature review in this study shows, most of the research on trigeneration has been conducted in the last few years. This huge increment in the research is a result of the known benefits of using trigeneration, which lead to more demand on the energy produced from trigeneration. In terms of electricity produced, CHP accounts for more than 11% of the electricity produced in the G8 countries, as well as Brazil, China, India, Mexico, and South Africa in 2008. This percentage is expected to increase to 15% in 2015 and to 24% in 2030, [3]. In other words, the electricity produced by CHP is expected to reach around 430 GWe in 2015 and more than 830 GWe in 2030 [3]. Examples where trigeneration plants could be used are chemical and food industries, airports, shopping centers, hotels, hospitals, and houses.

However, some barriers need to be resolved to increase the benefit of using CHP. These barriers [3] include the lack of:

- A planned integration of CHP to urban areas;
- A flexibility in the regulations to connect CHP with the electricity grid;
- An awareness of the benefits of CHP; and
- A common standard and methodology with some metrics to measure energy savings and environmental benefits.

A schematic that shows the components of a trigeneration plant is shown in Figure 1.1. The figure shows that the trigeneration plant consists of four main units:

- A power generation unit, which is known as the plant's prime mover, such as a gas turbine;
- A cooling unit, such as a single-effect absorption chiller;
- A heating unit, such as the boiler of the plant; and
- An electrical generator.

The energy process in a trigeneration plant can be described as follows:

- Mechanical power is produced from a mechanical power generator unit, such as a gas turbine.
- The mechanical power produced is used to rotate an electrical generator.
- Waste heat from the mechanical generator unit – which includes exhaust gases, lubrication oil, and jacket water – is recovered to partially or totally meet the cooling and heating loads.

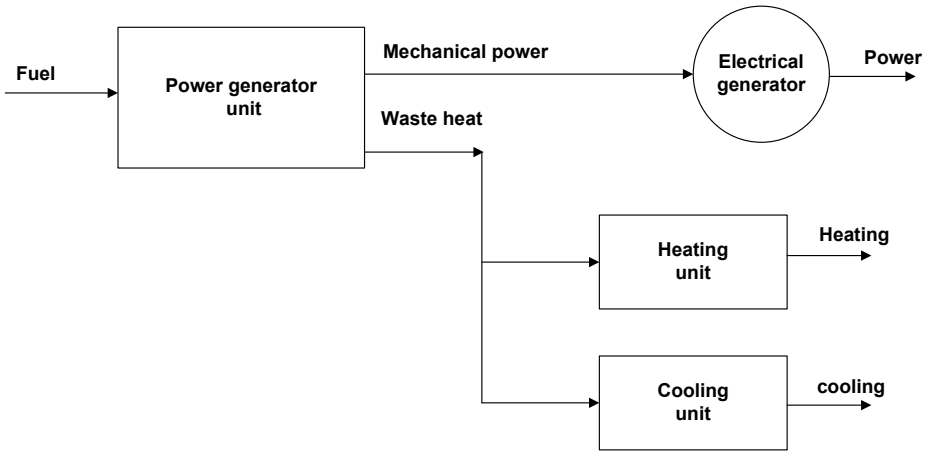

Figure 1.1 Schematic of a typical trigeneration plant.

- The waste heat is used to totally or partially meet the heating load, such as a building heating load.
- The waste heat is used to meet totally or partially the cooling load. The cooling energy is obtained from, for example, a thermally activated single-effect absorption chiller.

In some trigeneration plants, such as the plants used for residential purposes, the heating system works during winter while the cooling system works during the summer.

To achieve a highly efficient and economic trigeneration plant, some criteria are recommended. A report by the International Energy Agency [3] stated certain criteria that need to be satisfied so that a CHP power plant can be utilized. These criteria are:

- A ratio of electricity to fuel costs of at least 2.5:1.
- Relatively high demands for heating and/or cooling. This demand should be at least 5,000 hours a year.
- The ability to connect to the grid, if possible, at an acceptable price.

- The plant should be located close to the end user. This reduces the heating and/ or cooling losses through piping.

To optimize the use of a trigeneration plant, two important points should be considered in designing a trigeneration plant. A trigeneration plant should be flexible enough to meet the variation in the heating and cooling demands. Also, since the heating and/or cooling demand might be minimal for a specific time of the year, a storage system might be needed as a subsystem of a trigeneration plant.

In this chapter, the benefits of trigeneration plants are presented. Then, a summary of the prime mover types is presented with some guidelines on prime mover selection for trigeneration. Lastly, the motivation, significance, and objectives of this study are presented.

1.2 Benefits of Trigeneration Plants

There are many benefits of trigeneration plants, including higher plant efficiency, reduced thermal losses and waste heat, reduced operating cost, reduced greenhouse gas emissions, better use of resources, short transmission lines, fewer distribution units, multiple generation options, increased reliability, and less grid failure. These benefits are discussed below.

First, trigeneration improves the overall efficiency of the plant and reduces operating costs. The overall efficiency of conventional power plants that use fossil fuel with a single prime mover is usually less than 39%. That is, more than 60% of the heating value of the fuel entering a conventional power plant is lost. On the other hand, the overall efficiency of a conventional power plant that produces electricity and heat separately is around 60% [4]. However, with the utilization of the waste heat from the prime mover, the efficiency of the trigeneration plants could reach 80% [3,4]. In a trigeneration plant, the waste heat from the power production is used to operate the cooling and heating systems without the need for extra fuel, unlike a conventional power plant that requires extra fuel or energy resources.

Thus, a trigeneration plant uses less fuel to produce the same output as a conventional power plant. Therefore, the energy produced by a trigeneration plant costs less.

Second, trigeneration reduces greenhouse gas (GHG) emissions. Since a trigeneration plant uses less fuel to produce the same output compared with a conventional power plant, the amount of fuel burned is less for a trigeneration plant. Therefore, a trigeneration plant produces lower GHG emissions. The expected reduction in CO_2 emissions as a result of using trigeneration and cogeneration plants will be 170 Mt/year in 2015, while in 2030 the expected reduction will be 950 Mt/year [3]. Although the gas emissions from trigeneration plants are less than that of conventional plants, there could be some restrictions in using trigeneration plants as distribution plants because of their on-site gas emissions. When using an on-site trigeneration plant, the gas emissions are highly concentrated on the end-user site, unlike a centralized plant where the gas emissions are usually at a distance from the end-user site.

Third, trigeneration reduces cost and energy losses since it needs significantly fewer electricity transmission lines and distribution units. The conventional production of electricity is usually from a centralized plant that is generally located far away from the end user. The electricity, produced from the centralized plant, is transferred through long transmission lines and many distribution units. These long transmission lines and distribution units are very costly. In addition, as a result of the long transmission lines, there are losses in electricity from the lines. It was reported that the losses due to the transmission and distribution of electricity from the centralized plants to the end user could reach 9% [3, 4]. Conversely, these losses are significantly lower for trigeneration plants compared with the centralized plants.

Fourth, trigeneration produces energy as it is needed. The centralized plant is planned to produce the electricity based on the history of power demand. However, in the case of a trigeneration plant that is located in the end-user site, a better estimation of how much

electricity is needed can be obtained. Therefore, the energy is produced as it is needed.

Fifth, trigeneration has a high reliability rate. For example, the 2003 blackout of the Northeastern USA and Ontario cost billions of dollars and left millions of people in darkness. Many hospitals in New York suffered from the electricity shortage because of this blackout [5]. In another incident, electricity transmission lines and distribution poles suffered from an ice storm in Canada and the USA in 1998. In this ice storm, the freezing rain destroyed more than 30,000 distribution poles and 1,000 wooden high voltage transmission towers. As a result of the storm, around 5.2 million people were without electricity [6]. However, using a trigeneration plant as a decentralized plant for a facility, improves the reliability to the point where the chance of grid failure is negligible since the transmission lines and distribution units are significantly reduced.

The benefits mentioned above have encouraged many researchers and engineers to develop advanced trigeneration plants for trigeneration purposes. It should be noted that the improvement in efficiency when trigeneration is used is in thermal efficiency. Further assessments before selecting trigeneration plants, such as initial capital and operating costs, are needed in addition to the recommended criteria for the highly efficient and economic trigeneration plants, as mentioned in the previous section.

1.3 Prime Movers

Prime movers are the main components of trigeneration plants. Therefore, selecting a prime mover of a trigeneration plant is a major concern. Examples of prime mover types are internal combustion engines, external combustion engines (e.g. Stirling engines), steam turbines, gas turbines, microturbines, and fuel cells. The characteristics of these prime movers are shown in Table 1.1. By defining the electricity, heating, and cooling demands of a trigeneration plant, this table can help to select the appropriate prime mover. In selecting

a prime mover, the following guidelines could be used:

1. The demand of the electricity load is determined by taking into consideration the power efficiency and possibility of having more than one prime mover.

2. The total amount of heat needed for heating and/or cooling demands is determined. Based on these demands, the power to cooling and heating ratios of the desired plant are calculated.

3. The operating range of the prime movers can be extended. For example, a reheating system for a multi-stage prime mover can be used for this purpose.

4. A prime mover that can operate with more than one fuel type adds flexibility to the operation of the prime mover. On the other hand, the fuel type has an impact on the greenhouse gas emission rate. For example, the greenhouse gas emissions from the natural gas combustion are less than the emissions from diesel combustion.

5. The location of the plant may have a restriction on the acceptable noise level, on-site emissions, and the trigeneration plant size. Therefore, the prime mover's noise level, emissions, and power density should be considered.

6. If a prime mover is to be used as a backup system for emergencies, the start-up time should be considered.

7. The type of fuel has an impact on both operation and maintenance costs. The fuel type may affect the internal coating life time of the prime mover, and, therefore, more frequent maintenance may be needed.

After selecting a prime mover, thermal and economic analyses need to be conducted to obtain detailed results of the feasibility of using the selected prime mover for the proposed trigeneration plant.

Table 1.1 Prime movers characteristics

	ICE	Stirling engine	Steam turbines	Gas turbines	Microturbines	Fuel cells
Size (kW) [7]	<75,000	1 - 55 [8]	50 - 250,000	500 -250,000	30 - 250	5 - 2000 [e]
Power efficiency (HHV) (%) [7]	22 - 40	∼ 35 [a], [d][9, 10]	15 - 38	22 - 36 (simple cycle)	18 - 27	30 - 50
CHP overall efficiency (HHV) (%) [7]	70 - 80	60 - 80 for cogeneration [a][11]	80	70 - 75	65 - 75	55- 80
Effective electrical efficiency (%) [b][7]	70 - 80	-	75	50 - 70	50 - 70	55 - 80
Power to heat ratio [7]	0.5 - 1	1.2 - 1.7, with cogeneration [11]	0.1-0.3	0.5 - 2	0.4 - 0.7	1 - 2
Partial load [7]	OK	Good [11]	OK	Poor	OK	Good
Fuel pressure (KPa) [7]	7 - 310	>14 [8]	n/a	689 - 3,447 (compressor)	345 - 552 (compressor)	3.4 - 310
Fuel type [7]	Natural gas, biogas, propane, landfill gas	All [8]	All	Natural gas, biogas, propane, oil	Natural gas, biogas, propane, oil	Hydrogen, natural gas, propane, methanol
Noise [7]	High	Moderate [8]	High	Moderate	Moderate	Low
Power density (kW/m^2) [7]	35 - 50	-	>100	20 - 500	5 - 70	5 - 20
CO_2 (kg/MWh) [12]	504 - 651	673 for STM 4-260 [8]	-	525 - 680	725	430 - 490
NOx (kg/MWh) [12]	0.23 - 9.9	0.18 - 0.91 [13]	-	0.14 - 0.5	0.18	0.0045 - 0.014
lb/MWh$_{TotalOutput}$ (not including selective catalytic reduction) [7]	0.06 rich burn 3-way cat.; 0.8 lean burn	-	Gas 0.4-0.8, Wood 0.9-1.4, Coal 1.2-5.0	0.17-0.25	0.08-0.20	0.011 - 0.016
Start-up time [7]	10 sec	-	1 hr - 1 day	10 min - 1hr	60 sec	3 hrs - 2 days
Operation and maintenance cost ($/kWh$_e$) [7]	0.009 - 0.022	-	<0.005	0.004 - 0.011	0.012 - 0.025	0.032 - 0.038
Hours to overhauls [7]	25,000 - 50,000	-	>50,000	25,000 - 50,000	20,000 - 40,000	32,000 - 64,000 [f]
Equipment life (years) [8]	20	-	>25	20	10	10
Availability (%) [7]	92 - 97	85 - 90 (expected) [11]	Near 100	90 - 98	90 - 98	> 95
Uses for thermal output [7]	Hot water, LP steam	-	LP-HP steam	Heat, hot water, LP-HP steam	Heat, hot water, LP steam	Hot water, LP - HP steam
Waste heat temperature (^{o}C) [14]	38 - 128	-	-	316- 649 without recuperator	204 - 260	40 -1000 [15]
Useable temperature for CHP (^{o}C) [16]	82 - 360	-	-	260 - 593	204 - 338	60 - 371
CHP installed costs ($/kWe) [7]	1,100-2,200	1,300 STM Power Model 4-120 [8]	430 - 1,100	970 - 1,300 (5-40 MW)	2,400 - 3,000	5,000 - 6,500
Heat recovery added cost ($/kW) [17]	75 - 150 for gas engine	-	-	100 - 200	75 - 350	Included
Thermal output (kJ/kWh) [c][8]	3,376 - 5,908	-	1,055- 52,753	3,376 - 7,174	4,748 - 6,858	1,900 - 4,431
Turnkey cost (no heat recover) ($/kW) [17]	350 - 1000	-	-	650 - 900	600 - 1,100	1900 - 3500

Note: the data in each row is based on the reference in the first column except where it is excepted.

Note: all costs from [7] are in 2007 US dollar.

a : Not specified (HHV or LHV).

b : Ratio of net power output to net fuel consumption, where net fuel consumption excludes the portion of fuel used for producing useful heat output.

c : Thermal output is based on recoverable thermal energy available per kWh of power generated.

d : With regenerator. For simple Stirling engine the efficiency is usually less than 20%.

e : Size for CHP applications.

f : Replacement of major parts of the SOFC (such as shift catalyst, reformer catalyst and stack). Filters are recommended to replace every 2,000 to 4,000 hours.

1.4 Motivation and Significance of the Study

Considering the issues of fossil fuel depletion and global warming, using efficient systems, such as trigeneration systems, is becoming more crucial. Recently, trigeneration plants for combined cooling, heating, and power production have received more attentions due to their high thermal efficiency, low operating cost per energy output, and low greenhouse gas (GHG) emissions. Organic Rankine cycle (ORC) is a potential subsystem that can be integrated into trigeneration plants. However, using ORC as a power producer in trigeneration plants is one of the possible configurations that have not received attention by the researchers. Therefore, this study will provide the industry and researchers with significant knowledge on the performance of such trigeneration plants.

ORC is expected to play an important role in energy production in the near future. This is mainly because the ORC can be integrated with a thermal system where a relatively low- or medium-temperature waste heat is available from the thermal system. The literature review discussed in the next chapter shows that there has been no thermodynamic or thermoeconomic studies that consider an ORC as a prime mover of a trigeneration plant. The current study, intends to cover this gap. This study provides a comprehensive thermodynamic modeling and thermoeconomic optimization of three novel trigeneration systems using ORC as a prime mover. In this study, three different prime movers combined with ORC for a trigeneration system are examined. These prime movers are: combined ORC with solid oxide fuel cell (SOFC), combined ORC with biomass combustor, and combined ORC with solar subsystem. The current study contributes to the assessment of the ORC as a prime mover of a trigeneration plant through a comprehensive thermodynamic analysis, GHG emissions assessment, thermoeconomic modeling, and thermoeconomic optimization. To the best knowledge of the author, there is no study that has considered the thermoeconomic optimization of a trigeneration system. Hence, this type of analysis is considered

original, which will provide significant knowledge to the industry and researchers.

1.5 Objectives

The overall objective of the thesis is to provide a better understanding of the performance of the three novel trigeneration systems considered, including their true efficiencies, exergy losses, and GHG emissions, as well as the cost rate and cost per exergy unit of electrical power and trigeneration using thermoeconomic optimization. The examined systems are designed such that each one can produce 500 kW of electrical power. To assess the improvement in the performance of each trigeneration system considered, as compared to conventional systems, four cases are considered for each system: electrical-power, cooling-cogeneration, and heating-cogeneration cases, as well as trigeneration case.

The specific objectives of this study are

- To propose three novel trigeneration systems;
- To conduct energy and exergy analyses of the trigeneration systems considered to assess their performance;
- To develop an exergy destruction model to predict the quantities and locations of the exergy destructions in the trigeneration systems considered;
- To carry out an environmental impact assessment to evaluate the GHG emissions from the trigeneration systems considered;
- To develop thermoeconomic models to assess the thermoeconomic performance of the trigeneration systems considered;
- To carry out thermoeconomic optimization to minimize the cost per exergy unit of the combined cooling, heating, and electrical powers; and

- To compare the results of the thermoeconomic optimization of the three trigeneration systems through thermodynamic modeling and thermoeconomic optimization.

Chapter 2

Literature Review

2.1 Introduction

The review of trigeneration plants can be classified based on the prime movers, cooling systems, application type, or analysis type. However, what mainly distinguishes one trigeneration plant from another is the prime mover of the plant. Therefore, the review of the trigeneration plants in this section focuses on the prime movers of these plants. The categorization of the sections and subsections are based on the type(s) of the prime movers. Under each subsection that identifies the prime mover type(s), the review is classified based on the type of analysis that has been conducted. The prime mover types are internal combustion engines, external combustion engines, Rankine cycles, gas turbines, micro-turbines, and fuel cells. The types of these analyses are energy, economic (excluding exergoeconomic), environment, optimization, exergy, and exergoeconomic (thermoeconomic).

This chapter begins with the details of the literature review and then provides the summary of the literature review. The details of the literature review are organized as follows. It starts with the review of the studies that conducted analyses with one and two types of prime movers. Then, a review of the studies with more than two prime movers is presented.

Lastly, the review of the studies that did not specify a specific type of prime movers of the trigeneration plant is presented.

2.2 Single Prime Mover

2.2.1 Internal Combustion Engine

Several studies have been conducted with internal combustion engines as the only prime movers of trigeneration plants, e.g. [18–49]. A description of a trigeneration pilot plant for two office buildings and measurement methodology to monitor them was discussed by Cardona and Piacentino [26].

Studies where only energy analysis was carried out have been conducted by [27–32]. A micro-scale building cooling, heating and power (BCHP) system with an adsorption chiller was experimentally studied by Huangfu et al. [27]. The authors studied the performance of the adsorption chiller under different heating conditions. They found that there was almost a linear relation between the adsorption chiller and the change of hot water inlet temperature for the two investigated models.

The energy analysis of trigeneration plants with heat pumps was examined by [28–30]. Design and development of a trigeneration plant with a reversible heat pump were performed by Miguez et al. [28]. In another study, Porteiro et al. [29] extended Miguez et al. [28] study to compare different operating modes. They concluded that the heat pump was important for plant efficiency enhancement. An experimental analysis of solid sorption heat pumps was carried out by Vasiliev [30]. It was found that a saving of 15-20% can be gained with the solid sorption heat pumps.

Pospisil et al. [31] compared cogeneration and trigeneration plants for energy supply of tertiary buildings. They found that compared with the separated energy production of power, heating, and cooling, the cogeneration plant consumed 31% less of the primary

energy source and the trigeneration plant consumed 39% less of the primary energy source. In another study, the application of trigeneration plants in supermarkets was discussed by Maidment and Tozer [32]. An energy analysis was performed on five schemes where each scheme had a different absorption chiller. The study revealed that for the short to medium term of time the trigeneration plant could result in significant primary energy savings and reduction in CO_2 emission compared to the production of energy that was based upon a gas boiler and coal derived electricity.

Studies that included only energy and economic analyses were carried by [33–37]. Chicco and Mancarella [33] compared six different designs for cooling production where one of the designs was not a trigeneration plant. They examined the effect of electricity and gas price variation on the pay-pack time. This analysis provided a reasonably good picture for comparing different trigeneration solutions. In a different study, Chicco and Mancarella [34] proposed some energy indicators to assess the fuel efficiency of a trigeneration plant as opposed to a conventional plant with separate production of cooling, heating, and power. In another study, Chicco and Mancarella [35] applied these energy indicators to introduce a planning criterion called equivalent gas price. The authors applied this planning criterion to several case studies. Also, in another study, Chicco and Mancarella [36] used the trigeneration primary energy saving indicator as defined by [34]. They applied the indicator on different scenarios where each scenario had different cooling, heating, and power loading ratio.

A few papers investigated the pollution emission of the trigeneration plants with internal combustion engines as prime movers, e.g. [38–41]. Lin et al. [38] compared experimentally the thermal efficiency and pollution emission of a household size trigeneration plant with another plant producing only power. The authors found an increase of total thermal efficiency between 2 and 4.4 times compared with the plant that produced only power, which is considered huge. The reduction of CO_2 emissions per unit kWh in the trigener-

ation plant were between 67.2% and 81.4%. In their analysis, the authors compared the trigeneration plant with the power plant. However, ideally the trigeneration plant should be compared with another plant that had a power generation unit, cooling system, and heating system where each one of these three systems operates independently using different energy sources. In a different study, Chicco and Mancarella [39] defined poly-generation primary energy saving and poly-generation CO_2 emission reduction indicators. Godefroy et al. [40] conducted experimental and mathematical analyses of a small-scale combined heating, power, and cooling system. The cooling system contained ejector cycles which is not the common case for trigeneration plants where either absorption and/or adsorption chillers are used. It was found that using some of the electrical output to operate the cooling cycle improved the cooling capacity. However, it did not improve overall efficiency and resulted in an increase of CO_2 emissions. In their study, the authors pointed out the effect of using some of the electrical output for the cooling cycle but not the use of more power generation waste heat to increase the cooling cycle power. Therefore, the authors' conclusion should not be considered as a basis to judge the feasibility of using the trigeneration plant with ejector cycles cooling system. In another study, Lindmark et al. [41] compared five different configurations of absorption chillers. The plant prime movers were humidified internal combustion engines. The study aimed to investigate the effect of each configuration on the electrical yield. In the humidified internal combustion engine, the vapor content of the flue gas condensed in a pressurized condenser. It was found that utilizing a trigeneration plant for extra electricity and cooling production, instead of mechanical chillers, could decrease CO_2 emissions. The study revealed that the humidified trigeneration plant was profitable as long as the operating hours were more than 3500 hours per year.

Optimization of trigeneration plants with internal combustion engines as prime movers have been conducted by [42–45]. Cho et al. [42] presented a linear programming formulation of a typical trigeneration plant. The inputs consisted of electricity and fuel cost and

the constraints consisted of the load demands of cooling, heating, and electricity. Several scenarios with different operating conditions were examined. It was concluded that the optimization of the trigeneration plant components will result in a significant economic gain. Cardona et al. [43] carried out an optimization analysis of the design and operation of trigeneration plants that have a heat pump. They used multi-objective criterion to select the operation mode that was dependent on energy demand and price. The study showed a complete match between economic and environmental choices was not feasible since this match would require a special plan for each case study.

A few studies have applied an exergy analysis on trigeneration plants that contain internal combustion engines as prime movers, e.g. [44–49]. Huangfu et al. [46] performed cost and exergy analyses on a micro-scale trigeneration plant with an adsorption chiller. It was observed in both the combined operation mode of cooling and power, or heating and power that the primary energy ratio and exergy efficiency were higher than the conventional power generation without cooling or heating (not a combined mode). Also, it was concluded from the exergy analysis, to get an improvement in the trigeneration plant, the electrical efficiency of the internal combustion engine should be improved. Tracy and Ordonez [47] conducted first and second law thermodynamic analyses of a trigeneration plant. They studied the effect of splitting the waste heat proportionately between the heating and cooling systems.

Exergy and exergoeconomic analyses were performed by [44, 45, 48, 49]. Deng et al. [48] carried out an exergy cost analysis of a small-scale trigeneration plant using the structural theory of thermoeconomics. They observed that as the electricity output increases, the unit exergy cost of product for all plant components drops slowly. The authors found that when the electricity output reaches above 10.3 kW, the production performance of the adsorption chiller improved. In their study, the electrical output range is from 7 to 12 kW. In another study, Temir and Bilge [49] analyzed the exergoeconomics factor versus

the unit exergetic cost of natural gas. They noticed that as the fuel cost increases, the exergoeconomics factor of the absorption chiller unit, internal combustion engine and waste heat boiler decreases. The study showed that the exergoeconomics factor of the internal combustion engine was the most sensitive to the fuel cost while the waste heat boiler was the least sensitive.

More comprehensive studies that include exergy, exergoeconomics, and sensitivity analyses were performed by [44, 45]. Cardona and Piacentino [44] proposed a modified exergoeconomics optimization approach to trigeneration plants. The approach was based on the use of aggregate energy flow or average flow rates that can be derived from any trigeneration plants' software. The authors examined the effect of the prime mover, which was an internal combustion engine, and the absorption chiller size on different variables that included unit exergy cost of streams, decision function, average unit cost of thermal exergy, unit cost of cooling exergy, and unit cost of electricity. They showed at which prime mover and absorption chiller sizes these variables have low exergy costs. A similar sensitivity analysis to [44] was carried out by Cardona and Piacentino [45]. This analysis was applied to a 300-bed hospital located in a Mediterranean area. The study helped to minimize the overall annual cost of energy supply and to determine what energy outputs have margins of profitability over the conventional generation plants.

2.2.2 External Combustion Engine (Stirling Engine)

To the author's best knowledge, only a single paper has been published using a Stirling engine as a prime mover for a trigeneration plant, [13]. Kong et al. [13] compared the energy and economic efficiency of a trigeneration plant using a Stirling engine as a prime mover with a conventional plant with separate production of cooling, heating and power. They found that the trigeneration plant with the Stirling engine saved more than 33% of the primary energy compared to the conventional plant. In their study, a double-effect

absorption chiller was assumed. The study revealed that the absorption chiller thermal performance had a large effect on the energy efficiency of the trigeneration plant.

2.2.3 Steam Turbines

Studies that discussed trigeneration plants operating with steam turbines were conducted by [50–53]. Schroeder et al. [50] discussed ice water production in a centralized trigeneration plant. They recommended three different ways of co-operation of a single-effect absorption chiller with an existing circulation of low-pressure steam and hot water. The authors discussed the details of these three ways of co-operation.

Costa et al. [51] analyzed the economics of operating a trigeneration plant in a pulp mill. The authors compared trigeneration, cogeneration, and absorption heat pump models. The heat pump was included in the analysis to allow for examination of the maximal reduction of the energy consumption without power production. They concluded that the trigeneration model had the best overall net positive value. However, the cogeneration model did not include a cooling load, and the absorption heat pump model did not produce power. Therefore, their conclusion on the overall best value produced by the trigeneration model was not precise.

Rong and Lahdelma [52] developed an optimization model for three energy components. The objectives of this model were to minimize the production and purchase cost of these energy components beside CO_2 emissions cost. The authors applied the model on a plant based on a steam turbine. The authors assumed power production and two heating loads with no cooling load. This study focused on comparing the performance of the proposed optimization model, which is called Tri-Commodity Simplex (TCS), with a linear programming (LP) model. The study revealed that the proposed TCS model was much faster to converge.

Poredos et al. [53] carried out an energy and exergy efficiency analyses of cooling

chillers in a trigeneration plant. The study compared the efficiency of five cooling systems: four different absorption chillers and an electrical compressor. The analysis revealed that the exergy efficiency of the absorption chillers increased when they were used in the trigeneration plant compared to the exergy efficiency of the individual absorption chillers operating without using the trigeneration plant. The exergy efficiency of the electrical compressor remained the same.

2.2.4 Gas Turbines

Different studies have been carried out on trigeneration plants that have gas turbines as prime movers, e.g. [54–64]. A study where only energy analysis was carried out was conducted by [55]. Calva et al. [55] developed a simple model used to evaluate various available gas turbine systems and showed how to design trigeneration plants based on the results obtained from the model.

Energy and economic analyses were carried out by [56–60]. The use of a trigeneration plant in Shanghai Hospital was discussed by Daolin and Shifei [56]. They presented the plant commissioning issues and the accompanying problems, as well as an economic assessment of the plant. Ziher and Poredos [57] addressed the economics of using a trigeneration plant in a hospital. They provided the cooling, heating, and power price per kWh on a monthly basis for one year. To obtain the cooling energy, the authors recommended including steam absorption and compression chillers with a cold storage system in the plant. Cardona et al. [58] analyzed typical energy demand profiles in airports and assessed the feasibility of using trigeneration plants in the airports. Their analysis showed a large potential for primary energy saving and reduction in the operating cost of the plant.

An environmental analysis was performed by [59]. Casten [59] analyzed the economic and environmental impact of different trigeneration plants using ammonia chillers. The author discussed how difficult to obtain both economic and environmental solutions at the

same time.

Optimization studies were carried out by [60, 61]. The analysis of the influence of energy demand ratios on optimal capacity of facilities and feasibility indices were conducted by Chao-zhen et al. [60]. The design variables of the optimization in this study were capacities, maximum purchased gas, and maximum purchased electricity. The objective functions were annual cost, maintenance cost and operation cost, and the constraints were facility and energy balance. Twenty five numerical cases were analyzed and in many of these cases the cooling demands had more effect on the gas turbine capacity than the heating demands.

An exergy analysis on a trigeneration plant based on a gas turbine was conducted by [61–64]. Khaliq and Kumar [62] and Khaliq [63] used similar trigeneration model to study the performance assessment of a trigeneration plant based on a gas turbine. Both studies examined the effect of the variation of the compressor pressure ratio and process heat pressure on first law efficiency, second law efficiency, and electrical to thermal energy ratio. Khaliq [63] performed a further analysis that included the effect of variation of turbine inlet temperature, pressure drop percentage of combustion chamber and heat recovery steam generator, and evaporation temperature on first law efficiency, second law efficiency and electrical to thermal energy ratio. The study revealed that more than 80% of the total exergy destruction in the overall plant occurred during the combustion and steam generation process.

Exergy and exergoeconomic analyses were carried out by [61, 64]. Cao [64] investigated thermodynamic performance of building cooling, heating, and power (BCHP). The study examined the effect of power load on the efficiencies of energy and exergy and the exergetic costs in unit amount of power, steam , and cooling water versus power load rates. It was concluded that the investigated model could be economical if its power load rates were maintained higher than 50%. A study by Cao and Liu [61] used a model similar to [64] to analyze the performance of a BCHP plant in China during air-conditioning sea-

son. The authors studied the overall exergetic efficiency under different power loads, mass proportion of steam, and compressor inlet temperatures. The optimization analysis used the overall exergetic efficiency as the objective function, and the constraints were power load, mass proportion of steam, and compressor inlet temperature. The authors found that the plant produced positive benefits only at high power load rates.

2.2.5 Microturbines

Several studies on trigeneration plants, with microturbines as the only prime movers, have been conducted, e.g. [65–81]. Studies where only energy analysis has been conducted were presented by [68–72, 74]. A plant design of a novel trigeneration microturbine combined cycle for ice production was proposed by Lear et al. [68]. The authors carried out heat and performance analyses of a double-effect absorption chiller, and concluded that their proposed design can increase the total thermal efficiency of the trigeneration plant, or can be used to cool another system. Ryu et al. [69] performed dynamic modeling of ice production to improve the load-leveling during the peak summer utility period using two single-effect ammonia/water absorption chillers and a cooling storage system. Based on the application, for example, air conditioning or ice making, they explained how to operate the plant for better performance. In another study, the impact of some technological advancements, such as thermally activated cooling systems on BCHP, was studied by Jalazadaeh-Azar [70]. The author observed that a microturbine without a recuperator can have a negative impact on the total primary energy consumption. The author provided the detail electricity output and cost of the plant. Fairchild et al. [71] carried out an experimental and analytical performance study of a microturbine used for a BCHP. In another study, Labinov et al. [72] presented algorithms to predict the performance of a microturbine used as a prime mover for a BCHP.

Energy and economic analyses studies were carried out by [73–79]. Jääskeläinen and

Wallace [74] investigated a trigeneration plant that used a 240 kW microturbine as a prime mover. The economic analysis of this plant revealed that it was not attractive to utilize due to high natural gas prices and low electricity rates.

Environmental and economic analyses were performed by [75, 76]. Tassou et al. [75] showed that as the absorption refrigeration system coefficient of performance increased from 0.5 to 1, the payback period reduced from 4.5 to 3 years and the savings in CO_2 emissions increased from 0.2 to 1.4 tCO_2. Also, it was observed that, with current installation costs at the time of the study (2006-2007) of microturbine used in trigeneration plants, their economic feasibility was very sensitive to the price of natural gas relative to the price of grid electricity. To have a reasonable payback period, the ratio of the natural gas price to the grid electricity price should be less than 0.3. In another study, Bruno et al. [76] investigated the performance, emission, and economics of utilizing biogas into different trigeneration plant systems. The authors used a sewage treatment plant as a case study. The best model was the one that met the sewage treatment plant heating demands using all the available biogas with additional natural gas.

A sensitivity analysis was conducted by [77, 78]. Campanari et al. [77] and Campanari and Macchi [78] used the same sensitivity model that consisted of single-effect and electrical chillers. They performed sensitivity and cost analyses of a trigeneration plant. Campanari et al. [77] found that as a result of the large load variation, the optimum nominal output of the microturbine was around 70% of the electric peak demand. Campanari and Macchi [78] showed that with the improvement in microturbines performance producing a net electrical efficiency of 35 to 40%, microturbines will be very competitive in trigeneration plant applications.

Huang et al. [80] carried out multi-objective optimization and performance analysis using generic algorithms. The optimization was based on four load conditions that consisted of annual average energy demand, variable thermal power rate, cooling power rate, and typ-

ical monthly load demand. Their study was limited to certain load demands and equipment integration. Therefore, further improvement is needed for the optimization algorithms.

Studies that applied exergy analysis on trigeneration plants that are based on microturbines were carried out by [79, 81]. Liang and Wang [79] evaluated the exergy efficiency of a trigeneration plant with a double-effect absorption chiller. They compared the exergy efficiency of the trigeneration plant with another similar plant that used an electrical chiller, which was not a trigeneration plant. They found that the trigeneration plant with the absorption chiller had a higher exergy efficiency. Medrano et al. [81] compared the exergy efficiency of three trigeneration plants operated with a single-effect, a double-effect and combined single and double-effect chillers. The authors found that the variation of the exergy efficiency of the three plants was less than 1%, which is considered small.

2.2.6 Fuel Cells

A few studies have been conducted on trigeneration plants using fuel cells as prime movers, e.g. [82–87]. Henderson et al. [83] developed a trigeneration plant model that combined a fuel cell model with an hour-by-hour building simulation and described how to predict the performance of the plant using their model.

Phosphoric acid fuel cells (PAFC) type was examined by [84–86]. Seifert [84] studied experimentally a PAFC system that consisted of adsorption and electrical chillers, and a cold storage. The heat recovery system did not succeed as expected and at low loading the system had a low electricity efficiency. Bizzarri [85] examined different hybrid scenarios of PACF trigeneration as applied to nine hospitals. The study included cost and CO_2 emissions analyses and recommended a methodology to size the investigated plants. In another study, Gamou et al. [86] carried out an optimization analysis to examine the effect of uncertain load demands variation. The objective function was to minimize the predicted annual cost. The study revealed that if the system was designed taking into consideration

the uncertainty of demands, the optimal capacity of the fuel cell unit reduced.

Weber et al. [87] used SOFC as a prime mover for trigeneration plants. They carried out detailed CO_2 emissions and cost analyses of a trigeneration plant in an office building. They found that the model produced 30% reduction in CO_2 emissions at an approximate increase in cost of 70% compared with a conventional plant.

2.2.7 A Prime Mover and Solar Energy

A few papers discussed the utilization of solar energy in trigeneration plants, e.g. [88–90]. Buck and Fredmann [88] studied experimentally the performance of a trigeneration plant based on a microturbine and assessed by a small solar tower. The study assessed the economics of using single and double-effect absorption chillers. The authors recommended using the double-effect chiller since it showed better thermal performance and lower operating cost compared to the single-effect absorption chiller.

Bizzarri and Fabiano [89] compared the monthly primary energy consumption and the predicted monthly CO_2 emissions of four plants. Two plants were trigeneration plants where one of them was based on a PAFC and the other was based on a solar thermal system. The other two plants were a conventional plant with electricity from a grid and a similar plant to the conventional plant with integrated photovoltaic solar cells. They found that the plant with the PAFC had constant pollution reduction whereas the other plant operating with the solar thermal system showed favorable pollution reduction in summer. On the other hand, the solar thermal system has the most energy saving.

Medrano et al. [90] used thermal collectors to support the cooling and heating production of a trigeneration plant that had an internal combustion engine as a prime mover. The study revealed that there were a significant saving in energy, as well as reduction in CO_2 emissions.

2.3 Two Prime Movers

2.3.1 Internal Combustion Engine and Gas Turbine

A number of studies discussed within the same study both internal combustion engines and gas turbines, e.g. [91–98]. Li et al. [92] studied a trigeneration plant based on an internal combustion engine and another plant based on a gas turbine. The authors compared the electrical and thermal efficiency of both plants under different electric power loads. Also, they compared the fuel energy saving ratio with the variation of the electrical power load of both plants when each plant operated under heating or cooling mode. The study revealed that, both plants at high electric power demands, had more energy savings compared to low electric power demands. Also, the study showed that the trigeneration plant with the gas turbine had less energy saving potential compared to the trigeneration plant based on the internal combustion engine. A detailed analysis and design of thermal storage as part of a trigeneration project was examined by Dharmadhikari et al. [93]. The author compared different equipments and capital costs with and without a thermal storage subsystem. It was concluded that the thermal storage subsystem reduced the required capacity of the plant chiller. Consequently, the initial chiller cost and plant power load demands reduced. Therefore, the authors recommended including in the plant design, the thermal storage system for economic and environmental reasons.

An optimization analysis was carried out by [94–97]. Colonna and Gabrielli [94] carried out optimization on two plants. The first plant has an internal combustion engine as a prime mover and the other plant has a gas turbine. The optimization constraints were the temperatures at different locations of each plant. The authors analyzed the waste heat from the prime movers using Cycle-Tempo software. The study revealed that the plant with the internal combustion engine was economically better than the plant with the gas turbine.

Environmental analysis and optimization were conducted by [95–97]. Arcuri et al.

[95] presented a mixed integer programming optimization model for energy management of a hospital complex. The objective of the short term optimization was to optimize the gross operation margin while the objective of the long term optimization was to maximize the net positive value. On the other hand, the constraints for both short and long terms were the performance of both compression and absorption heat pumps, as well as energetic balance of different variables. The authors found that the integration of the heat pumps into the trigeneration plant had significant economic, energy, and environmental gains. The trigeneration plant based on the internal combustion engine showed better economic benefits compared to the plant based on the gas turbine.

A thermoeconomic optimization of a proposed trigeneration plant at an urban residential area in Beijing, to assess the economic and emission criteria of the trigeneration plant, was performed by Li et al. [96]. The analysis included a mixed integer and non-linear programming, and was solved with a generic algorithm optimizer. The objective was to maximize the plant net present value. The authors examined the effect of changing the emission taxes of CO_2 and NO_x and they found that four trigeneration plant configurations were optimum since they had the lowest emission tax levels. Three of these four plant configurations were based on gas turbines, and the fourth one was based on an internal combustion engine. In a different study, a hybrid optimization approach was presented by Piacentino and Cardona [97]. The objective was to obtain a minimum primary energy saving factor of less than 0.1 on an annual basis. The analysis showed the effectiveness of using this optimization approach to increase the plant profits and reduce the pollution emission.

Exergy and exergoeconomic analyses of two trigeneration plants, where each one was based on a different prime mover, were conducted by Ziher and Poredos [98]. The first plant had a gas turbine and the other one had two internal combustion engines. The study compared the cost of using different cooling devices under different cooling loading demands

from March to October. The cooling devices were single and double-effect absorption chillers and a compressor chiller. The study demonstrated that in almost the entire cooling season, it was more efficient to produce cooling from the compression chiller. In the low cooling demand period, March, April, September, and October, the cooling power from the plant based on the internal combustion engine that used the single effect absorption chiller had the lowest cost.

2.3.2 Internal Combustion Engine and Microturbine

Analyzing trigeneration plants with internal combustion engines and microturbines as prime movers was carried out by [99–101]. Chicco and Mancarella [100] applied the trigeneration primary energy saving indicator as presented by [34]. The authors examined this indicator under different trigeneration plants topology and operational points. They recommended carrying out a sensitivity study considering both partial load and off-design models of the cooling, heating, or power generation equipment.

Exergy and exergoeconomic analyses of different BCHP trigeneration plants were carried out by Huang et al. [101]. In this study, one of the plants was based on an internal combustion engine whereas the other plants were based on microturbines. The authors showed that the exergy efficiency of the trigeneration plants was much higher than the conventional plant with separate generation of cooling, heating, and electricity. However, this gain in efficiency was a function of the load. On the other hand, the trigeneration plant that was based on the internal combustion engine showed better payback periods and economic exergy rates compared to the trigeneration plants that were based on the microturbines.

2.3.3 Gas Turbine and Steam Turbine

Combined cycles, gas turbine and steam turbine, as prime movers of trigeneration plants were carried out by [102–106]. As a result of the study conducted by Cardona et al. [58], Cardona et al. [105] extended the analysis to apply it at Malpensa International Airport. The trigeneration plant is based on a combined cycle consisting of three gas turbines with two steam turbines. It was recommended doing minor changes to the operation mode of the airport to reduce energy consumption and pollution's emission. In another study, a comparison between a cogeneration plant based on a gas turbine and a trigeneration plant based on a combined cycle was presented by Santoyo and Sanchez-Cifuentes [106]. It was shown that the trigeneration plant had less fuel consumption compared to the cogeneration plant.

2.3.4 Gas Turbine and Fuel Cells

A comparison between a trigeneration plant using a fuel cell as a prime mover with another three plants powered by a gas turbine was conducted by Kowalski and Zenouzi [107]. The refrigeration device of the plant based on the fuel cell was a vapor compression whereas the refrigeration devices for the plants based on the gas turbine were a vapor compression cycle, absorption cycle, or combined absorption/vapor compression cycle. For large refrigeration to total thermal load ratios, the combined vapor compression/absorption refrigeration for the gas turbine-based plant had larger first law utilization factors and a lower carbon dioxide production rate. On the other hand, the fuel cell based system performed better than the gas turbine based system at high refrigeration load applications.

A system that combined both SOFC with a gas turbine as a prime mover of a trigeneration plant was analyzed by Burer et al. [108]. The system consisted of half, single and double-effect chillers, a compression chiller, a heat recovery boiler, an auxiliary boiler, a

cooling system, and a heat pump. The authors performed first and second law efficiencies of the potential on integrating the heat pump into the trigeneration plant. The study was mainly focused on cost and CO_2 emissions analysis using multi-criteria optimization that was based on multi-objective evolutionary algorithm. The optimization objectives were the annual total cost of power, heating, and cooling generation, and the annual CO_2 emission rates. The analysis demonstrated that the combined system of SOFC and gas turbine was an attractive economical and environmental solution when high electricity and natural gas prices were encountered.

2.3.5 Microturbine and Fuel Cells

An analysis of a hybrid system of microturbine and fuel cell as a prime mover of trigeneration plants was carried out by [109]. Saito et al. [109] carried out energy demand and consumption analyses of apartments, offices and hotels in Japan with the use of the hybrid system. They found that the annual fuel consumption dropped by 32%, 36% and 42% for the apartments, offices, and hotels, respectively.

2.4 Multi Prime Movers

Wang et al. [110] developed a fuzzy multi-criteria decision making model. They applied the model to five different trigeneration plants. For all the five plants, lithium bromide absorption water heater/chiller cooling equipment was assumed. The prime movers for the first four plants were a Stirling engine, gas turbine, internal combustion engine and SOFC. The fifth plant used electricity from an electricity grid. The cooling and heating loads of the fifth plant were produced by a direct-fired lithium bromide absorption water heater/chiller equipment operated by a gas fuel. The trigeneration plant with the internal combustion engine showed the best match to different criteria assigned by the Chinese government.

On the other hand, from the environmental perspective, the SOFC showed the best prime mover.

Mancarella and Chicco [111] used the trigeneration CO_2 emissions reduction indicator as introduced by [112] to examine its effectiveness on different trigeneration plants. Five trigeneration plants with different prime movers were considered. These prime movers were a combined gas turbine and steam turbine cycles, internal combustion engine, and gas turbine and microturbine, as well as integrated fuel cells with a gas turbine. In their analysis, the authors showed the effect of the electrical and thermal efficiencies on CO_2 emissions.

Bing et al. [113] carried out a multi-objective optimization of trigeneration plants. The authors applied the optimization to five different schemes where two schemes had microturbines as prime movers and the other schemes had a Stirling engine, an internal combustion engine and a PAFC as prime movers. The study revealed that the microturbine was the optimal prime mover because of its economic, energy conservation, environmental, and reliability outcomes compared to the other prime movers. The study showed that PAFC was not an economical prime mover; however, its energy conservation, environmental protection, and reliability were very high.

2.5 Studies Without Specifying Prime Movers

Several studies were conducted without identifying a type of a prime mover, e.g. [112, 114–125]. Studies that have been conducted with only energy analysis of trigeneration plants were carried out by [116–118]. Plura et al. [116] compared the performance of different absorption chiller configurations as integrated into a trigeneration plant. These configurations were double and single-effect chillers without direct coupling and the others had different chiller coupling configurations. One of the configurations was selected

to be the best design since only minor modifications were required to the standard plant technology. In this coupling, only one low temperature generator was needed unlike the other coupling that required either two or three generators. In another study, a methodology for the selection and management of trigeneration plants was introduced by Cardona and Piacentino [117]. The proposed methodology was based on thermal and cooling consumption data obtained from several European hotels. In another analysis, Chicco and Mancarella [118] presented a characterization and planning approach to distributed multi-generation plants. They introduced trigeneration system lambda analysis that was based on the cooling power generation impact over the thermal and electrical demand. In another study, Chicco and Mancarella [119] applied lambda analysis to evaluate multi-generation alternatives.

An economic analysis of trigeneration plants was conducted by [120, 121]. Henning et al. [120] discussed the use of a desiccant air cooling system in a Mediterranean climate, where the climate was characterized by high humidity. One type of cooling system, which contained sorptive wheels and cooling coils, was recommended among other configurations that had been considered. It was estimated that the electricity saving in the trigeneration plant was more than 30% as compared to a conventional air handling unit.

An environmental analysis was performed by [112, 122]. Chicco and Mancarella [112] introduced a trigeneration CO_2 emission reductions indicator. The indicator used to assess trigeneration and cogeneration plants CO_2 emission reductions as compared to a conventional plant with separate production of cooling, heating, and power. In another study, Chevalier and Meunier [122] applied a life cycle analysis methodology to assess the environmental impact of biogas co- or tri-generation plants. The authors demonstrated the positive impact of the trigeneration plants on environment compared to a conventional plant with a separate production of the cooling, heating, and power. They pointed out that as the efficiency of a trigeneration plant increased, the positive impact on the environment

increased.

An optimization was carried out by [121, 123, 124]. Rong et al. [121] introduced a Lagrangian relaxation based algorithm for trigeneration planning with storage subsystems. The objective of the optimization of the trigeneration plant was to minimize the overall net acquisition costs. The study focused on explaining the methodology of using the introduced optimization model.

A comparison of exergy and energy efficiencies of a plant with an electric chiller and two trigeneration plants one with a single-effect chiller and the other with a double-effect chiller was conducted by Rosen et al. [125]. The analysis revealed that the overall variation of energy efficiencies for the three plants was from 83% to 94% while the exergy efficiencies variation was from 28% to 29%.

Exergoeconomic analysis and optimization were conducted by [123, 124]. Piacentino and Cardona [123] discussed exergoeconomic analysis of systems that were under unsteady case. Also, they introduced a new optimization algorithm using the Lagrange multipliers method and a multi-objective decision function. The proposed optimization method was applied to a trigeneration plant operating in a large hotel. However, the proposed optimization method was limited to only simple layout of trigeneration plants. In another study, Piacentino and Cardona [124] conducted optimization using mixed integer linear programming model. The objective of the optimization was the net present value of the trigeneration plants. The authors showed how to integrate the exergoeconomic analysis into the optimization model and applied the optimization model into a large hotel and hospital trigeneration plants as case studies.

2.6 Summary of Literature Review

The summary of the literature review is presented in Table 2.1. In this table, the studies are tabulated according to the prime mover type. For each study, usually the prime mover, absorption chiller, and fuel type are specified. However, in some studies, one or more of these three types is not specified in the studies. Therefore, the corresponding box in the table is left blank. That is, each box in the table is checked if there is an indication to it in the corresponding study.

In summary, the studies on the feasibility of trigeneration plants are growing fast and most of the studies have been conducted in the last few years. It is observed that there are several studies that used internal combustion engines as prime movers; however, there are fewer studies on gas turbines and microturbines. On the other hand, there is less research on the other three prime movers: fuel cells, Rankine cycles, and Stirling engines. In terms of analysis type, most of the studies have been conducted using energy and economic analyses. On the other hand, less attention has been given to environmental, exergy, and exergoeconomic analyses of trigeneration plants. In different studies that compared gas turbines with internal combustion engines, it was shown that internal combustion engines are more economical. Also, a few studies, showed that fuel cells are less harmful to the environment as compared to other prime movers.

The literature review shows that there has been no thermodynamic modeling done on ORC as a prime mover of a trigeneration plant. Therefore, the current study has a significant contribution by assessing the use of ORC as a prime mover for a trigeneration plant.

Table 2.1 Summary of literature review

Reference	Prime movers							Fuel type				Cooling equipments						Other equipments					ExMo		Analysis type					Enviro		Sus	SU	
	RE	SEE	ST	GT	MT	FC	SoE	NG	DO	OFF	Bio	SiE	DoE	TrE	Ads	DH	Ele	CT	HRB	AB	CS	HP	Exp	Mod	Eng	Exg	Exo	EE	Opt	GW	AP	Sus	SA	USA
Santo [18]	x							x				x											x		x	x								x
Li and Wu [19]	x														x									x	x								x	
Siddiqui et al. [20]	x							x													x			x	x									x
Sibilio et al. [21]	x							x															x		x			x		x				x
Wang and AlShemmeri [22]	x							x		x														x	x					x				x
Emho [23]	x																								x			x						x
Canova et al. [24]	x																x							x	x			x						x
Frankovic et al. [25]	x																x	x						x	x				x					x
Cadona and Piacentrino [26]	x							x										x		x		x		x	x								x	
Huangfu et al. [27]	x							x		x					x			x					x		x								x	
Miguez et al. [28]	x							x														x		x	x								x	
Porteiro et al. [29]	x							x														x		x	x									x
Vasiliev [30]	x									x												x		x	x									
Pospisil et al. [31]	x											x												x	x									x
Maidment and Tozer [32]	x							x				x	x		x		x				x			x				x					x	
Chicco and Mancarella [33]	x							x									x					x		x	x			x						x

Continued on the next page...

Table 2.1 – Continued

Reference	Prime movers							Fuel type				Cooling equipments						Other equipments					ExMo		Analysis type					Enviro		Sus	SU	
	RE	SEE	ST	GT	MT	FC	SoE	NG	DO	OFF	Bio	SiE	DoE	TrE	Ads	DH	Ele	CT	HRB	AB	CS	HP	Exp	Mod	Eng	Exg	Exo	EE	Opt	GW	AP	Sus	SA	USA
Chicco and Mancarella [34]	x							x									x							x	x			x						x
Chicco and Mancarella [35]	x																							x	x			x						x
Chicco and Mancarella [36]	x							x				x	x									x		x	x			x						x
Temir et al. [37]	x							x					x					x	x	x				x	x			x		x	x		x	
Lin et al. [38]	x									x		x											x		x					x	x		x	
Chicco and Mancarella [39]	x							x				x	x				x							x	x			x		x			x	
Godefroy et al. [40]	x							x									x		x				x	x	x					x			x	
Lindmark et al. [41]	x							x				x	x				x							x	x			x		x			x	
Cho et al. [42]	x							x				x												x	x			x	x	x				x
Cardona et al. [43]	x							x														x		x	x			x	x					x
Cardona and Piacentino [44]	x							x				x					x	x		x				x	x	x	x		x				x	
Cardona Piacentrino [45]	x							x				x					x	x		x				x	x	x	x		x				x	
Huangfu et al. [46]	x							x		x					x			x						x	x	x		x					x	
Tracy et al. [47]	x									x		x												x	x	x							x	
Deng et al. [48]	x									x					x			x						x	x	x	x						x	
temir and Bilge [49]	x							x				x							x					x	x	x	x						x	

Continued on the next page. . .

Table 2.1 – Continued

Reference	Prime movers							Fuel type				Cooling equipments						Other equipments					ExMo		Analysis type					Enviro		Sus	SU	
	RE	SEE	ST	GT	MT	FC	SoE	NG	DO	OFF	Bio	SiE	DoE	TrE	Ads	DH	Ele	CT	HRB	AB	CS	HP	Exp	Mod	Eng	Exg	Exo	EE	Opt	GW	AP	Sus	SA	USA
Kong et al. [13]		x						x					x				x	x						x	x			x						x
Schroeder et al. [50]			x									x							x					x	x								x	
Costa et al. [51]			x						x		x	x										x		x	x			x		x				x
Rong et al. [52]			x																					x					x	x			x	
Poredos et al. [53]			x									x	x				x	x						x	x	x							x	
Genrup et al. [54]				x														x						x	x								x	
Calva et al. [55]				x				x				x					x		x					x	x								x	
Daolin and Shifei [56]				x				x				x							x					x	x			x					x	
Ziher and Poredos [57]				x				x				x					x				x			x	x			x						x
Cardona et al. [58]				x				x				x	x				x		x	x				x	x			x						x
Casten [59]				x				x				x	x						x		x							x		x	x		x	
Chao-Zhen et al. [60]				x				x				x					x							x	x			x	x					x
Cao and Liu [61]				x				x	x				x						x	x				x	x	x	x		x				x	
Khaliq and Kumar [62]				x				x				x												x	x	x							x	
Khaliq [63]				x				x				x												x	x	x							x	
Cao et al. [64]				x					x				x						x	x					x	x	x							
Liao and Radermacher [65]					x			x				x												x	x								x	
Liekens et al. [66]					x			x		x	x		x				x						x		x					x	x		x	
Smugeresky [67]					x			x							x									x					x	x			x
Lear eat al. [68]					x						x										x			x	x									x
Ryu et al. [69]					x							x									x			x	x									x

Continued on the next page. . .

Table 2.1 – Continued

Reference	Prime movers							Fuel type				Cooling equipments						Other equipments					ExMo		Analysis type					Enviro		Sus	SU	
	RE	SEE	ST	GT	MT	FC	SoE	NG	DO	OFF	Bio	SiE	DoE	TrE	Ads	DH	Ele	CT	HRB	AB	CS	HP	Exp	Mod	Eng	Exg	Exo	EE	Opt	GW	AP	Sus	SA	USA
Jalazadeh-Azar [70]					X							X	X												X									X
Fairchild et al. [71]					X			X				X				X		X						X	X					X	X		X	
Labinove et al. [72]					X			X				X												X	X								X	
Sugiartha et al. [73]					X			X				X	X				X			X	X		X	X	X			X		X				X
Jaaskelainen and Wallace [74]					X			X					X				X				X		X		X			X						X
Tassou et al. [75]					X			X				X								X			X		X			X		X				X
Bruno et al. [76]					X			X			X	X	X				X		X	X				X	X			X		X				X
Campanari et al. [77]					X			X				X					X	X	X	X		X		X	X			X	X		X				X
Campanari and Macchi [78]					X			X				X					X	X	X	X		X		X	X			X	X						X
Liang and Wang [79]					X			X					X				X		X					X	X	X		X					X		
Huang et al. [80]					X			X				X					X							X					X				X	
Medrano et al. [81]					X			X				X	X											X	X	X							X	
Malico et al. [82]						X		X																X	X			X						X
Henderson et al. [83]						X												X			X			X	X			X						X
Seifert et al. [84]						PA									X		X				X		X		X									X
Bizzarri [85]						PA		X				X					X					X		X	X			X		X			X	
Gamou et al. [86]						PA		X				X								X				X	X			X	X					X
Weber et al. [87]						SO		X				X	X				X	X				X		X	X			X		X				X
Buck and Friedmann [88]					X		X	X				X	X					X					X					X					X	

Continued on the next page. . .

Table 2.1 – Continued

Reference	Prime movers							Fuel type				Cooling equipments						Other equipments					ExMo		Analysis type					Enviro		Sus	SU	
	RE	SEE	ST	GT	MT	FC	SoE	NG	DO	OFF	Bio	SiE	DoE	TrE	Ads	DH	Ele	CT	HRB	AB	CS	HP	Exp	Mod	Eng	Exg	Exo	EE	Opt	GW	AP	Sus	SA	USA
Bizzarri and Morini [89]						PA	X	X				X					X					X		X	X			X		X	X			X
Medrano et al. [90]	X						X	X				X					X				X			X	X			X		X				X
Gao et al. [91]	X			X					X		X		X				X		X					X	X	X		X		X	X		X	
Li et al. [92]	X			X				X	X			X	X				X							X	X								X	
Dharmadhikari et al. [93]	X			X								X	X				X		X		X	X		X	X					X	X			X
Colonna [94]	X			X				X				X					X	X						X	X			X	X				X	
Arcuri et al. [95]	X			X				X				X	X				X			X		X		X	X			X	X	X	X			X
Li et al. [96]	X			X				X					X											X	X			X	X	X	X		X	
Piacentino and Cardona [97]	X			X													X			X		X		X	X			X	X	X				X
Ziher and Poredos [98]	X			X				X				X	X				X							X	X	X	X							X
Arteconi et al. [99]	X				X							X					X							X	X			X		X				X
Chicco and Mancarella [100]	X				X							X	X									X		X	X			X				X		
Huang et al. [101]	X				X			X				X					X		X			X		X	X	X	X							X
Meckler [102]			X	X								X						X	X		X			X										
Becchis and Genon [103]			X	X																X				X				X		X	X			X
Wallace and Fuchs [104]			X	X				X		X									X					X									X	

Continued on the next page. . .

Table 2.1 – Continued

Reference	Prime movers							Fuel type				Cooling equipments						Other equipments					ExMo		Analysis type					Enviro		Sus	SU	
	RE	SEE	ST	GT	MT	FC	SoE	NG	DO	OFF	Bio	SiE	DoE	TrE	Ads	DH	Ele	CT	HRB	AB	CS	HP	Exp	Mod	Eng	Exg	Exo	EE	Opt	GW	AP	Sus	SA	USA
Cardona et al. [105]			X	X				X	X			X						X	X	X	X			X	X				X	X				X
Hernandez-Santoyo and Sanchez-Cifuentes [106]			X	X				X											X						X			X				X		
Kowalski and Zenouzi [107]				X		X		X				X					X							X	X									X
Burer et al. [108]				X		SO		X				X	X				X		X	X	X	X		X	X	X		X	X	X				
Saito et al. [109]					X	X														X		X			X				X					X
Al-Sulaiman et al. [126]			ORC			SO		X			X	X												X	X								X	
Al-Sulaiman et al. [127]			ORC			SO		X			X	X												X	X					X			X	
Wang et al. [110]	X	X		X		SO		X																X	X	X		X	X	X	X		X	
Mancarella and Chicco [111]	X		X	X	X			X	X			X	X	X											X					X	X		X	
Bing et al. [113]	X	X			X	X		X																	X			X	X	X	X			X
Mago et al. [114]								X		X		X							X					X	X			X		X			X	
Khaliq et al. [115]												X							X					X	X	X							X	
Plura et al. [116]												X	X											X	X								X	
Cardona and Piacentrino [117]																								X	X									X

Continued on the next page. . .

Table 2.1 – Continued

Reference	Prime movers							Fuel type				Cooling equipments						Other equipments					ExMo		Analysis type					Enviro		Sus	SU	
	RE	SEE	ST	GT	MT	FC	SoE	NG	DO	OFF	Bio	SiE	DoE	TrE	Ads	DH	Ele	CT	HRB	AB	CS	HP	Exp	Mod	Eng	Exg	Exo	EE	Opt	GW	AP	Sus	SA	USA
Chicco and Mancarella [118]																	x					x		x	x									x
Chicco and Mancarella [119]																								x	x			x						
Henning et al. [120]															x	x	x				x	x		x	x			x						x
Rong et al. [121]																					x			x				x	x					x
Chicco and Mancarella [112]																								x						x	x			
Chevalier and Meunier [122]											x		x				x							x						x	x	x	x	
Piacentino and Cardona [123]																	x			x				x	x	x	x		x					x
Piacentino and Cardona [124]								x									x			x				x	x	x	x		x					x
Rosen et al. [125]								x				x	x				x							x	x	x								x

AB: auxiliary boiler, Ads: adsorption chiller, AP: air pollution, Bio: biogas, CS: cooling storage, CT: cooling tower, DoE: double-effect absorption chiller, DH: desiccant humidification, DO: distilled oil, EE: engineering economic, Ele: electrical chiller, Eng: energy, Enviro: environmental, Exg: exergy, ExMo: experimental or modeling, Exo: exergoeconomic, Exp: experimental analysis, FC: fuel cell, GT: gas turbine, GW: global warming, HP: heat pump, HRB: heat recovery boiler, Mod: modeling analysis, MT: microturbine, NG: natural gas, OFF: other fossil fuel, Opt: optimization, ORC: organic Rankine cycle. PA: phosphoric acid fuel cell, RE: reciprocating engine, SA: steady from the trigeneration point of view, SE: Stirling engine, SiE: single-effect absorption chiller, SO: solid oxide fuel cell, SoE: solar energy, ST: steam turbine, SU: steady or unsteady, TrE: triple-effect absorption chiller, Sus: sustainability, USA: Unsteady from the trigeneration point of view.

Chapter 3

Thermodynamic Modeling and Thermoeconomic Optimization

3.1 Thermodynamic Equations of Control Volume Systems

3.1.1 Mass Balance

The conservation of mass principle is a fundamental principle in analyzing any thermodynamic system. This principle is defined for a control volume, as shown in Figure 3.1, as follows:

Total mass flow rate entering the control volume	-	*Total mass flow rate leaving the control volume*	=	*Net change in mass flow rate*

or

$$\sum_k \dot{m}_i - \sum_k \dot{m}_e = \frac{dm_{cv}}{dt} \tag{3.1}$$

where m and $\dot{m}$ are the mass and mass flow rate, respectively, and the subscripts i and e refer to the inlet of the control volume and exit of the control volume, respectively. The subscript cv indicates the control volume.

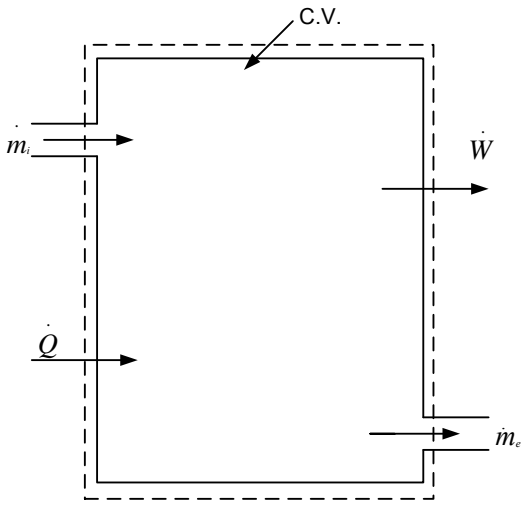

Figure 3.1 Control volume.

3.1.2 Energy Balance

The energy principle of a control volume deals with all the energy components of a selected control volume. The conservation of energy principle, which is known as the first law of thermodynamics, is defined as

Net rate at which energy is being transferred in by heat transfer	-	*Net rate at which energy is being transferred out by work*	+	*Net rate of energy transfer into the control volume accompanying mass flow*	=	*Time rate of change of the energy contained within the control volume*

or

$$\dot{Q} - \dot{W} + \sum_i \dot{m}_i(h_i + \frac{\mathrm{V}_i^2}{2} + gz_i) - \sum_e \dot{m}_e(h_e + \frac{\mathrm{V}_e^2}{2} + gz_e) = \frac{dE_{cv}}{dt} \qquad (3.2)$$

where E, $\dot{Q}$, $\dot{W}$ and t are the energy, heat transfer rate, power and time, respectively. The other symbols, h, V, g and z, stand for specific enthalpy, velocity, gravity, and elevation,

respectively.

3.1.3 Entropy Balance

Entropy generation is associated with the losses in the system. The entropy generated within a process is called entropy generation and it is denoted by S_{gen}. The entropy generation rate for a control volumes is defined as

$$\dot{S}_{gen} = \sum_i \dot{m}_e s_e - \sum_i \dot{m}_i s_i - \sum_k \frac{\dot{Q}_k}{T_k} + \frac{dS_{CV}}{dt} \tag{3.3}$$

where S is the entropy and s is the specific entropy.

3.1.4 Exergy Balance

Unlike energy, exergy is not conserved. It is defined as the maximum work that could be obtained from a system at a given state. To understand the exergy, reversible work should be defined first. Reversible work is the maximum useful work that can be obtained as a system goes through a process between two defined states. Another exergy terminology is the exergy destruction. It is defined as the potential work lost due to irreversibility. The exergy balance of a control volume system is defined as

Rate of exergy change = *Rate of exergy transfer* - *Rate of exergy destruction*

or

$$\frac{dEx_{cv}}{dt} = \sum_j (1 - \frac{T_0}{T_j})\dot{Q}_j - (\dot{W}_{cv} - p_0 \frac{dV_{cv}}{dt}) + \sum_i \dot{m}_i ex_i - \sum_e \dot{m}_e ex_e - \dot{E}x_d \tag{3.4}$$

where T, p, V, ex and $\dot{E}x_d$ are, temperature, pressure, volume, specific exergy, and rate of exergy destruction, respectively. The subscript j is the property value at state j and the

subscript 0 is the value of a property at the surrounding. The physical exergy, ex^{ph}, at a given state is defined as

$$ex^{ph} = (h - h_0) - T_0(s - s_0) + \frac{\mathrm{V}^2 - \mathrm{V}_0^2}{2} + g(z - z_0) \tag{3.5}$$

The chemical exergy of an ideal gas is defined as [128]

$$ex_j^{CH} = x_j \cdot \bar{ex}_j^{CH} + R \cdot T_0 \cdot x_j \cdot \ln(x_j) \tag{3.6}$$

where $\bar{ex}_j^{CH}$ is the standard chemical exergy value of species j

3.1.5 Energy Efficiency

The energy efficiency is a measure of the useful energy from a system to the input energy for this system. The energy efficiencies of different systems are defined in the following text. The thermal efficiency of a thermal cycle is defined as

$$\eta_{cycle} = \frac{\dot{W}_{cycle}}{\dot{Q}_i} = 1 - \frac{\dot{Q}_e}{\dot{Q}_i} \tag{3.7}$$

The isentropic thermal efficiency of work-producing devices is defined as

$$\eta_{is} = \frac{\dot{W}_{ac}}{\dot{W}_{is}} \tag{3.8}$$

On the other hand, the isentropic thermal efficiency of work-consuming devices is defined as

$$\eta_{is} = \frac{\dot{W}_{is}}{\dot{W}_{ac}} \tag{3.9}$$

The performance of refrigerators is known as the coefficient of performance (COP). It is defined as

$$COP_R = \frac{\textit{desired output}}{\textit{required input}} = \frac{Q_L}{Q_H - Q_L} = \frac{1}{\frac{Q_H}{Q_L} - 1} \tag{3.10}$$

where the subscripts is, ac, R, H, and L indicate isentropic, actual, refrigerator, high temperature reservoir, and low temperature reservoir, respectively.

3.1.6 Exergy Efficiency

The exergy efficiency is defined as the ratio of the actual thermal efficiency to the maximum reversible thermal efficiency when both are under the same conditions. In general, the exergy efficiency can be defined as

$$\eta_{ex} = \frac{\textit{Exergy recovered}}{\textit{Exergy supplied}} = 1 - \frac{\textit{Exergy destroyed}}{\textit{Exergy supplied}} \tag{3.11}$$

The exergetic efficiencies of different systems are defined as follows. For heat engines the exergetic efficiency is defined as

$$\eta_{ex} = \frac{\eta_{th}}{\eta_{rev}} \tag{3.12}$$

The exergetic efficiency of work-producing devices is defined as

$$\eta_{ex} = \frac{\dot{W}_{cv}}{\dot{W}_{rev}} = \frac{\dot{W}_{cv}}{\dot{E}x_i - \dot{E}x_e} \tag{3.13}$$

For work-consuming devices, the exegetic efficiency is defined as

$$\eta_{ex} = \frac{\dot{W}_{rev}}{\dot{W}_{cv}} = \frac{\dot{E}x_i - \dot{E}x_e}{W_{cv}} \tag{3.14}$$

For heat exchanger, the exergetic efficiency is defined as

$$\eta_{ex} = \frac{\dot{E}x_{cold,e} - \dot{E}x_{cold,i}}{\dot{E}x_{hot,i} - \dot{E}x_{hot,e}} \tag{3.15}$$

3.2 Thermoeconomics

The term thermoeconomics is defined usually as the methodologies combing exergy and economics to obtain a better design and operation of a thermal system. Since thermoeconomics is based on exergy and cost, it is sometimes called exergoeconomics.

For a k^{th} component receiving heat transfer, q, and generating power, w, the thermoeconomic balance equation of this component is

$$\sum_{e}(\dot{C}_{e,k}) + \dot{C}_{w,k} = \dot{C}_{q,k} + \sum_{i}(\dot{C}_{i,k}) + \dot{Z}_k \tag{3.16}$$

where $\dot{Z}$ is the levelized cost rate to own, maintain, and operate the kth component. Here $\dot{C}$ is the cost rate in \$ per hour, for example. For exergy costing, $\dot{C}$ is defined as

$$\dot{C} = c\dot{E}x_j \tag{3.17}$$

where c is the cost per unit of exergy in \$ per kW/h, or \$ per GJ, for instance, and $\dot{E}x$ is the exergy transfer rate.

Thermoeconomics can be best explained through an example. The example on thermoeconomics from Moran and Shapiro [128] is adopted to explain it. Assume that a simple cogeneration system consists of a boiler and turbine, as in Figure 3.2. Apply the cost analysis on the boiler to get

$$\dot{C}_1 + \dot{C}_P = \dot{C}_F + \dot{C}_a + \dot{C}_w + \dot{Z}_b \tag{3.18}$$

where $\dot{C}$ is the cost rate and $\dot{Z}_b$ is the cost rate associated with owning and operating the boiler each in \$ per hour, for instance. The subscripts 1, p, F, a, w and b indicate stream at the exit of the boiler, combustion products, fuel, air, feed-water, and boiler, respectively. For simplicity, the exergy and cost of the feed-water and combustion air that enter the boiler are assumed to be negligible. Using this assumption, substitute Equation 3.17 into Equation 3.18 to obtain

$$c_1\dot{E}x_{f1} = c_F\dot{E}x_{fF} + \dot{Z}_b \tag{3.19}$$

Similarly, apply cost analysis on the turbine to obtain

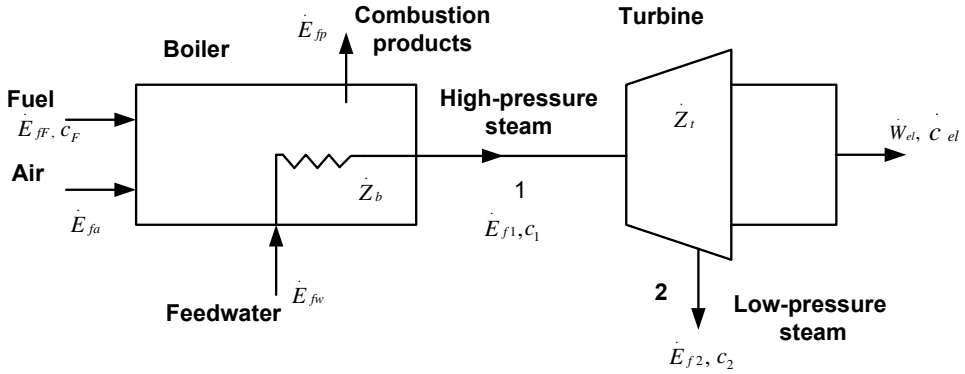

Figure 3.2 Simple cogeneration system, modified from [128].

$$\dot{C}_{el} + \dot{C}_2 = \dot{C}_1 + \dot{Z}_t \tag{3.20}$$

where the subscripts el and 2 refer to electricity and low-pressure steam exit, respectively. The letter $\dot{Z}_t$ refers to the cost rate of the operating and owing the turbine. Now, redefine Equation 3.20 in terms of cost and exergy to obtain

$$c_{el}\dot{W}_{el} + c_2\dot{E}x_{f2} = c_1\dot{E}x_{f1} + \dot{Z}_t \tag{3.21}$$

3.2.1 The SPECO Method

The SPECO method refers to specific exergy costing. In this study, the SPECO method is used to carry out the thermoeconomic analysis, see Figure 3.3. The SPECO method is selected in this study since it is the most widely accepted thermoeconomic method in the literature. An overview of the SPECO method was presented in [129]. The discussion of the SPECO method in this section is based on this reference. This method consists of the

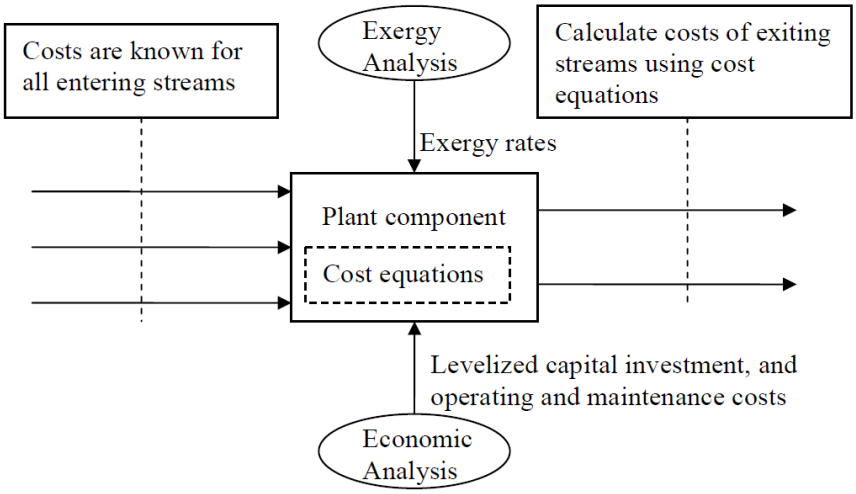

Figure 3.3 SPECO method [130].

following three steps.

1- Identification of exergy streams:

In this step, all exergy streams associated with the entering and existing exergy streams of each component are identified and calculated. These exergy streams are in the power unit and not in power per mass flow rate.

2- Definition of fuel and product costs:

The product cost is defined to be equal to the sum of

- *All the exergy values at the exit, plus*
- *All the exergy increases between inlet and exit.*

Likewise, the fuel cost is defined to be equal to

- *All the exergy values at the inlet, plus*

- *All the exergy decreases between inlet and exit, minus*
- *All the exergy increases between the inlet and exit of a component that are not related to the component purpose.*

3- Identification of cost equations

Cost equations are the cost rate and cost per exergy unit equations, as defined above at the beginning of this section and through Equations 3.16-3.21.

The *F* (Fuel) and *P* (Product) rules

When carrying thermoeconomic analysis using the SPECO method, usually further auxiliary equations are needed. These equations are obtained using the *F* and *P* rules. The *F* and *P* rules, according to [129], are cited below.

The *F* rule for a considered component refers to the removal of exergy from an exergy stream within the component when, for this stream, the exergy difference between inlet and outlet is considered in the definition of the fuel. The *F* rule states that the specific cost (cost per exergy unit) associated with this removal of exergy from a fuel stream must be equal to the average specific cost at which the removed exergy was supplied to the same stream in upstream components.

The *P* rule for a considered component refers to the supply of exergy to an exergy stream within the component. The *P* rule states that each exergy unit is supplied to any stream associated with the product at the same average cost.

3.3 Optimization

Optimization is an essential tool for many engineering designs. Using optimization modeling, one can find an optimum design, for instance, without the need to examine all possible

cases and how each case affects the desired optimum design. That is, optimization will ensure an optimum case and reduce simulation time. To carry out optimization, some elements of optimization formulation need to be explained. These elements include system boundaries, optimization criteria, variables, and mathematical model.

System boundaries

The system boundaries are simply the boundaries of the system to be optimized. These boundaries are real or imaginary surfaces that isolate the system from the surrounding. In the case of a complex system, the system could be divided into subsystems. The optimization could be done on each subsystem independently and the optimization of these subsystems is called sub-optimization.

Optimization criteria

After selecting the system boundaries, optimization criteria are selected. These criteria could be for the purpose of having the best economical design and/or operating parameters of the system. Other criteria could be the best design/operating thermal efficiency and/or the lowest air pollution.

Variables

The third element is selecting the optimization independent variables. It is important in selecting these variables to put into consideration the optimization boundaries and criteria. If the criterion of the optimization is to have the lowest operating cost, all major independent variables that affect the operating cost need to be selected. Also, in selecting these variables, the reasonable range where these variables are operated needs to be identified.

The Mathematical model

The Mathematical model of optimization is the mathematical description of the optimization criteria and variables within the system boundaries. The mathematical model consists of

- Optimization criteria: objective function(s) to be minimized or maximized; and
- Equality and inequality constraints.

3.3.1 The Direct Search Optimization Method

Several optimization methods have been proposed in the literature. Each method has its advantages and limitations. In Engineering Equations Solver (EES), four search methods for multi-variables optimization are available: direct search, variable metric, generic, and Nelder-Mead simplex methods. For the trigeneration systems considered in this study, the direct search method was the appropriate one since it provides a good design criteria and has a converged solution. In EES, when there are two or more degrees of freedom (independent variables), as in the considered trigeneration systems in this study, direct search optimization method executes in two steps. First, EES uses Brent's method to find the minimum or maximum along a particular direction. Second, the direction of the optimization path is determined through Powell's method. These two methods are summarized below. As indicated in the EES manual, the direct search method that are implemented in the EES code is based on [131, 132]. Therefore, these two references are selected to be the main sources of optimization discussion in this section.

Brent's optimization method

Brent's method is considered a root-finding algorithm that combines root bracketing, bisection, and inverse quadratic interpolation [133]. The description of the Brent method below

is based on [132].

This method is characterized by tracking six function points, say a, b, u, v, w, and x but are not necessarily all distinct. These function points are defined next. The minimum solution is bracketed between a and b; x is the point with the very least function value found so far; w is the point with the second least function value; v is the previous value of w; and u is the point where the function most recently evaluated. The midpoint between a and b is denoted as xm. The flowchart of the Brent method is shown in Figure 3.4.

Powell's direct search optimization method

Search optimization methods differ in the path (direction) the optimization function decides in the next simulation step. One of the most successful direct search methods is the method developed by Powell [131, 134]. The Powell's direct search method was originally developed by Powell as in [135] and its description can be found in different optimization books. The Powell's direct search method is considered as an extension of the basic search method and it depends on successive line minimization. A contours plot that shows how this method works is in Figure 3.5. Powell's method is a quadratic model and, thus, represents one of the simplest types of nonlinear functions to minimize [131]. Also, near the optimum, all nonlinear functions can be approximated by a quadratic function. The direction of Powell's method depends on a research direction called conjugate direction. The definitions of quadratic functions and conjugate direction that are explained below are based on [131].

Quadratic function

Using a quadratic function, the optimum function can be found after N single-variable searches one with respect to each of the transformed function. This can be performed if a quadratic function in N variables can be transformed. An example of a quadratic function

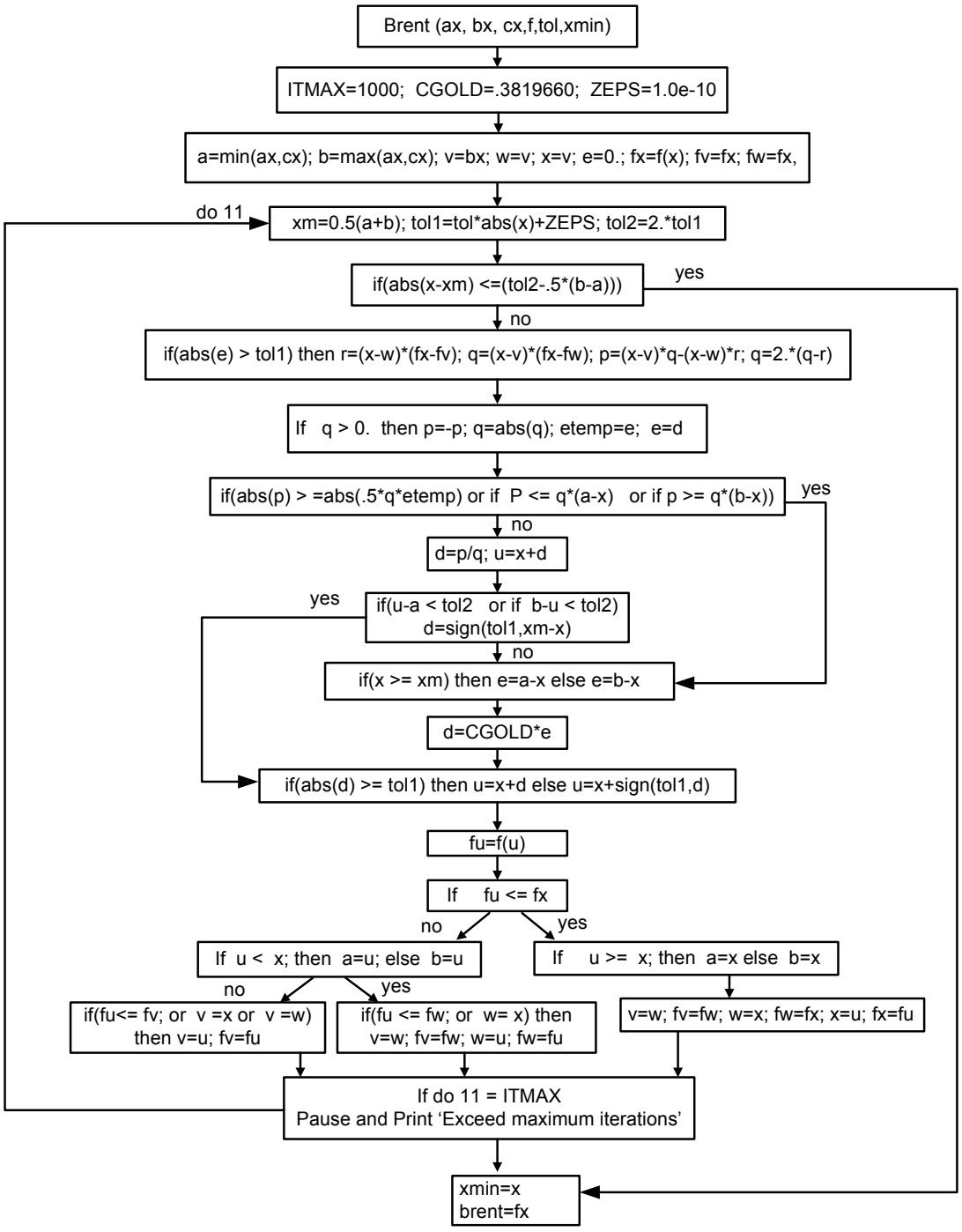

Figure 3.4 The Brent's method.

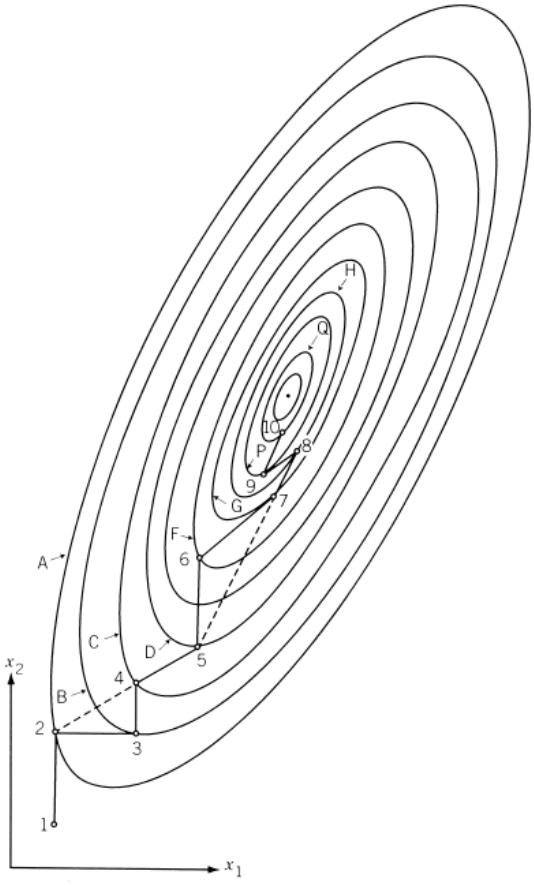

Figure 3.5 Schematic of Powell's method [134].

is

$$f(x) = a + b^T x + \frac{1}{2} x^T C x \tag{3.22}$$

To transfer this function into a sum of a perfect square, is similar to finding a transformation matrix T, such that the quadratic term is reduced to a diagonal form. This transformation process is shown below. Assume the quadratic form to be

$$F(x) = x^T C x \tag{3.23}$$

Thus, the desired transformation is

$$x = Tz \tag{3.24}$$

This will yield

$$F(x) = z^T T^T C T = z^T D z \tag{3.25}$$

where D is a diagonal matrix. Now, assume that t_j to be the jth column of T. In this case, the transformation in Equation 3.24 shows each vector x as a linear combination of the column vectors t_j. That is,

$$x = Tz = t_1 z_1 + t_2 z_2 + ...t_N z_N \tag{3.26}$$

This equation shows that x can be expressed in a new coordinate system given by the set of vectors t_j.

Conjugate directions

For a given symmetric matrix C with $N \times N$ size, the directions $s^1, s^2, ..., s^r$, where $r \leq N$, are said to be C conjugate if the directions are linearly independent, and

$$s^{(i)T} C s^j = 0, \textit{ for all } i \neq j \tag{3.27}$$

Considering the quadratic function as in Equation 3.22, the points along the direction d from x^1 can be represented by

$$x = x^1 + \lambda d \tag{3.28}$$

The minimum value of function $f(x)$ along d is obtained by finding λ^* such that $\partial f / \partial \lambda = 0$. The partial derivative is calculated using the chain rule as

$$\frac{\partial f}{\partial \lambda} = \frac{\partial f}{\partial x}\frac{\partial x}{\partial \lambda} = (b^T + x^T C)d \tag{3.29}$$

Assume the minimum value occurs at $y^{(1)}$, therefore,

$$[((y^{(1)})^T C + b^T)]d = 0 \tag{3.30}$$

Likewise, because the minimum value of $f(x)$ along d from $x^{(2)}$ is attained at $y^{(2)}$, we have

$$[((y^{(2)})^T C + b^T)]d = 0 \tag{3.31}$$

Subtracting Equation 3.30 from Equation 3.31 to have

$$(y^{(2)} - y^{(1)})^T C d = 0 \tag{3.32}$$

As a result, the directions d and $y^{(2)} - y^{(1)}$ are C conjugate.

The flow chart of Powell's method is shown in Figure 3.6. Powell's method depends on finding a line minimization function as a subroutine in this method, which could be called *linmin*. This function works as follows [132]: for given input vectors P and n, and a function f, the scalar λ is found that minimizes $f(P + \lambda n)$. Then, replace P by $P + \lambda n$ and replace n by λn.

3.4 Thermoeconomic Optimization

Thermodynamic optimization is minimizing the thermodynamic inefficiencies in the system [136]. The thermodynamic inefficiencies are the exergy destruction and exergy loss. On the other hand, thermoeconomic optimization is minimizing the costs, including the cost of the thermodynamic inefficiencies. Thermoeconomics can be considered as exergy-aided cost minimization. The optimal design of a system is characterized by a maximum

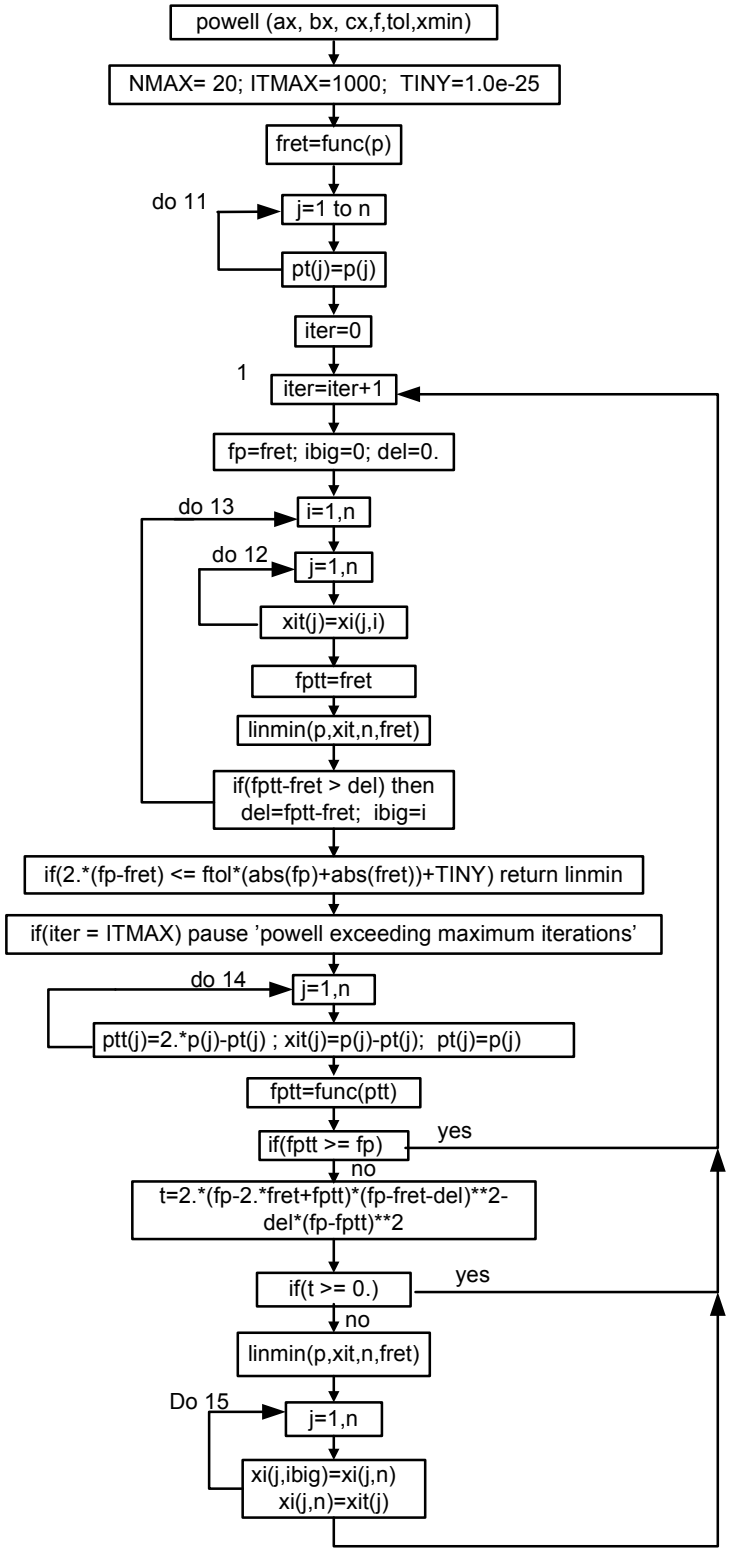

Figure 3.6 The Powell's flowchart.

or minimum value of one or more selected criteria. The other criteria (the non-selected criteria) are considered as problem constraints [136].

Different criteria can be selected for optimization. For example, when the overall thermal exergy efficiency of a plant is selected as an optimization criterion, the optimization will provide the best operating conditions within the simulation constraint(s) that results in the highest exergy efficiency. However, this optimization criterion does not consider the cost effect and it could result in high operating cost conditions. Similarly, finding the best operating condition(s) for the lowest operating cost could result in a low exergy efficiency. Therefore, there is a need to find a parameter that takes into consideration both the cost and exergy of the plant considered for optimization. This parameter can be obtained through thermoeconomic analysis [136]. As mentioned in [136], the cost per exergy unit of of the final product (trigeneration) is an important parameter to optimize. Therefore, it is considered in this study as the thermoeconomic optimization objective. For an electrical power plant with a constant electrical power output, a main parameter to optimize is the product cost rate, [136]. That is,

$$\dot{C}_{product,total} = \dot{C}_{fuel,total} + \dot{Z}_{total} \tag{3.33}$$

3.5 Summary

In this chapter, the thermodynamic modeling and optimization are presented. The mass, energy, entropy, exergy, and efficiency equations are given. Also, thermoeconomic and optimization modelings are discussed. For the optimization, Brent's and Powell's methods are used. For the thermoeconomic analysis, the SPECO method is used. An overview chart of the modeling equations used in this study is shown in Figure 3.7.

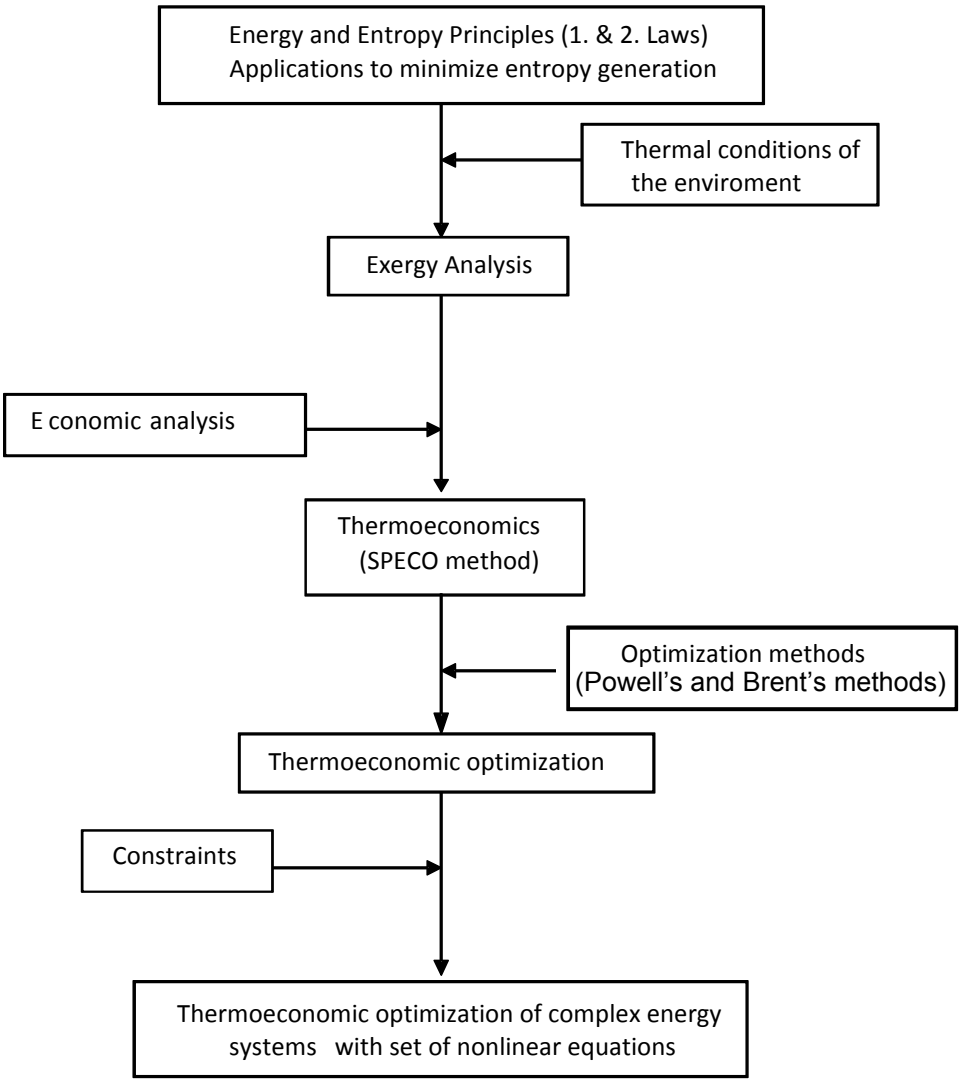

Figure 3.7 Overview of the modeling steps in the thermoeconomic optimization.

Chapter 4

Case Studies

4.1 Introduction

ORC is similar to the steam Rankine cycle but uses an organic working fluid instead of water. A steam Rankine cycle can be used when a high-temperature waste heat is available while ORC can be used when low- or medium-temperature waste heat is available. The input heat to ORC can be from a non-renewable or renewable energy source. ORC can be integrated with a microturbine or SOFC, as an example of a system that is based on a non-renewable energy source. Also, ORC can be integrated with solar collectors, biomass, or geothermal energy, as an example of a system that is based on a renewable energy source. As discussed earlier, there has been no thermodynamic modeling conducted using an ORC as a prime mover of a trigeneration system. This study helps in evaluating the feasibility of using ORC in trigeneration systems.

This chapter is organized as follow. First, introduction to the systems considered is presented. Then, organic fluid selection for the ORC is discussed. Next, thermodynamic modeling of the ORC, single-effect absorption chiller, SOFC-trigeneration system, biomass-trigeneration system, and solar-trigeneration system are illustrated. Lastly, ther-

moeconomic modeling and thermoeconomic optimization of the systems considered are demonstrated.

4.2 Systems Studied

The ORC can be used as a prime mover for a trigeneration system or it can be combined with another prime mover. In this study, three systems are examined. These systems are combined SOFC with ORC, combined biomass combustor with ORC, and combined solar collectors with ORC. Schematic diagrams of these systems are shown in Figures 4.1- 4.3. SOFC has a potential application in the future since it has higher efficiency and less air pollution compared with fossil fuel systems. Therefore, a trigeneration system based on SOFC and ORC is selected. Biomass fuel and solar energy are renewable energy sources that can be combined with ORC. Recent potential research that examines the feasibility of these two renewable energy sources is on ongoing. Therefore, trigeneration systems based on biomass combustor and solar collectors are selected in this study.

All the systems examined consist of an ORC as a prime mover to produce the electrical power, single-effect absorption chiller to supply the cooling load, and a heat exchanger to supply the heating load. It can be noticed that in these systems there are two cycles: ORC and cooling cycles. The flow stream in the ORC is described first and then the flow stream in the cooling cycle.

The flow in the ORC according to Figure 4.1 is described as follows. The fluid exits the generator (desorber) (state 1) as saturated liquid. Next, the pump increases the pressure of the saturated liquid (state 2). Then, the working fluid enters the evaporator in a liquid state and exits as vapor (state 3). Next, the organic fluid expands through the turbine to produce the mechanical energy. The mechanical energy is used to rotate the electrical generator which is connected to the turbine. Then, the working fluid exits the turbine (state 4) and

supplies heat to the heating-process heat exchanger. The heating-process heat exchanger rejects heat to supply the heating load. After that, the organic fluid enters the generator (state 5) as saturated vapor. The generator absorbs heat to supply the cooling load for the single-effect absorption chiller. Then, the organic fluid exits from the generator again as saturated liquid (state 1).

The heat rejected to the generator is the input energy to the single-effect absorption chiller. The flow streams transport between the components of this cooling cycle as either water or a mixture of lithium-bromide (LiBr) and water. As a result of the input heat into the generator, water evaporates from the mixture of the LiBr and water and enters the condenser (state 6). In the condenser, the heat is rejected. Therefore, the water cools down and exits the condenser as saturated liquid (state 7). After that, the water is throttled before entering the evaporator (state 8) at low temperature. The evaporator supplies the cooling load. After that, water exits the evaporator and enters the absorber (state 9). The water mixes with the mixture of the LiBr and water. The mixture exits the absorber (state 10) and is pumped to the heat exchanger (state 11). Then, the mixture exits from the heat exchanger and enters the generator (state 12). The mixture is heated in the generator and part of the water in the mixture evaporates and exits the generator (state 6). As a result of the water evaporation, the mixture exits the generator with a higher LiBr concentration in the mixture to enter the heat exchanger (state 13) to gain heat. After that, it exits the heat exchanger (state 14) and is throttled into the absorber (state 15). This discussion in this paragraph summarizes the fluids cycle in the single-effect absorption chiller.

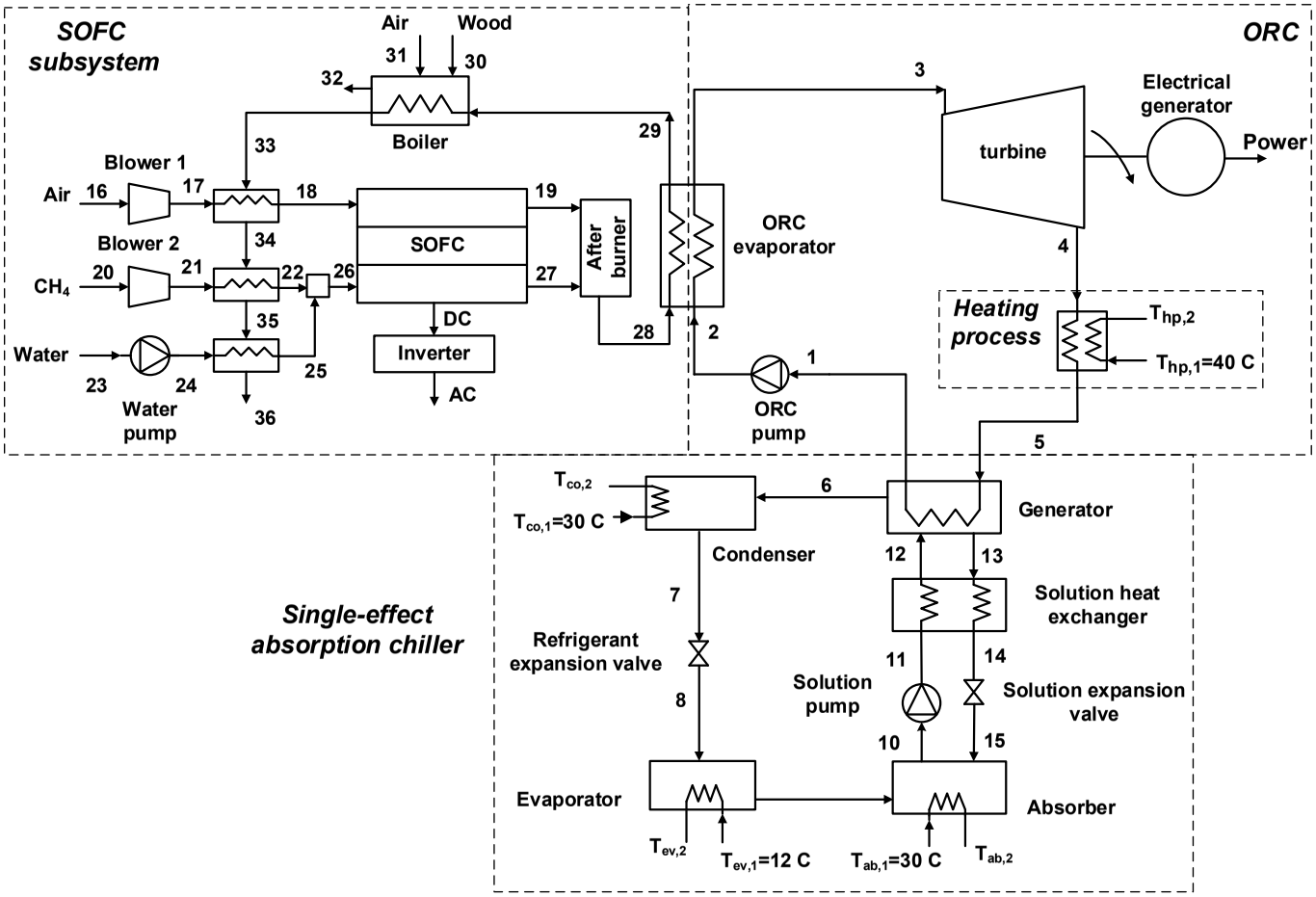

Figure 4.1 Case study I: SOFC-Trigeneration system.

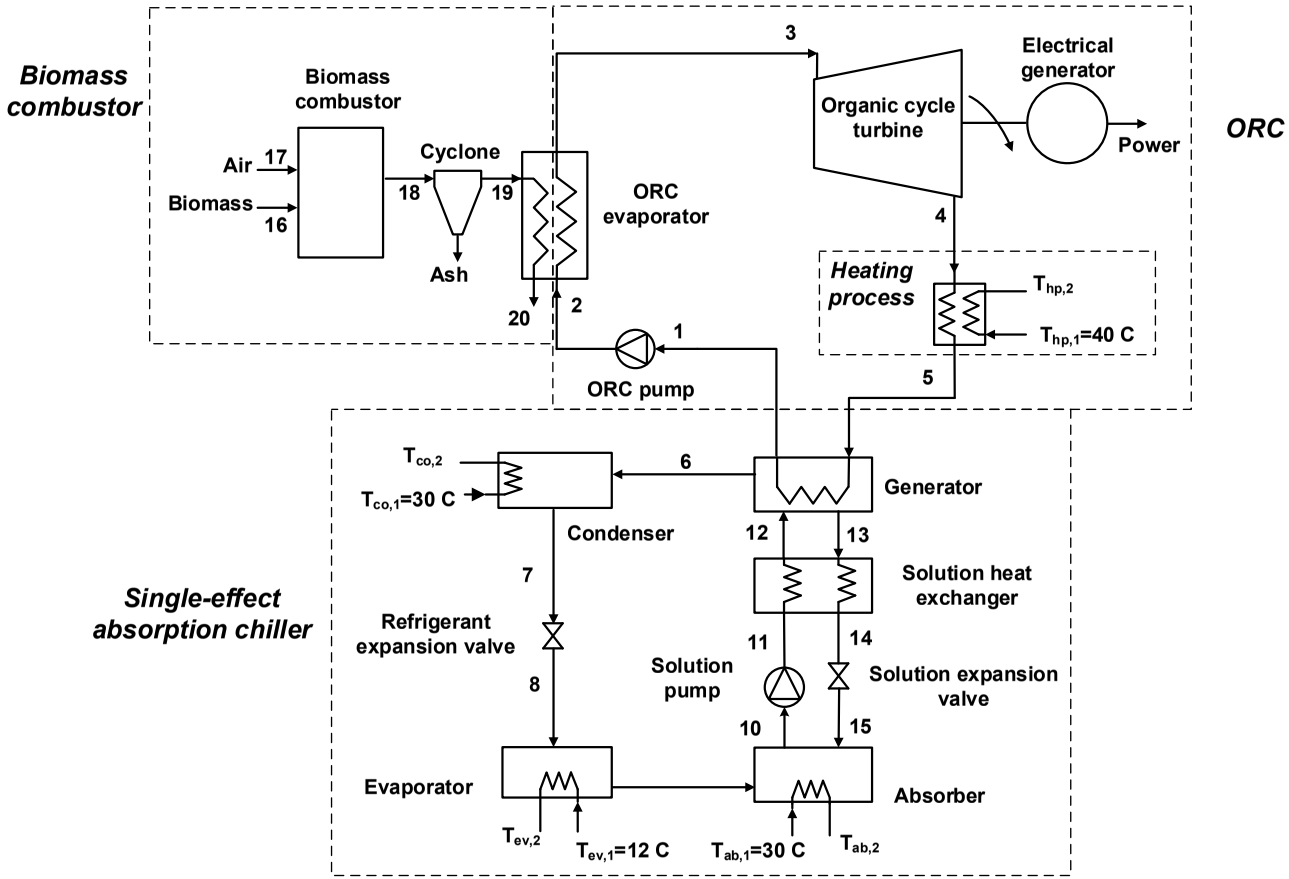

Figure 4.2 Case study II: Biomass-trigeneration system.

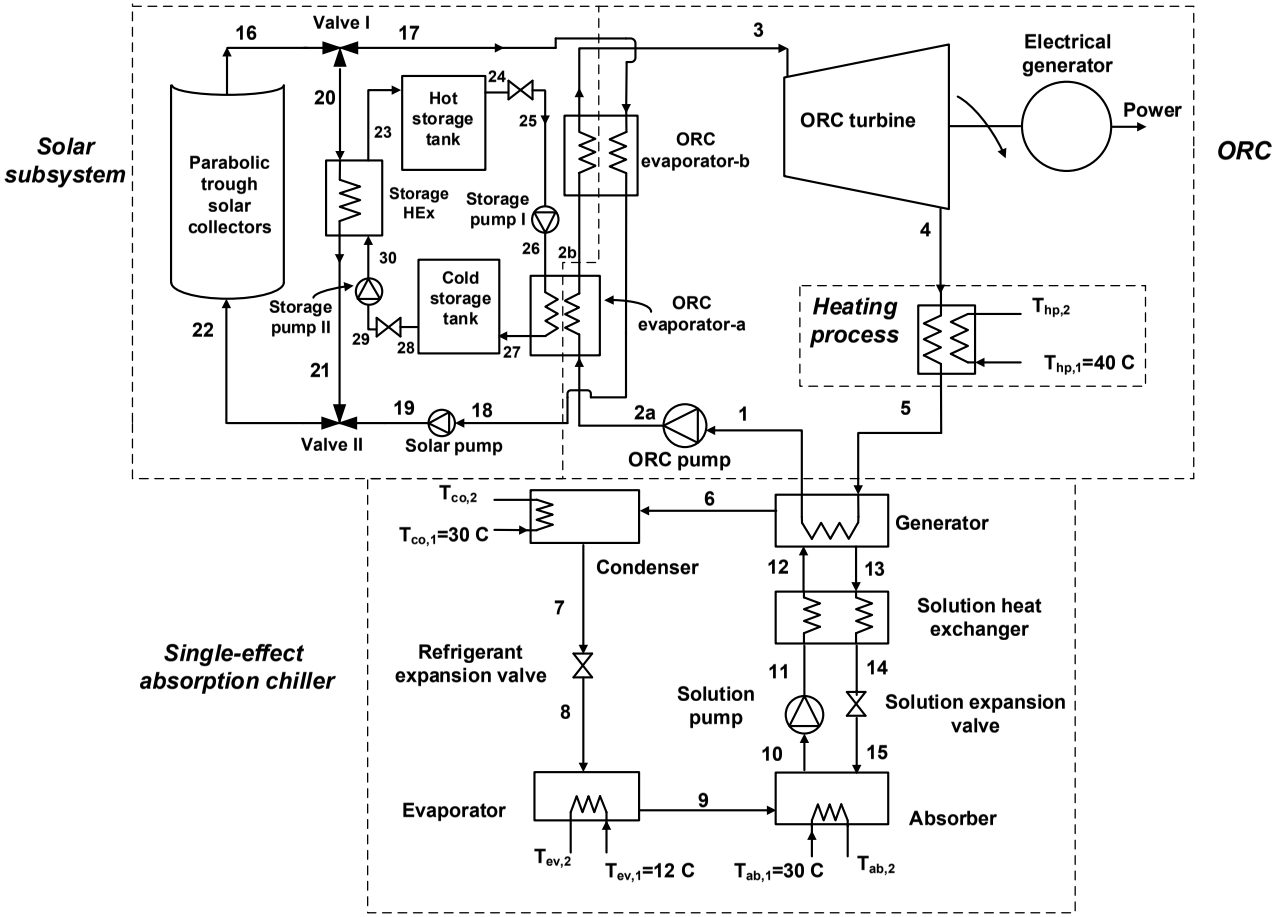

Figure 4.3 Case study III: Solar-trigeneration system.

4.3 Fluid Selection for the Organic Rankine Cycle

Many types of organic fluids can be used for ORC. However, only the organic fluids that operate with a high temperature are efficient for ORC. A typical working fluid that has a high critical temperature and, thus, high ORC efficiency is n-octane. Therefore, this fluid is selected for the ORC [137, 138]. The properties of n-octane are shown in Table 4.1.

4.4 Thermodynamics Modeling of the ORC and Cooling Cycles

The ORC and cooling cycle in all the systems considered are similar. Therefore, the thermodynamic modeling of the ORC and cooling cycle are presented first in this section. Then, the thermodynamic modeling of the SOFC, biomass combustor, and solar collectors is presented in the subsequent sections.

The thermodynamic modeling of the ORC and cooling cycle presented in this section is for the system shown in Figure 4.1. The analysis is carried out by applying the governing equations to the control volumes enclosing each component of the system. For each component, mass, energy, and exergy balance equations are presented. The analysis starts with the ORC and then the cooling cycle. Some assumptions were made to carry out the analysis. It was assumed that the system is at steady state and pressure drops are neglected except in pumps, valves, and the turbine. Also, the kinetic and potential energies were neglected. Further assumptions for specific components are mentioned later where appropriate.

Mass balance equations of the ORC

The mass flow rate is constant throughout the ORC. The mass balance equations are

Table 4.1 Thermodynamic properties of n-octane

Substance name	n-octane
Mol. formula	C8H18
Mol. weight	114.231
Freeze point (^{o}C)	-56.77
Boiling point (^{o}C)	125.68
Crit. temp. (^{o}C)	295.68
Crit. pressure (bar)	24.86
Crit. volume (cm^3/mol)	492.1
Crit. density (g/cm^3)	0.2322
Crit. compressibility	0.259
Accentric factor	0.396

Source: [139]

$$\dot{m}_1 = \dot{m}_2 = \dot{m}_3 = \dot{m}_4 = \dot{m}_5 = \dot{m}_o$$

where the subscripts $1-5$ refer to the states shown in Figure 4.1 and the subscript o indicates the flow inside the organic Rankine cycle.

ORC pump

The energy and exergy balance equations of the ORC pump are

$$\dot{W}_{op} = \dot{m}_o \cdot (h_2 - h_1)$$

$$\dot{E}x_{d,op} = \dot{W}_{op} + \dot{m}_o \cdot (ex_1 - ex_2)$$

where the subscript op indicates the ORC pump. The isentropic efficiency of the pump is defined as

$$\eta_{op,is} = \dot{W}_{op,is}/\dot{W}_{op}$$

where $\dot{W}_{op,is}$ is defined as

$$\dot{W}_{op,is} = \dot{m}_o \cdot (h_{s,2} - h_1)$$

where the subscript is refers to isentropic.

ORC evaporator: SOFC

The energy and exergy balance equations of the ORC evaporator in the case of the trigeneration system, using the SOFC are

$$Q_{oe} = \dot{m}_o \cdot (h_3 - h_2) = N_{FC} \cdot \left(\dot{H}_{28} - \dot{H}_{29}\right)$$

$$\dot{E}x_{d,oe} = N_{FC} \cdot \left(\dot{E}x_{28} - \dot{E}x_{29}\right) + \dot{m}_o \cdot (ex_2 - ex_3)$$

where N_{FC} is the total number of cells, $\dot{m}_o$ is the mass flow rate of the organic fluid in the ORC, and the subscript oe indicates the ORC evaporator. The effectiveness of the ORC evaporator is defined as

$$\epsilon_{oe} = \frac{\dot{m}_o \cdot (h_3 - h_2)}{N_{FC} \cdot \dot{H}_{28} - \dot{m}_o \cdot h_2}$$

ORC evaporator: biomass

The energy and exergy balance equations of the ORC evaporator in the case of the trigeneration system, using the biomass combustor as shown in Figure 4.2, are

$$\dot{Q}_{oe} = \dot{m}_o \cdot (h_3 - h_2) = \left(\dot{H}_{19} - \dot{H}_{20}\right)$$

$$\dot{E}x_{d,oe} = \dot{E}x_{19} - \dot{E}x_{20} + \dot{m}_o \cdot (ex_2 - ex_3)$$

ORC evaporator: solar subsystem

The energy and exergy balance equations of the ORC evaporator in the case of the trigeneration system, using the solar subsystem as shown in Figure 4.3, are presented below. For evaporator-a, the energy and exergy equations are

$$\dot{Q}_{oe} = \left(\dot{H}_{26} - \dot{H}_{27}\right)$$

$$\dot{E}x_{d,ev,a} = \left(\dot{E}x_{26} - \dot{E}x_{27} + \dot{m}_o \cdot (ex_2 - ex_3)\right) \cdot \frac{\Delta t_{hdhst}}{24 \ [\text{hr}]}$$

For evaporator-b, the energy and exergy equations are

$$\dot{Q}_{oe} = \left(\dot{H}_{17} - \dot{H}_{18}\right)$$

$$\dot{E}x_{d,ev,b} = \left(\dot{E}x_{17} - \dot{E}x_{18} + \dot{m}_o \cdot (ex_2 - ex_3)\right) \cdot \left(\frac{24 \ [\text{hr}] - \Delta t_{hdhst}}{24 \ [\text{hr}]}\right)$$

where Δt_{hdhst} is the total discharging time from the hot storage tank.

ORC turbine

The energy and exergy balance equations of the ORC turbine are

$$\dot{W}_{ot} = \dot{m}_o \cdot (h_3 - h_4)$$

$$\dot{E}x_{d,ot} = -\dot{W}_{ot} + \dot{m}_o \cdot (ex_3 - ex_4)$$

where the subscript ot indicates the ORC turbine. The isentropic efficiency of the turbine is

$$\eta_{t,is} = \dot{W}_{ot}/\dot{W}_{ot,is}$$

where $W_{ot,is}$ is defined as

$$\dot{W}_{ot,is} = \dot{m}_o \cdot (h_3 - h_{s,4})$$

Heating process

The energy and exergy balance equations of the heating process are

$$\dot{Q}_{hp} = \dot{m}_o \cdot (h_4 - h_5) = \dot{m}_{hp} \cdot (h_{hp,2} - h_{hp,1})$$

$$\dot{E}x_{d,hp} = \dot{m}_{hp} \cdot (ex_{hp,1} - ex_{hp,2}) + \dot{m}_o \cdot (ex_4 - ex_5)$$

where the subscript hp indicates the heating process.

The mass, energy, and exergy balance equations of the single-effect absorption chiller are presented next.

4.4.1 Single-Effect Absorption Chiller (SEAC)

The performance analysis applied to the single-effect absorption chiller is similar to the approach used by ASHRAE [140] and Herold et al. [141]. The assumptions used in the single-effect absorption chiller are [141]

- The refrigerant is considered pure water (States 6-9).
- States 7, 10, and 13 are considered saturated liquid.
- State 9 is considered saturated vapor.
- The pressure in the generator and condenser is considered equal.
- The pressure in the evaporator and the absorber is considered equal.

The mass, energy, and exergy equations of each component in the single-effect absorptions chiller are derived next.

Generator

The mass balance equations of the generator are

$$\dot{m}_{12} = \dot{m}_{13} + \dot{m}_6$$

$$\dot{m}_{12} \cdot x_{12} = \dot{m}_{13} \cdot x_{13}$$

The energy balance equation of the generator is

$$h_{12} \cdot \dot{m}_{12} - h_{13} \cdot \dot{m}_{13} - h_6 \cdot \dot{m}_6 + \dot{Q}_g = 0$$

where $\dot{Q}_g$ is defined as

$$\dot{Q}_g = \dot{m}_5 \cdot (h_5 - h_1) = LMTD_g \cdot UA_g$$

where $LMTD_d$ of the generator is defined as

$$LMTD_g = \frac{T_5 - T_{13} - T_1 + T_6}{\ln\left((T_5 - T_{13})\right) - \ln\left((T_1 - T_6)\right)}$$

The exergy balance equation is defined as

$$\dot{E}x_{d,d} = \dot{m}_{12} \cdot ex_{12} - \dot{m}_6 \cdot ex_6 - \dot{m}_{13} \cdot ex_{13} + \dot{m}_o \cdot (ex_5 - ex_1)$$

where $LMTD$ is the log mean temperature difference, x is the concentration of the lithium-bromide into the LiBr/water mixture, and the subscript d indicates the generator.

Condenser of the SEAC

The mass, energy, and exergy balance equations of the condenser of the cooling cycle are

$$\dot{m}_7 = \dot{m}_6$$

$$\dot{Q}_{cond} = \dot{m}_6 \cdot (h_6 - h_7) = \dot{m}_{cond} \cdot (h_{cond,2} - h_{cond,1}) = LMTD_{cond} \cdot UA_{cond}$$

$$\dot{E}x_{d,cond} = \dot{m}_{cond} \cdot (ex_{cond,1} - ex_{cond,2}) + \dot{m}_6 \cdot (ex_6 - ex_7)$$

where the subscript $cond$ indicates the condenser. The effectiveness and $LMTD$ of this condenser are

$$\epsilon_{cond} = \frac{T_{cond,1} - T_{cond,2}}{T_{cond,1} - T_7}$$

$$LMTD_{cond} = \frac{T_7 - T_{cond,1} - T_6 + T_{cond,2}}{\ln\left((T_7 - T_{cond1})\right) - \ln\left((T_6 - T_{cond2})\right)}$$

Refrigerant Valve

The mass, energy, and exergy balance equations of the second throttling valve (10-11) are

$$\dot{m}_8 = \dot{m}_7$$

$$h_8 = h_7$$

$$\dot{E}x_{d,rv} = \dot{m}_7 \cdot (ex_7 - ex_8)$$

Evaporator

The mass, energy, and exergy balance equations of the evaporator are

$$\dot{m}_9 = \dot{m}_8$$

$$\dot{Q}_{ev} = \dot{m}_8 \cdot (h_9 - h_8) = \dot{m}_{ev} \cdot (h_{ev,1} - h_{ev,2}) = LMTD_{ev} \cdot UA_{ev}$$

$$\dot{E}x_{d,ev} = \dot{m}_{ev} \cdot (ex_{ev,1} - ex_{ev,2}) + \dot{m}_8 \cdot (ex_8 - ex_9)$$

where the subscript ev indicates the evaporator. The effectiveness and $LMTD$ of this evaporator are

$$\epsilon_{ev} = \frac{T_{ev,1} - T_{ev,2}}{T_{ev,1} - T_9}$$

$$LMTD_{ev} = \frac{T_{ev,1} - T_9 - T_{ev,2} + T_8}{\ln\left((T_{ev1} - T_9)/(T_{ev2} - T_8)\right)}$$

Absorber

The energy balance equation of the absorber is

$$\dot{m}_9 \cdot h_9 + \dot{m}_{15} \cdot h_{15} - \dot{Q}_{ab} - \dot{m}_{10} \cdot h_{10} = 0$$

where

$$\dot{Q}_{ab} = \dot{m}_{ab} \cdot (h_{ab,2} - h_{ab,1}) = LMTD_{ab} \cdot UA_{ab}$$

The exergy balance equation of the absorber is

$$\dot{E}x_{d,ab} = \dot{m}_{ab} \cdot (ex_{ev,1} - ex_{ev,2}) + \dot{m}_8 \cdot (ex_8 - ex_9)$$

where the subscript ab indicates the absorber. The effectiveness and $LMTD$ of this absorber are

$$\epsilon_{ab} = \frac{T_{ab,2} - T_{ab,1}}{T_{15} - T_{ab,1}}$$

$$LMTD_{ab} = \frac{T_{15} - T_{ab,2} - T_{10} + T_{ab,1}}{\ln\left(\frac{T_{15} - Tab2}{T_{10} - T_{ab,1}}\right)}$$

Solution pump

The mass, energy, and exergy balance equations of the solution pump are

$$\dot{m}_{11} = \dot{m}_{10}$$

$$\dot{W}_{sp} = \dot{m}_{10} \cdot v_{10} \cdot (P_{high} - P_{low}) = \dot{m}_{10} \cdot (h_{11} - h_{10})$$

$$\dot{E}x_{d,sp} = \dot{W}_{sp} + \dot{m}_{14} \cdot (ex_{14} - ex_{15})$$

where the subscript sp indicates the solution pump.

Heat Exchanger

The mass balance equations of the heat exchanger are

$$\dot{m}_{12} = \dot{m}_{11}$$

$$\dot{m}_{14} = \dot{m}_{13}$$

The energy and exergy balance equations are

$$\dot{Q}_{hx} = \dot{m}_{10} \cdot (h_{12} - h_{11}) = \dot{m}_{13} \cdot (h_{13} - h_{14}) = LMTD_{Hx} UA_{Hx}$$

$$\dot{E}x_{d,hx} = \dot{m}_{13} \cdot (ex_{13} - ex_{14}) + \dot{m}_{11} \cdot (ex_{11} - ex_{12})$$

The effectiveness and $LMTD$ of this heat exchanger are

$$\epsilon_{Hx} = \frac{T_{13} - T_{14}}{T_{13} - T_{11}}$$

$$LMTD_{Hx} = \frac{(T_{13} - T_{12}) - (T_{14} - T_{11})}{\ln\left(\frac{T_{13} - T_{12}}{T_{14} - T_{11}}\right)}$$

where ϵ_{Hx} and UA are effectiveness of the heat exchanger and overall heat transfer coefficient multiplies by the area, respectively. The subscript hx indicates the heat exchanger.

Solution expansion valve

The mass, energy, and exergy balance equations of the solution expansion valve are

$$\dot{m}_{15} = \dot{m}_{14}$$

$$h_{15} = h_{14}$$

$$\dot{E}x_{d,sev} = \dot{m}_{14} \cdot (ex_{14} - ex_{15})$$

where the subscript sev indicates the solution expansion valve.

Validation of the single-effect absorption chiller model

The analysis of the single-effect absorption chiller is validated with Herold et al. [141], as shown in Figure 4.4. The figure shows a very good agreement between the current single-effect absorption chiller model and the Herold et al. model.

Input data for the ORC and single-effect absorption chiller

The input data for the ORC and single-effect absorption chiller is shown in Table 4.2.

4.5 Case Study I: Thermodynamic Modeling of the SOFC

4.5.1 Introduction

In this section, a brief introduction to solid oxide fuel cell (SOFC) is presented. A schematic diagram of a SOFC is shown in Figure 4.5. The electricity is produced from the electrochemical reaction of air and a fuel that can be reformed into hydrogen, such as methane, propane, butane, natural gas, or other similar hydrocarbons. In this study, methane, CH_4, is selected as a fuel for the SOFC.

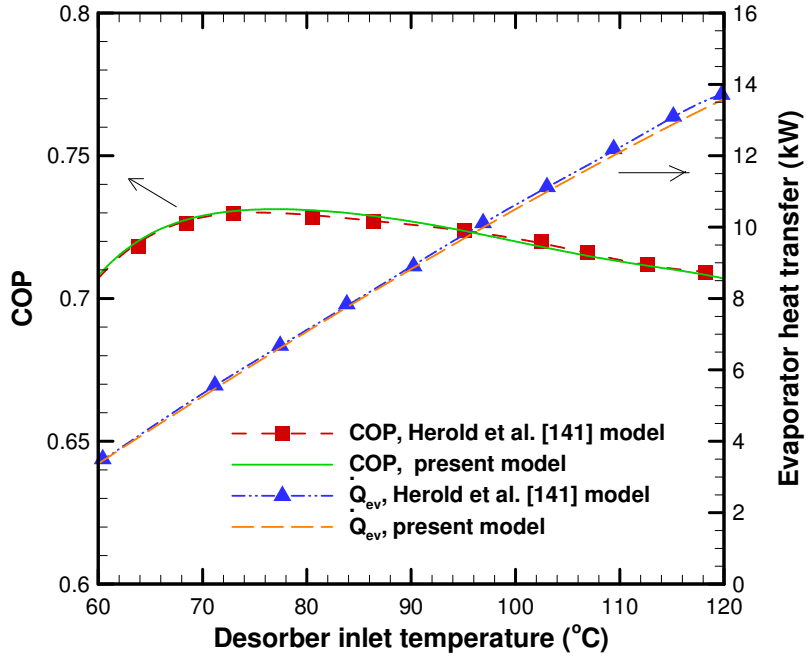

Figure 4.4 Validation of the single-effect absorption chiller model as compared to Herold et al. model [141].; COP and evaporator heat rate versus generator inlet temperature.

The production of electricity from the SOFC is described as follows. The air enters from the cathode side and O_2 diffuses through the cathode layer and interacts with the electron e^-. As a result of the reaction, $O^=$ ions are produced. The electrolyte layer allows only $O^=$ ions to migrate from the cathode to the anode. On the other side of the cell, the fuel, CH_4, diffuses through the anode layer and reforms into hydrogen H_2. The hydrogen reacts with $O^=$ ions to produce water and electrons e^-. The electrons that are produced from the chemical interaction pass through the external electric circuit and, thus, the electrical current is produced. The equations of the chemical reaction through the SOFC are shown below.

The chemical equilibrium equations that occur within the anode and cathode of the fuel

Table 4.2 Input data for the ORC and single-effect absorption chiller

ORC		
	ORC turbine isentropic efficiency	80%
	ORC pump isentropic efficiency	80%
	Effectiveness of the ORC evaporator	85%
	Baseline turbine inlet pressure	2000 kPa
	Organic pump inlet temperature	365 K
	Electrical generator efficiency	95%
	Electrical motor efficiency	95%
Cooling cycle		
	Overall heat transfer coefficient of the generator	70 kW/K
	Overall heat transfer coefficient of the condenser	80 kW/K
	Overall heat transfer coefficient of the evaporator	95 kW/K
	Overall heat transfer coefficient of the absorber	75 kW/K
	Effectiveness of solution heat exchanger	70%

Source: [142–145]

cell are

$$CH_4 + H_2O \leftrightarrow CO + 3H_2 \tag{4.1}$$

$$CO + H_2O \leftrightarrow H_2 + CO_2 \tag{4.2}$$

The overall electrochemical equilibrium equation is

$$H_2 + \frac{1}{2}O_2 \rightarrow H_2O \tag{4.3}$$

The assumptions for this SOFC model are [146]

- Air that enters the SOFC consists of 79% N_2 and 21% O_2.
- Gas mixture at the exit of the fuel channel reaches at chemical equilibrium.
- Both air and fuel flows have the same temperature at the inlet to the SOFC.
- Both air and fuel flows have the same temperature at the exit of the SOFC.
- The radiation heat transfer between gas channels and solid structure is negligible.
- Contact resistances are negligible.

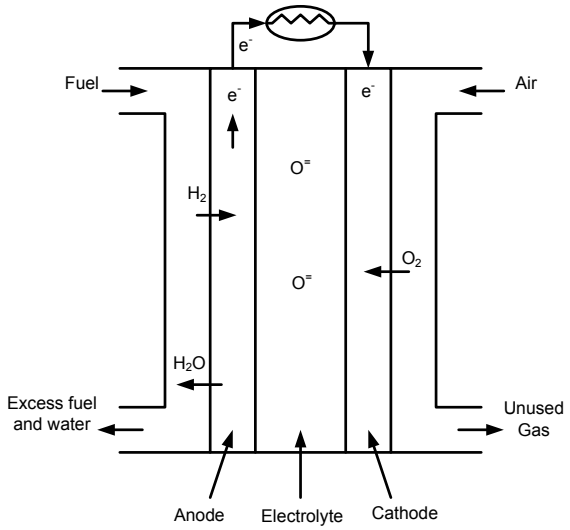

Figure 4.5 Schematic diagram of SOFC.

4.5.2 SOFC Analysis

The cell voltage produced by the cell is the difference between the reversible cell voltage and the sum of the voltage loss. It is defined as

$$V_c = V_N - V_{loss} \tag{4.4}$$

where V_c, V_N and V_{loss} are cell voltage, reversible cell voltage, and voltage loss, respectively. The equation of the reversible cell voltage is derived from Nernst equation and is defined as

$$V_N = -\frac{\Delta \bar{G}_f}{2 \cdot F} - R \cdot \frac{T_{FC,exit}}{2 \cdot F} \cdot \ln\left(\frac{x_{H2O,27}}{x_{H2,27} \cdot \sqrt{x_{O2,19}}}\right) \tag{4.5}$$

where G_f is the Gibs free energy, R is the universal gas constant (8.314 J/[mole-K]), and F is the Faraday constant (96,485 coulombs/[g-mole]).

The voltage loss (V_{loss}) is the sum of three voltage losses, which include the ohmic, activation polarization, and concentration losses. That is, the voltage loss is defined as

$$V_{loss} = V_{ohm} + V_{act} + V_{cont} \tag{4.6}$$

where V_{ohm} is defined by Bossel [147] as follows:

$$V_{ohm} = (R_{contact} + \rho_a \cdot L_a + \rho_c \cdot L_c + \rho_e \cdot L_e + \rho_{int} \cdot L_{int}) \cdot j \tag{4.7}$$

where ρ is the electrical resistivity of cell components, L is thickness of a cell component, R is resistivity contact and j is current density. The activation polarization losses are defined by Kim [148] as follows:

$$V_{act} = V_{act,a} + V_{act,c} \tag{4.8}$$

$$V_{act,a} = \frac{R \cdot T_{FC,exit}}{F} \cdot \left(\sinh^{-1} \left(\frac{j}{2 \cdot j_{oa}} \right) \right) \tag{4.9}$$

$$V_{act,c} = \frac{R \cdot T_{FC,exit}}{F} \cdot \left(\sinh^{-1} \left(\frac{j}{2 \cdot j_{oc}} \right) \right) \tag{4.10}$$

The concentration voltage loss is defined by Chan et al. [149] as follows:

$$V_{cont} = V_{cont,a} + V_{cont,c} \tag{4.11}$$

$$V_{cont,a} = -\frac{R \cdot T_{FC,exit}}{2 \cdot F} \cdot \ln\left(1 - j/j_{as}\right) + \frac{R \cdot T_{FC,exit}}{2 \cdot F} \cdot \ln\left(1 + \frac{P_{H2,27} \cdot j}{P_{H2O,27} \cdot j_{as}}\right) \tag{4.12}$$

$$V_{cont,c} = -\left(\frac{R \cdot T_{FC,exit}}{4 \cdot F} \cdot \ln\left(1 - j/j_{cs}\right) \right) \tag{4.13}$$

where j_{as} is the exchange current density of anode and j_{cs} is the exchange current density of cathode and defined as

$$j_{as} = \frac{\frac{2 \cdot F \cdot P_{H2,27} \cdot D_{aeff}}{\left(R \cdot T_{FC,exit} \cdot L_a\right)}}{1000000 \ [\mathrm{cm}^3/\mathrm{m}^3]} \tag{4.14}$$

$$j_{cs} = \frac{\frac{4 \cdot F \cdot P_{O2,19} \cdot D_{ceff}}{\left(\left(\frac{P_{00} - P_{O2,19}}{P_{00}}\right) \cdot R \cdot T_{FC,exit} \cdot L_c\right)}}{1000000 \ [\mathrm{cm}^3/\mathrm{m}^3]} \tag{4.15}$$

where D_{ceff} is effective gaseous diffusivity through the cathode and D_{aeff} is effective gaseous diffusivity through the anode. The subscripts $ohm, act, cont, a, c, e$, and int indicate ohmic, activation, concentration, anode, cathode, electrolyte, and interconnect, respectively. The electrical resistivity defined as [147]

$$\rho_e = \left(C1_e \cdot \exp\left(C2_e / T_{FC,exit}\right)\right)^{-1} \tag{4.16}$$

$$\rho_a = \left(C1_a / T_{FC,exit} \cdot \exp\left(C2_a / T_{FC,exit}\right)\right)^{-1} \tag{4.17}$$

$$\rho_c = \left(C1_c / T_{FC,exit} \cdot \exp\left(C2_c / T_{FC,exit}\right)\right)^{-1} \tag{4.18}$$

$$\rho_{int} = \left(C1_{int} / T_{FC,exit} \cdot \exp\left(C2_{int} / T_{FC,exit}\right)\right)^{-1} \tag{4.19}$$

where $C1_e$-$C2_{int}$ are constants defined in [147]. The model used to carry out the equilibrium equations of the SOFC is based on a validated model developed by Colpan et al. [146], assuming the methane is fully converted. The molar conversion rates of Equations 4.1- 4.3 are a, b, and c, respectively. The molar flow rates of the gases are derived next. The molar flow rates of the reactions Equations 4.1- 4.3 are given in Table 4.3. In this table, $\dot{n}$, $\dot{U}_f$, and $\dot{U}_{O2}$ are molar flow rate, fuel utilization ratio, and oxygen utilization ratio, respectively. The molar concentration of the elements are given in Table 4.4. In this table, x is a concentration of an element in a stream.

The constants a and b are found using the equilibrium constant and current equations. The equilibrium constant is defined as

$$K_{wgs} = \exp\left(-\frac{\Delta G^0}{R \cdot T_{FC,exit}}\right) = \frac{x_{CO2,27} \cdot x_{H2,27}}{x_{CO,27} \cdot x_{H2O,27}} \tag{4.20}$$

where K_{wgs} is the waste gas shift equation. The current and current density are defined respectively as

$$I = j \cdot A_a \tag{4.21}$$

$$j = \frac{2 \cdot F \cdot c}{A_a} \tag{4.22}$$

where I is the current and A_a is the active surface area. The work of the fuel cell, $\dot{W}_{FC}$, is defined as

Table 4.3 Molar flow rates of the gases

$\dot{n}_{H2O,26} = 2.5 \cdot a$
$\dot{n}_{CH4,26} = a$
$\dot{n}_{H2,27} = 3 \cdot a + b - c$
$\dot{n}_{CO,27} = a - b$
$\dot{n}_{CO2,27} = b$
$\dot{n}_{H2O,27} = 1.5 \cdot a - b + c$
$\dot{n}_{O2,u} = c/2$
$\dot{n}_{O2,18} = \dot{n}_{O2,19} + \dot{n}_{O2,u}$
$\dot{n}_{O2,19} = c/2 \cdot (1/U_{O2} - 1)$
$\dot{n}_{N2,19} = 79/21 \cdot \frac{c}{2 \cdot U_{O2}}$
$\dot{n}_{N2,18} = \dot{n}_{N2,19}$
$c = (3 \cdot a + b) \cdot U_f$
$\dot{n}_{anode,exit} = \dot{n}_{H2,27} + \dot{n}_{CO,27}+$
$\dot{n}_{CO2,27} + \dot{n}_{H2O,27}$
$\dot{n}_{cathode,exit} = \dot{n}_{O2,19} + \dot{n}_{N2,19}$
$\dot{n}_{anode,inlet} = \dot{n}_{H2O,26} + \dot{n}_{CH4,26}$
$\dot{n}_{cathode,inlet} = \dot{n}_{O2,18} + \dot{n}_{N2,18}$

$$\dot{W}_{FC} = I \cdot V_c \tag{4.23}$$

Validation of the SOFC model

The SOFC model was validated with Tao et al. [150]. The model shows a good agreement as presented in Figure 4.6.

Table 4.4 Molar concentration of the elements

$x_{O2,18} = \dot{n}_{O2,18}/\dot{n}_{cathode,inlet}$
$x_{N2,18} = \dot{n}_{N2,18}/\dot{n}_{cathode,inlet}$
$x_{O2,19} = \dot{n}_{O2,19}/\dot{n}_{cathode,exit}$
$x_{N2,19} = \dot{n}_{N2,19}/\dot{n}_{cathode,exit}$
$x_{CH4,26} = \dot{n}_{CH4,26}/\dot{n}_{anode,inlet}$
$x_{H2O,26} = \dot{n}_{H2O,26}/\dot{n}_{anode,inlet}$
$x_{H2,27} = \dot{n}_{H2,27}/\dot{n}_{anode,exit}$
$x_{CO,27} = \dot{n}_{CO,27}/\dot{n}_{anode,exit}$
$x_{CO2,27} = \dot{n}_{CO2,27}/\dot{n}_{anode,exit}$
$x_{H2O,27} = \dot{n}_{H2O,27}/\dot{n}_{anode,exit}$
$x_{N2,28} = \dot{n}_{N2,28}/\dot{n}_{28}$
$x_{O2,28} = \dot{n}_{O2,28}/\dot{n}_{28}$
$x_{CO2,28} = \dot{n}_{CO2,28}/\dot{n}_{28}$
$x_{H2O,28} = \dot{n}_{H2O,28}/\dot{n}_{28}$

4.5.3 SOFC-Subsystem Components Analysis

The energy and exergy balance equations of the blowers, heat exchangers, after burner, and boiler are derived next.

Blower 1

The energy and exergy balance equations of blower 1 are

$$\dot{W}_{b1} = \dot{W}_{b1,s}/\eta_{b1,is} = N_{FC} \cdot \dot{n}_{cathode,inlet} \cdot (\bar{h}_{17} - \bar{h}_{16})$$

$$\dot{E}x_{d,b1} = W_{b1} + \dot{n}_{cathode,inlet} \cdot (ex_{16} - ex_{17})$$

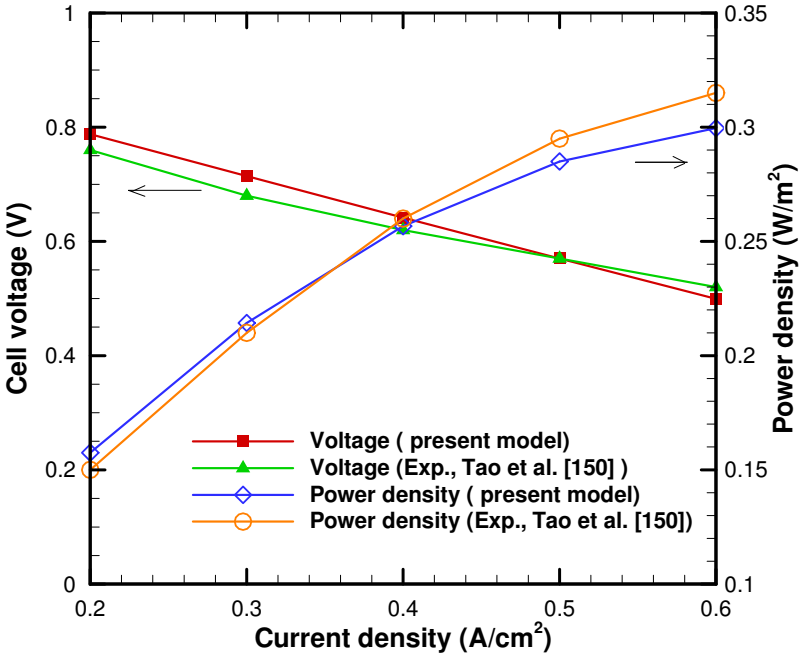

Figure 4.6 Validation of the SOFC model with Tao et al. [150]: cell voltage and power density versus current density.

where N_{FC} is the number of fuel cells and subscript $b1$ indicates blower 1. $\dot{W}_{b1,s}$ is defined as

$$\dot{W}_{b1,s} = N_{FC} \cdot \dot{n}_{cathode,inlet} \cdot (\bar{h}_{17,s} - \bar{h}_{16})$$

Blower 2

The energy and exergy balance equations of blower 2 are

$$\dot{W}_{b2} = \dot{W}_{b2,s}/\eta_{b2,is} = N_{FC} \cdot \dot{n}_{CH4,26} \cdot (\bar{h}_{21} - \bar{h}_{20})$$

$$\dot{E}x_{d,b2} = \dot{W}_{b2} + \dot{n}_{CH4,26} \cdot (ex_{20} - ex_{21})$$

where the subscript $b2$ indicates blower 2. $\dot{W}_{b2,s}$ is defined as

$$\dot{W}_{b2,s} = N_{FC} \cdot \dot{n}_{CH4,26} \cdot (\bar{h}_{21,s} - \bar{h}_{20})$$

Water pump

The energy and exergy balance equations of the water pump are

$$\dot{W}_{wp} = \dot{W}_{wp,s}/\eta_{wp,is} = N_{FC} \cdot \dot{n}_{H2O,26} \cdot (\bar{h}_{24} - \bar{h}_{23})$$

$$\dot{E}x_{d,wp} = \dot{W}_{wp} + \dot{n}_{H2O,26} \cdot (ex_{23} - ex_{24})$$

where the subscript wp indicates water pump. $\dot{W}_{wp,s}$ is defined as

$$\dot{W}_{wp,s} = N_{FC} \cdot \dot{n}_{H2O,26} \cdot (\bar{h}_{24,s} - \bar{h}_{23})$$

Air heat exchanger

The energy and exergy balance equations of the air heat exchanger are

$$\dot{n}_{cathode,inlet} \cdot (\bar{h}_{18} - \bar{h}_{17}) = \dot{H}_{33} - \dot{H}_{34}$$

$$\dot{E}x_{d,HEx,air} = \dot{E}x_{33} - \dot{E}x_{34} + \dot{n}_{cathode,inlet} \cdot (ex_{17}) - \dot{E}x_{18}$$

Methane heat exchanger

The energy and exergy balance equations of the methane heat exchanger are

$$\dot{n}_{CH4,26} \cdot (\bar{h}_{22} - \bar{h}_{21}) = \dot{H}_{34} - \dot{H}_{35}$$

$$\dot{E}x_{d,HEx,CH4,22} = \dot{E}x_{34} - \dot{E}x_{35} + \dot{n}_{CH4,26} \cdot (ex_{21} - ex_{22})$$

where H_{35} is defined as

$$\dot{H}_{35} = \dot{n}_{H2O,28} \cdot \bar{h}_{H2O,35} + \dot{n}_{CO2,28} \cdot \bar{h}_{CO2,35} + \dot{n}_{O2,28} \cdot \bar{h}_{O2,35} + \dot{n}_{N2,28} \cdot \bar{h}_{N2,35}$$

Water heat exchanger

The energy and exergy equations of the water heat exchanger are

$$\dot{n}_{H2O,26} \cdot (\bar{h}_{25} - \bar{h}_{24}) = \dot{H}_{35} - \dot{H}_{36}$$

$$\dot{Ex}_{d,HEx,h2O} = \dot{Ex}_{35} - \dot{Ex}_{36} + \dot{n}_{H2O,26} \cdot (ex_{25} - ex_{24})$$

After burner

The molar flow rate balance equations of the after burner are

$$\dot{n}_{H2O,28} = \dot{n}_{H2,27} + \dot{n}_{H2O,27}$$

$$\dot{n}_{CO2,28} = \dot{n}_{CO,27} + \dot{n}_{CO2,27}$$

$$\dot{n}_{H2O,28} + 2 \cdot \dot{n}_{CO2,28} + 2 \cdot \dot{n}_{O2,28} = \dot{n}_{CO,27} + 2 \cdot \dot{n}_{CO2,27} + \dot{n}_{H2O,27} + 2 \cdot \dot{n}_{O2,19}$$

$$\dot{n}_{N2,28} = \dot{n}_{N2,19}$$

$$\dot{n}_{28} = \dot{n}_{CO2,28} + \dot{n}_{H2O,28} + \dot{n}_{N2,28} + \dot{n}_{O2,28}$$

The energy balance equation of the after burner is

$$\dot{H}_p = \dot{H}_r$$

where $\dot{H}_p$ and $\dot{H}_r$ are the product and reaction enthalpy, respectively. H_p is defined as

$$\dot{H}_p = \dot{n}_{H2O,28} \cdot \bar{h}_{H2O,28} + \dot{n}_{CO2,28} \cdot \bar{h}_{CO2,28} + \dot{n}_{O2,28} \cdot \bar{h}_{O2,28} + \dot{n}_{N2,28} \cdot \bar{h}_{N2,28}$$

and $\dot{H}_r$ is defined as

$$\dot{H}_r = \dot{n}_{H2,27} \cdot \bar{h}_{H2,27} + \dot{n}_{CO,27} \cdot \bar{h}_{CO,27} + \dot{n}_{CO2,27} \cdot \bar{h}_{CO2,27} + \dot{n}_{H2O,27} \cdot \bar{h}_{H2O,27} + \dot{n}_{N2,19} \cdot \bar{h}_{N2,19} + \dot{n}_{O2,19} \cdot \bar{h}_{O2,19}$$

The exergy balance equation of the after burner is

$$\dot{Ex}_{d,afterburner} = Ex_{27,CH} + Ex_{19,CH} - Ex_{28}$$

Boiler

The molar rate balance equations are

$$\dot{n}_{H2O,32} = 0.72 \cdot \dot{n}_{CO2,32}$$

$$\dot{n}_{N2,32} = 3.76 \cdot \lambda \cdot \dot{n}_{CO2,32}$$

$$\dot{n}_{32} = \dot{n}_{CO2,32} + \dot{n}_{H2O,32} + \dot{n}_{N2,32}$$

The energy balance equation is

$$\dot{H}_{33} = \dot{H}_{29} + \dot{Q}_{boiler}$$

where

$$\dot{Q}_{boiler} = \dot{n}_{CO2,32} \cdot \bar{h}_{CO2,32} + \dot{n}_{H2O,32} \cdot \bar{h}_{H2O,32} + \dot{n}_{N2,32} \cdot \bar{h}_{N2,32}$$

and

$$\dot{H}_{33} = \dot{n}_{H2O,28} \cdot \bar{h}_{H2O,33} + \dot{n}_{CO2,28} \cdot \bar{h}_{CO2,33} + \dot{n}_{O2,28} \cdot \bar{h}_{O2,33} + \dot{n}_{N2,28} \cdot \bar{h}_{N2,33}$$

The exergy balance equation is

$$\dot{E}x_{d,boiler} = \dot{E}x_{29} - \dot{E}x_{32} + \dot{E}x^{ch}_{wood} - \dot{E}x_{33}$$

The equations analyzed in this section are used to carry out the thermodynamic modeling of the trigeneration system that is based on SOFC and ORC.

4.5.4 Overall Analysis of the SOFC-Trigeneration System

The equations used to assess the performance of the trigeneration system, using SOFC and ORC, are presented in this subsection. The input energy to the plant is defined as

$$\dot{Q}_{in} = N_{FC} \cdot \dot{n}_{CH4,26} \cdot LHV_{CH4} + N_{FC} \cdot \dot{Q}_{boiler} \tag{4.24}$$

The electrical generator power is defined as

$$\dot{W}_g = \eta_g \cdot \dot{W}_{ot} \tag{4.25}$$

The stack power of the fuel cell is defined as

$$\dot{W}_{FC,stack,ac} = \eta_{inverter} \cdot \dot{W}_{FC,stack} \tag{4.26}$$

The net power of the cycle is defined as

$$\dot{W}_{net} = \dot{W}_{FC,stack,ac} + \dot{W}_g - \dot{W}_{op} - \dot{W}_{sp} - \dot{W}_{b1} - \dot{W}_{b2} - \dot{W}_{wp} \tag{4.27}$$

The net electrical efficiency of the cycle is defined as

$$\eta_{el} = \dot{W}_{net}/\dot{Q}_{in} \tag{4.28}$$

The efficiency of the heating cogeneration is defined as

$$\eta_{cog,h} = \frac{\dot{W}_{net} + \dot{Q}_h}{\dot{Q}_{in}} \tag{4.29}$$

where $\dot{Q}_h$ is the heating power and the subscript cog, h indicates the heating cogeneration. The heating power is defined as

$$\dot{Q}_h = \dot{m}_{hp} \cdot (h_{hp,2} - h_{hp,1}) \tag{4.30}$$

where $\dot{m}_{hp}$ is the mass flow rate of the heating process, and $h_{hp,1}$ and $h_{hp,2}$ are the specific enthalpy of the water at the inlet and exit of the heating-process heat exchanger, respectively. The efficiency of the cooling cogeneration is defined as

$$\eta_{cog,c} = \frac{\dot{W}_{net} + \dot{Q}_{ev}}{\dot{Q}_{in}} \tag{4.31}$$

where the subscripts cog, c and ev indicate the cooling cogeneration and cooling energy produced by the system through the evaporator, respectively. The cooling power of the evaporator is defined as

$$\dot{Q}_{ev} = \dot{m}_8 \cdot (h_9 - h_8) = \dot{m}_{ev} \cdot (h_{ev,1} - h_{ev,2}) \tag{4.32}$$

where $h_{ev,1}$ and $h_{ev,2}$ are the specific enthalpy of the water at the inlet and exit of the cooling evaporator, respectively. The efficiency of the trigeneration is defined as

$$\eta_{tri} = \frac{\dot{W}_{net} + \dot{Q}_{ev} + \dot{Q}_h}{\dot{Q}_{in}} \tag{4.33}$$

The SOFC efficiency is defined as

$$\eta_{FC} = \frac{\dot{W}_{FC,stack,ac}}{\dot{Q}_{in}} \tag{4.34}$$

The ORC efficiency is defined as

$$\eta_{ORC} = \frac{\dot{W}_{ot} - \dot{W}_{op}}{\dot{Q}_{in}} \tag{4.35}$$

The electrical to heating ratio is defined as

$$r_{el,h} = \dot{W}_{net}/\dot{Q}_h \tag{4.36}$$

The electrical to cooling ratio is defined as

$$r_{el,c} = \dot{W}_{net}/\dot{Q}_{ev} \tag{4.37}$$

The exergy of the fuel entering the SOFC is defined as

$$\dot{E}x_{f,CH4} = N_{FC} \cdot \dot{E}x^{ch}_{CH4,26} \tag{4.38}$$

The exergy of the fuel entering the boiler is defined as

$$\dot{E}x_{f,wood} = N_{FC} \cdot \dot{E}x^{ch}_{wood} \tag{4.39}$$

The total exergy is defined as

$$\dot{E}x_{f,total} = \dot{E}x_{f,CH4} + \dot{E}x_{f,wood} \tag{4.40}$$

The exergetic efficiency of the SOFC subsystem is defined as

$$\eta_{ex,FC} = \frac{\dot{W}_{FC,stack,ac} - \dot{W}_{b1} - \dot{W}_{b2} - \dot{W}_{wp}}{\dot{E}x_{f,total}} \tag{4.41}$$

The exergetic efficiency of the ORC is defined as

$$\eta_{ex,ORC} = \frac{\dot{W}_{ORC} - \dot{W}_{op}}{\dot{E}x_{f,total}} \tag{4.42}$$

The exergetic efficiency of net electrical power is defined as

$$\eta_{ex,el} = \dot{W}_{net}/\dot{E}x_{f,total} \tag{4.43}$$

The exergetic efficiency of the heating cogeneration is defined as

$$\eta_{ex,cog,h} = \frac{\dot{W}_{net} + \dot{m}_{hp} \cdot (ex_{hp,1} - ex_{hp,2})}{\dot{E}x_{f,total}} \tag{4.44}$$

The exergetic efficiency of the cooling cogeneration is defined as

$$\eta_{ex,cog,c} = \frac{\dot{W}_{net} + \dot{m}_{ev} \cdot (ex_{ev,1} - ex_{ev,2})}{\dot{E}x_{f,total}} \tag{4.45}$$

The exergetic efficiency of the trigeneration is defined as

$$\eta_{ex,tri} = \frac{\dot{W}_{net} + \dot{m}_{hp} \cdot (ex_{hp,1} - ex_{hp,2}) + \dot{m}_{ev} \cdot (ex_{ev,1} - ex_{ev,2})}{\dot{E}x_{f,total}} \tag{4.46}$$

The CO_2 emissions in kg per kWh produced for electrical and trigeneration productions are calculated respectively as

$$Emi_{CO2,20,el} = \dot{m}_{CO2,20}/\dot{W}_{net} \cdot 3600 \tag{4.47}$$

$$Emi_{CO2,20,tri} = \frac{\dot{m}_{CO2,20}}{\dot{W}_{net} + \dot{Q}_{ev} + \dot{Q}_h} \cdot 3600 \tag{4.48}$$

where $\dot{m}_{CO2,20}$ is the mass flow rate of CO_2 at the exhaust, state 20, and defined as

$$\dot{m}_{CO2,20} = MW_{CO2} \cdot \dot{n}_{CO2,20} \tag{4.49}$$

where MW_{CO2} is the molecular weight of CO_2.

Input Data to the SOFC-trigeneration system

The input data used to carry out the thermodynamic modeling of the SOFC subsystem are given Table 4.5.

Table 4.5 Input data for the SOFC-trigeneration system

dc–ac converter efficiency	95%
Fuel utilization factor	0.85
Active surface area	100 cm^2
Base current density	0.75 A/cm^2
Exchange current density of anode	0.65 A/cm^2
Exchange current density of cathode	0.25 A/cm^2
Effective gaseous diffusivity through the anode	0.2 cm^2/s
Effective gaseous diffusivity through the cathode	0.05 cm^2/s
Thickness of the anode	0.05 cm
Thickness of the cathode	0.005 cm
Thickness of the electrolyte	0.001 cm
Thickness of the interconnect	0.3 cm
Pressure of the cell	101. 3kPa
Base inlet temperature to the SOFC	1000 K
Temperature difference between the inlet and the exit of the SOFC	100 K

Source: [146]

4.6 Case Study II: Thermodynamic Modeling of the Biomass Combustor

4.6.1 Introduction

One of the renewable energy resources is biomass waste, such as pine sawdust. Biomass waste can be used as a fuel for a biomass combustor. In this study, the biomass combustor consists of two inlets and two exits. One inlet has a biomass waste conveyor and the other inlet has an air suction blower. On the other hand, one exit of the combustor is at the bottom of the combustor where the ash can be removed. The other exit is for the heated air. This second exit has a cyclone to filter out the solid particles and clean the exhaust gases.

One of the most common waste wood products is pine sawdust. Pine trees grow widely throughout the world and, thus, they are widely used for wood-based products. Pine saw-

Table 4.6 Biomass fuel characteristics

Type of biomass fuel	Pine sawdust
Moisture content in biomass (%wt)	10%
Ultimate analysis	(%wt dry basis)
ZC	50.54%
ZH	7.08%
ZO	41.11%
ZS	0.57%

Source: [151]

dust is produced as a result of pine wood processing. This wasted sawdust is commonly used for biomass combustion. In this study, the biomass fuel selected is pine sawdust. The chemical compound of a biomass fuel is $C_{ZC}H_{ZH}O_{ZO}S_{ZS}$. The elements C, H, O, and S refer to carbon, hydrogen, oxygen, and sulphur, respectively. The subscripts of these components represent the percentage of these elements in the fuel compound. For the pine sawdust considered, the values of these percentages are listed in Table 4.6. The percentage of the sulphur in the pine sawdust compound is very small and, therefore, can be neglected. The energy and exergy analyses of the biomass combustor are presented below. The analyses is based on Figure 4.2.

Biomass combustor

The chemical equation of the biomass combustion with air assuming complete combustion is

$$C_{ZC}H_{ZH}O_{ZO}+\omega(H_2O)_{16}+\gamma(O_2+79/21N_2)_{17} \longrightarrow \alpha_1(CO_2)_{18}+\alpha_2(H_2O)_{18}+\alpha_3(N_2)_{18} \tag{4.50}$$

where ω is the moisture content in the biomass fuel. ω can be shown to be equal to

$$\omega = \frac{MC \cdot M_{CHO}}{1 - MC \cdot M_{H2O}} \tag{4.51}$$

The molar flow rate of the biomass is defined as

$$\dot{n}_{CHO} = \dot{m}_{biomass}/M_{CHO} \cdot 1000 \quad \texttt{(mole/second)} \tag{4.52}$$

To find the coefficients of the right hand side of Equation 4.50, elements balances are carried out as shown below.

$$\alpha_1 = ZC$$
$$\alpha_2 = \frac{ZH + 2\omega}{2}$$
$$\alpha_3 = 79/21 \cdot \lambda$$
$$\gamma = \frac{2 \cdot \alpha_1 + \alpha_2 - \omega - ZO}{2}$$

To find the flame temperature of the combustor, we need to carry out the enthalpy balance between the combustor inlets and exit. The enthalpy balance equation is

$$\bar{h}_{CHO,16}+\omega\cdot\bar{h}_{H2O,16}+\gamma\cdot\bar{h}_{O2,17}+79/21\cdot\gamma\cdot\bar{h}_{N2,17} = \alpha_1\cdot\bar{h}_{CO2,18}+\alpha_2\cdot\bar{h}_{H2O,18}+79/21\cdot\gamma\cdot\bar{h}_{N2,18} \tag{4.53}$$

Here $\bar{h}_{CHO,16}$ is unknown. It can be found from this equation

$$\bar{h}_{CHO,16} = ZC \cdot \bar{H}_{CO2,16} + ZH/2 \cdot \bar{h}_{H2O,16,l} + HHV_{biomass} \cdot M_{CHO} \tag{4.54}$$

Here $HHV_{biomass}$ is unknown. It can be found using Dulong and Perit equation [152]

$$HHV_{biomass} = 338.3 \cdot ZC + 1443 \cdot (ZH - ZO/8) + 94.2 \cdot ZS \tag{4.55}$$

On the other hand, the LHV can be found using this equation [153]

$$LHV_{biomass} = HHV_{biomass} - 226.04 \cdot ZH - 25.82 \cdot \omega \tag{4.56}$$

Since the combustor involves chemical reaction, we need to calculate both the physical and chemical exergies at the inlets and exit of the combustor. The physical exergy at the inlets of the combustor is zero since the fuel and air enter at surrounding conditions. The physical exergies at the exit of the combustor are

$$\bar{ex}_{CO2,18} = \bar{h}_{CO2,18} - \bar{h}_{CO2,0} - T_0 \cdot (\bar{s}_{CO2,18} - R \cdot \ln(x_{CO2,18}) - \bar{s}_{CO2,0})$$

$$\bar{ex}_{H2O,18} = \bar{h}_{H2O,18} - \bar{h}_{H2O,0} - T_0 \cdot (\bar{s}_{H2O,18} - R \cdot \ln(x_{H2O,18}) - \bar{s}_{H2O,0})$$

$$\bar{ex}_{N2,18} = \bar{h}_{N2,18} - \bar{h}_{N2,0} - T_0 \cdot (\bar{s}_{N2,18} - R \cdot \ln(x_{N2,18}) - \bar{s}_{N2,0})$$

To find the chemical exergy of the species at the inlets and exit of the combustor, we need to know the standard chemical exergies of these species. The standard chemical exergies of the species at the inlets and exit, except for the biomass fuel, are shown in Table 4.7. The standard chemical exergy of the biomass fuel is defined as

$$\bar{ex}_{biomass} = \beta \cdot LHV_{biomass} \tag{4.57}$$

where β for solid hydrocarbons fuel (for $O/C < 2$) is defined as [154]

$$\beta = \frac{1.044 + 0.016 \cdot (ZH/ZC) - 0.3493 \cdot (ZO/ZC) \cdot (1 + 0.0531 \cdot ZH/ZC)}{1 - 0.4124 \cdot ZO/ZC} \tag{4.58}$$

Now, the chemical exergy of the fuel at the combustor inlet in kW can be calculated from

$$\dot{E}x^{ch}_{biomass,16} = \dot{n}_{CHO} \cdot \beta \cdot LHV_{biomass} \cdot M_{CHO}/1000 \tag{4.59}$$

Table 4.7 Standard chemical exergy

$\bar{ex}_{H2O}^{CH}$	9.5 kJ/mol
$\bar{ex}_{O2}^{CH}$	3.97 kJ/mol
$\bar{ex}_{N_2}^{CH}$	0.72 kJ/mol
$\bar{ex}_{CO_2}^{CH}$	19.87 kJ/mol

Source: [154]

The total enthalpy at state 19 can be found from this equation

$$\dot{H}_{19} = \dot{n}_{CO2,19} \cdot \bar{h}_{CO2,19} + \dot{n}_{H2O,19} \cdot \bar{h}_{H2O,19} + \dot{n}_{N2,19} \cdot \bar{h}_{N2,19} \tag{4.60}$$

Similarly, the total enthalpy at state 20 can be found from this equation

$$\dot{H}_{20} = \dot{n}_{CO2,19} \cdot \bar{h}_{CO2,20} + \dot{n}_{H2O,19} \cdot \bar{h}_{H2O,20} + \dot{n}_{N2,19} \cdot \bar{h}_{N2,20} \tag{4.61}$$

The physical exergies at states 19 and 20 can be calculated similarly as state 18.

4.6.2 Overall Analysis of the Biomass-Trigeneration System

The equations used to analyze the trigeneration system based on the ORC and biomass combustor are presented in this section. The input energy to the system in kW is defined as

$$\dot{Q}_{in} = \dot{n}_{CHO} \cdot LHV_{biomass} \cdot M_{CHO}/1000 \tag{4.62}$$

The net electrical power is defined as

$$\dot{W}_{net} = \dot{W}_g - \dot{W}_{op}/\eta_{motor} - \dot{W}_{sp}/\eta_{motor} \tag{4.63}$$

The energy and exergy efficiencies of electrical, cooling-cogeneration, heating- cogeneration, and trigeneration for this system are defined similarly as for the SOFC-trigeneration

system, as discussed in the previous section. Also, the definition of the electrical to heating and cooling ratios, as well as the CO_2 emissions for electrical and trigeneration are defined similarly as in the previous section.

4.7 Case Study III: Thermodynamic Modeling of the Solar Subsystem

4.7.1 Introduction

There is a considerable increase in power plants operated partially or completely by solar energy. The solar energy can be used directly to obtain electrical power through photovoltaic solar cells or to obtain thermal heat and then generate electrical power through a power cycle. In solar thermal system applications, there are several devices that can be used, such as parabolic-trough solar collectors (PTSC), solar dishes, and a solar tower. Solar parabolic trough collectors are the most established technology among the thermal solar technologies for power production and have been used in large power plants since the 1980s. Currently, several thermal solar power plants are under constructions and most of them are based on PTSC. Therefore, PTSC is selected for the solar trigeneration system considered in this study.

PTSC consists of a reflecting mirror in a parabolic shape and a pipe (receiver) at the focus of the parabolic mirror. This receiver could be enclosed by a cover to reduce the heat losses and, thus, improve the collector efficiency, which is considered in this study. A set of a mirror, receiver, and receiver cover is called a collector. The collector works as follows: the mirror receives the solar radiation. Then, the radiation is reflected from the mirror to the receiver. The pipe receives high intense-focus radiation and, therefore, the temperature of the fluid in the pipe increases. The temperature of the fluid at the pipe

exit increases considerably. Higher fluid temperatures can be achieved by placing a set of collectors in a series. The fluid in the receiver could be a commercial oil. Therminol-66 oil is the selected oil in this study. It is a commercial oil that could be used in both thermal solar systems and thermal storage tanks [155]. This oil has an operating temperature ranges from 0 to 345^oC [156]. Furthermore, this oil has a low relative pressure and its pressure is not sensitive to the increase in the temperature. In this study, the solar subsystem consists of two thermal storage tanks. One tank is used to store the hot oil. And when the hot oil is used to provide the heat input to the ORC, it cools down and is stored in the second storage tank, a cold storage tank.

Since there is a change in the solar radiation in 24 hours of operation, the solar - trigeneration system considered in this study is assumed to operate in three modes. These three modes are selected based on the change in solar radiation intensities, as presented in [157]. The first mode is from 6 am to 8 am and from 4 pm to 6 pm. In this mode, only the solar collectors are working and there is no energy storage. That is, all the energy collected from the solar energy is used to operate the trigeneration system. This mode is called the solar mode. The second mode is from 8 am to 4 pm. In this mode, part of the solar energy is used to operate the trigeneration system and the other part of the solar energy is stored in the hot storage tank. This mode is called the solar and storage mode. The third mode is from 6 pm to 6 am. In this mode, only the storage system is working. In this mode, the input energy into the trigeneration system is from the energy stored in the hot tank storage. This mode is called the storage mode.

4.7.2 Solar Collectors

In this subsection, the energy and exergy analyses of the PTSC are presented. The energy formulations of the PTSC in this section are based on the equations presented in [157, 158]. These energy formulations are validated with these two references and with the

experimental study by Dudley et al. [159]. The validation with [159] is presented at the end of this section. The useful power from the collector is defined as

$$\dot{Q}_u = \dot{m}_r \cdot \left(Cp_{r,o} \cdot T_{r,o} - Cp_{r,i} \cdot T_{r,i}\right) \tag{4.64}$$

where $\dot{Q}_u$ is the useful power and $\dot{m}_r$ is the mass flow rate of the oil in the receiver (pipe). The subscripts r, i, and o indicate receiver, inlet, and outlet, respectively. Also, this power can be calculated from

$$\dot{Q}_u = A_{ap} \cdot F_R \cdot (S - A_r/A_{ap} \cdot U_L \cdot (T_{r,i} - T_0)) \tag{4.65}$$

where A_{ap} is the collector aperture area, F_R is the heat removal factor, S is the absorbed radiation by the receiver, A_r is the receiver area, and U_L is the solar collector overall heat loss coefficient. The aperture area is defined as

$$A_{ap} = (w - D_{c,o}) \cdot L \tag{4.66}$$

where w is the collector width, $D_{c,o}$ is the cover outer diameter, and L is the collector length. The absorbed radiation by the receiver is defined as

$$S = G_b \cdot \eta_r \tag{4.67}$$

where G_b is the solar radiation in W/m^2 and η_r is the receiver efficiency. The heat removal factor is defined as

$$F_R = \frac{\dot{m}_r \cdot Cp_r}{A_r \cdot U_L} \cdot \left(1 - \exp\left(-\frac{A_r \cdot U_L \cdot F_1}{\dot{m}_r \cdot Cp_r}\right)\right) \tag{4.68}$$

where Cp_r is the specific heat of the oil in the receiver and F_1 is the collector efficiency factor and defined as

$$F_1 = U_o/U_L \tag{4.69}$$

The solar collector heat loss coefficient between the ambient and receiver is defined as

$$U_L = \left(\frac{A_r}{(h_{c,ca} + h_{r,ca}) \cdot A_c} + 1/h_{r,cr} \right)^{-1} \tag{4.70}$$

where $h_{c,ca}$ is the convection heat transfer coefficient between the cover and the ambient and it is defined as

$$h_{c,ca} = (Nus \cdot k_{air}/D_{c,o}) \tag{4.71}$$

where Nus, k_{air}, and $D_{c,o}$ are Nusselt number, thermal conductivity of the air, and outer diameter of the cover, respectively. The radiation heat transfer coefficient is defined as

$$h_{r,ca} = \left(\epsilon_{cv} \cdot \sigma \cdot (T_c + T_a) \cdot \left(T_c^2 + T_a^2 \right) \right) \tag{4.72}$$

where T,ϵ_{cv}, and σ are the temperature, emittance, and Stefan-Boltzmann constant, respectively. The subscripts c and a indicate the cover and ambient, respectively. The radiation heat transfer coefficient between the cover and receiver is

$$h_{r,cr} = \left(\frac{\sigma \cdot (T_c + T_{r,av}) \cdot \left(T_c^2 + T_{r,av}^2 \right)}{1/\epsilon_r + A_r/A_c \cdot (1/\epsilon_{cv} - 1)} \right) \tag{4.73}$$

The overall heat transfer coefficient is defined as

$$U_o = \left(1/U_L + \frac{D_{r,o}}{h_{c,r,in} \cdot D_{r,i}} + \left(\frac{D_{r,o}}{2 \cdot k_r} \cdot \ln \left(D_{r,o}/D_{r,i} \right) \right) \right)^{-1} \tag{4.74}$$

where $h_{c,r,in}$ is defined as

$$h_{c,r,in} = \frac{Nus_r \cdot k_r}{D_{r,i}} \tag{4.75}$$

where the subscripts r indicates the receiver. The cover average temperature can be calculated using this equation

$$T_c = \frac{h_{r,cr} \cdot T_{r,av} + A_c/A_r \cdot (h_{c,ca} + h_{r,ca}) \cdot T_0}{h_{r,cr} + A_c/A_r \cdot (h_{c,ca} + h_{r,ca})} \tag{4.76}$$

The amount of the solar radiation that falls on the collector is calculated using this equation

$$\dot{Q}_{solar} = A_{ap} \cdot F_R \cdot S \cdot Col_r \tag{4.77}$$

where Col_r is the total number of the solar collectors rows. The exergy of a solar collector is defined as [160]

$$\dot{E}x_{coll} = A_{ap,t} \cdot G_b \cdot \left(1 + (1/3) \cdot (T_0/T_s)^4 - (4/3) \cdot (T_0/T_s)\right) \tag{4.78}$$

where T_s is the sun temperature and equals to 6000 K [160]. The exergy destruction of the solar collectors is

$$\dot{E}x_{d,coll,solar} = (\dot{E}x_{22} - \dot{E}x_{16} + \dot{E}x_{coll})(\Delta t_{h,solar})/24[hr] \tag{4.79}$$

where $\Delta t_{h,solar}$ is the total time in hour where the solar collectors are working and equals to

$$\Delta t_{h solar} = 24 \ [\text{hr}] - \Delta t_{hchst} - \Delta t_{hdhst} \tag{4.80}$$

where Δt_{hdhst} is the total time where there is a discharge from the hot storage tank and Δt_{hchst} is the total time where there is charging to the hot storage tank.

Validation of the solar collectors model

The validation of the solar collectors model is shown in Figure 4.7. The model is examined by considering the design data for the black chrome receiver material case for a vacuum space between the receiver and its cover, as in Dudley et al. [159]. This case is selected since Dudley et al. believed that the measurement of this case is more accurate as compared to the other case presented in their report. That is, the technique used in the experiment to measure the heat loss would produce more accurate results for the black chrome receiver material case as compared to a cermet receiver material case. In this study, the baseline simulation of the solar-trigeneration system has an absorber fluid temperature of less than

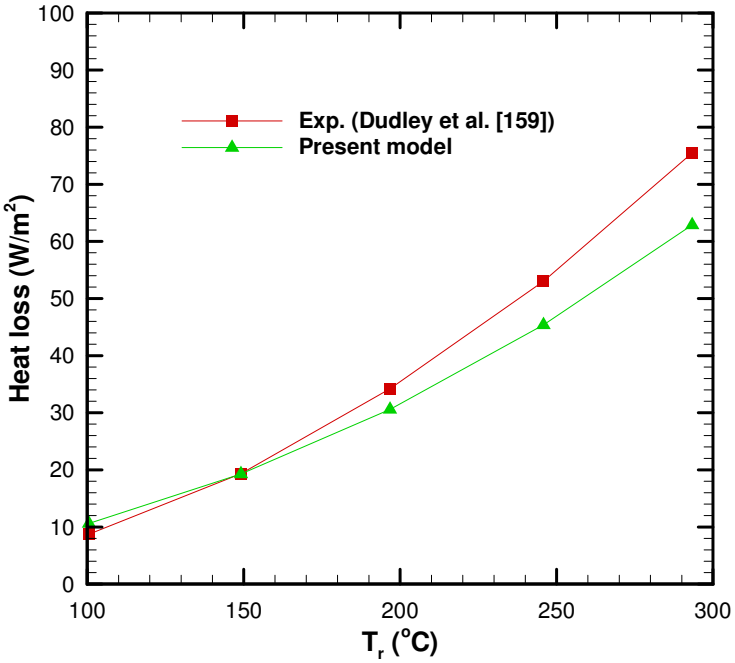

Figure 4.7 Validation of the solar collectors model; heat losses versus average temperature above the ambient of the fluid inside the absorber as compare with Dudley et al. [159].

200 ^oC above ambient temperature. Therefore, the model is in good agreement with the experimental results, as shown in this figure.

4.7.3 Thermal Storage Tanks

There are commonly two thermal storage configurations in thermal solar energy applications: thermocline tank and two tanks. The fluid heated by the solar energy can be stored in a single tank and, in this case, it is called thermocline thermal storage tank. This tank would require using advanced technology to separate the hot fluid from the cold fluid in the tank, Herrmann and Kearney [161]. The other option is to use two thermal storage tanks. In this study, the two thermal storage tanks option is selected. The two tanks option is

widely used in parabolic trough solar collector [161–166]. For parabolic trough solar collectors, two tanks thermal storage is more cost-effective in the near term option based on the field experience and technical confident as compared with the single tank option [161]. The modeling of the thermal storage tanks is presented below. The modeling considers charging, storing, and discharging the fluid from both tanks.

Hot fluid tank: charging

The rate in which the heat enters the storage tank is

$$\dot{Q}_{hst} = \dot{Q}_{23} - \dot{Q}_{l,hst}$$

where the subscripts hst and l, hst indicate hot storage tank and lost heat from the heat storage tank, respectively. The lost heat from the storage tank is

$$\dot{Q}_{l,hst} = UA_h \cdot (T_{hst} - T_0)$$

where U is the overall heat transfer coefficient. The total heat lost from the hot storage tank is

$$\sum Q_{hst} = \dot{Q}_{hst} \cdot \Delta t_h$$

where Δt_h is the total time of charging. The temperature in the storage tank can be found from

$$T_{hst} = \frac{\sum Q_{hst}}{Cp_{hst} \cdot M_{hst}}$$

where M_{hst} is the total oil mass in the hot storage tank.

Hot fluid tank: storing

The change in the temperature of the tank with time can be calculated using

$${T_{hst}}^{+} = T_{hst} + \frac{\Delta t_h}{M_{hst} \cdot Cp_{hst}} \cdot (-UA_h \cdot (T_{hst} - T_0))$$

The total heat lost during storage is

$$Q_{hst,tlost} = (M_{hst} \cdot Cp_{hst} \cdot \Delta T_{hst})$$

where ΔT_{hst} is the change in the temperature during storing in the hot tank and equals to

$$\Delta T_{hst} = T_{hst} - {T_{hst}}^{+}$$

The exergy destruction in the tank is

$$Ex_{d,hst} = \frac{\Delta t_{hchst}}{24\ [\text{hr}]} \cdot Ex_{23} - \frac{\Delta t_{hdhst}}{24\ [\text{hr}]} \cdot Ex_{24} - (1 - T_0/T_{ct,outer}) \cdot \dot{Q}_{l,hst}$$

Hot fluid tank: discharging

The total heat at discharging is

$$Q_{24} = \sum Q_{hst} - Q_{hst,tlost}$$

Cold fluid tank: storing

The total amount of heat storing in the cold tank is

$$Q_{cst,tlost} = (M_{cst} \cdot Cp_{cst} \cdot \Delta T_{cst})$$

where the subscript cst indicates cold storage tank. ΔT_{cst} is the change of the temperature in the cold storage tank and equals to

$$\Delta T_{cst} = T_{cst} - {T_{cst}}^{+}$$

where ${T_{cst}}^{+}$ is equal to

$${T_{cst}}^{+} = T_{cst} + \frac{\Delta t_c}{M_{cst} \cdot Cp_{cst}} \cdot (-UA_{cv} \cdot (T_{cst} - T_0))$$

Cold fluid tank: discharging

The heat rate discharged from the cold tank is

$$Q_{28} = \sum Q_{cst} - Q_{cst,tlost}$$

4.7.4 Overall Analysis of the Solar-Trigeneration System

The equations used to analyze the trigeneration system based on the solar subsystem are presented in this subsection. The input energy to the plant is defined as

$$\dot{Q}_{in} = \dot{Q}_{solar}$$

where $\dot{Q}_{solar}$ is the total heat collected by the solar collectors. The net electrical power is defined as

$$\dot{W}_{net} = \eta_g \cdot \dot{W}_{ot} - \dot{W}_{op}/\eta_{motor} - \dot{W}_{sp}/\eta_{motor} - \dot{W}_{sol,p}/\eta_{motor} - \dot{W}_{st1,p}/\eta_{motor} - \dot{W}_{st2,p}/\eta_{motor}$$

The energy and exergy efficiencies of electrical, cooling-cogeneration, heating- cogeneration, and trigeneration for the solar trigeneration system are defined similarly as for SOFC, presented above. Also, the definitions of the electrical to heating and cooling ratios are defined similarly as presented above for the SOFC analysis. The input data to the solar trigeneration system is listed in Table 4.8.

4.8 Thermoeconomic Optimization of the Trigeneration Systems

In this section, the thermoeconomic modeling and thermoeconomic optimization of the three trigeneration systems considered are presented. The thermoeconomic modeling is based on the SPECO method. The optimization method is based on Powell's direct research method. The descriptions of these two methods are presented in Chapter 3.

Table 4.8 Input data for the solar trigeneration system

w	5.76 m [167]
L	12.27 m [167]
η_r	0.765 [167]
${G_b}^a$	0.5 kW/m^2 [157]
${G_b}^b$	0.85 kW/m^2 [157]
ϵ_r	0.92 [168]
${Col_n}^c$	50
${Col_r}^c$	7
$\dot{m}_r^c$	8 kg/s
${D_{r,i}}^c$	0.045 m

[a]: During low sun radiation

[b]: During high sun radiation

[c]: Based on the thermoeconomic optimization results

4.8.1 Thermoeconomic Modeling of the SOFC-Trigeneration System

In this subsection, the thermoeconomic modeling of the SOFC-trigeneration system is presented. The first step in thermoeconomic modeling is finding the capital investment and maintenance costs of the SOFC-trigeneration system considered. These costs are shown in Table 4.9. In this table, PEC refers to purchase equipment cost and Z^t is the total levelized cost assuming the plant has a lifetime of 20 years. The thermoeconomic modeling of the components of the SOFC-trigeneration system is presented next.

ORC pump

For a control volume around the ORC pump, the cost-rate equation is

$$\dot{C}_2 = \dot{C}_1 + \dot{C}_{op} + \dot{Z}_{op}$$

Table 4.9 Purchase equipment costs and levelized costs of the SOFC-trigeneration system

	PEC (US$)	Z^t(US$/h)
ORC pump	14000	0.1254
ORC turbine	100000	0.8959
Heat process heat Ex	20000	0.1792
Evaporator	25000	0.224
Single-effect Abs. Ch.	22000	0.1971
SOFC	400/kW (SOFC)	1.52
Inverter	33/kW(SOFC)	0.1254
After burner	180000	1.613
Biomass boiler	57000	0.5106
Air-heat exchanger	180000	1.613
Methane-heat exchanger	90000	0.8063
Water-heat exchanger	70000	0.6271
Air blower	120000	1.075
Methane blower	30000	0.2688
Water pump	12000	0.1075
Electrical generator	120000	1.075
Methane fuel	0.000012 $/kJ	80.14
Biomass wood cost	0.01 $/kWh (LHV)	30.99

Sources: [169–173]

ORC turbine

For a control volume around the ORC turbine, the cost-rate equation is

$$\dot{C}_4 + \dot{C}_{ot} = \dot{C}_3 + \dot{Z}_{ot}$$

where

$$c_4 = c_3 \quad (F \text{ rule})$$

ORC heat exchanger

For a control volume around the ORC heat exchanger, the cost-rate equation is

$$\dot{C}_5 + \dot{C}_{hp,2} = \dot{C}_4 + \dot{C}_{hp,1} + \dot{Z}_{o,HEx}$$

where

$$c_5 = c_4 \quad (F \text{ rule})$$

and

$$\dot{C}_{hp,1} = 0$$

Here $C_{hp,1}$ is assumed to be zero since the cost of the stream enters the heating-heat exchanger for heating is not part of the trigeneration system considered.

Single-effect absorption chiller

For a control volume around the single-effect absorption chiller, the cost-rate equation is

$$\dot{C}_1 + \dot{C}_{chiller,2} = \dot{C}_5 + \dot{C}_{chiller,1} + \dot{Z}_{chiller}$$

where

$$\dot{C}_{chiller,1} = 0$$

and

$$c_1 = c_5 \quad (F \text{ rule})$$

Here $C_{hp,1}$ is assumed to be zero since the cost of the stream entering the absorption chiller is not part of the trigeneration system considered.

ORC evaporator

For a control volume around the ORC evaporator, the cost-rate equation is

$$\dot{C}_3 + \dot{C}_{29} = \dot{C}_2 + \dot{C}_{28} + \dot{Z}_{oe}$$

where

$$c_{29} = c_{28} \quad (F \text{ rule})$$

Blower-1 (air blower)

For a control volume around the air blower, the cost-rate equation is

$$\dot{C}_{17} = \dot{C}_{16} + \dot{C}_{b1} + \dot{Z}_{b1}$$

where

$$\dot{C}_{16} = 0$$

Here C_{16} is assumed to be zero since the air enters at zero cost.

Air heat exchanger

For a control volume around the air heat exchanger, the cost-rate equation is

$$\dot{C}_{18} + \dot{C}_{34} = \dot{C}_{17} + \dot{C}_{33} + \dot{Z}_{HEx,air}$$

where

$$c_{34} = c_{33} \quad (F \text{ rule})$$

Blower-2 (methane blower)

For a control volume around the methane blower, the cost-rate equation is

$$\dot{C}_{21} = \dot{C}_{20} + \dot{C}_{b2} + \dot{Z}_{b2}$$

where

$$\dot{C}_{20} = \dot{Z}_{CH4}$$

Methane heat exchanger

For a control volume around the methane heat exchanger, the cost-rate equation is

$$\dot{C}_{22} + \dot{C}_{35} = \dot{C}_{21} + \dot{C}_{34} + \dot{Z}_{HEx,CH4}$$

where

$$c_{35} = c_{34} \quad (F \text{ rule})$$

Water pump

For a control volume around the water pump, the cost-rate equation is

$$\dot{C}_{24} = \dot{C}_{23} + \dot{C}_{wp} + \dot{Z}_{wp}$$

where

$$\dot{C}_{23} = 0$$

Here C_{23} is assumed to be zero since the cost of the stream entering the water pump is not part of the trigeneration system considered.

Water heat exchanger

For a control volume around the water heat exchanger, the cost-rate equation is

$$\dot{C}_{25} + \dot{C}_{36} = \dot{C}_{24} + \dot{C}_{35} + \dot{Z}_{HEx,H2O}$$

where

$$c_{36} = c_{35} \quad (F \text{ rule})$$

SOFC

For a control volume around the SOFC, the cost-rate equation is

$$\dot{C}_{27} + \dot{C}_{19} + \dot{C}_{inverter} = \dot{C}_{18} + \dot{C}_{22} + \dot{C}_{25} + \dot{Z}_{SOFC}$$

where

$$\dot{C}_{19}/\dot{E}x_{19} = \dot{C}_{inverter}/\dot{W}_{FC,stack} \quad (P \text{ rule})$$

and

$$\dot{C}_{27}/\dot{E}x_{27} = \dot{C}_{inverter}/\dot{W}_{FC,stack} \quad (P \text{ rule})$$

After burner

For a control volume around the after burner, the cost-rate equation is

$$\dot{C}_{28} = \dot{C}_{19} + \dot{C}_{27} + \dot{Z}_{AfterBurner}$$

Biomass boiler

For a control volume around the biomass boiler, the cost-rate equation is

$$\dot{C}_{33} + \dot{C}_{32} = \dot{C}_{29} + \dot{C}_{30} + \dot{C}_{31} + \dot{Z}_{boiler}$$

where

$$\dot{C}_{30} = \dot{Z}_{wood}$$

$$\dot{C}_{31} = 0$$

and

$$c_{32} = 0 \quad [136]$$

C_{31} equals zero since it does not cost any money and also it is not part of the SOFC-trigeneration system considered.

To solve the above thermoeconomic equations, further auxiliary equations are needed. These equations can be obtained by considering a control volume around the electrical generator [174–176]. Apply the cost-rate equation around this control volume to obtain

$$\dot{C}_{net} + \dot{C}_{op} + \dot{C}_{b1} + \dot{C}_{b2} + \dot{C}_{wp} = \dot{C}_{gen} + \dot{C}_{inverter} + \dot{Z}_{gen} + \dot{Z}_{inverter} \quad (4.81)$$

Table 4.10 Purchase equipment costs and levelized costs of the biomass-trigeneration system

	PEC (US$)	Z^t(US$/h)
ORC pump	25000	0.224
ORC turbine	200000	1.792
Heat process heat Ex	40000	0.3583
Evaporator	70000	0.6271
Single-effect Abs. Ch.	22000	0.1971
Biomass boiler	300000	2.688
Electrical generator	400000	3.583
Biomass wood fuel	0.01 $/kWh (LHV) [173]	66.92

Sources: [169, 170]

Now, use the *P* rule to solve the cost rate of the pumps and blowers. These cost-rate equations are shown below

$$\dot{C}_{op}/\dot{W}_{op} = \dot{C}_{net}/\dot{W}_{net}$$

$$\dot{C}_{b1}/\dot{W}_{b1} = \dot{C}_{net}/\dot{W}_{net}$$

$$\dot{C}_{b2}/\dot{W}_{b2} = \dot{C}_{net}/\dot{W}_{net}$$

$$\dot{C}_{wp}/\dot{W}_{wp} = \dot{C}_{net}/\dot{W}_{net}$$

4.8.2 Thermoeconomic Modeling of the Biomass-Trigeneration System

In this subsection, the thermoeconomic modeling of the biomass-trigeneration system is presented. The purchase equipment costs and the levelized cost assuming 20 years of the plant's life operation are presented in Table 4.10. The thermoeconomic modeling of the biomass-trigeneration system components are presented next.

ORC pump

For a control volume around the ORC pump, the cost-rate equation is

$$\dot{C}_2 = \dot{C}_1 + \dot{C}_{op} + \dot{Z}_{op}$$

ORC Turbine

For a control volume around the ORC turbine, the cost-rate equation is

$$\dot{C}_4 + \dot{C}_{ot} = \dot{C}_3 + \dot{Z}_{ot}$$

where

$$c_4 = c_3 \quad (F \text{ rule})$$

ORC heat exchanger

For a control volume around the ORC heat exchanger, the cost-rate equation is

$$\dot{C}_5 + \dot{C}_{hp,2} = \dot{C}_4 + \dot{C}_{hp,1} + \dot{Z}_{o,HEx}$$

where

$$\dot{C}_{hp,1} = 0$$

and

$$c_5 = c_4 \quad (F \text{ rule})$$

SEAC

For a control volume around the single-effect absorption chiller, the cost rate-equation is

$$\dot{C}_1 + \dot{C}_{chiller,2} = \dot{C}_5 + \dot{C}_{chiller,1} + \dot{Z}_{chiller}$$

where

$$\dot{C}_{chiller,1} = 0$$

and

$$c_1 = c_5 \quad (F \text{ rule})$$

ORC evaporator

For a control volume around the ORC evaporator, the cost-rate equation is

$$\dot{C}_3 + \dot{C}_{20} = \dot{C}_2 + \dot{C}_{19} + \dot{Z}_{oe}$$

where

$$c_{20} = c_{19} \quad (F \text{ rule})$$

Biomass wood boiler

For a control volume around the biomass boiler, the cost-rate equation is

$$\dot{C}_{18} = \dot{C}_{16} + \dot{C}_{17} + \dot{Z}_{boiler}$$

where

$$\dot{C}_{16} = \dot{Z}_{wood}$$

and

$$\dot{C}_{17} = 0$$

A further auxiliary equation is needed to solve the above equations in this subsection. This equation can be obtained by applying a control volume around the electrical generator [174–176], using the *P* rule. Apply a control volume around the electrical generator to obtain

Table 4.11 Purchase equipment costs and levelized costs of the solar-trigeneration system

	PEC (US$)	Z^t(US$/h)
ORC pump	25000	0.2162
ORC turbine	200000	1.729
Heat process heat Ex	40000	0.3459
Evaporator-a	45000	0.7782
Evaporator-b	45000	0.7782
Single-effect Abs. Ch.	22000	0.1902
Solar collectors	5500000	74.82
Solar-storage Heat Ex	45000	1.167
Hot storage Tank	145000	3.761
Cold storage Tank	145000	2.508
Solar pump	20000	0.3459
Storage pump I	20000	0.3459
Storage pump II	20000	0.5188
Electrical generator	400000	3.459

Sources: [170, 177, 178]

$$\dot{C}_{op}/\dot{W}_{op} = \dot{C}_{net}/\dot{W}_{net} \tag{4.82}$$

4.8.3 Thermoeconomic Modeling of the Solar-Trigeneration System

In this subsection, the thermoeconomic modeling of the solar-trigeneration system is presented. The purchase equipment cost and the levelized cost assuming 20 years of the system life operation is presented in Table 4.11. The thermoeconomic equations of the equipments in the trigeneration system considered are presented next.

ORC pump

For a control volume around the ORC pump, the cost-rate equation is

$$\dot{C}_{2a} = \dot{C}_1 + \dot{C}_{op} + \dot{Z}_{op}$$

ORC evaporator-a

For a control volume around ORC evaporator-a when the solar collectors are operating, the cost per exergy equations are

$$c_{2a} = c_{2b}$$

and

$$c_{27} = c_{26} = 0$$

When the solar collectors are not working and there is only discharging from the hot storage tank, the cost-balance equation becomes

$$\dot{C}_{2b} + \dot{C}_{27} = \dot{C}_{2a} + \dot{C}_{26} + \dot{Z}_{oev,a}$$

where

$$c_{27} = c_{26} \quad (F \text{ rule})$$

ORC evaporator-b

For a control volume around ORC evaporator-b when solar collectors are operating, the cost-rate equation is

$$\dot{C}_3 + \dot{C}_{18} = \dot{C}_{2a} + \dot{C}_{17} + \dot{Z}_{oev,b}$$

where

$$c_{18} = c_{17} \quad (F \text{ rule})$$

When the solar collectors are not working and there is only discharging from the hot storage tank, the cost-balance equation becomes

$$c_3 = c_{2b}$$

ORC turbine

For a control volume around the ORC turbine, the cost-rate equation is

$$\dot{C}_4 + \dot{C}_{ot} = \dot{C}_3 + \dot{Z}_{ot}$$

where

$$c_4 = c_3 \quad (F \text{ rule})$$

ORC heat exchanger

For a control volume around the ORC heat exchanger, the cost-rate equation is

$$\dot{C}_5 + \dot{C}_{hp,2} = \dot{C}_4 + \dot{C}_{hp,1} + \dot{Z}_{o,HEx}$$

where

$$c_5 = c_4 \quad (F \text{ rule})$$

and

$$\dot{C}_{hp,1} = 0$$

Here, $C_{hp,1}$ is assumed to be zero since the cost of the stream enters the heating-heat exchanger for heating is not part from the trigeneration system considered.

Single-effect absorption chiller

For a control volume around the single-effect absorbtion chiller, the cost-rate equation is

$$\dot{C}_1 + \dot{C}_{chiller,2} = \dot{C}_5 + \dot{C}_{chiller,1} + \dot{Z}_{chiller}$$

where

$$c_1 = c_5 \quad (F \text{ rule})$$

and

$$\dot{C}_{chiller,1} = 0$$

Here $C_{chiller,1}$ is assumed to be zero since the cost of the stream enters the chiller for cooling is not part of the trigeneration system considered.

Solar collectors

For a control volume around the solar collectors, the cost-rate equation is

$$\dot{C}_{16} = \dot{C}_{22} + \dot{C}_{PSC} + \dot{Z}_{PSC}$$

where

$$\dot{C}_{PSC} = 0$$

Hot storage tank

For a control volume around the hot storage tank, the cost-rate equation is

$$\dot{C}_{24} = \dot{C}_{23} + \dot{C}_{Q,lhst} + \dot{Z}_{hst}$$

where

$$c_{lhst} = \dot{C}_{Q,lhst}/\dot{E}x_{lhst}$$

and

$$c_{lhst} = c_{23} \quad [136]$$

Cold storage tank

For a control volume around the cold storage tank, the cost-rate equation is

$$\dot{C}_{28} = \dot{C}_{27} + \dot{C}_{Q,lcst} + \dot{Z}_{cst}$$

where

$$c_{lcst} = \dot{C}_{Q,lcst} / \dot{E}x_{lcst}$$

and

$$c_{lcst} = c_{27} \qquad [136]$$

Solar heat exchanger

For a control volume around the solar heat exchanger, the cost-rate equation is

$$\dot{C}_{21} + \dot{C}_{23} = \dot{C}_{20} + \dot{C}_{30} + \dot{Z}_{StHEx}$$

where

$$c_{21} = c_{20} \qquad (F \text{ rule})$$

Solar pump

For a control volume around the solar pump, the cost-rate equation is

$$\dot{C}_{19} = \dot{C}_{18} + \dot{C}_{p,sol} + \dot{Z}_{p,sol}$$

Storage pump I

For a control volume around the storage pump I, the cost-rate equation is

$$\dot{C}_{26} = \dot{C}_{25} + \dot{C}_{p,st1} + \dot{Z}_{p,st1}$$

Storage pump II

For a control volume around the storage pump II, the cost-rate equation is

$$\dot{C}_{30} = \dot{C}_{29} + \dot{C}_{p,st2} + \dot{Z}_{p,st2}$$

Valve I

For a control volume around the valve I, neglecting the valve price, the cost per exergy unit equations are

$$c_{17} = c_{16}$$

and

$$c_{20} = c_{16}$$

Valve II

For a control volume around the valve II, neglecting the valve price, the cost-rate equation is

$$\dot{C}_{22} = \dot{C}_{19} + \dot{C}_{21}$$

Valve (24-25)

For a control volume around the valve 28-29, neglecting the valve price, the cost per exergy unit equation is

$$c_{25} = c_{24}$$

Valve (28-29)

For a control volume around the valve 28-29, neglecting the valve price, the cost per exergy unit equation is

$$c_{29} = c_{28}$$

To solve the above thermoeconomic equations, further auxiliaries equations are needed. This can be obtained by considering a control volume around the electrical generator [174–176]. Apply the cost-rate equation around this control volume to obtain

$$\dot{C}_{net} + \dot{C}_{op} + \dot{C}_{p,st1} + \dot{C}_{p,st2} + \dot{C}_{p,sol} = \dot{C}_{ot} + \dot{Z}_{gen} \tag{4.83}$$

From the *P* rule around this control volume, we obtain

$$\dot{C}_{op}/\dot{W}_{op} = \dot{C}_{p,sol}/\dot{W}_{p,sol} = \dot{C}_{p,st1}/\dot{W}_{p,st1} = \dot{C}_{p,st2}/\dot{W}_{p,st2} = \dot{C}_{net}/\dot{W}_{net} \tag{4.84}$$

4.8.4 Cost Per Unit Exergy of Power, Cooling Cogeneration, Heating Cogeneration, and Trigeneration

The main objective of a thermoeconomic modeling of a trigeneration system is to find the cost per exergy unit of the trigeneration powers. These costs are defined below. The cost per unit exergy of the net electrical, cooling cogeneration, heating cogeneration, and trigeneration, respectively, are

$$c_{net} = \dot{C}_{net}/\dot{W}_{net} \tag{4.85}$$

$$c_{cooling} = \dot{C}_{chiller,2}/\dot{Q}_{ev} \tag{4.86}$$

$$c_{heating} = \dot{C}_{hp,2}/\dot{Q}_{h} \tag{4.87}$$

$$c_{tri} = c_{net} + \dot{C}_{chiller,2}/\dot{Q}_{ev} + \dot{C}_{hp,2}/\dot{Q}_{h} \tag{4.88}$$

4.8.5 Thermoeconomic Optimization

The optimization method in this study is based on Powell's method as presented in the previous chapter. An important objective in thermoeconomic optimization is to minimize the product cost per exergy unit [136]. The objective of the optimization of the three trigeneration systems considered is to minimize the cost per exergy unit of the trigeneration (power, cooling, and heating) products. To the best knowledge of the author, there is no study that considered minimizing the product cost per exergy unit of a trigeneration system and, therefore, this analysis can be considered original. The objective equation is

$$\texttt{min}[c_{tri}] = \texttt{min}[c_{net} + c_{cooling} + c_{heating}] \tag{4.89}$$

The sequence of the optimization process can be explained as follows. First, the code finds a general solution for the objective function. Then, the direction of the optimum function is determined through Powell's method. Next, the solution of the optimum function is found through Brent's method. The last two steps are repeated until the code finds the optimum solution for the objective function. The optimization variables of the three systems considered are presented next. These variables are selected from the components of the energy source inputs to the ORC. The energy source inputs are the SOFC subsystem, biomass subsystem, and solar subsystem. The ranges of the constraints are selected to have a converged solution; and each system would be able to produce a net electrical power of 500 kW within the selected operating parameters. The constraints and their ranges are presented next. Their optimization values are given in Table 4.12. For the SOFC-trigeneration system the constraints are

$$0.75 \leq j \leq 0.85 \tag{4.90}$$

$$10000 \leq N_{FC} \leq 11000 \tag{4.91}$$

$$950 \leq T_{FC,in} \leq 1000 \tag{4.92}$$

$$2 \leq H_2O/CH_4 \leq 2.5 \tag{4.93}$$

For the biomass-trigeneration system the constraint is

$$0.05 \leq MC \leq 0.4 \tag{4.94}$$

For the solar-trigeneration system the constraints are

$$35 \leq Col_n \leq 50 \tag{4.95}$$

Table 4.12 Optimum values of the constraints

SOFC subsystem		
	j	0.85 A/cm^2
	N_{FC}	11000
	$T_{FC,in}$	1000 K
	H_2O/CH_4	2
Biomass combustor	MC	10.1%
Solar subsystem	Col_n	50
	Col_r	7
	$D_{r,i}$	0.045 m
	m_r	8 kg/s

$$6 \leq Col_r \leq 7 \tag{4.96}$$

$$0.45 \leq D_{r,i} \leq 0.65 \tag{4.97}$$

$$6 \leq \dot{m}_r \leq 8 \tag{4.98}$$

Chapter 5

Results and Discussion

5.1 Introduction

The degree of improvement of a trigeneration system is sensitive to the performance of each unit and the approach used to integrate these units into the system ; it is also sensitive to the operating parameters. Therefore, energy, exergy, and environmental modeling of any proposed system are important to assess the system performance and to examine possible degree of improvement in the system. The exergy modeling includes exergy destruction rate analysis, which helps in identifying and quantifying the sources of the irreversibilities in the system that are associated with each component. The environmental impact analysis shows how much reduction in CO_2 emissions when the trigeneration system is used, as compared to a simple electrical power system.

Further improvement of a thermal system can be obtained by conducting thermoeconomic optimization (Bejan et al.) [136]. Therefore, the three trigeneration systems considered are examined further, using thermoeconomic optimization. The thermoeconomic optimization includes the effect of varying some operating parameters on the cost per exergy unit and cost rate. According to the author's best knowledge, there is no study that

had considered the effect of varying an operating parameter on the thermoeconomic performance of a trigeneration plant under thermoeconomic optimization conditions. Therefore, this type of analysis is considered new.

In this chapter, different output key parameters are investigated. These parameters are energy and exergy efficiencies, electrical power, electrical to heating and cooling ratios, exergy destruction rate, and emissions of CO_2. For the thermoeconomic optimization, further two parameters are considered: cost per exergy unit and cost rate. This chapter discusses the results as follows: thermodynamic analysis of the SOFC-trigeneration system, thermodynamic analysis of the biomass-trigeneration system, thermodynamic analysis of the solar-trigeneration system, and, finally, the comparison of the thermodynamic and thermoeconomic analyses of the three systems under thermodynamic optimization conditions.

5.2 Energy, Exergy, and GHG Emissions Results of the SOFC-Trigeneration System

This section presents the effect of varying different variables on the performance of the SOFC-trigeneration system considered. These variables are the effect of current density of the SOFC, inlet flow temperature of the SOFC, inlet pressure of the turbine, and inlet temperature of the ORC pump. The examined output parameters are efficiency, net electrical power, electrical to heating and cooling ratios, exergy efficiency, GHG emissions, and exergy destruction rate.

5.2.1 Effect of Current Density

The effect of the current density of the SOFC on the efficiency, voltage, power, methane inlet flow rate, electrical to heating and cooling ratios, exergy efficiency, exergy destruction

rate, and CO_2 emissions is shown in Figures 5.1-5.8, respectively, under a constant SOFC inlet flow temperature of 1000 K. In these figures, the current density from 0.6 to 0.9 A/cm^2 is examined. This range is within the operating range that is found in the literature; and for the considered SOFC-trigeneration system this range produces a net output electrical power of around 500 kW.

Figure 5.1 shows that the efficiency of the SOFC decreases as the current density increases. The drop in the efficiency is attributed to the decrease in the cell voltage, V_c, as the current density increases, as shown in Figure 5.2. As illustrated in this figure, the total voltage loss, V_{loss}, increases as the current density increases. The total voltage loss consists of three types of losses. These losses are ohmic, activation, and concentration polarization voltages. In this figure, it can be observed that the voltage losses are mainly due to the activation polarization voltage loss. However, at a high current density the concentration voltage increases steeply, and it has a higher value than the activation polarization voltage. This steep increase in the voltage loss causes an abrupt drop in the efficiency of the SOFC.

As the efficiency of the SOFC decreases with the increase of the current density, the waste heat from the SOFC increases. Therefore, more energy is available to operate the ORC. However, the net electrical efficiency decreases with the increase in the current density. The highest net electrical cycle efficiency, 46%, is obtained with a current density of 0.6 A/cm^2. The efficiency of the cooling cogeneration (integration of the power cycle, SOFC, and ORC, with the cooling cycle) has, on average, a 7% gain in efficiency. The maximum cooling cogeneration efficiency is 57% while the minimum efficiency is 17%. On the other hand, the highest efficiency of the heating cogeneration (integration of the power cycle with the heating process) is 69% whereas the lowest efficiency is 59%. Figure 5.1 shows that the minimum trigeneration efficiency of the cycle is 70% at 0.6 A/cm^2 while the maximum efficiency is 72% at 0.9 A/cm^2. It can be observed in Figure 5.1 that the minimum gain in the efficiency of the trigeneration cycle, compared with the net electrical

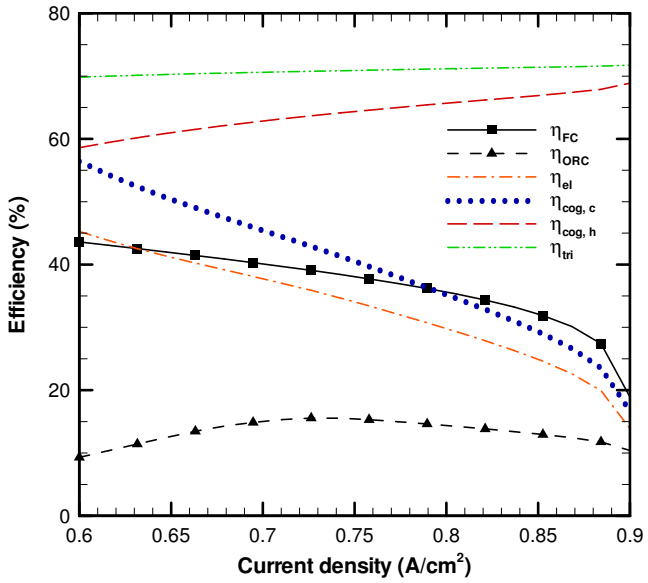

Figure 5.1 Effect of the current density on efficiency at $T_{FC,in}$ = 1000 K, P_3=1600 kPa.

efficiency is 22%, showing a significant gain.

Figure 5.3 shows the effect of the current density on the power produced by SOFC-AC and electrical generator, and the power consumed by blowers and pumps, and the net power. The SOFC-AC power increases with the increase in the current density although the efficiency decreases. The increase in the SOFC power is associated with the linear increase of the fuel inlet molar rate as the current density increases, as shown in Figure 5.4 and in Equations 4.22 and 4.23. This behavior explains why there is an increase in the power produced by the SOFC although there is a drop in the efficiency of the SOFC as the current density increases. The increase in the current density raises the power produced from the ORC, as shown in Figure 5.3. This increase in ORC power is associated with the increase in the waste heat from the SOFC, as discussed above. Consequently, the net electrical power increases as the current density increases. However, at high current density there is a drop in the net power because of the sudden increase in the voltage loss, V_{loss}. Figure 5.3

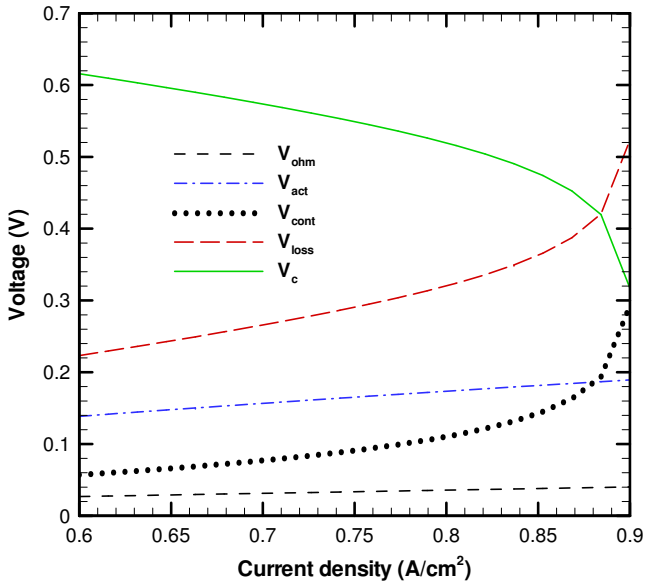

Figure 5.2 Effect of the current density on voltages at $T_{FC,in}$ = 1000 K, P_3=1600 kPa.

shows that the net power at low current density is lower than the SOFC power because of the power consumed by the pumps and blowers in the system. The net electrical power of the system varies from almost 400 kW to 540 kW.

The influence of the current density on the electrical to heating and cooling ratios is shown in Figure 5.5. This figure shows that the electrical to cooling ratio changes from 4 to 5.5 as the current density increases. On the other hand, the electrical to heating ratio changes from almost 3 at 0.6 A/cm^2 to 0.25 at 0.9 A/cm^2.

The effect of the current density of the SOFC on the exergy efficiency is shown in Figure 5.6. This figure shows that the net electrical exergy efficiency decreases as the current density increases. This reduction in the exergy efficiency is because of the decrease in the cell voltage as the current density increases and, thus, less power output from the SOFC, as discussed above. The highest net electrical exergy efficiency is 43% at a current density of 0.6 A/cm^2 and the lowest exergy efficiency is 11% at 0.9 A/cm^2. The cooling cogeneration

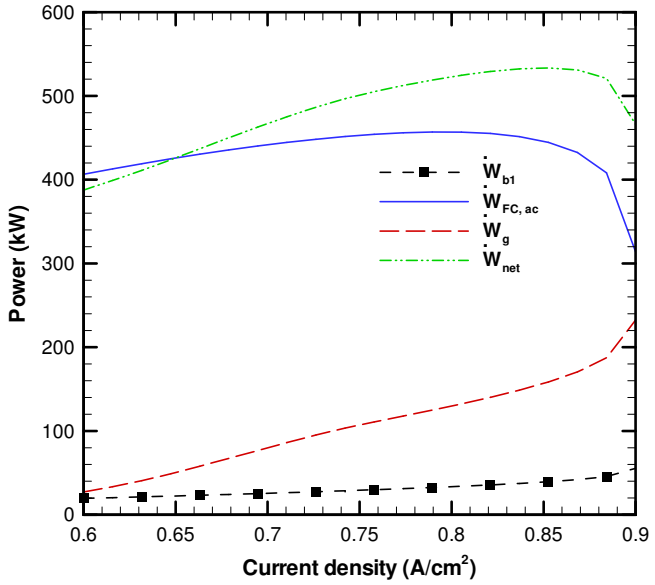

Figure 5.3 Effect of the current density on power at $T_{FC,in}$ = 1000 K, P_3=1600 kPa.

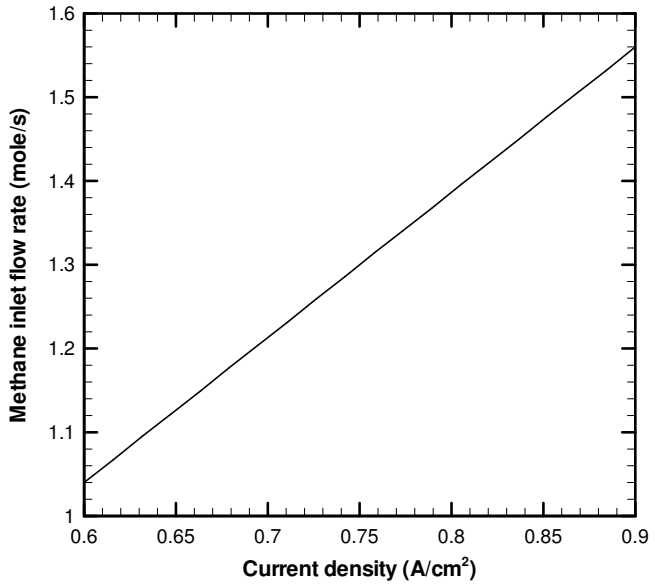

Figure 5.4 Effect of the current density on the methane flow rate at the inlet of the SOFC at $T_{FC,in}$ = 1000 K, P_3=1600 kPa.

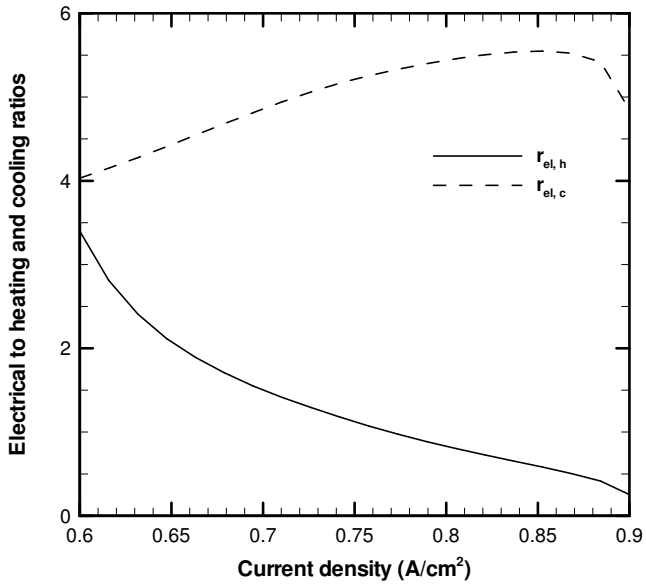

Figure 5.5 Effect of the current density on electrical to heating and cooling ratios at $T_{FC,in}$ = 1000 K, P_3=1600 kPa.

exergy efficiency is 1% or less higher than the net electrical exergy efficiency. This small difference in the efficiency gained is because of the small amount of the cooling energy to the electrical energy in the cycle, which is around 20% of the electrical energy. The heating cogeneration exergy efficiency decreases as the current density increases. The highest heating cogeneration exergy efficiency is 45% at a current density of 0.6 A/cm^2 and the lowest exergy efficiency is 34.5% at 0.9 A/cm^2. The trigeneration exergy efficiency is around 1% higher than the heating cogeneration exergy efficiency. This small difference in the efficiency is because of the small gain of the cooling cogeneration exergy efficiency compared with the net electrical exergy efficiency where trigeneration is defined as combined cooling, heating, and power.

The effect of the current density on the exergy destruction rate of different components of the system is shown in Figure 5.7. Only the components of the system that show a significant amount of exergy destruction rates are shown in this figure. It can be observed that

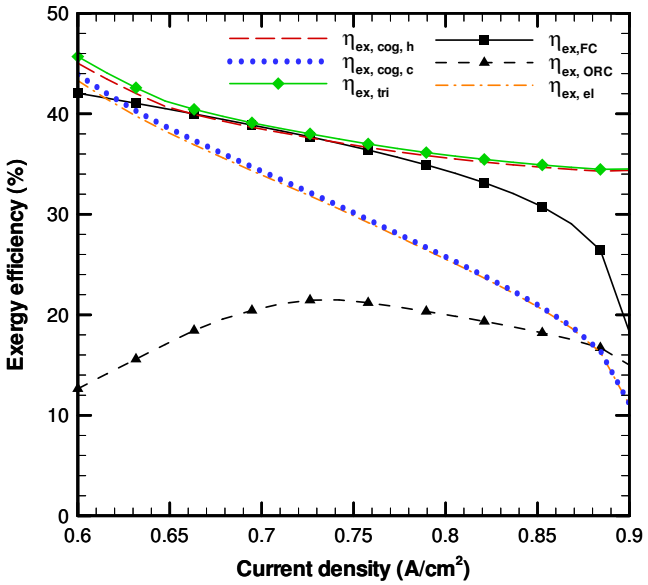

Figure 5.6 Effect of the current density on exergy efficiency at $T_{FC,in}$ = 1000 K, P_3=1600 kPa.

all the exergy destruction rates of the components increase as the current density increases. The study reveals that the exergy destruction rates of blower 1 (air blower) and the after burner increase slightly as the current density increases. The amount of the increase in the exergy destruction rate is less than 50 kW. On the other hand, the change in the exergy destruction rate with current density is considerably higher for the other components. This study shows that most of the exergy destructions occur at the ORC evaporator and air heat exchanger. However, at a high current density, the exergy destruction rate of the heat exchanger of the heating process is very high and reaches 580kW at 0.9 A/cm^2. This significant increase in the exergy destruction rate of the heat exchanger of the heating process is because of the increase in the amount of the available waste heat for heating where the net electrical exegetic efficiency drops abruptly. The parametric study on the effect of the current density on the exergy destruction rate suggests that further design improvement and optimization are needed to reduce the exergy destruction rate of the air heat exchanger,

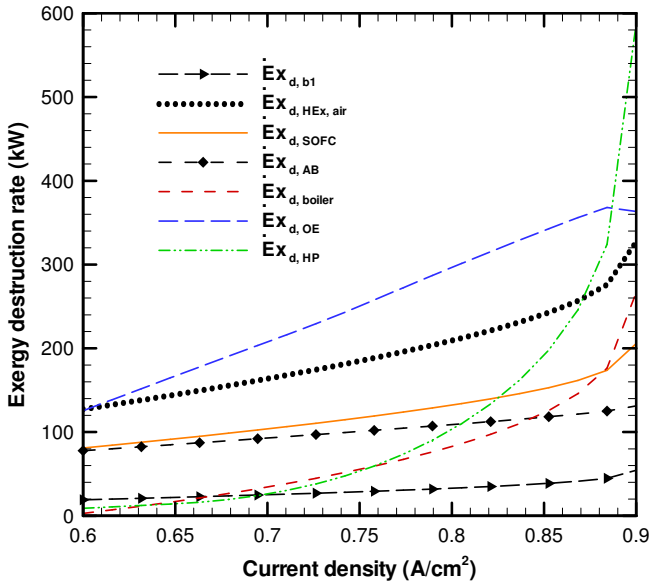

Figure 5.7 Effect of the current density on exergy destruction at $T_{FC,in}$ = 1000 K, P_3=1600 kPa.

ORC evaporator, and heat exchanger of the heating process.

Figure 5.8 shows that there is a strong coupling between the efficiency of the SOFC and the CO_2 emissions. This coupling is explained as follows. The system shown in Figure 4.1 consists of a biomass boiler. This boiler provides the heat needed to heat the inlet flow to the SOFC. When the efficiency of the SOFC decreases, more heat, in addition to the exit heat at state 29, is needed to heat the inlet flow to the SOFC. In this figure, it can be observed that at a high current density there is an abrupt increase in CO_2 emissions for the electrical power at state 32. This abrupt increase in CO_2 emissions is because of the abrupt drops in the SOFC efficiency. This figure shows that the total emissions of the CO_2 for net electrical power are very sensitive to the current density change. At the lowest current density, 0.6 A/cm^2, the total emissions of the CO_2 for the net electrical power are 470 kg/MWh and increase drastically with the increase in the current density to reach 2300 kg/MWh at 0.9 A/cm^2. On the other hand, the total CO_2 emissions for trigeneration are

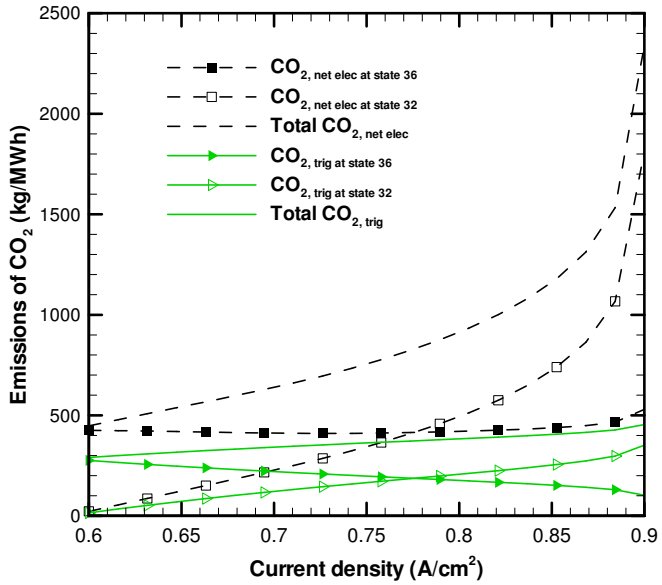

Figure 5.8 Effect of the current density on CO_2 emissions at $T_{FC,in}$ = 1000 K, P_3=1600 kPa.

significantly lower than that of the total emissions of the CO_2 for net electrical power. The total CO_2 emissions for trigeneration are between 290 and 440 kg/MWh.

5.2.2 Effect of the Inlet Flow Temperature of the SOFC

The variation in the inlet flow temperature of the fuel cell has a different effect on the performance of the trigeneration plant as compared with the change in the current density, as shown in Figures 5.9-5.15. The effect of varying SOFC inlet flow temperature is studied under a constant current density of 0.8 A/cm^2. This value is chosen since the system is closed to its highest efficiency and produces a net electrical power of approximately 500 kW.

The trend of the efficiency of the SOFC, η_{FC}, as shown in Figure 5.9, is similar to the trend of the cell voltage, as shown in Figure 5.10. In this figure, the highest cell voltage is

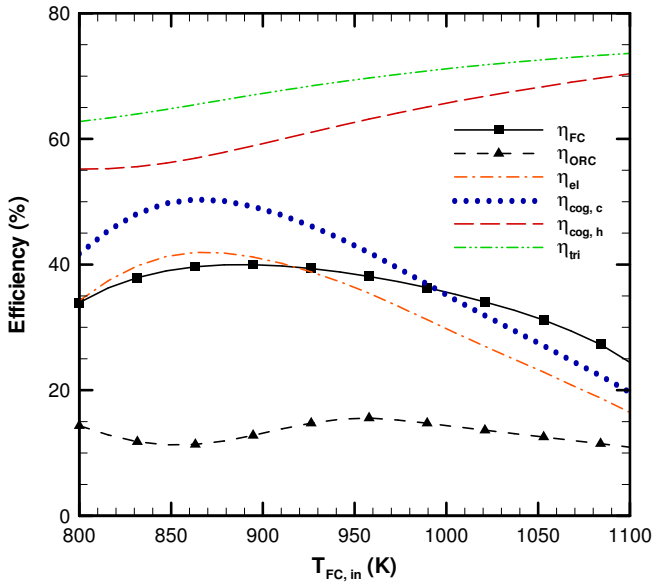

Figure 5.9 Effect of the SOFC inlet flow temperature on efficiency at j = 0.8 A/cm^2, P_3=1600 kPa.

obtained at 890 K, which is the point where the SOFC has the highest efficiency. On the other hand, the study reveals that there is on average a gain in the efficiency of the cooling cogeneration of about 7% for the case shown in Figure 5.9. The maximum efficiency of the cooling cogeneration is 51% while the minimum efficiency is 20%. On the other hand, the maximum efficiency of the heating cogeneration is 71% while the minimum efficiency is 55%. The trigeneration efficiency has a similar trend to the heating cogeneration efficiency. The maximum efficiency is 74% while the minimum trigeneration efficiency is 63%.

As the inlet temperature increases, the SOFC-AC power increases and reaches its maximum at 890 K, as shown in Figure 5.11. Beyond this temperature, 890 K, the power produced by the SOFC decreases while the power produced by the ORC increases. The reason why these two power components behave like that is similar to what was discussed above on the effect of the current density on the cell voltage. The net electrical power of the system varies from 450 to 520 kW.

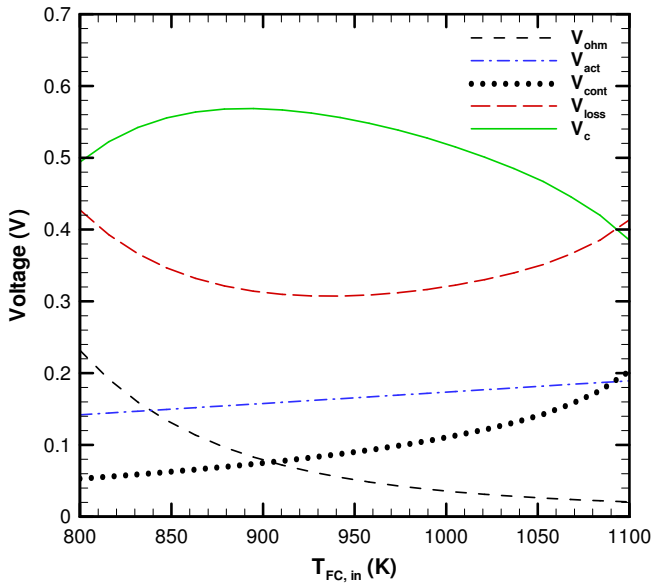

Figure 5.10 Effect of the SOFC inlet flow temperature on voltage at $j = 0.8$ A/cm^2, P_3=1600 kPa.

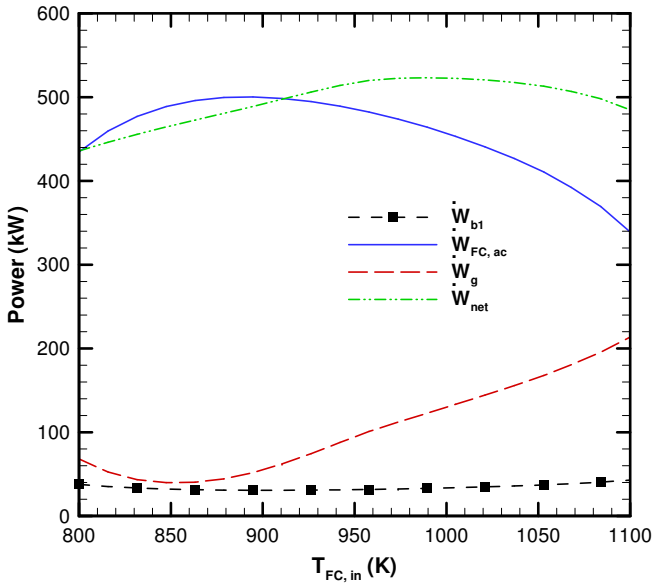

Figure 5.11 Effect of the SOFC inlet flow temperature on power at $j = 0.8$ A/cm^2, P_3=1600 kPa.

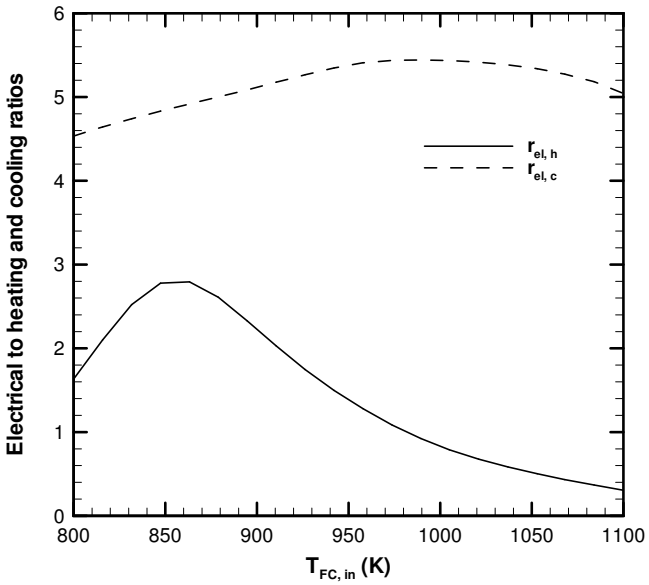

Figure 5.12 Effect of the SOFC inlet flow temperature on electrical to heating and cooling ratios at j = 0.8 A/cm^2, P_3=1600 kPa.

Figure 5.12 shows the effect of the inlet flow temperature of the SOFC on the electrical to heating and cooling ratios. The heating ratio is highest at the lowest electrical power of the organic turbine with a value of 2.8. On the other hand, the electrical to cooling ratio is around 5. This ratio has behavior similar to the electrical power. This similarity is owing to the constant value of the cooling power during the change of the current density where both the inlet and exit temperature and pressure of the desorber are constant. Therefore, this ratio is controlled only by the variation of the electrical power.

The effect of the inlet flow temperature of the SOFC on the exergy efficiency is shown in Figure 5.13. This figure shows that the change in the exergy efficiency as the inlet flow temperature change is different from that of the current density. The reason for this difference is because the cell voltage changes differently with the inlet flow temperature of the SOFC compared with the current density of the SOFC. The study reveals that the temperature where the net electrical efficiency is the highest is the same temperature where the

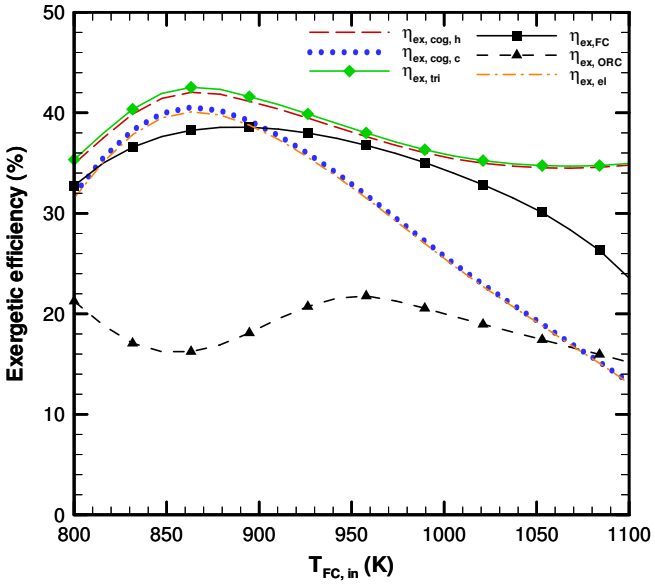

Figure 5.13 Effect of the SOFC inlet flow temperature on exergy efficiency at j = 0.8 A/cm^2, P_3=1600 kPa.

cooling cogeneration, heating cogeneration, and trigeneration efficiencies are the highest. The reason for having the same temperature, where the highest efficiency is obtained, is because all of these four efficiencies are defined based on the chemical exergy of the fuel. Therefore, the highest efficiency is obtained at the same point where the most efficient combustion occurs. The physical exergy of the incoming fuel is zero since it enters into the system at atmospheric conditions. The maximum exergy efficiencies for the electrical power is 39%, for the cooling cogeneration is 40%, for the heating cogeneration is 41%, and the for trigeneration is 42%.

Figure 5.14 shows the effect of the inlet flow temperature of the SOFC on the exergy destruction rate of different components of the system. This figure shows that the exergy destruction rates of the air blower and after burner are almost constant. Also, it can be noticed that the highest exergy destruction rate occurs at the air heat exchanger and ORC evaporator. Nevertheless, at a high inlet flow temperature the exergy destruction rate of the

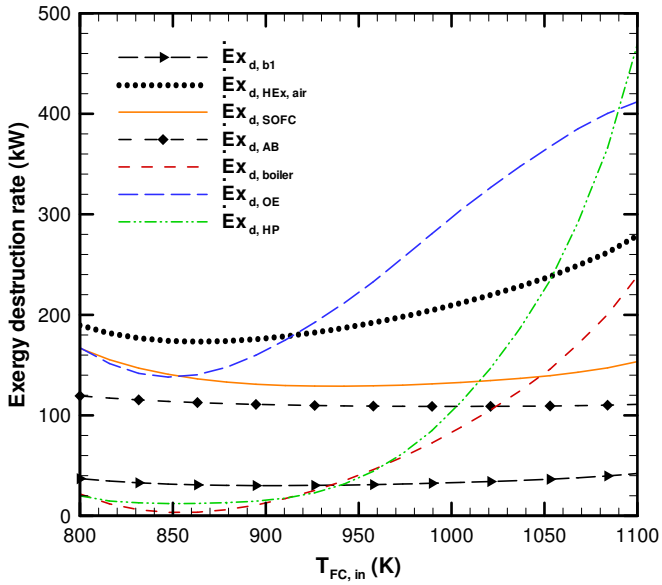

Figure 5.14 Effect of the SOFC inlet flow temperature on exergy destruction at j = 0.8 A/cm^2, P_3=1600 kPa.

heat exchanger of the heating process is considerable. This abrupt increase in the exergy destruction rate of the heat exchanger of the heating process as the inlet flow temperature increases is associated with the increase in the amount of the waste heat as the net electrical efficiency drops. This figure shows that as this temperature increases, the exergy that is destructed by the air-heat exchanger increases from almost 200 kW at 800 K to 280 kW 1100 K. The exergy destructed in the ORC evaporator increases from 180 kW at 800 K to 410 kW at 1100 K. On the other hand, the exergies destructed by the heating-process heat exchanger and boiler are very low at a low SOFC inlet temperature. However, as this temperature increases roughly to 950 K and beyond, these destructed exergies increase drastically to reach 240 kW for the boiler and to 470 kW for the heat-exchanger heating process at 1100 K. This abrupt increase is attributed to the abrupt drop in the exergy efficiency.

Figure 5.15 shows the effect of the inlet flow temperature of the SOFC on the CO_2

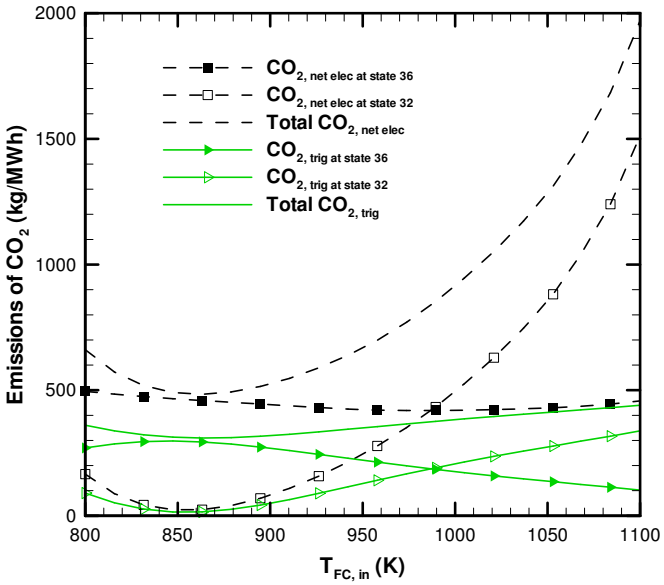

Figure 5.15 Effect of the SOFC inlet flow temperature on CO_2 emissions at j = 0.8 A/cm^2, P_3=1600 kPa.

emissions per MWh. The emissions of CO_2 are defined per MWh of the net electricity of the system and per MWh of the trigeneration. The study reveals that there are significant reductions in the CO_2 emissions per MWh of the trigeneration compared to the CO_2 emissions per net electricity. It can be observed from Figure 5.15 that there is at least a reduction of 200 kg/MWh of CO_2 emissions when trigeneration is used. Also, it can be observed that the lowest CO_2 emissions occur at a temperature of 870 K, which is the same temperature where the highest net electricity is obtained. This figure reveals that operating the SOFC at high inlet temperature would result in high CO_2 emissions when there is only electrical power production.

5.2.3 Effect of the Inlet Pressure of the Turbine

In this subsection, the effect of the turbine inlet pressure is examined. The study shows that the change in the inlet pressure of the turbine has a minimal effect on the efficiency, as shown in Figure 5.16. It was found that the variation of the efficiency of the ORC is within 5%, which is similar to what was found by [179, 180] for the examined range of the inlet turbine pressure in this study. The efficiency of the SOFC is constant since the performance of the SOFC is independent of the turbine inlet pressure. The power of the ORC changes within 50 kW, as shown in Figure 5.17. The trends of the electrical to heating and cooling ratios with the change in the inlet pressure of the turbine, as shown in Figure 5.18, are unlike the previous two cases shown in Figures 5.5 and 5.12. Figure 5.18 shows that the electrical to heating ratio is almost constant, 0.9, since the ORC power is almost constant with the change in inlet pressure of the turbine. Similarly, the electrical to cooling ratio is almost constant, 5.5.

The effect of the inlet pressure of the turbine on the exergy efficiency is shown in Figure 5.19. It can be observed that the effect of the inlet pressure of the turbine on the exergy efficiencies of the net electricity, cooling cogeneration, heating cogeneration, and trigeneration is insignificant. The net electrical and cooling cogeneration exergy efficiencies increases 3% as the turbine inlet pressure increases, and the heating cogeneration and trigeneration efficiencies increase by 1%. On the other hand, the exergy efficiency of the ORC increases from 15% at 500 kPa to 22% at 5000 kPa. The exergy efficiency of the SOFC system is constant since it is independent of the change in the turbine inlet pressure. This figure shows that as compared with the exergy efficiency of the power cycle there is on average a gain in exergy efficiency of 0.5% for cooling cogeneration, 10% for heating cogeneration, and 11% for trigeneration.

Figure 5.20 shows that only the exergy destruction rate of the ORC evaporator and heat exchanger of the heating process varies with the change in the inlet pressure of the turbine.

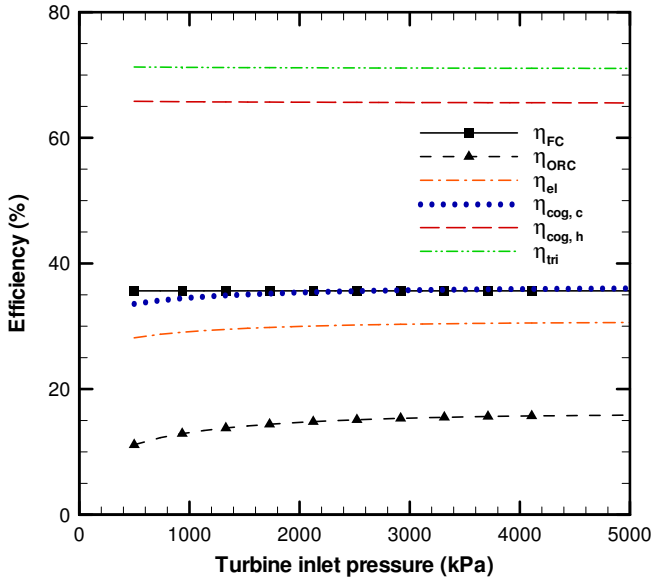

Figure 5.16 Effect of the turbine inlet pressure on efficiency at j = 0.8 A/cm^2, $T_{FC,in}$ = 1000 K.

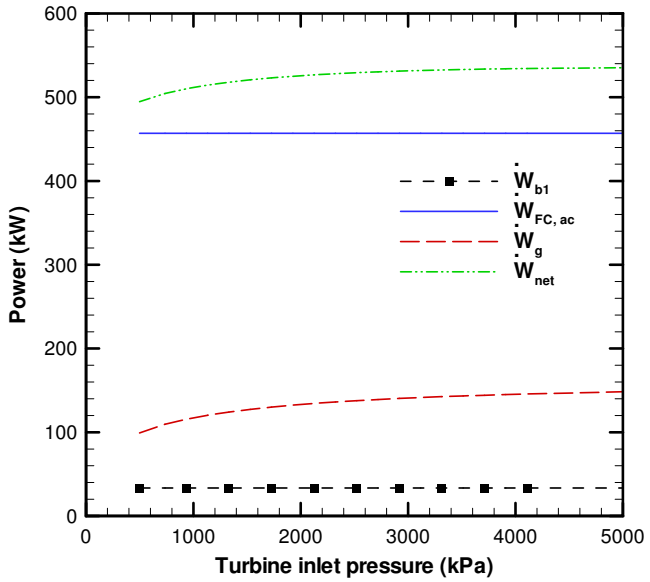

Figure 5.17 Effect of the turbine inlet pressure on power at j = 0.8 A/cm^2, $T_{FC,in}$ = 1000 K.

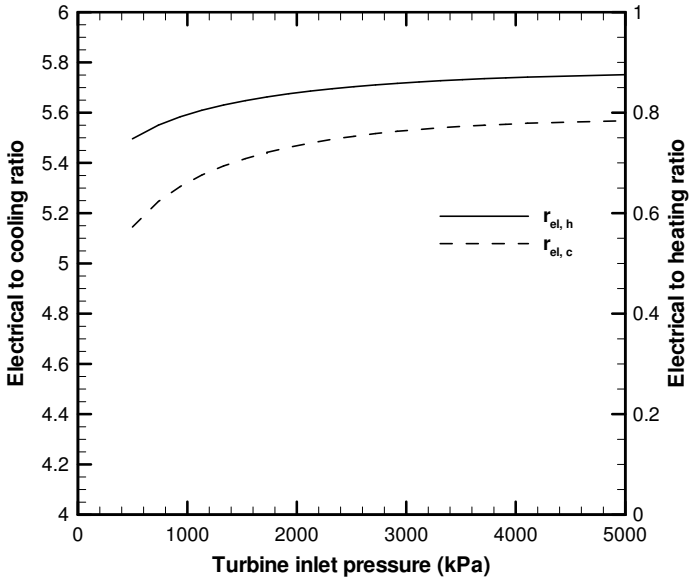

Figure 5.18 Effect of the turbine inlet pressure on electrical to heating and cooling ratios at j = 0.8 A/cm^2, $T_{FC,in}$ = 1000 K.

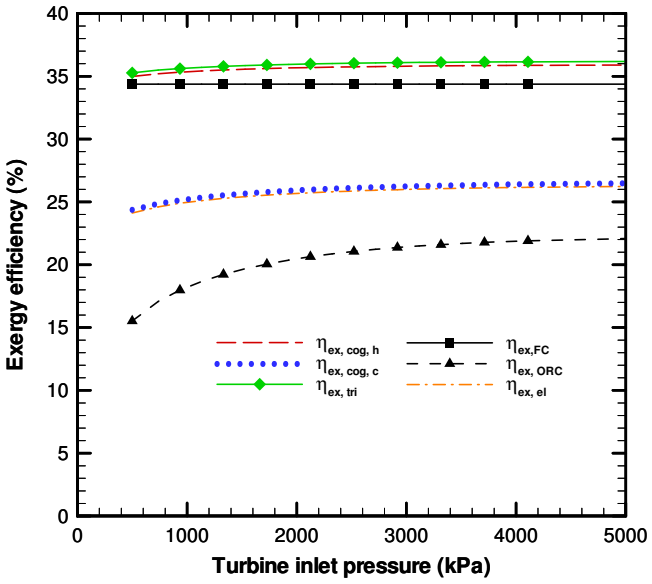

Figure 5.19 Effect of the turbine inlet pressure on exergy efficiency at j = 0.8 A/cm^2, $T_{FC,in}$ = 1000 K.

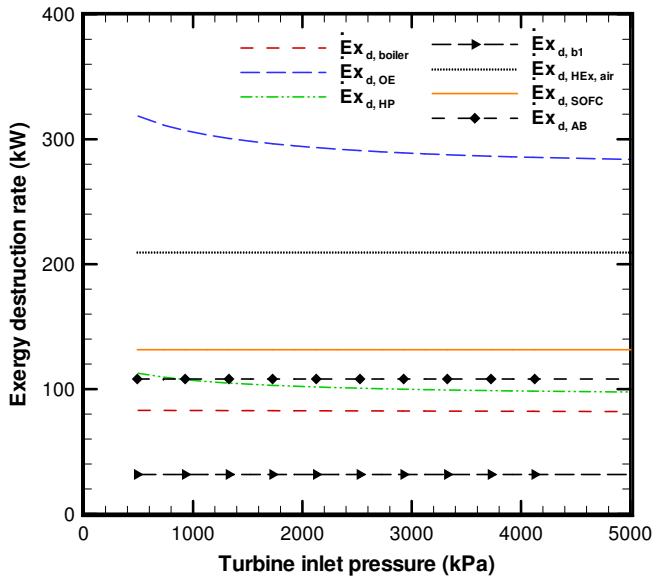

Figure 5.20 Effect of the turbine inlet pressure on exergy destruction rate at j = 0.8 A/cm^2, $T_{FC,in}$ = 1000 K.

Conversely, the other components of the system are constants since they are independent of the change in the turbine inlet pressure. The exergy destruction rate of the ORC evaporator decreases from 320kW at 500 kPa to 280 kW at 5000 kPa while the exergy destruction rate of the heat exchanger of the heating process decreases from 120 kW at 500 kPa to 100kW at 5000 kPa.

Figure 5.21 illustrates the emissions of CO_2 in kg of CO_2 per MWh produced versus the turbine inlet pressure. This figure shows that the effect of pressure on the emissions is insignificant. This insignificant effect is because the pressure variation has a negligible effect on the emissions of CO_2 where the emissions are a function of the SOFC and biomass boiler flue exits. This figure shows that the emissions of CO_2 is around 900 kg/MWh for electrical power production while, when trigeneration is used, the emissions reduce considerably to around 400 kg/MWh.

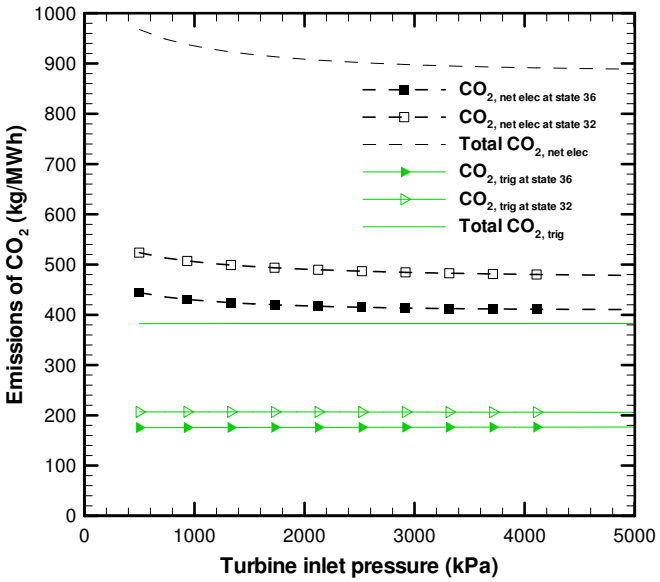

Figure 5.21 Effect of the turbine inlet pressure on CO_2 emissions at j = 0.8 A/cm^2, $T_{FC,in}$ = 1000 K.

5.2.4 Effect of the Inlet Temperature of the ORC Pump

The effect of the ORC pump inlet temperature on the performance of the systems considered in this section is presented in Figures 5.22-5.27. Figure 5.22 illustrates the efficiency compared with the ORC pump inlet temperature. This figure shows that there is only a small effect from changing the temperature on the electrical efficiency. This small effect is attributed to the relatively small portion of the electrical power that is produced by the ORC as compared to the SOFC. This electrical efficiency is around 30%. Alternatively, when cooling cogeneration is used the efficiency increases by at least 5%. The cooling cogeneration efficiency increases from 35% at 345 K to 42% at 380 K. Nevertheless, when heating cogeneration is used, the heating cogeneration efficiency increases further to at least 57%. The heating cogeneration efficiency decreases from 66% at 345 K to 57% at 380 K. This drop in efficiency is attributed to the decrease in the temperature difference

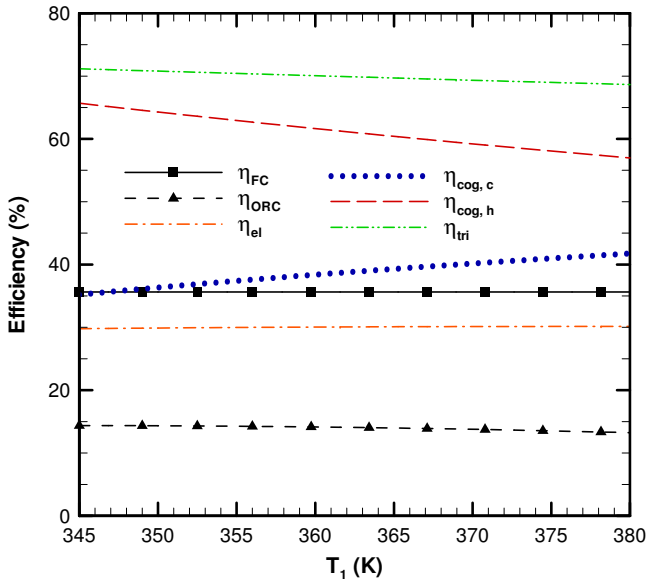

Figure 5.22 Effect of the ORC pump inlet temperature on efficiency at j = 0.8 A/cm^2, $T_{FC,in}$ = 1000 K and P$_2$ = 1600 kPa.

between the maximum temperature in the ORC and minimum temperature in the ORC. Therefore, when the temperature difference decreases as T_1 increases, smaller amount of heat is available for the heating cogeneration and, therefore, the heating cogeneration efficiency decreases. On the other hand, when trigeneration is used, the maximum trigeneration efficiency in the system reaches 72%. The trigeneration efficiency is insensitive to the change in the temperature. This insensitivity in the efficiency is because the cooling efficiency increases as the temperature increases while the heating efficiency decreases as the temperature increases. Therefore, the trigeneration efficiency, which is a combination of electrical, cooling, and heating powers, is insensitive to the temperature change.

Figure 5.23 presents the effect of the ORC pump inlet temperature on the electrical power. This figure shows that the net electrical power produced by the SOFC is insignificant to the change in the ORC pump inlet temperature since the SOFC is not part of the ORC. The net electrical power produced by the SOFC is around 450 kW. This figure shows

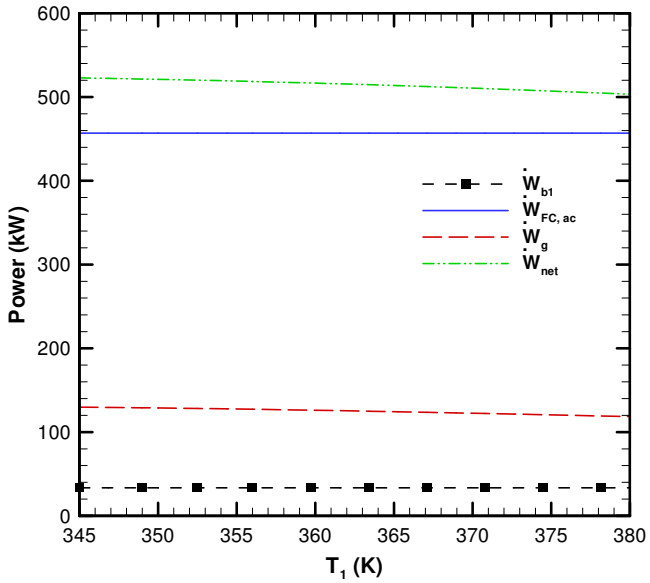

Figure 5.23 Effect of the ORC pump inlet temperature on power at j = 0.8 A/cm^2, $T_{FC,in}$ = 1000 K and P_2 = 1600 kPa.

that the electrical power produced by the electrical generator decreases from 118 kW at 345 K to 110 kW at 380 K. This small drop is attributed to the small electrical efficiency drop, as discussed above. The maximum total net electrical power produced by the system is 510 kW. The net power decreases from 510 kW at 345 K to 500 kW at 380 K. This decrease is due to the drop in the electrical power produced by the electrical generator, as discussed above.

Figure 5.24 presents the effect of the ORC pump inlet temperature on the electrical to heating and cooling ratios. This figure shows that when this temperature increases from 345 K to 380 K, the electrical to heating ratio increases from 0.9 to 1.1. This increase is owing to the decrease in the heating cogeneration efficiency. On the other hand, the electrical to cooling ratio decreases from almost 5.5 to around 2.5 as this temperature increases. This decrease is attributed to the increase in the cooling cogeneration efficiency.

The effect of the ORC pump inlet flow temperature on the exergy efficiency is shown in

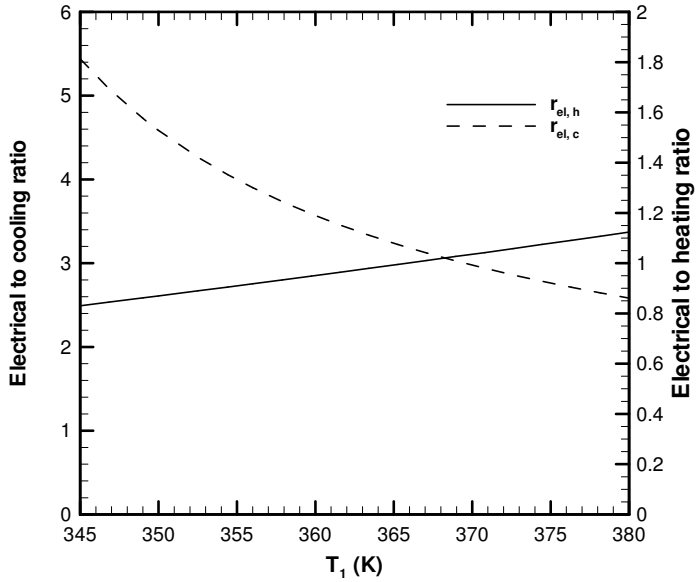

Figure 5.24 Effect of the ORC pump inlet temperature on electrical to heating and cooling ratios at j = 0.8 A/cm^2, $T_{FC,in}$ = 1000 K, and P_2 = 1600 kPa.

Figure 5.25. This figure shows that the change in the inlet temperature has an insignificant effect on the exergy efficiencies of the power, cooling cogeneration, heating cogeneration, and trigeneration. The exergy efficiency of the net electrical efficiency is around 25%. Using cooling cogeneration, the exegetic efficiency increases to 26%. The reason for this small increase in the efficiency is the small size of the cooling power as compared to the electrical power (1:5). On the other hand, the exergy efficiency of heating cogeneration is around 35% and the exergy efficiency of trigeneration is around 36%.

Figure 5.26 shows the variation of the exergy destruction rates of the ORC evaporator, boiler, and heat exchanger of the heating process with the ORC pump inlet flow temperature. As the temperature increases, the exergy destruction rate of the ORC evaporator decreases. It decreases from 300 kW at 345K to 240 kW at 380 K. This reduction in exergy destruction rate is attributed to the lower exergy difference available between the inlets and exits of the evaporator. Also, the study shows that there is an insignificant change in

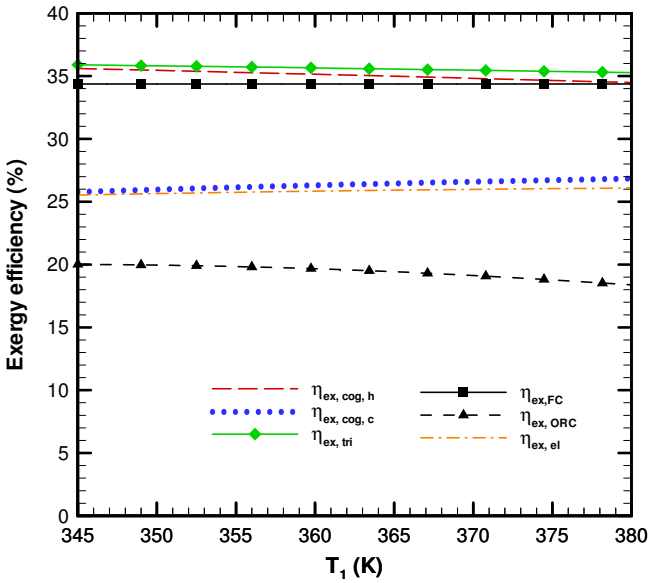

Figure 5.25 Effect of the ORC pump inlet temperature on exergy efficiency at j = 0.8 A/cm^2, $T_{FC,in}$ = 1000 K and P$_2$ = 1600 kPa.

the exergy destruction rates of the boiler and heat exchanger of the heating process as the temperature increases.

Figure 5.27 illustrates the effect of the ORC pump inlet temperature on the CO_2 emissions. It can be noticed that the effect of changing this temperature on the emissions is negligible since this temperature is not part of the SOFC system where the CO_2 is emitted to atmosphere. This figure shows that the emissions based on the electrical production are around 900 kg of CO_2 per MWh of electrical power production. Alternatively, when trigeneration is used the emissions drop significantly to around 400 kg per MWh of trigeneration. This drop demonstrates again one major significant benefit of trigeneration where lower emissions per MWh can be obtained.

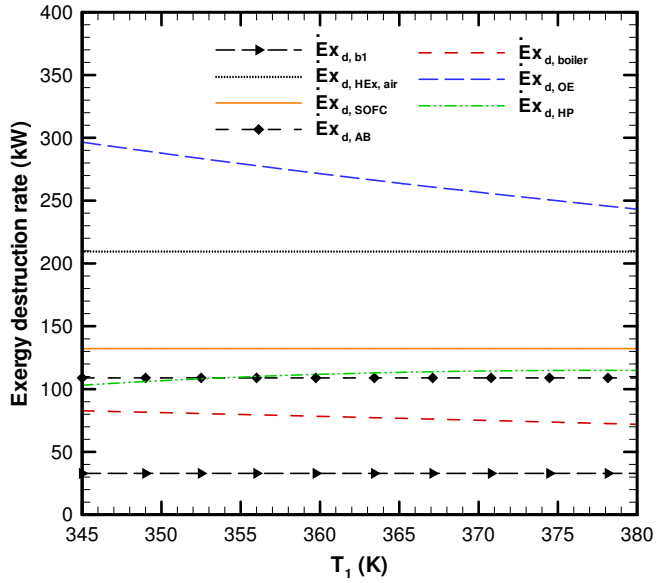

Figure 5.26 Effect of the ORC pump inlet temperature on exergy destruction at j = 0.8 A/cm^2, $T_{FC,in}$ = 1000 K and P_2 = 1600 kPa.

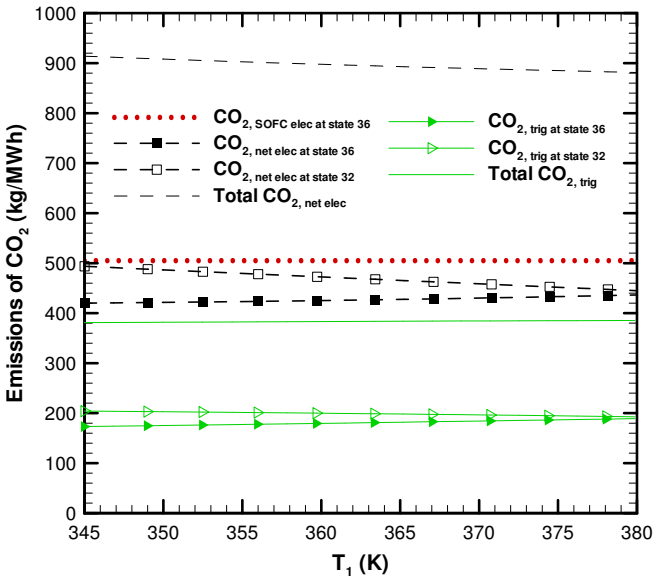

Figure 5.27 Effect of the ORC pump inlet temperature on electrical to heating and cooling ratios at j = 0.8 A/cm^2, $T_{FC,in}$ = 1000 K and P_2 = 1600 kPa.

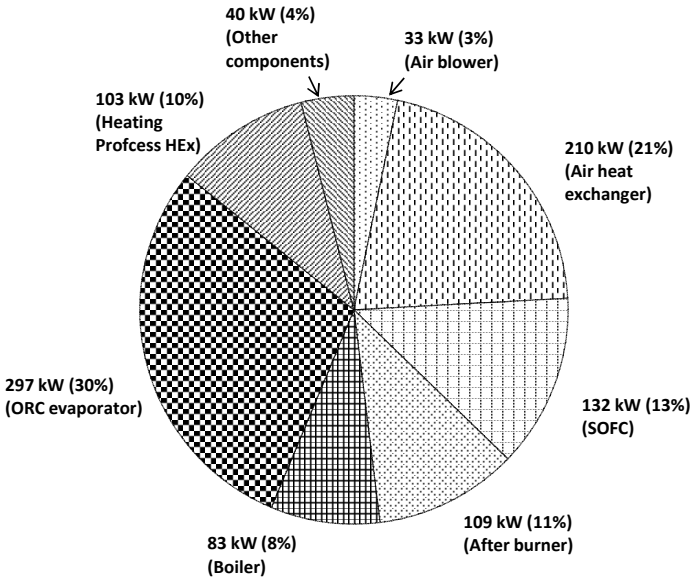

Figure 5.28 Exergy destruction in kW and in percentage of the total exergy destructed for different SOFC-trigeneration plant components at j = 0.8 A/cm^2, $T_{FC,in}$ = 1000 K and P_2 = 1600 kPa.

5.2.5 Overall Exergy Destruction

The distribution of the exergy destruction of different components of the system at the baseline input data is shown in Figure 5.28. The exergy destruction percentage that is shown in this figure is the percentage of the exergy destructed and not the available exergy in the system. The exergy destruction analysis shows that 30% of the exergy destruction takes place in the ORC evaporator and 21% in the air heat exchanger at the inlet of the SOFC. The other components of the system that have high exergy destruction are the SOFC (13%), the after burner (11%), the heating-process heat exchanger (10%), the biomass boiler (8%), and the air blower (4%). Therefore, further improvement to the performance of these components is needed, especially the ORC evaporator and the air heat exchanger.

5.2.6 Summary

Energy, exergy, and environmental analyses of the SOFC-trigeneration system are conducted. The plant's performance is studied under the variation of the current density of the SOFC, inlet flow temperature of the SOFC, inlet pressure of the turbine, and inlet temperature of the ORC pump. The main findings in this study are:

- The energy analysis of the trigeneration plant shows that there is at least a 22% gain in efficiency compared with the electrical power case (net electrical efficiency).
- The maximum efficiencies of trigeneration is 74%, heating cogeneration is 71%, cooling cogeneration is 57%, and net electricity is 46%.
- The efficiency of the SOFC decreases as the current density increases. At a current density higher than 0.88 A/cm^2, the SOFC and electrical cycle efficiencies drop abruptly because of the abrupt decrease in the cell voltage.
- All the examined efficiencies vary with the change in the inlet fuel cell temperature, as being different from the change in the current density, due to the dissimilar behaviors of the voltage loss components (especially the ohmic loss component) in the two cases.
- As the SOFC inlet flow temperature increases, the trigeneration efficiency increases. Conversely, the change in the current density of the SOFC has a negligible effect on the trigeneration efficiency.
- The electrical to cooling ratio is more sensitive to the ORC pump inlet temperature change as compared to the SOFC current density, SOFC inlet temperature, or turbine inlet pressure.

- The change in the inlet pressure of the turbine has a negligible effect on the efficiencies. Therefore, it is recommended to operate the turbine with low pressure since this requires a lower pumping ratio and, thus, cost saving.

- The exergy analysis of the trigeneration plant shows that the gain in the exergy efficiency when trigeneration is used, as compared with only the power cycle is from 3 to 25%, depending on the operating condition.

- The exergy efficiencies of the electrical power, cooling cogeneration, heating cogeneration, and trigeneration are insensitive to the change of the turbine inlet pressure and ORC pump inlet temperature.

- The most significant sources of exergy destruction rates are the ORC evaporator, air heat exchanger at the SOFC inlet, and heating-process heat exchanger. Therefore, further improvements in designing these three components are needed.

- There is a significant reduction of CO_2 emissions (kg/MWh) when trigeneration is used, as compared to utilizing only electrical power. This reduction is more than 200 kg of CO_2 /MWh.

5.3 Energy, Exergy, and GHG Emissions Results of the Biomass-Trigeneration System

The performance of the trigeneration system based on the biomass combustor and ORC is examined under the variation of some variables. These variables are the ORC evaporator pinch point temperature, pump inlet temperature and turbine inlet pressure. The ranges of the ORC evaporator pinch point temperature [181], pump inlet temperature [141, 145] and turbine inlet pressure [179, 180, 182, 183] that are considered here are taken from the

literature.

5.3.1 Thermodynamic properties of the stations

The thermodynamic properties of the states in the biomass-trigeneration system under optimum conditions are listed in Table 5.1 below.

5.3.2 Effect of the Pinch Point Temperature of the ORC Evaporator

Designing an ORC evaporator with a low pinch point temperature improves the evaporator effectiveness; however, it increases its cost and design requirements. On the other hand, this study shows that the exergy destruction of the ORC evaporator is significant. Therefore, studying the effect of the pinch point temperature of the ORC evaporator is important to assess its effect on the trigeneration system considered. The effect of the pinch point temperature of the ORC evaporator is examined under the baseline pump inlet temperature, 365 K, and baseline turbine inlet pressure, 2000 kPa. The effect of pinch point temperature variation is examined in Figures 5.29-5.34. The pinch point temperature of the evaporator is defined as [181]

$$T_{pp} = T_{20} - T_2 \tag{5.1}$$

Figure 5.29 presents the effect of the pinch point temperature on the energy efficiencies. This figure shows the efficiencies of electrical power, cooling-cogeneration, heating-cogeneration, and trigeneration cases. This figure demonstrates that as the pinch point temperature increases, the efficiencies of the electrical, heating-cogeneration, and trigeneration cases decrease; however, the efficiency of the cooling-cogeneration is almost constant. These results are explained as follows. As the pinch point temperature increases, the amount of the heat input to the ORC evaporator decreases. Therefore, T_3 decreases.

Table 5.1 Thermodynamic properties of the stations

state	m (kg/s)	T (K)	P (kPa)	h (kJ/kg)	ex (kJ/kg)
1	7	365	35.7	157.5	15.6
2	7	365.9	2000	161.3	18.8
3	7	549	2000	708.4	209.2
4	7	432.85	35.7	625	111.2
5	7	365	35.7	186	20.8
6	0.067	336.46	5.4	2618	78.27
7	0.067	307.52	5.4	144	0.508
8	0.067	278.16	0.87	144	-6
9	0.067	278.15	0.87	2510	-176
10	0.34	303.4	0.87	67.3	11.1
11	0.34	303.41	5.4	67.3	11.1
12	0.34	332.21	5.4	128.3	71.81
13	0.273	365	5.4	244.5	117.3
14	0.273	321.88	5.4	168.5	41.64
15	0.273	329	0.87	168.5	41.6
16	259.2	298.15	101.3	-9442	18.43
17	1472	298.15	101.3	0	0.003
18	1730	2077.51	101.3	-65.4	1.433
19	1730	2077.51	101.3	-65.4	1.433
20	1730	405	101.3	-203.5	-0.051

As T_3 decreases, the electrical power produced through the use of the turbine decreases and, thus, the electrical efficiency decreases. In addition, as T_3 decreases, the amount of the total heat available at state 4 decreases and, hence, the heating-cogeneration efficiency decreases. Also, depending on the operating condition of the turbine, the pressure changes. What controls the cooling power is the values of the properties of the fluid at states 5 and 1. The only possible change for state 5 at the current condition is the pressure. Note that state 5 always has the same temperature, pressure, and mass flow rate as state 1, but state 5 is saturated vapor and state 1 is saturated liquid. Therefore, what controls the cooling power as the pinch point temperature varies is the pressure change at state 5. Since the change in the pressure is small under this condition, the change in the cooling-cogeneration efficiency is almost constant. It can be observed that when trigeneration is used, the energy efficiency increases significantly. It increases from around 12% for electrical power to around 89% when trigeneration is used. In addition, this figure shows that the efficiencies of the trigeneration and heating cogeneration drop 5% as the pinch point temperature increases from 20 to 60 K while the electrical efficiency is less sensitive to the pinch temperature. Its electrical efficiency drops by about 3% as the pinch point temperature increases. In contrast, for cooling cogeneration the efficiency is insensitive to the pinch point temperature change and its efficiency is around 16%.

Figure 5.30 illustrates the net electrical power variation with the pinch point temperature of the ORC evaporator. It can be observed that as the pinch point temperature of the ORC evaporator increases, the net electrical power decreases. It decreases from 600 kW at 20 K to almost 450 kW at 60 K. This decrease is attributed to the decrease in the amount of heat input to the ORC evaporator as the pinch point temperature of the ORC evaporator increases.

Figure 5.31 presents the electrical to heating ratio and electrical to cooling ratio variation with the change in the pinch point temperature of the ORC evaporator. It can be noticed

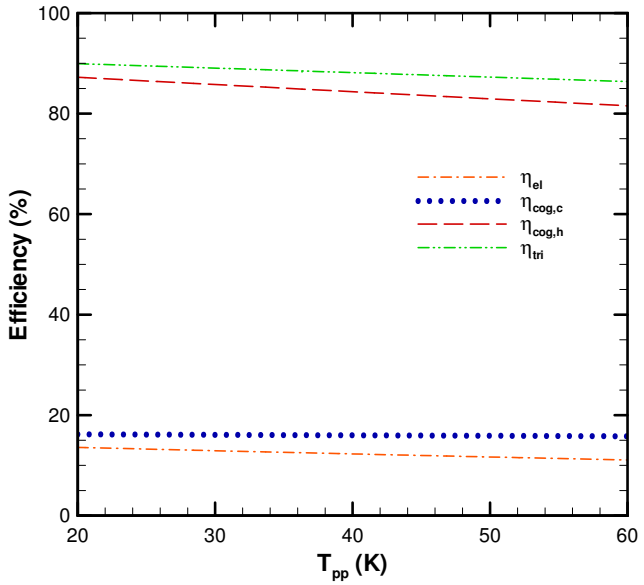

Figure 5.29 Effect of the ORC evaporator pinch point temperature on the efficiency at P_3=2,000 kPa, T_1=365 K.

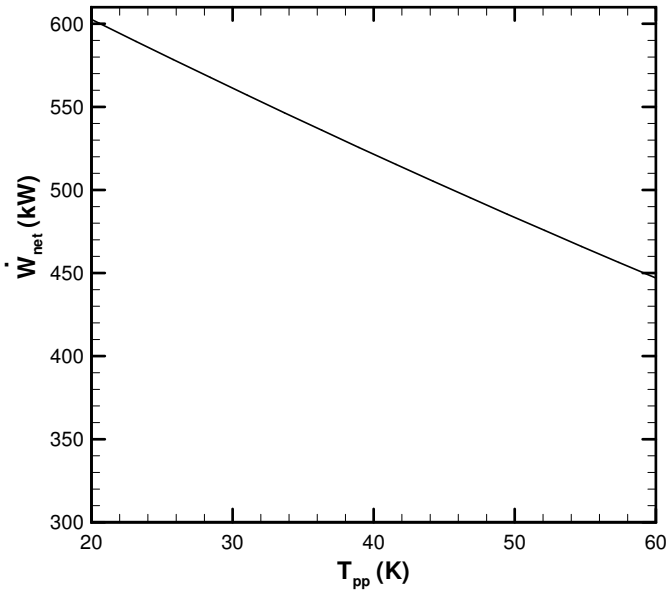

Figure 5.30 Effect of the ORC evaporator pinch point temperature on the electrical power at P_3=2,000 kPa, T_1=365 K.

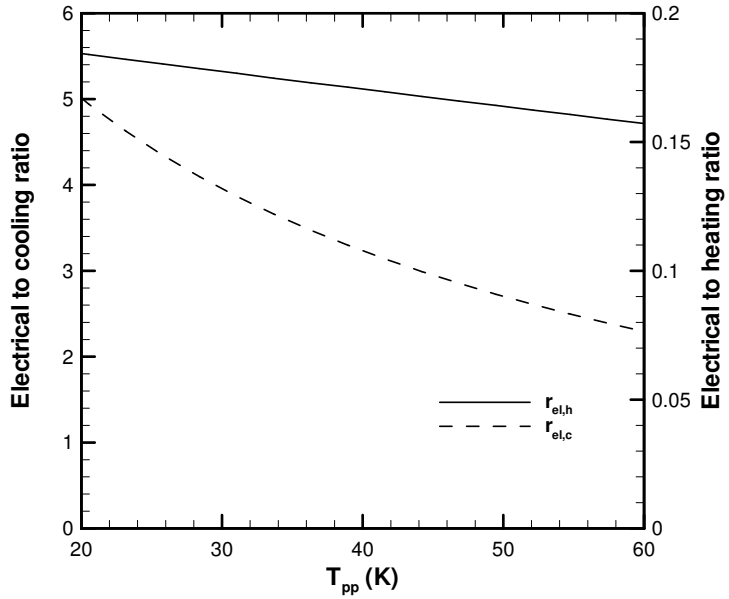

Figure 5.31 Effect of the ORC evaporator pinch point temperature on the electrical to heating and cooling ratios at P_3=2,000 kPa, T_1=365 K.

that the electrical to cooling ratio is sensitive to the change in the ORC evaporator pinch point temperature. This sensitivity is attributed to the size of the single-effect absorption chiller, which has smaller cooling power capacity compared to the electrical power. This ratio decreases from 5.0 at 20 K to 2.3 at 60 K. The electrical to heating ratio is insensitive to the change in the ORC evaporator pinch point temperature. The main reason is the large size of the heating power as compared with the electrical power produced by the system.

Figure 5.32 shows the exergy efficiency variation with the change in the pinch point temperature of the ORC evaporator. This figure reveals that the exergy efficiencies of all four cases decrease as the pinch point temperature increases. This behavior is explained as follows. The numerators of the exergy efficiencies of all four efficiencies are a function of the electrical power. Therefore, the reduction of the electrical power as the pinch point temperature increases reduces the exergy efficiencies. The heating-cogeneration exergy ef-

ficiency is a function of the heat power and the heat exchanger temperature of the heating process. The increase in the pinch point temperature results in a reduction in T_3 and, thus, T_4. Therefore, both the heating power and the temperature of the heat exchanger of the heating process decreases. Hence, the heating-cogeneration exergy efficiency decreases. Similarly, as the pinch point temperature increases, the cooling power decreases and, thus, the cooling-cogeneration efficiency drops. It can be noticed that the exergy efficiency increases significantly when the trigeneration is used, as compared with the electrical-power case. The exergy efficiency increases from around 11% for the electrical-power case to 27% for the trigeneration case. In addition, it can be observed that the electrical and cooling-cogeneration exergy efficiencies are more sensitive to the change in the pinch point temperature as compared with trigeneration and heating-cogeneration exergy efficiencies. The electrical exergy efficiency decreases from 12% at 20 K to 10% at 60 K. Conversely, the trigeneration and heating-cogeneration exergy efficiencies remain almost constant at 28% and 27%, respectively.

Figure 5.33 shows the exergy destruction rate versus the ORC pinch point temperature. This figure shows the exergy destruction rates of the biomass combustor, heating-process heat exchanger, ORC evaporator, turbine, and desorber. It shows that the biomass combustor and ORC evaporator contributes significantly to the exergy destructed by the system. The destructed exergy by these two components decreases as the pinch point temperature increases. This decrease is mainly due to the decrease in the temperature difference between states 19 and 20, as well as to the decrease in the fuel mass flow rate as the pinch point temperature increases. The exergy destruction of the biomass combustor decreases from 2200 kW at 20 K to 2000 kW at 60 K, and the exergy destruction rate of the ORC evaporator decreases from 1500 kW at 20 K to 1300 kW at 60 K. The other components of the system contribute significantly less to the total exergy destruction rate. The exergy destruction rate of the heating process increases from nearly zero at 20 K to 160 kW at 60

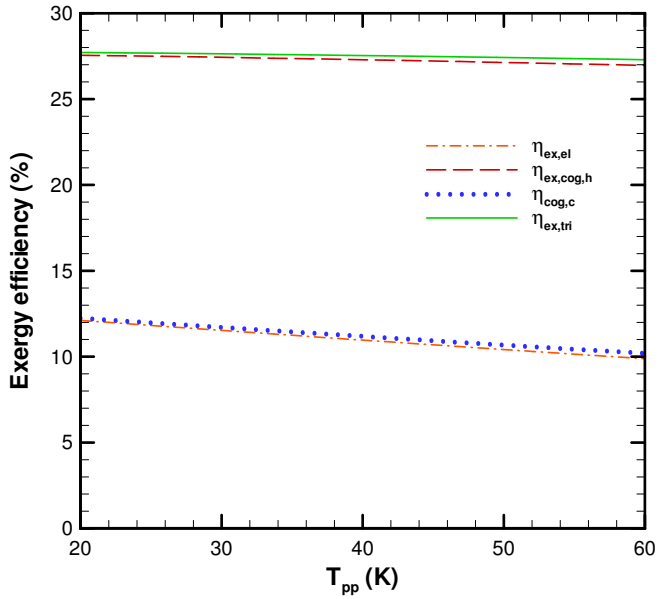

Figure 5.32 Effect of the ORC evaporator pinch point temperature on the exergy efficiency at P_3=2,000 kPa, T_1=365 K.

K while the exergy destruction rate of the turbine decreases from 120 kW at 20 K to 70 kW at 60 K. The exergy destruction rate of the desorber increases from 7 kW at 20 K to 40 kW at 60 K. The exergy destruction rates of the remaining components of the system are considerably lower and, therefore, they can be considered negligible.

Figure 5.34 illustrates CO_2 emissions in kg/MWh versus the pinch point temperature of the ORC evaporator. This figure shows the emissions of CO_2 when the electrical power case is used and the emissions of CO_2 when trigeneration is used. This figure reveals that the CO_2 emissions rates increase as the pinch point temperature increases. These increments are owing to the decrease in the efficiency of the system as the pinch point temperature increases. It can be noticed that CO_2 emissions decrease considerably when the trigeneration is used, as compared with only electrical power production. In other words, when an ORC system that is based on a biomass combustor is used for power

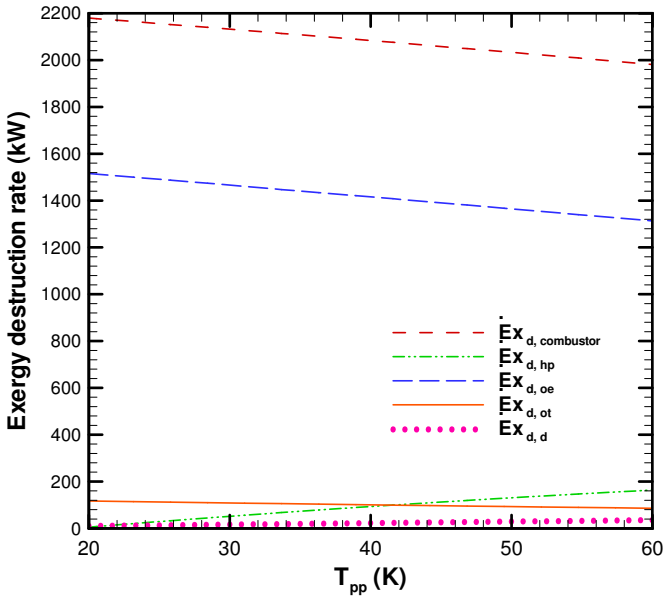

Figure 5.33 Effect of the ORC evaporator pinch point temperature on the exergy destruction at P_3=2,000 kPa, T_1=365 K.

production, this configuration will result in high CO_2 emissions rate, which is in the order of 3000 kg/MWh, as shown in this figure. Conversely, when trigeneration is used, CO_2 emissions decrease significantly to around 400 kg/MWh. Although the CO_2 emissions are high when electrical power is considered, the environmental impact is considered low. This low impact is attributed to the carbon cycle for biomass combustion.

5.3.3 Effect of the Inlet Temperature of the ORC Pump

Each single-effect absorption chiller is designed for a specific range of heat input. Therefore, it is important to identify the best operating temperature range for the best desired output(s). In this study, the pump inlet temperature is examined from 345 to 380 K, which represents the operating temperature of an ideal single-effect absorption chiller from the industry. This temperature range is selected based on what is available in the literature, as

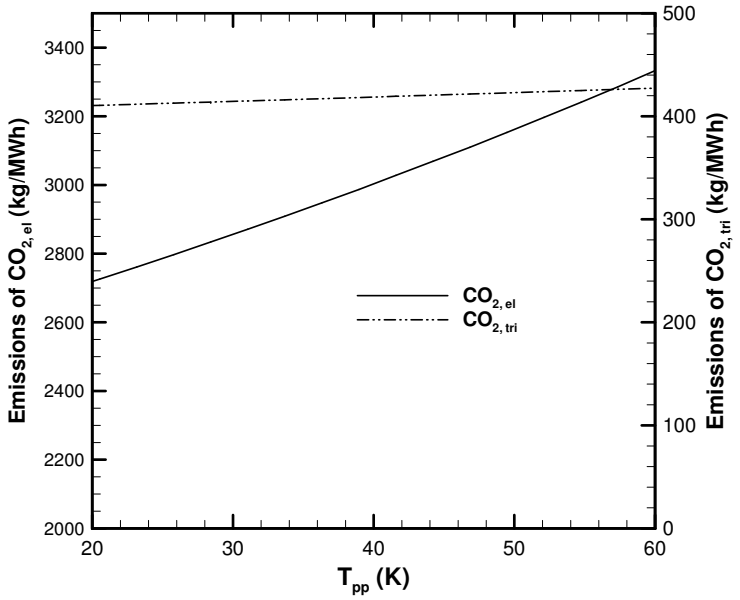

Figure 5.34 Effect of the ORC evaporator pinch point temperature on the CO_2 emissions at P_3=2,000 kPa, T_1=365 K.

mentioned above, to match the operating temperature of the desorber of the single-effect absorption chiller. The effect of pump inlet temperature is examined under the baseline turbine inlet pressure, 2,000 kPa, and baseline pinch point temperature of the ORC evaporator, 40 K.

Figure 5.35 shows the electrical efficiency, cooling-cogeneration efficiency, heating-cogeneration efficiency, and trigeneration efficiency versus pump inlet temperature. It can be observed that the electrical efficiency decreases from 14% at 345 K to 11% at 380 K. On the other hand, with the use of cooling cogeneration, the efficiency increases from 16% at 345 K to 17% at 380 K. This small gain in cooling-cogeneration efficiency, as compared with electrical efficiency, is associated with the size of the single effect-absorption chiller that was selected based on what is available in the industry [145] for cooling-cogeneration applications. On the other hand, since only a small portion of the waste heat was used for

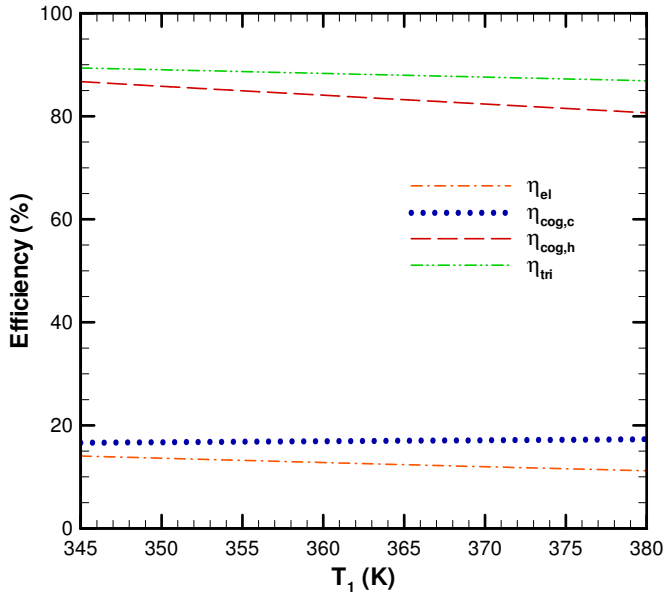

Figure 5.35 effect of the ORC pump inlet temperature on the efficiency at P_3=2,000 kPa, T_{pp}=40 K.

cooling, the gain in the heating-cogeneration efficiency is high. The heating-cogeneration efficiency decreases from 87% at 345 K to reach 80% at 380 K. Alternatively, the trigeneration efficiency decreases from 89% at 345 K to 87% at 380 K.

Figure 5.36 shows the effect of the pump inlet temperature on electrical power. It can be observed that electrical power decreases from 510 kW at 345 K to 350 kW at 380 K. The decrease in the power with the increase in the pump inlet temperature is attributed to the decrease in the temperature difference between the maximum temperature in the ORC, T_3, and minimum temperature in the ORC, T_1. The reduction in the temperature difference results in a reduction in the electrical efficiency and, therefore, the electrical power decreases.

Figure 5.37 illustrates the effect of the electrical to heating and cooling ratios. It can be noticed that the electrical to cooling ratio is sensitive to the change in the pump inlet

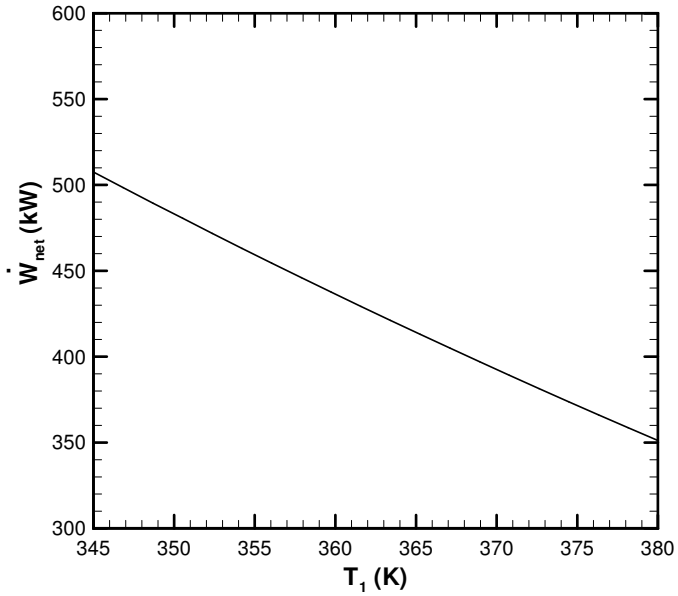

Figure 5.36 effect of the ORC pump inlet temperature on the electrical power at P_3=2,000 kPa, T_{pp}=40 K.

temperature. This sensitivity is attributed to the size of the single-effect absorption chiller, which has smaller cooling power capacity compared with the electrical power. This ratio decreases from 5.3 at 345 K to 1.8 at 380 K. Therefore, when further cooling energy is needed, the recommendation is to run the system at a higher pump inlet temperature. The electrical to heating ratio is insensitive to the variation in the pump inlet temperature. The main reason for this is the large amount of the heating power as compared to the electrical power produced by the system. The electrical to heating ratio decreases from 0.2 at 345 K to 0.15 at 380 K.

Figure 5.38 shows the exergy efficiency versus the ORC pump inlet temperature. This figure shows that the exergy efficiency of the electrical case decreases as this temperature increases. This decrement is attributed to the decrease in electrical power as this temperature increases. Also, the exergy efficiency of the cooling-cogeneration case decreases

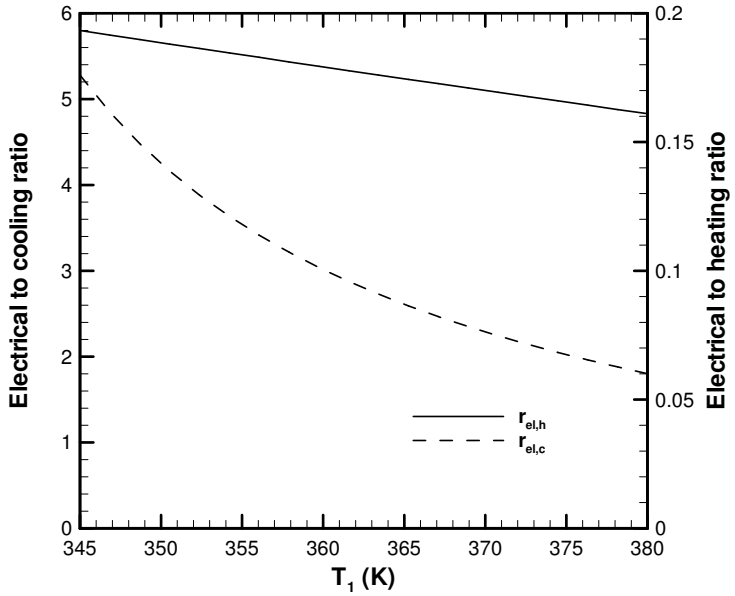

Figure 5.37 effect of the ORC pump inlet temperature on the electrical to heating and cooling ratios at P_3=2,000 kPa, T_{pp}=40 K.

as this temperature increases. The cause of this decrement is explained in the following text. The numerator of the cooling-cogeneration exergy efficiency consists of both electrical power and cooling power. The electrical power decreases as this temperature increases, as previously discussed, while the cooling power increases. Since the electrical power is larger than cooling power, which is shown in Figure 5.37, the exergy efficiency of the cooling cogeneration decreases as this temperature increases. The electrical exergy efficiency is 13% at 345 K, and it decreases as the turbine inlet temperature increases to reach 10% at 380 K. When cooling cogeneration is used, the exergy efficiency increases by 0.5%. Alternatively, when heating cogeneration or trigeneration is used, the heating-cogeneration exergy efficiency and trigeneration-exergy efficiency increase considerably by around 27% and 28%, respectively.

Figure 5.39 illustrates the exergy destruction rate versus the pump inlet temperature.

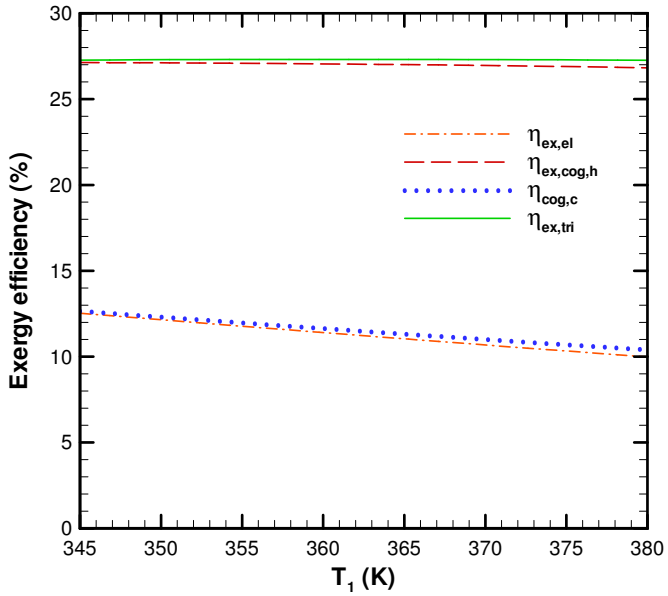

Figure 5.38 effect of the ORC pump inlet temperature on the exergy efficiency at P_3=2,000 kPa, T_{pp}=40 K.

This figure shows that the exergy destruction rate of the biomass combustor and the ORC evaporator destroy significantly more exergy than the other components. It is observed that the exergy destruction rate of the biomass combustor decreases from 1750 kW at 345 K to around 1550 kW at 380 K. This decrement is attributed to the decrease in the biomass flow rate as this temperature increases. Hence, the exergy difference between the biomass combustor inlets and exit is lower. Therefore, the destructed exergy decreases. The exergy destruction rate of the ORC evaporator decreases from approximately 1200 kW at 345 K to 1000 kW at 380 K. This decrement is due to the reduction in the heat input to the ORC evaporator. Moreover, this decrement is owing to the increase in T_2 and, thus, T_{20} where T_{pp} is constant. As T_{20} increases, the exergy at state 20 increases and, hence, the exergy difference ($Ex_{19} - Ex_{20}$) decreases. Therefore, the exergy destructed by the ORC evaporator decreases. The other components of the system destroy significantly less exergy,

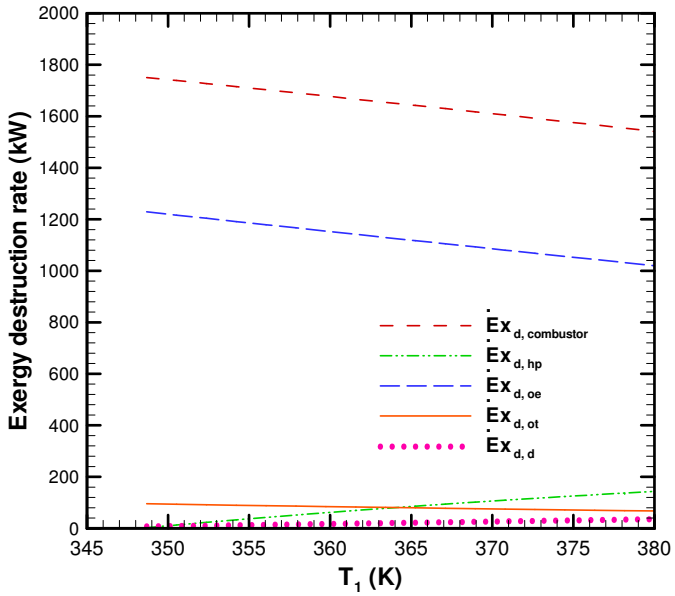

Figure 5.39 effect of the ORC pump inlet temperature on the exergy destruction at P_3=2,000 kPa, T_{pp}=40 K.

as shown in this figure.

Figure 5.40 illustrates CO_2 emissions in kg/MWh versus pump inlet temperature. It can be observed that the emissions of CO_2 are reduced considerably when trigeneration is used as compared with electrical power. The emissions of CO_2 for electrical power are 2600 kg/MWh at 345 K and increases to 3400 kg/MWh at 380 K. This increase is attributed to the decrease in the energy efficiency of the electrical power. On the other hand, when trigeneration is used the emissions decrease significantly to around 400 kg/MWh.

5.3.4 Effect of the Inlet Pressure of the Turbine

Figures 5.41-5.46 show the effect of the turbine inlet pressure on the performance of the trigeneration system. The baseline pump inlet temperature is 365 K and the baseline pinch point temperature of the ORC evaporator is 40 K. It can be observed that the effect of the

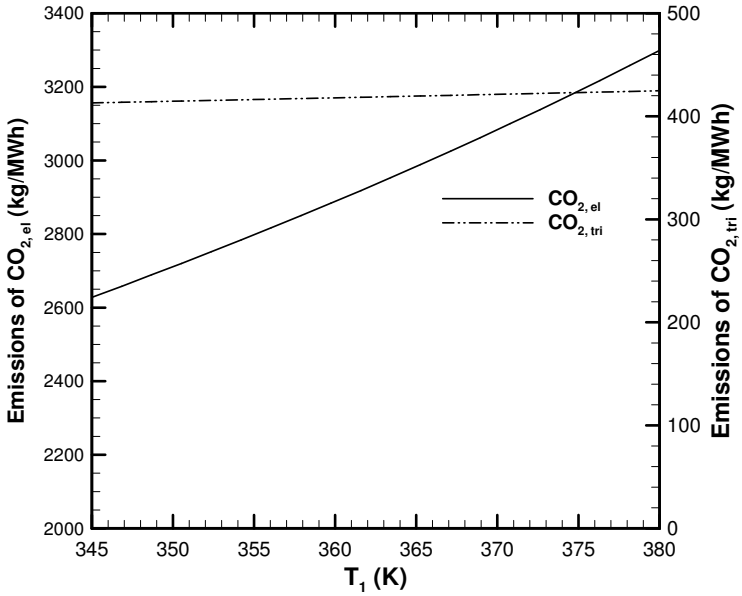

Figure 5.40 effect of the ORC pump inlet temperature on the CO_2 emissions at P_3=2,000 kPa, T_{pp}=40 K.

pressure change is insignificant on the performance of the system. This result is important since it indicates that the ORC can be operated under low pressure, and this results in cost savings.

Figure 5.41 presents the effect of the turbine inlet pressure on the efficiency. This figure shows that, as the pressure increases, the efficiencies of all the cases decrease by less than 0.5%. The small decrement is attributed to the range of the pressure that was selected, a selection that was based on the literature [179,180,182,183]. This figure illustrates that the electrical efficiency is 12.5% at 2,000 kPa and, as the pressure increases, it reaches 12% at 7,000 kPa. Alternatively, when cooling cogeneration is used, the cooling-cogeneration efficiency increases, on average, by 4% compared with the electrical power efficiency. On the other hand, when heating cogeneration is used, the heating-cogeneration efficiency increases to around 84%. Alternatively, when trigeneration is used, the efficiency increases

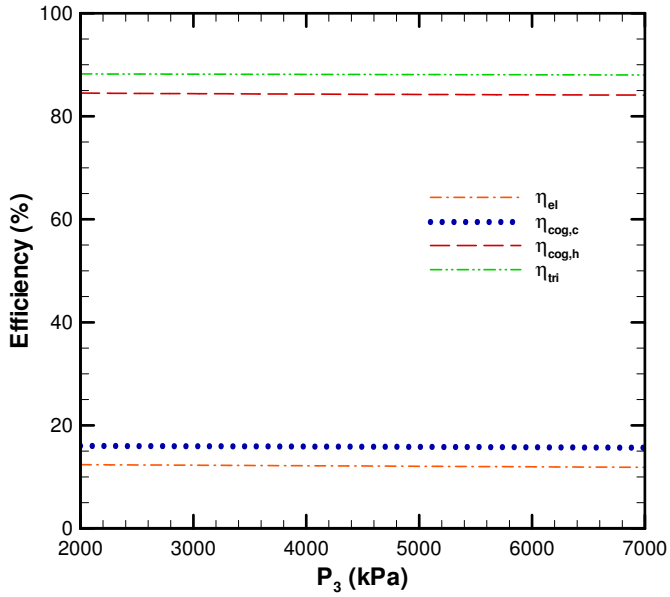

Figure 5.41 Effect of the turbine inlet pressure on the efficiency at T_1=365 K, T_{pp}=40 K.

to around 88%.

Figure 5.42 presents the net electrical power versus the turbine inlet pressure. The net power decreases from 530 kW at 2,000 kPa to 480 kW at 7,000 kPa. It can be observed that there is only a small drop in the power with the increase in the turbine inlet pressure. This small drop is attributed to the small drop in the efficiency as this pressure increases.

Figure 5.43 shows the electrical to heating and cooling ratios versus the turbine inlet pressure. It can be observed that the turbine inlet pressure is less sensitive to the electrical to cooling ratio as compared with the change in the ORC pump inlet temperature. This ratio is less sensitive since the electrical power and cooling power are less sensitive to the change in the pressure as compared to the ORC pump inlet temperature changes. The electrical to cooling ratio is 3.3 at 2,000 kPa and decreases as the pressure increases to reach 3 at 7,000 kPa. On the other hand, the electrical to heating ratio is around 0.2.

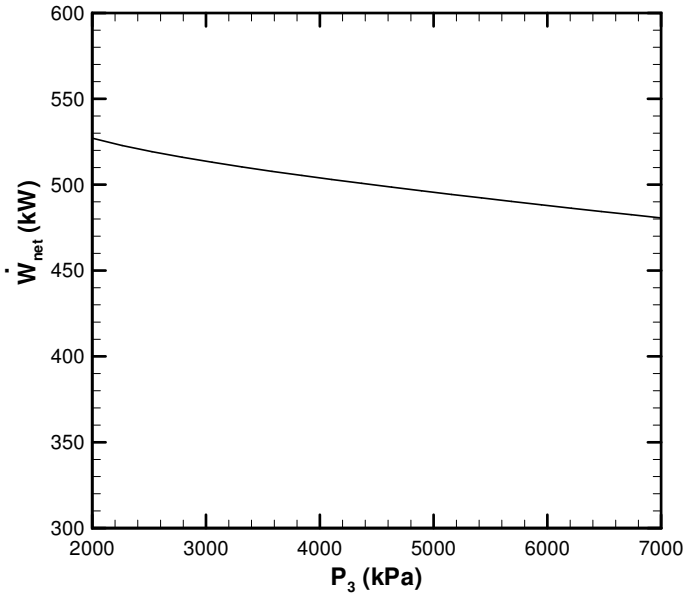

Figure 5.42 Effect of the turbine inlet pressure on the electrical power at T_1=365 K, T_{pp}=40 K.

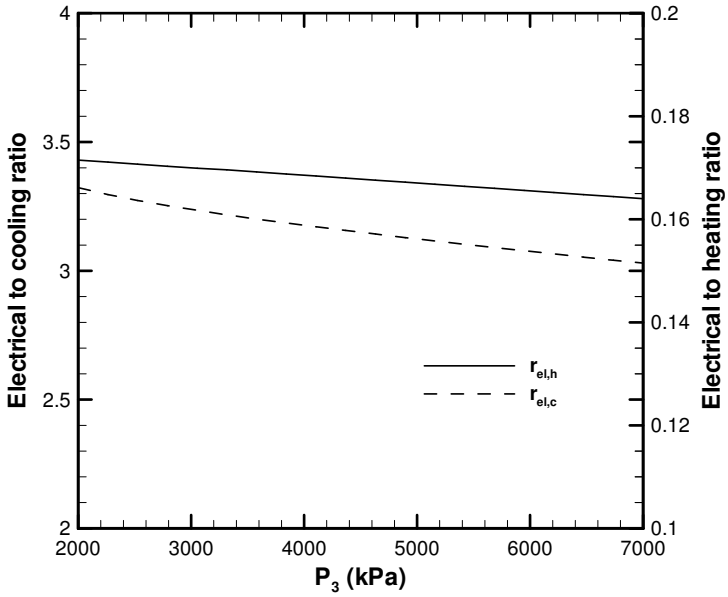

Figure 5.43 Effect of the turbine inlet pressure on the electrical to heating and cooling ratios at T_1=365 K, T_{pp}=40 K.

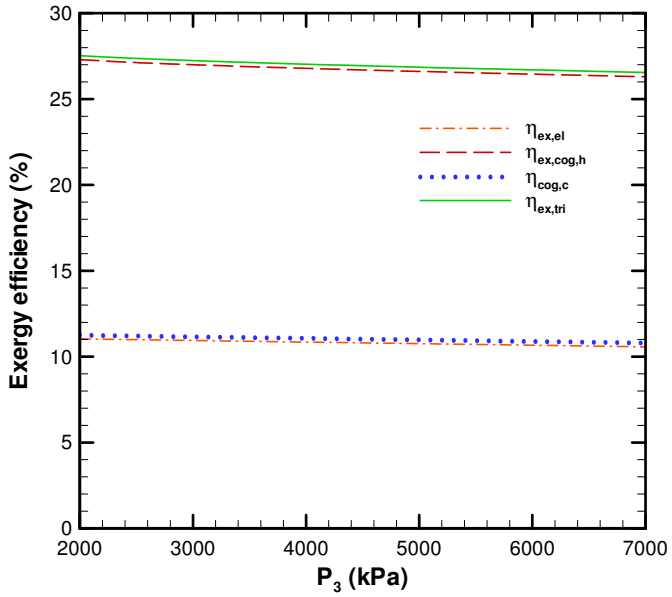

Figure 5.44 Effect of the turbine inlet pressure on the exergy efficiency at T_1=365 K, T_{pp}=40 K.

Figure 5.44 illustrates the exergy efficiency versus turbine inlet pressure. This figure reveals that the exergy efficiency decreases marginally as the pressure increases. This figure also shows that the electrical exergy efficiency decreases from 11% at 2,000 kPa to 10% at 7,000 kPa. As an alternative, when cooling cogeneration is used, the cooling exergy efficiency increases by 0.5%. Alternatively, when heating cogeneration or trigeneration is used, the exergy efficiency increases to 26% or 27%, respectively.

Figure 5.45 presents the exergy destruction rate versus the turbine inlet pressure. The figure presents the exergy destruction rate of the biomass combustor, heating-process heat exchanger, ORC evaporator, turbine, and desorber. The figure illustrates that the change in turbine inlet pressure has an insignificant effect on the exergy destruction rate. This result is attributed to the small change of the values of the exergy streams in the system as this pressure changes. It can be observed that the significant sources of exergy destruction

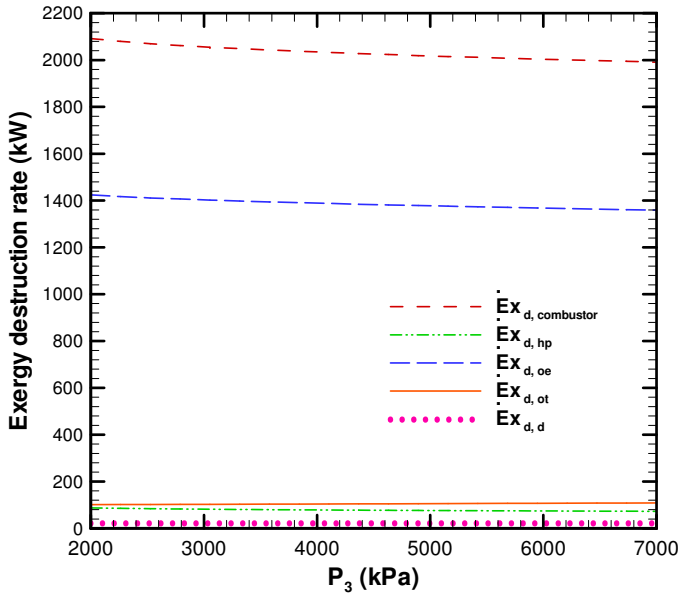

Figure 5.45 Effect of the turbine inlet pressure on the exergy destruction at T_1=365 K, T_{pp}=40 K.

rate are the biomass combustor and ORC evaporator. The exergy destruction rates of the biomass combustor and the ORC evaporator are around 2000 and 1400 kW, respectively.

Figure 5.46 illustrates the emissions of CO_2 in kg/MWh versus the turbine inlet pressure. It can be noticed that the emissions for only electrical power production are considerably high, around 3000 kg/MWh. The emissions increases marginally as this pressure increases since the electrical efficiency decreases marginally as this pressure increases. On the other hand, when trigeneration is used, the emissions are reduced considerably to 400 kg/MWh. This observation suggests that an ORC based on a biomass combustor for electrical power production only should not be used; and further utilization of the waste heat is recommended, such as using trigeneration.

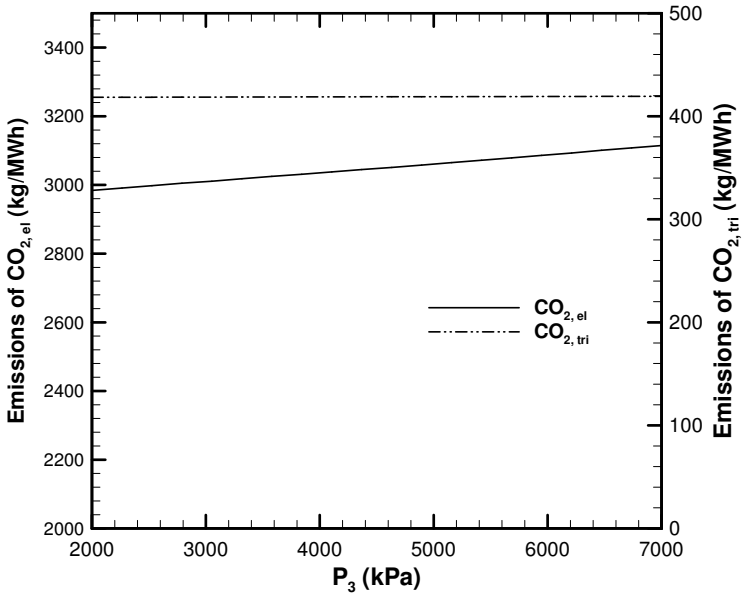

Figure 5.46 Effect of the turbine inlet pressure on the CO_2 emissions at T_1=365 K, T_{pp}=40 K.

5.3.5 Overall Exergy Destruction

Figure 5.47 illustrates the overall exergy destruction rate and its percentage for the biomass-trigeneration system under the baseline values. The baseline values considered here are 40 K for the ORC evaporator pinch point temperature, 365 K for the pump inlet temperature, and 2,000 kPa for the turbine inlet pressure. It should be noticed that each sector in this figure shows the exergy destruction rate percentage of the total exergy destructed and not the available exergy in the system. This figure illustrates that the significant sources of exergy destruction are the biomass combustor and the ORC evaporator. This figure shows that 55% (1642 kW) of the destructed exergy is destroyed in the biomass combustor and 38% (1117 kW) of the exergy destructed is destroyed in the ORC evaporator. On the other hand, 3% (86 kW) of the total destructed exergy is destroyed by the turbine and 3% (80 kW) of the total destructed exergy is destroyed by the heat exchanger of the heating process. The

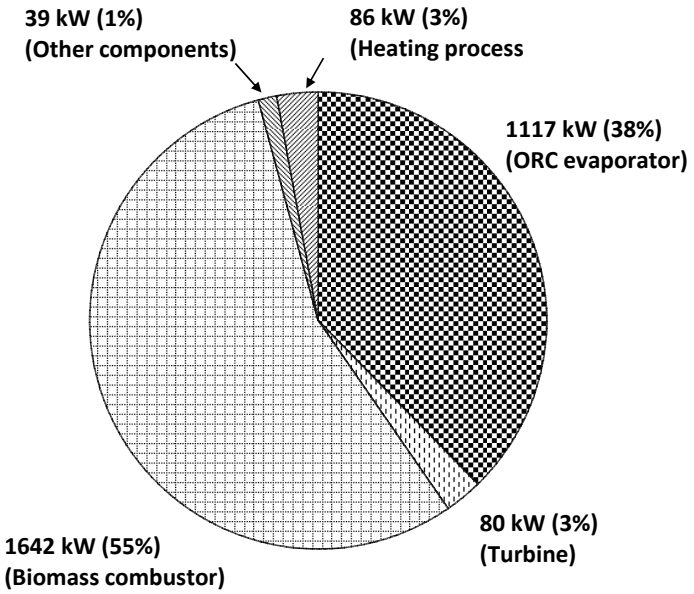

Figure 5.47 Overall exergy destruction rates and percentages (P_3=2000 K, T_1=365 K, and T_{pp}=40 K).

remaining components of the trigeneration system, in total, contribute to 1% (39 kW) of the total destructed exergy. This figure suggests having careful consideration to the design of the biomass combustor and the ORC evaporator is needed to reduce the exergy destroyed by them.

5.3.6 Summary

Energy, exergy, and environmental analyses of a trigeneration system based on an ORC and a biomass combustor are conducted. The performance of the system is examined under the variation of the ORC evaporator pinch point temperature, pump inlet temperature, and turbine inlet pressure. Moreover, exergy destruction analysis is conducted under selected baseline performance values. The main findings of this study are:

- The energy analysis of the system shows that when trigeneration is used as com-

pared with only electrical power, the efficiency of the system will increase from around 13% to around 88%. That is, there is, on average, a 75% gain in efficiency when trigeneration is used. In addition, the energy analysis shows that the maximum electrical power efficiency is 14%, the maximum cooling-cogeneration efficiency is 17%, the maximum heating-cogeneration efficiency is 87%, and the maximum trigeneration efficiency is 89%.

- The electrical-power and cooling-cogeneration exergy efficiencies decrease as the ORC evaporator pinch point temperature or pump inlet temperature increases. On the other hand, the heating-cogeneration and trigeneration exergy efficiencies are insensitive to these two variables.

- The performance of the trigeneration system is insensitive to the variation of the turbine inlet pressure. Therefore, it is recommended that the ORC be operated on low pressure since this will result in cost savings.

- The electrical to cooling ratio is sensitive to the variation of the ORC evaporator pinch point temperature and pump inlet temperature. Therefore, when further cooling energy is needed, it is recommended that the system be run at a higher ORC evaporator pinch point temperature and/or higher pump inlet temperature.

- The exergy analysis of the system shows that there is, on average, a 17% gain in exergy efficiency when trigeneration is used as compared with electrical-power exergy efficiency. The maximum electrical-exergy efficiency is 13%, the maximum cooling-cogeneration exergy efficiency is 13.5%, the maximum heating-cogeneration exergy efficiency is 27%, and the maximum trigeneration-exergy efficiency is 28%.

- The two main sources of the exergy destruction are the biomass combustor (55%) and the ORC evaporator (38%). Therefore, when designing a similar trigeneration

system as in this study, the most important components that need considerable care in their design and selection are the biomass combustor and ORC evaporator.

- The emission rates of CO_2 in kg/MWh are considerably high for the electrical-power case while, when trigeneration is used, the emissions are reduced to a relatively low rate.

5.4 Energy and Exergy Results of the Solar-Trigeneration System

In this section, the energy and exergy analyses of the trigeneration plant using solar energy are presented. Unlike the previous two systems discussed above, the solar-trigeneration system is a dynamic system where the energy input varies with time. After the sunrise, the solar radiation increases from zero until it reaches its maximum at noon and then decreases until it reaches zero at sunset. To have a continuously operating solar plant, another auxiliary subsystem is needed. A common subsystem that is combined with a solar system, is a thermal storage energy subsystem. The thermal storage subsystem stores the access solar energy during the day time and, thus, ensures running the system at night time. Therefore, to have a full picture of a thermal solar system performance, it needs to be designed considering a thermal storage subsystem. Indeed, considering a thermal storage subsystem is important when there is a need to have energy during night time, for example. The solar trigeneration plant operating modes are described next.

In this study, three modes of operation are considered: solar, solar and storage, and storage modes. During the early time of the day, after the sunrise, and later, before the sunset, all the solar energy collected by the solar collectors is used to run the trigeneration system. This mode is called the solar mode. At the other time of the day (high solar

radiation time), part of the solar energy collected by the solar collectors is used to run the trigeneration system. The remaining part of the solar energy is stored in the thermal storage tank. This mode is called the solar and storage mode. At night time, the trigeneration system runs using the energy stored in the thermal storage. This mode is called the storage mode. A representative diagram that shows these three modes of operation is shown in Figure 5.48. Also, this diagram shows the change of the solar radiation density during the day time. The solar radiation variation density in this study is taken from Kalogirou [157]. The selected data from [157] is for full tracking of solar collectors to sun radiation at Athens, Greece.

In this study, the analysis of the solar trigeneration system is based on these three modes (solar only, solar and storage, and storage only). The discussion of the results in this section is organized as follow. For example, when discussing the energy efficiency, the solar mode is described first, then, the solar and storage mode, and, finally, the storage mode. In this study, the effects of the ORC evaporator pinch point temperature, pump inlet temperature, and turbine inlet pressure are examined. The range of the ORC evaporator pinch point temperature [181] and pump inlet temperature [141, 145] considered here are taken from the literature.

5.4.1 Effect of the ORC Evaporator Pinch Point Temperature

The effect of the pinch point temperature on the performance of the solar trigeneration system is examined in Figures 5.49-5.61. Figures 5.49-5.51 show the effect of the pinch point temperature of the ORC evaporator on the efficiency of the solar trigeneration system. Figure 5.49 presents the efficiency variation for the solar mode. This figure shows that the net electrical efficiency at T_{pp} =10 K is around 13% and, as the pinch point temperature increases, the efficiency drops to 12.5% at T_{pp} =60 K. The electrical efficiency drops because the amount of the heat input to ORC decreases as this temperature increases. Using cooling

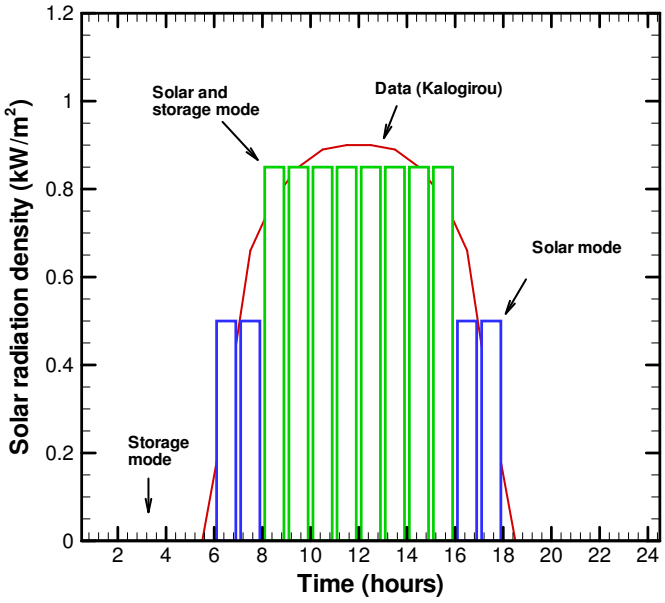

Figure 5.48 Solar radiation density variation versus time, Kalogirou [157].

cogeneration, the cooling-generation efficiency increases to around 16%. In contrast, using heating cogeneration, the heating-cogeneration efficiency increases considerably to 91%. As the pinch point temperature increases, the heating-cogeneration efficiency decreases. This efficiency decreases from 91% at T_{pp} =10 K to 86% at T_{pp} =60 K. This decrease again is attributed to the decrease in the amount of heat input into the ORC as the pinch point temperature increases. Alternatively, when trigeneration is used, the trigeneration efficiency increases to 94%.

Now, consider the solar and storage mode. Figure 5.50 presents the efficiency variation for this mode. It can be seen that the net electrical efficiency is around 7%. The drop in this efficiency, as compared to the electrical efficiency for the solar mode, is explained as follows. During this mode where high solar radiation is received by the solar collectors, 70% of the solar energy is stored in the thermal hot storage tank. This percentage of the stored energy is selected based on an initial assessment that was conducted for the solar

trigeneration system to obtain high efficiency. Since most of the received solar energy is stored, the electrical efficiency decreases to 7%. Using cooling cogeneration, the cooling-cogeneration efficiency increases to 9%. Alternatively, the heating-cogeneration efficiency increases to 45% and the trigeneration efficiency increases to 47%. It can be noticed in this figure that the efficiency increases as the pinch point temperature increases, unlike the case shown in the previous figure. This dissimilarity is explained as follows. As the pinch point temperature increases, the amount of the heat input into the ORC decreases. The exit stream of the ORC evaporator, state 18, is reused and mixes with the stream from state 21, where this mixture represents the input stream to the solar collectors. Therefore, as the temperature of this mixture increases, the temperature at the exit of the collector increases. That is, the pinch point temperature has an effect on the temperature at the inlet and exit by the solar collectors, as well as the amount of the heat input into the ORC evaporator. Therefore, depending on the operating condition, the increase in the pinch point temperature may help in increasing or decreasing the efficiency.

Now, consider the storage mode shown in Figure 5.51. This figure shows that the net electrical efficiency is around 6%. Using cooling cogeneration, its efficiency increases to 8%. Alternatively, using heating cogeneration or trigeneration, the efficiency increases to 40% or 42%, respectively. This figure shows that, as compared to the previous two figures, there is a drop in the efficiencies of the four cases. This is attributed to the amount of the thermal energy stored in the hot storage tank. If more energy is stored, these efficiencies will increase; and, vice versa, if less energy is stored, these efficiencies will decrease.

The effect of the pinch point temperature on the net electrical power is shown in Figure 5.52. This figure shows that as the pinch point temperature increases, the net electrical power decreases. The decrease in the power is attributed to the decrease in the amount of the heat input to the ORC as this temperature increases. This figure shows that for the solar mode, the net electrical power decreases from 750 kW at 10 K to 670 kW at 60 K. For the

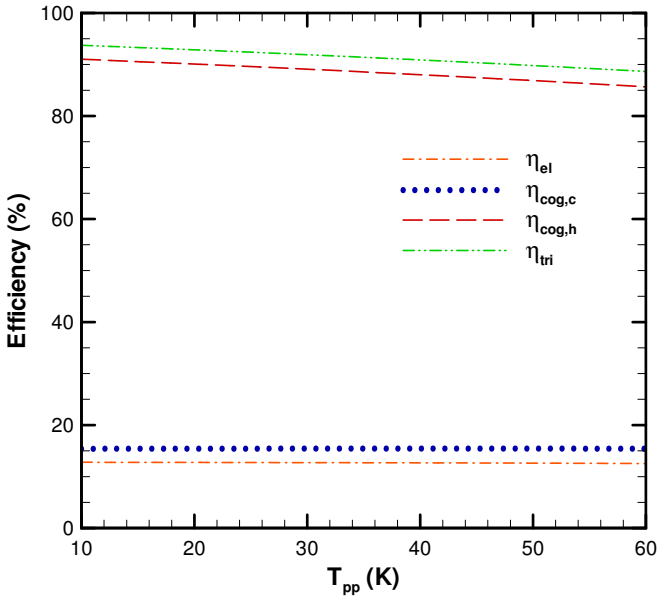

Figure 5.49 Effect of the ORC evaporator pinch point temperature on the efficiency at P_3=2,000 kPa, T_1=365 K, for solar mode.

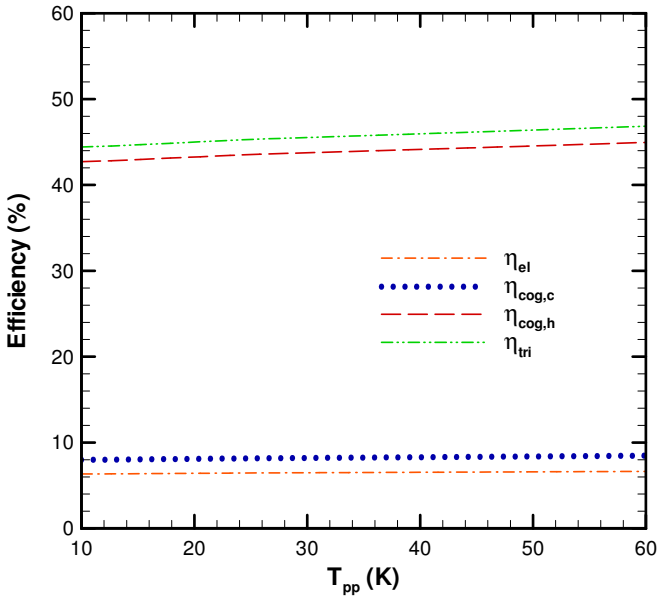

Figure 5.50 Effect of the ORC evaporator pinch point temperature on the efficiency at P_3=2,000 kPa, T_1=365 K, for solar and storage mode.

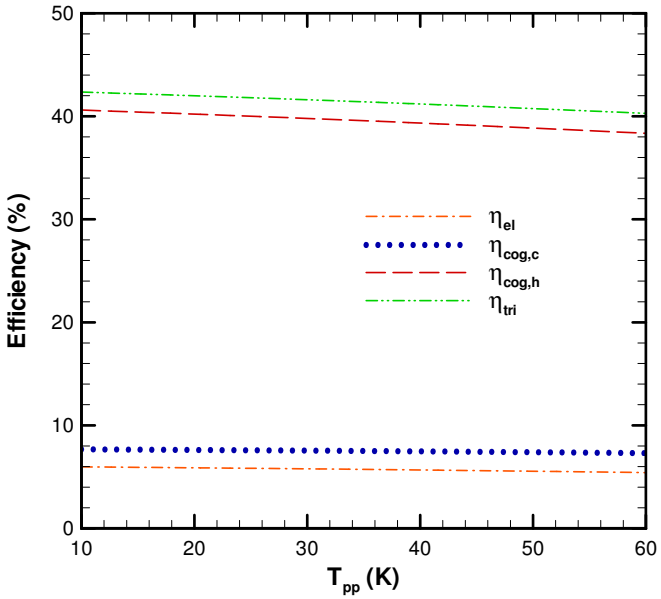

Figure 5.51 Effect of the ORC evaporator pinch point temperature on the efficiency at P_3=2,000 kPa, T_1=365 K, for storage mode.

solar and storage mode, the power decreases from 590 kW at 10 K to 560 kW at 60 K. For the storage mode, the power decreases from 540 kW at 10K to 440 kW at 60 K. It can be observed that net electrical power produced during the solar mode is the highest while for the storage mode it is the lowest. The variation of the amount of the net electrical power produced for each mode is owing to the amount of heat input into the ORC under each mode. The distribution of these heat amounts was discussed above.

The effect of the pinch point temperature on the electrical to heating and cooling ratios is shown in Figures 5.53-5.55. Figure 5.53 presents the solar mode. It can be noticed that, as the pinch point temperature increases, the electrical to cooling ratio decreases. This decrease is attributed to the increase in the cooling-cogeneration efficiency. The electrical to cooling ratios decreases from 4.8 at 10 K to 4.2 at 60 K. On the other hand, the electrical to heating ratio is almost constant and around 0.18. Figure 5.54 shows the solar and storage

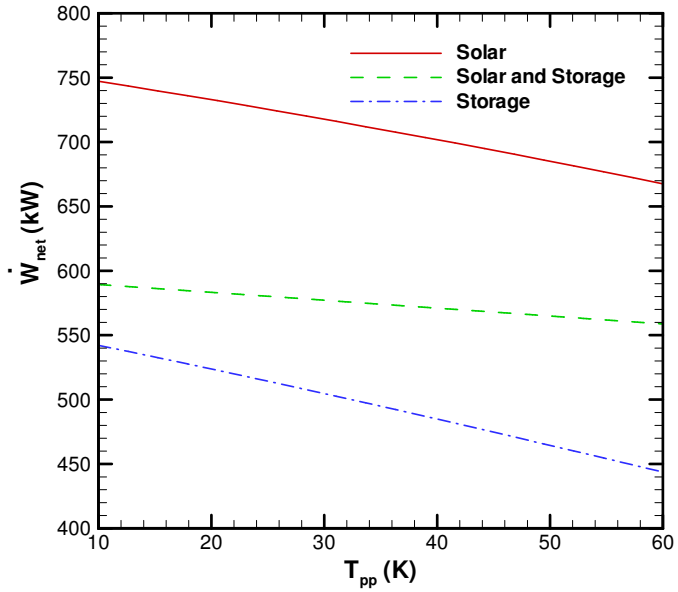

Figure 5.52 Effect of the ORC evaporator pinch point temperature on the net electrical power at P_3=2,000 kPa, T_1=365 K.

mode. This figure illustrates that the electrical to cooling ratio value is lower than the case for the solar mode. This decrease is attributed to the further decrease in the net electrical power for the solar and storage mode, as compared to the solar mode only. This ratio decreases from 3.7 at 10 K to 3.5 at 60 K. In contrast, the electrical to heating ratio is almost constant and around 0.2. Figure 5.55 presents the storage mode. It can be observed that the electrical to cooling ratio decreases more as compared to the previous two modes. This decrease is attributed again to the decrease in the net electrical power, as compared to the previous two modes. The electrical to cooling ratio decreases from 3.5 at 10 K to 2.8 at 60 K. Conversely, the electrical to heating ratio is almost constant and around 0.2.

The effect of the ORC evaporator pinch point variation on the exergy efficiency is shown in Figures 5.56-5.58. These figures show that the exergy efficiency is considerably less than the energy efficiency. As reported in the literature, the exergy efficiency of a solar system

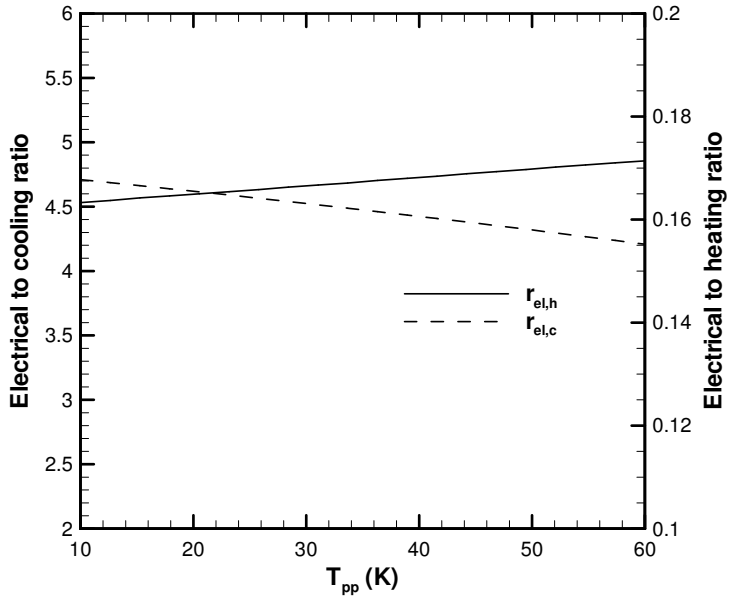

Figure 5.53 Effect of the ORC evaporator pinch point temperature on the electrical to heating and cooling ratios at P_3=2,000 kPa, T_1=365 K, for solar mode.

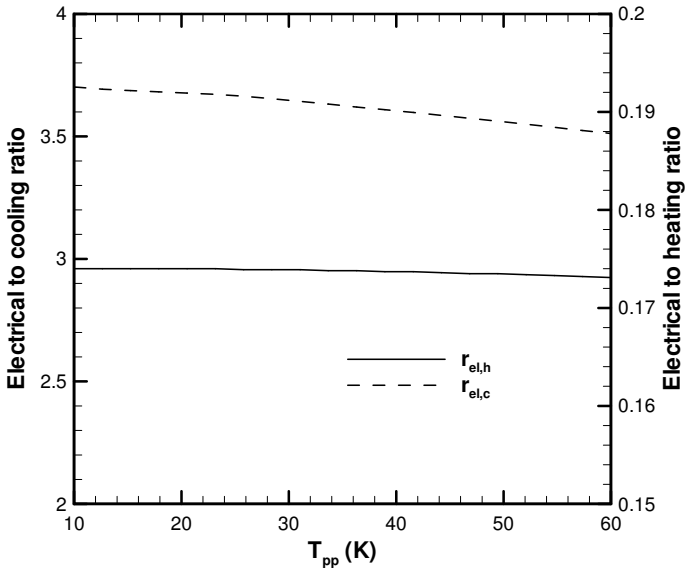

Figure 5.54 Effect of the ORC evaporator pinch point temperature on the electrical to heating and cooling ratios at P_3=2,000 kPa, T_1=365 K, for solar and storage mode.

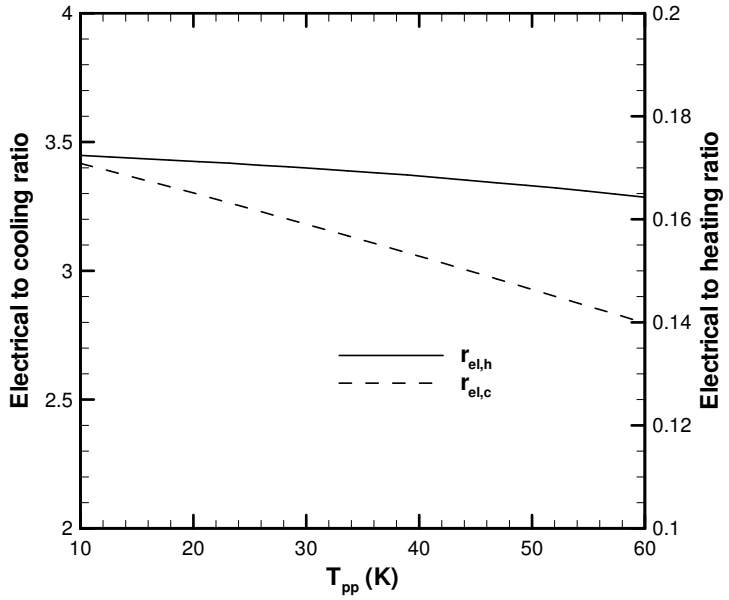

Figure 5.55 Effect of the ORC evaporator pinch point temperature on the electrical to heating and cooling ratios at P_3=2,000 kPa, T_1=365 K, for storage mode.

is considerably less than the energy efficiency [160]. Figure 5.58 shows that the electrical-exergy efficiency is around 6% and the cooling-cogeneration exergy efficiency is around 7%. This small improvement in efficiency is attributed to the small size of the single-effect absorption chiller as compared to the electrical system. This chiller was selected from the industry [145]. On the other hand, the heating-cogeneration exergy efficiency decreases from around 19% at 10 K to 15% at 60 K. Similarly, the trigeneration-exergy efficiency decreases from almost 20% at 10 K to 16.5% at 60 K. This decrease is due to the decrease in the amount of the heat input to the ORC as the pinch point temperature increases. Now, consider the solar and storage mode, as shown in Figure 5.57. This figure illustrates that the electrical and cooling-cogeneration efficiencies are around 3% and 3.5%, respectively. Alternatively, using heating cogeneration or trigeneration, this efficiency increases to around 7.5% or 8%, respectively. Figure 5.58 presents the exergy efficiency for the storage mode.

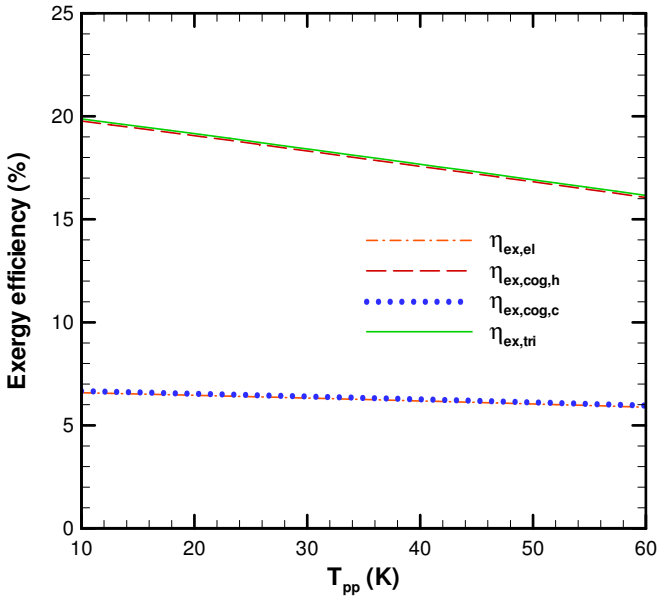

Figure 5.56 Effect of the ORC evaporator pinch point temperature on the exergy efficiency at P_3=2,000 kPa, T_1=365 K, for solar mode.

It can be observed that for this mode the exergy efficiencies decrease further more. This decrement is because there is less energy input from the storage tank, as compared to the energy inputs from the other two modes. The electrical and cooling-cogeneration exergy efficiencies are around 2.5% and the heating-cogeneration and trigeneration exergy efficiencies are around 6%.

The effect of the ORC evaporator pinch point on the exergy destruction is shown in Figures 5.59-5.61. Only the components that have high exergy destruction rates are presented. Figure 5.59 illustrates the exergy destruction rate of the heating-process heat exchanger, solar collectors, turbine, and evaporator-b for the solar mode. This figure reveals that most of the destructed exergy is destroyed by the solar collectors. The exergy destructed by this component is around 1400 kW. This figure shows that the exergy destructed by the solar collectors increases marginally as the pinch point temperature increases. This increment

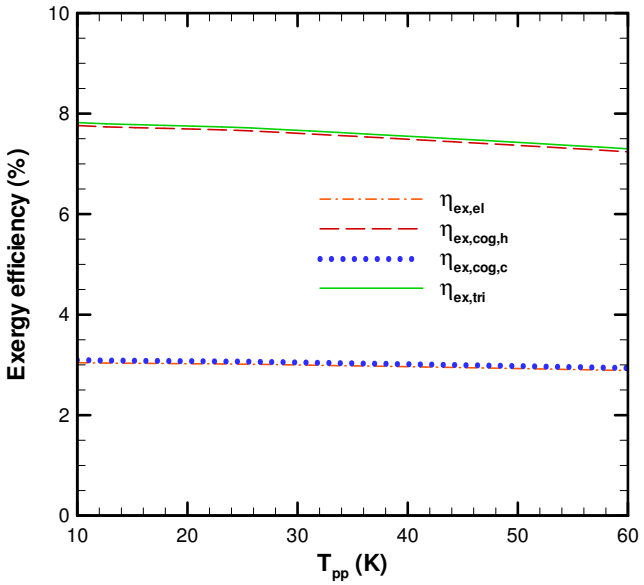

Figure 5.57 Effect of the ORC evaporator pinch point temperature on the exergy efficiency at P_3=2,000 kPa, T_1=365 K, for solar and storage mode.

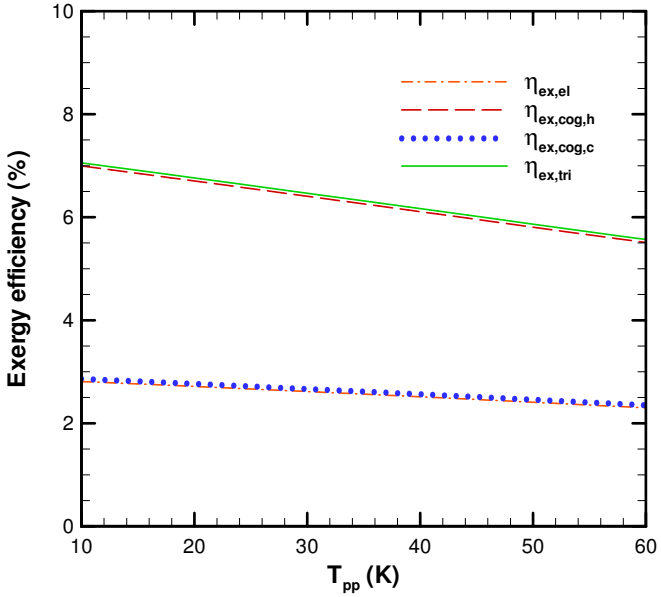

Figure 5.58 Effect of the ORC evaporator pinch point temperature on the exergy efficiency at P_3=2,000 kPa, T_1=365 K, for storage mode.

is because of the increase in the exergy difference between the inlet and exit of the solar collectors as the pinch point temperature increases. Similarly, the destructed exergy by evaporator-b increases as the pinch point temperature increases. It increases from 450 kW at 10 K to 550 kW at 60 K. This increase in the destructed exergy is owing to the increase in exergy difference between the inlets and exits of evaporator-b. Also, this figure illustrates that the destructed exergy by the heating-process heat exchanger decreases as the pinch point temperature increases. It decreases from 350 kW at 10 K to 200 kW at 60 K. This decrement is due to the decrease in the available exergy in the ORC as the pinch point increases and, thus, less exergy is available for the heating process. In addition, this figure shows that as the pinch point temperature increases, the destructed exergy by the turbine decreases. This destructed exergy decreases from 120 kW at 10 K to 115 kW at 60 K. Again, this decrease in the destructed exergy by the turbine is due to the decrease in the available exergy in the ORC as the pinch point temperature increases, as well as to the decrease in the turbine power output. Figure 5.60 illustrates the solar and storage mode. This figure shows that the destructed exergy of the solar collectors increases significantly as compared to the solar mode. This increase is mainly due to the increase in the solar radiation during this mode. The definition of the exergy of the solar collectors indicates that it increases linearly as the solar radiation increases. The destructed exergy by the solar collectors is around 4700 kW. On the other hand, the other components destroy considerably less exergy. The destructed exergy by evaporator-b is around 500 kW. Figure 5.61 shows the storage mode case. It can be observed that the significant source of the destructed exergy is evaporator-a. The destructed exergy by this component is around 600 kW. One the other hand, the destructed exergies by the turbine, heating-process heat exchanger, and hot storage tank are around 100 kW, 70 kW, and 30 kW, respectively.

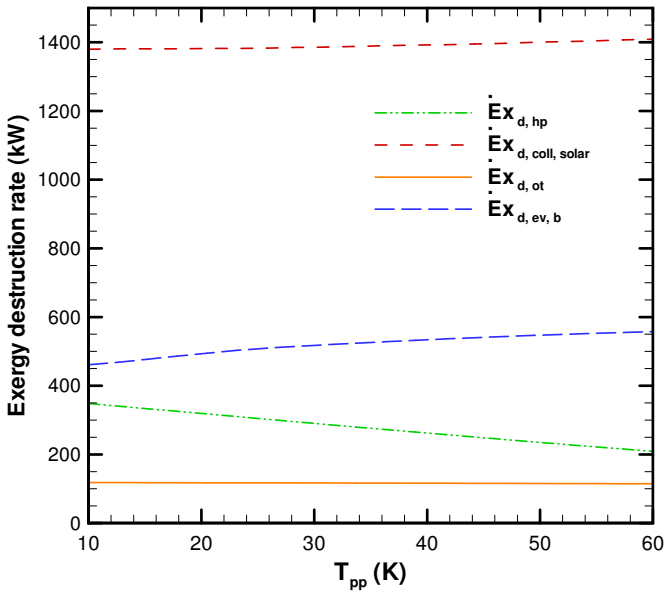

Figure 5.59 Effect of the ORC evaporator pinch point temperature on the exergy destruction rate at P_3=2,000 kPa, T_1=365 K, for solar mode.

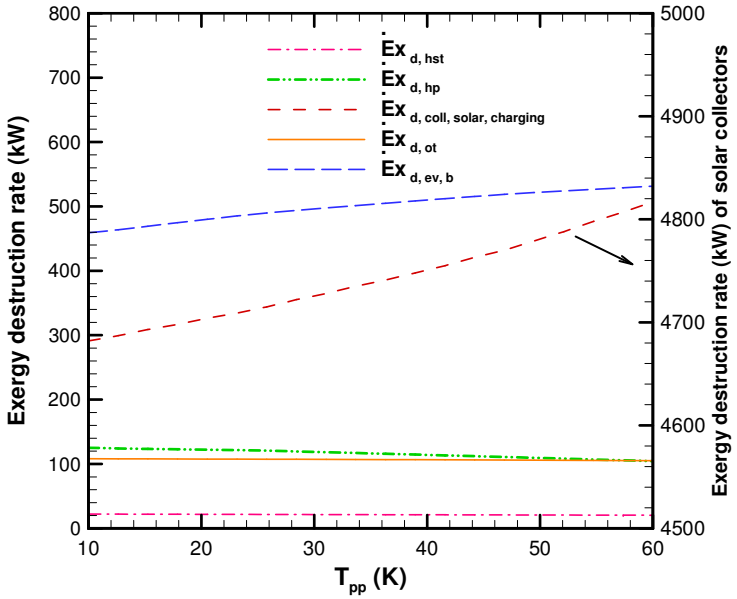

Figure 5.60 Effect of the ORC evaporator pinch point temperature on the exergy destruction rate at P_3=2,000 kPa, T_1=365 K, for solar and storage mode.

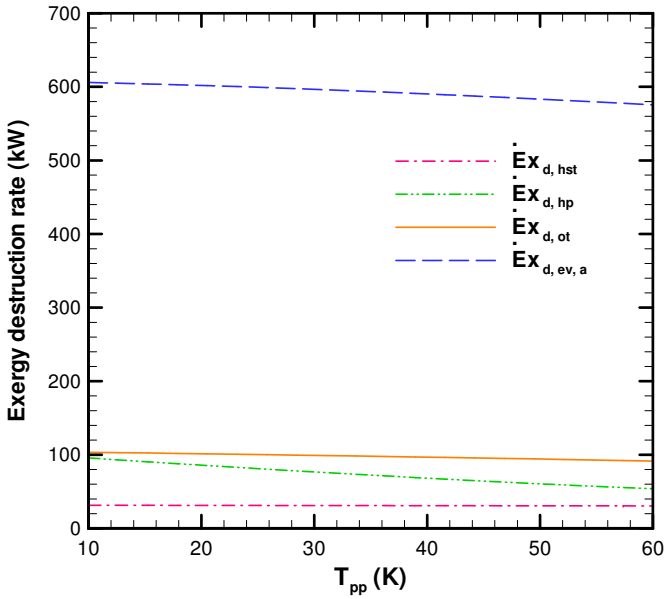

Figure 5.61 Effect of the ORC evaporator pinch point temperature on the exergy destruction rate at P_3=2,000 kPa, T_1=365 K, for storage mode.

5.4.2 Effect of the ORC Pump Inlet Temperature

The effect of the ORC pump inlet temperature variation on the plant's performance is presented in Figures 5.62-5.74. Figures 5.62-5.64 illustrate the effect of the ORC pump inlet temperature on the efficiency. Figure 5.62 presents the solar mode. This figure illustrates that as the pump inlet temperature increases, the efficiencies decrease. This decrease is attributed to the decrease in the temperature difference between the minimum and maximum temperatures in the ORC. The electrical efficiency decreases from 14% at 345 K to 11% at 380 K. Alternatively, the cooling-cogeneration efficiency decreases from 16% at 345 K to 15% at 380 K. On the other hand, using the heating cogeneration and trigeneration, their efficiencies increase considerably to 91% and 93%, respectively. Figure 5.63 illustrates the solar and storage mode. This figure shows that there is a considerable decrease in efficiency for this mode, as compared to the solar mode. This decrease is owing

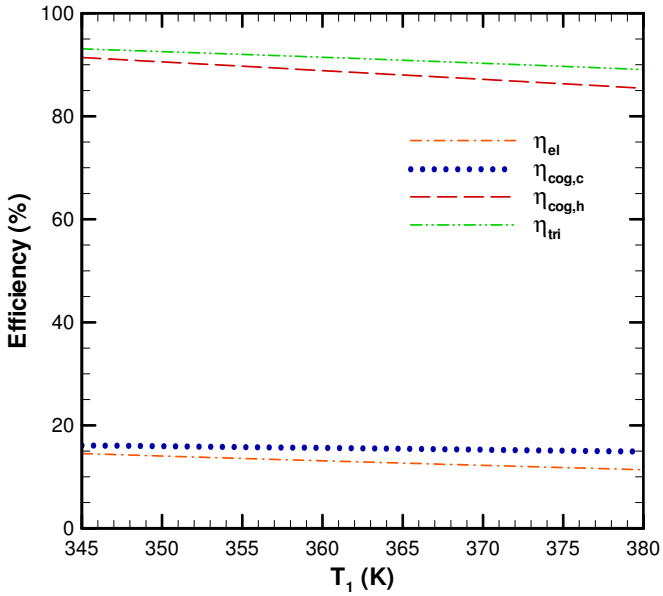

Figure 5.62 Effect of the ORC pump inlet temperature on the efficiency at P_3=2,000 kPa, T_{pp}=40 K, for solar mode.

to the relatively large amount of stored energy, as mentioned above. This figure shows that there is a marginal change in the efficiencies as the temperature changes. The electrical, cooling-cogeneration, heating-cogeneration, and trigeneration efficiencies are around 7%, 8%, 44%, and 46%, respectively. Figure 5.64 presents the storage mode. This figure shows that the efficiencies are less for this mode as compared to the solar mode, for the reasons discussed above. This figure illustrates that there is a marginal drop in the efficiencies as the temperature increases. The electrical efficiency drops from 6.5% at 345 K to 5% at 380 K. For cooling cogeneration, the efficiency is around 7.5%. For heating cogeneration, the efficiency drops from 41% at 345 K to 38% at 380 K. Alternatively, for trigeneration, the efficiency drops from 42% at 345 K to 40% at 380 K.

The effect of the ORC pump inlet temperature on the net electrical power is presented in Figure 5.65. This figure shows that the variation of the ORC pump inlet temperature

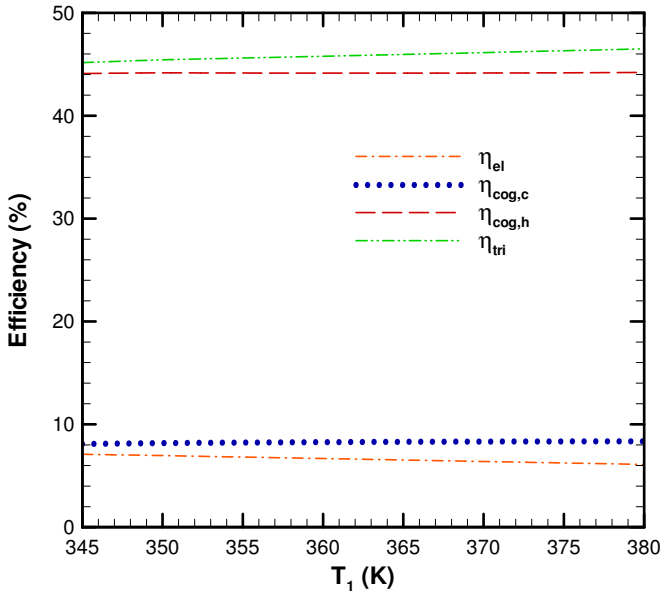

Figure 5.63 Effect of the ORC pump inlet temperature on the efficiency at P_3=2,000 kPa, T_{pp}=40 K, for solar and storage mode.

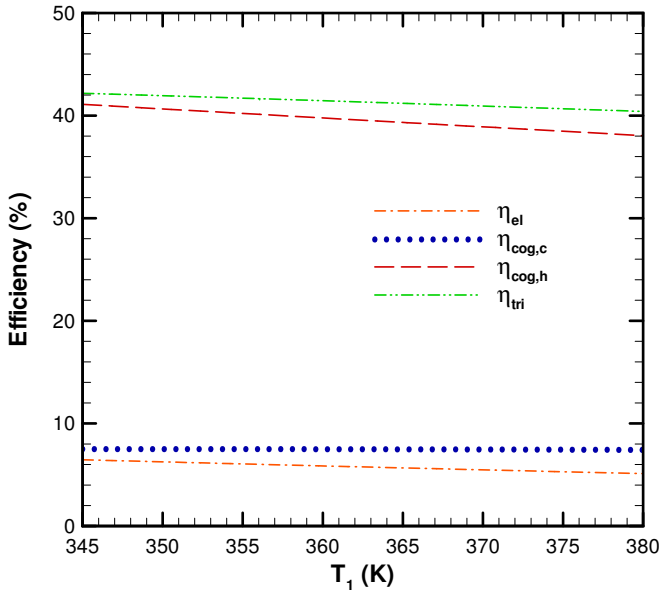

Figure 5.64 Effect of the ORC pump inlet temperature on the efficiency at P_3=2,000 kPa, T_{pp}=40 K, for storage mode.

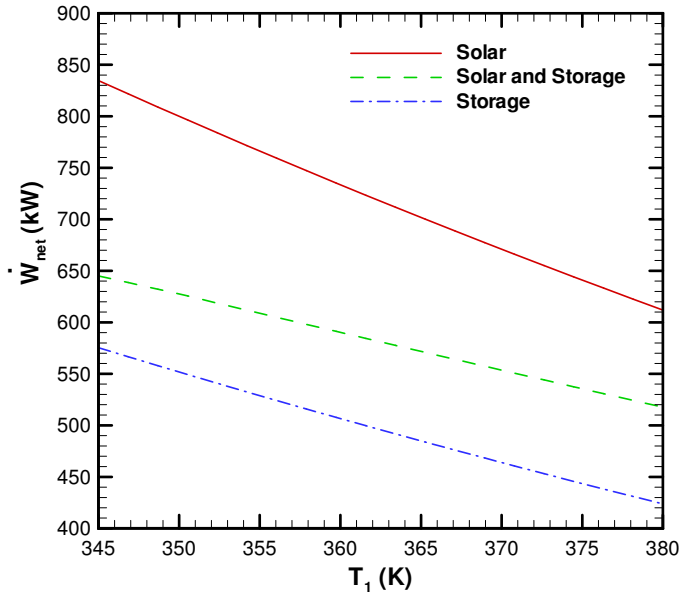

Figure 5.65 Effect of the ORC pump inlet temperature on the net electrical power at P_3=2,000 kPa, T_{pp}=40 K.

has a more significant effect on the power than the evaporator pinch point temperature variation. This is because the ORC pump inlet temperature is part of the ORC and, thus, has a direct effect on the electrical power produced. It can be noticed from this figure that as the temperature increases, the electrical power decreases. This decrease is attributed to the decrease in the temperature difference between the maximum and minimum temperatures in the ORC. This figure shows that the electrical power for the solar mode varies from 840 kW at 345 K to 600 kW at 380 K. For the solar and storage mode, the electrical power varies from 650 kW at 340 K to 510 kW at 380 K. For the storage mode, the power varies from 570 kW at 345 k to 420 kW at 380 K. It can be observed from this figure that the overall electrical power for the solar mode is the highest while for the storage mode it is the lowest. This variation in the electrical power is because of the change in the available heat input to the ORC for each mode, as discussed above.

The effect of the ORC pump inlet temperature on the electrical to heating and cooling ratios is presented in Figures 5.66-5.68. Figure 5.66 illustrates the solar mode. This figure reveals that the electrical to cooling ratio decreases from almost 9 at 345 K to 3 at 380 K. This significant drop is owing to the significant drop in the net electrical power as this temperature increases. In addition to that, the cooling power is small as compared to the electrical power. However, the electrical to heating ratio is around 0.2 with a marginal decrease in its value as the temperature increases. The drop is marginal since the size of the heating power is large as compared to the electrical power. Figure 5.67 presents the solar and storage mode. This figure shows that the electrical to cooling ratio decreases from almost 7 at 345 K to 2.5 at 380 K. Nevertheless, the electrical to heating ratio drops from 0.19 to 0.16 as the temperature increases. Figure 5.68 presents the storage mode. It can be observed that the electrical to cooling ratio drops from 6 at 340 K to 2.2 at 380 K. On the other hand, the electrical to heating ratio drops from 0.18 to 0.15 as the temperature increases. It can be noticed that the overall electrical to cooling ratio is high for the solar mode while for the other two modes it is lower. This difference is attributed to the available electrical power for each mode, where for the solar mode it is the highest.

The effect of the ORC pump inlet temperature on the exergy efficiency is presented in Figures 5.69-5.71. Figure 5.69 illustrates the solar mode. This figure shows that as this temperature increases, the electrical-exergy efficiency drops from 7% at 345 K to 5% at 380 K. This drop is due to the decrease in the electrical power as this temperature increases. Using cooling cogeneration, the exergy efficiency improves by less than 0.5%. However, using heating cogeneration or trigeneration, the exergy efficiency improves significantly to 18% or 18.5%, respectively. Figure 5.70 presents the solar and storage mode. This figure shows that the electrical, cooling-cogeneration, heating-cogeneration, and trigeneration efficiencies are around 3%, 3.5%, 7%, and 7.5%, respectively. Figure 5.71 shows the storage mode. This figure shows that the electrical, cooling-cogeneration, heating-cogeneration,

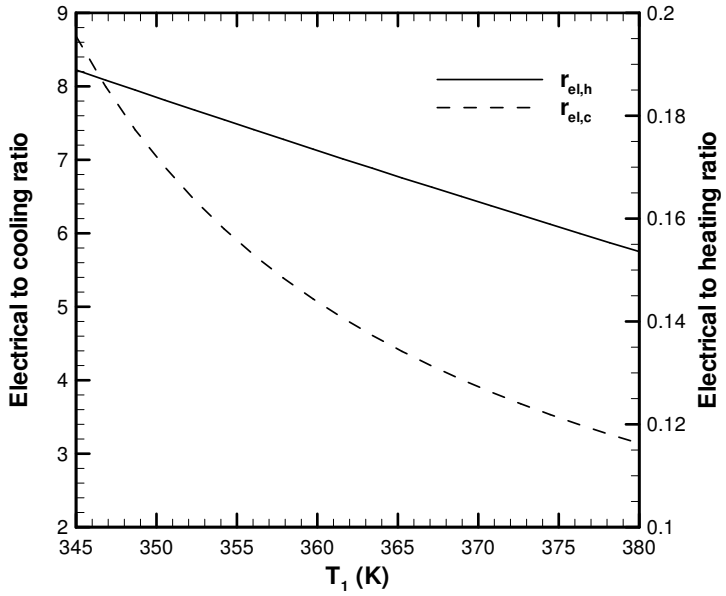

Figure 5.66 Effect of the ORC pump inlet temperature on the electrical to heating and cooling ratios at P_3=2,000 kPa, T_{pp}=40 K, for solar mode.

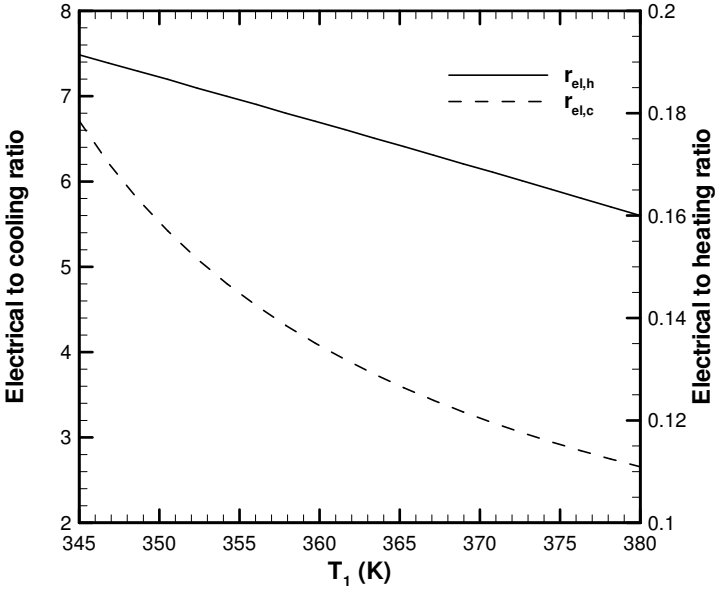

Figure 5.67 Effect of the ORC pump inlet temperature on the electrical to heating and cooling ratios at P_3=2,000 kPa, T_{pp}=40 K, for solar and storage mode.

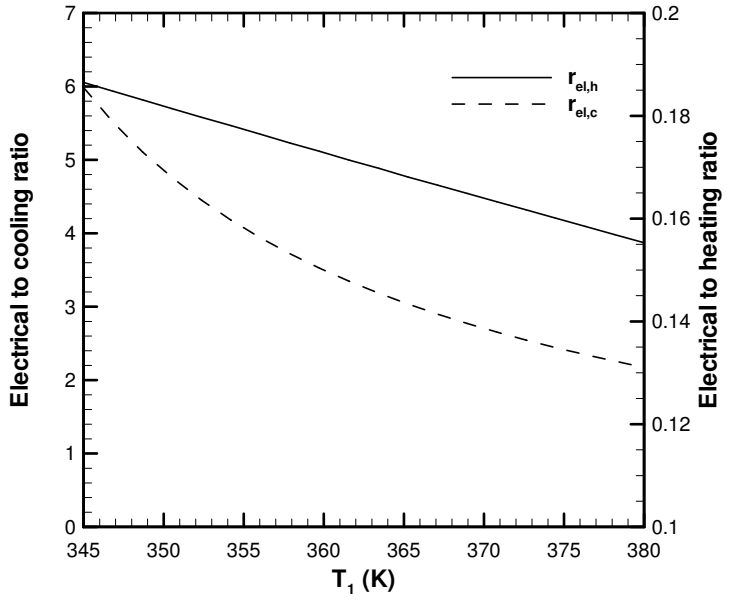

Figure 5.68 Effect of the ORC pump inlet temperature on the electrical to heating and cooling ratios at P_3=2,000 kPa, T_{pp}=40 K, for storage mode.

and trigeneration efficiencies are around 2.5%, 3%, 6%, and 6.5%, respectively. It can be noticed from the above three figures that the exergy efficiencies for the solar mode are the highest while for the storage mode are the lowest. This difference is because there is more energy input to the ORC for the solar mode and less for the storage mode, as discussed above.

The effect of the ORC pump inlet temperature on the exergy destruction rate is presented in Figures 5.72-5.74. These figures present only the components that have high exergy destruction rates. Figure 5.72 presents the solar mode. This figure shows the exergy destruction rate of the solar collectors, heating-process, turbine, and evaporator-b. It can be noticed that the solar collectors have the highest exergy destruction rate, around 1400 kW. The exergy destruction rate of the solar collectors increases marginally as the ORC pump inlet temperature increases. This increase is attributed to the increase in the temper-

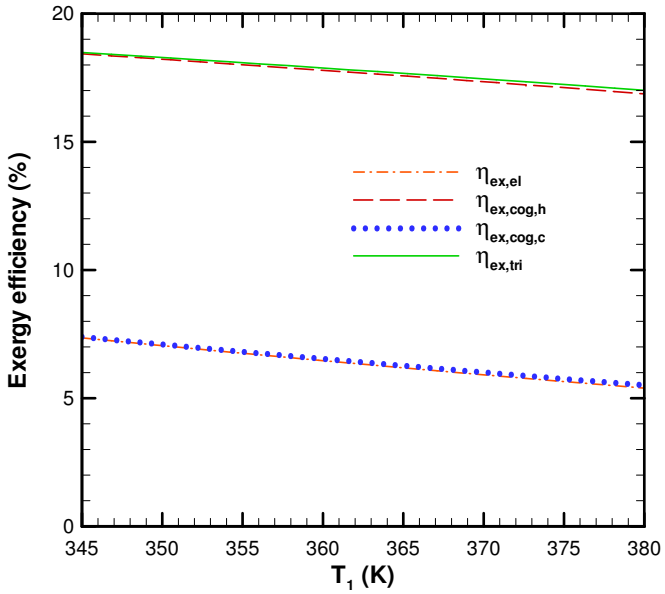

Figure 5.69 Effect of the ORC pump inlet temperature on the exergy efficiency at P_3=2,000 kPa, T_{pp}=40 K, for solar mode.

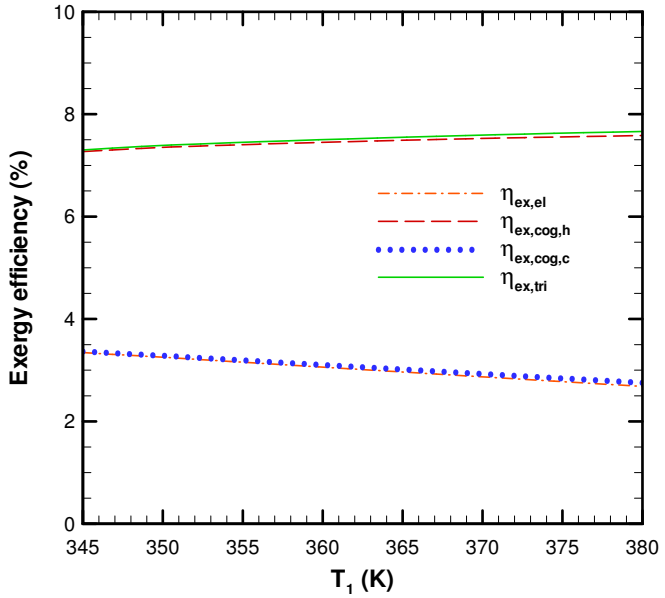

Figure 5.70 Effect of the ORC pump inlet temperature on the exergy efficiency at P_3=2,000 kPa, T_{pp}=40 K, for solar and storage mode.

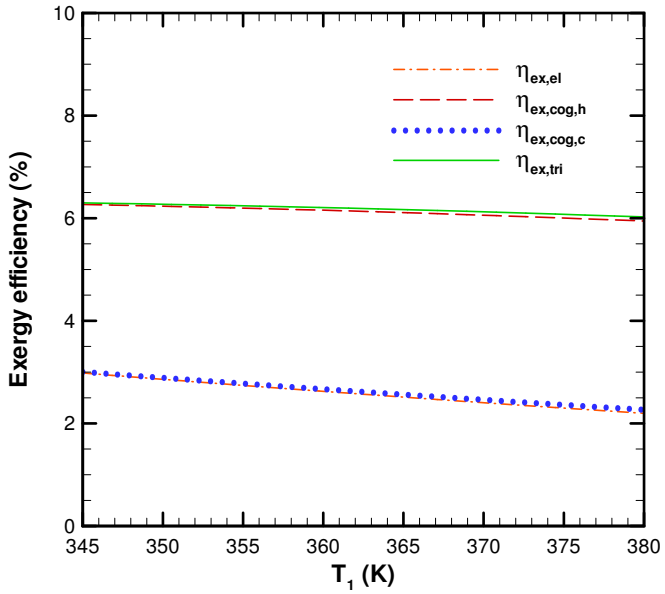

Figure 5.71 Effect of the ORC pump inlet temperature on the exergy efficiency at P_3=2,000 kPa, T_{pp}=40 K, for storage mode.

ature at the exit of evaporator-b, T_{18}, as the ORC pump inlet temperature increases. That is, the pinch point temperature is a function of the ORC pump inlet temperature, T_1, and T_{18}. Therefore, as T_1 increases, T_{18} increases and, thus, the inlet temperature to the solar collectors increases. This figure shows that as T_1 increases, the exergy destruction rate of evaporator-b decreases marginally. This decrease is due to the decrease in the available exergy in evaporator-b as T_1 increases. The exergy destruction rate of evaporator-b is around 550 kW. The exergy destructed by the heating-process heat exchanger increases as T_1 increases. This increase is owing to the increase in the available heat energy and the decrease in the heating-cogeneration exergy efficiency. The exergy destruction rate increases from 100 kW at 345 K to 360 kW at 380 K. The exergy destruction rate of the turbine is around 120 kW. The exergy destruction rate of the turbine decreases as T_1 increases. This decrement is owing to the decrease in the power produced by the turbine as this temperature

increases. Figure 5.73 presents the solar and storage mode. This figure reveals that the destructed exergy by the solar collectors for this mode are significantly high, around 4800 kW. The reason for this was discussed above. This figure shows that as the ORC pump inlet temperature increases, the destructed exergy by the solar collectors increases. It increases from 4700 kW at 348 K to 4800 kW at 380 K. The exergy destruction rate of evaporator-b decreases from 530 kW to 490 as this temperature increases. The exergy destruction rate of the turbine decreases from 125 kW to 90 kW as this temperature increases. The exergy destruction rate of the heating-process heat exchanger increases from almost zero to 220 kW as this temperature increases. The exergy destruction rate of the hot storage tank decreases from 22 kW to 20 kW as this temperature increases. Figure 5.74 presents the storage mode. This figure illustrates that as the ORC pump inlet temperature increases, the exergy destruction rate by evaporator-a decreases. It decreases from 650 kW at 345 K to 550 kW at 380 K. The exergy destruction rate by the turbine decreases from 120 kW to 80 kW as this temperature increases. The exergy destruction rate by the heating-process heat exchanger increases from almost zero to 150 kW as this temperature increases. The exergy destruction rate of the hot storage tank is almost constant and around 30 kW.

5.4.3 Effect of the Turbine Inlet Pressure

The effect of the turbine inlet pressure variation on the plant's performance is presented in Figures 5.75-5.87. The effect of the turbine inlet pressure variation on the efficiency is shown in Figures 5.75-5.77. Figure 5.75 illustrates the solar mode. It can be noticed that the variation of the turbine inlet pressure has an insignificant effect on efficiency. This small variation is owing to the selected range of the pressure variation. The variations of the efficiencies as this pressure increases are within 0.5%. This is an important result since it suggests that running the ORC at low pressure, which will result in cost savings. The electrical, cooling-cogeneration, heating-cogeneration, and trigeneration efficiencies

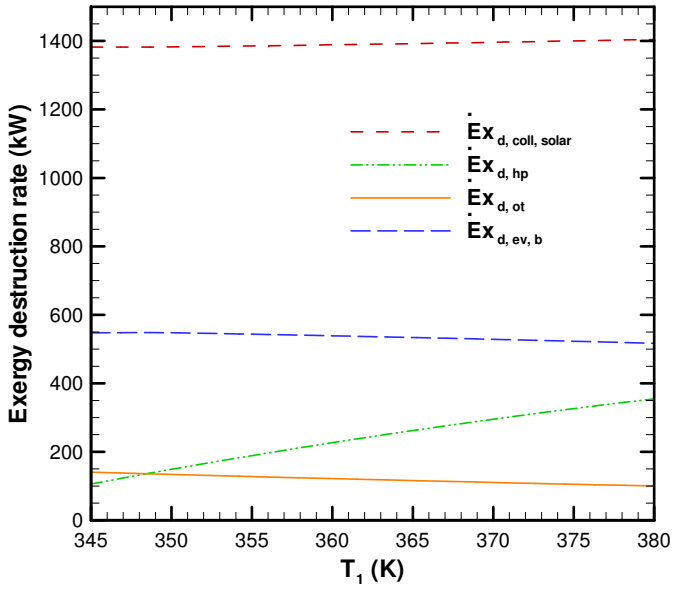

Figure 5.72 Effect of the ORC pump inlet temperature on the exergy destruction rate at P_3=2,000 kPa, T_{pp}=40 K, for solar mode.

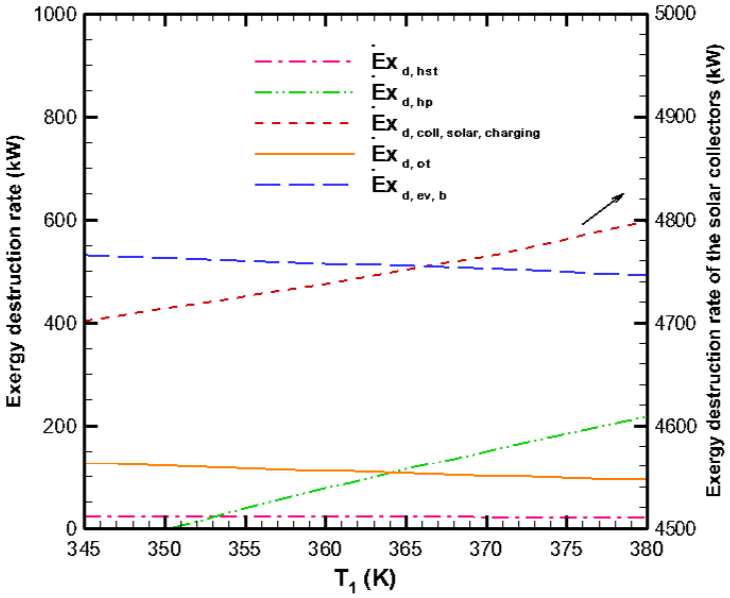

Figure 5.73 Effect of the ORC pump inlet temperature on the exergy destruction rate at P_3=2,000 kPa, T_{pp}=40 K, for solar and storage mode.

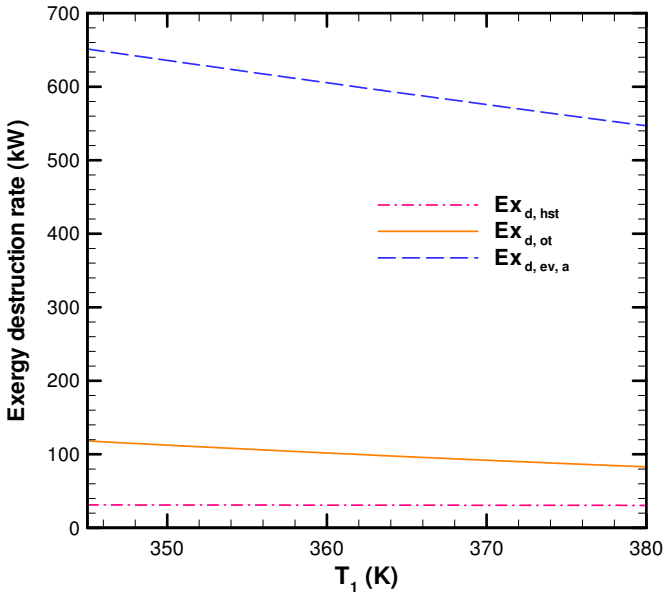

Figure 5.74 Effect of the ORC pump inlet temperature on the exergy destruction rate at P_3=2,000 kPa, T_{pp}=40 K, for storage mode.

are around 13%, 16%, 88%, and 91%, respectively. Figure 5.76 presents the solar and storage mode. The electrical, cooling-cogeneration, heating-cogeneration, and trigeneration efficiencies are around 6.5%, 8%, 44%, and 46%, respectively. Figure 5.77 shows the storage mode. The electrical, cooling-cogeneration, heating-cogeneration and trigeneration efficiencies are around 5.5%, 7.5%, 39% and 41%, respectively. It can be noticed that the efficiencies for the solar mode are considerably higher than the other two modes. The reason for that was discussed above.

The effect of the turbine inlet pressure on the net electrical power is shown in Figure 5.78. This figure shows that there is a small variation in net electrical power as the pressure changes. This variation in the power is within 30 kW. This small variation is owing to the small variation of the electrical efficiency. It is shown that the net electrical power for the solar mode is around 710 kW, for the solar and storage mode is around 665 kW, and for the

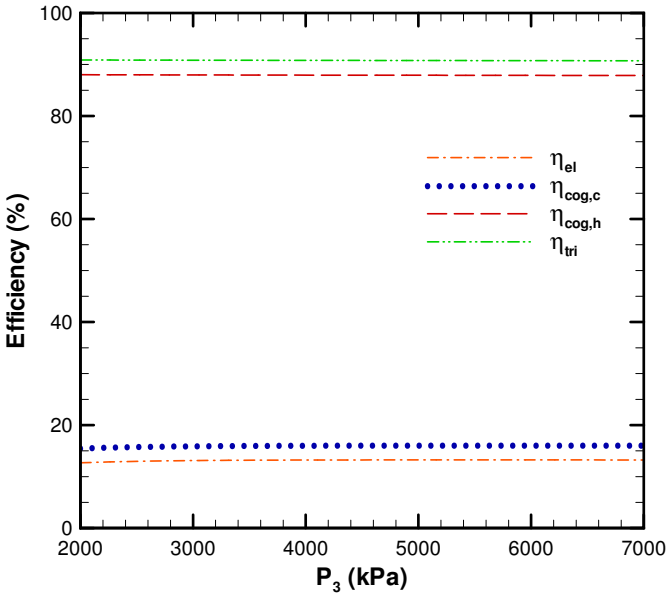

Figure 5.75 Effect of the turbine inlet pressure on the efficiency at T_1=365 K, T_{pp}=40 K, for solar mode.

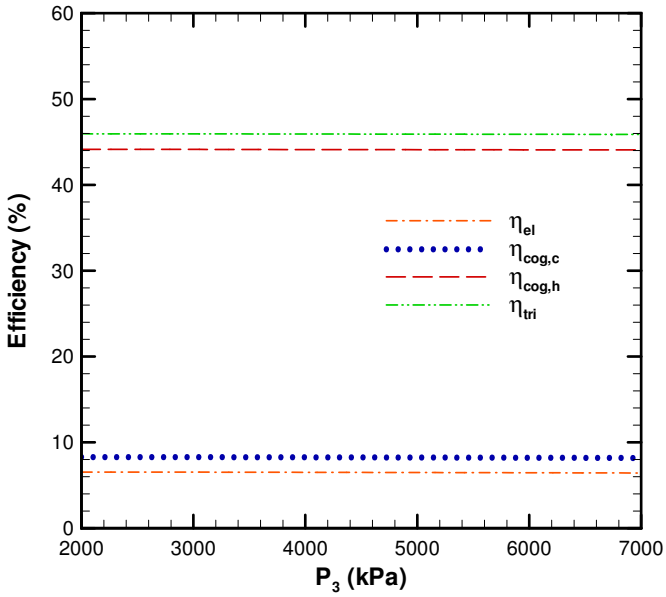

Figure 5.76 Effect of the turbine inlet pressure on the efficiency at T_1=365 K, T_{pp}=40 K, for solar and storage mode.

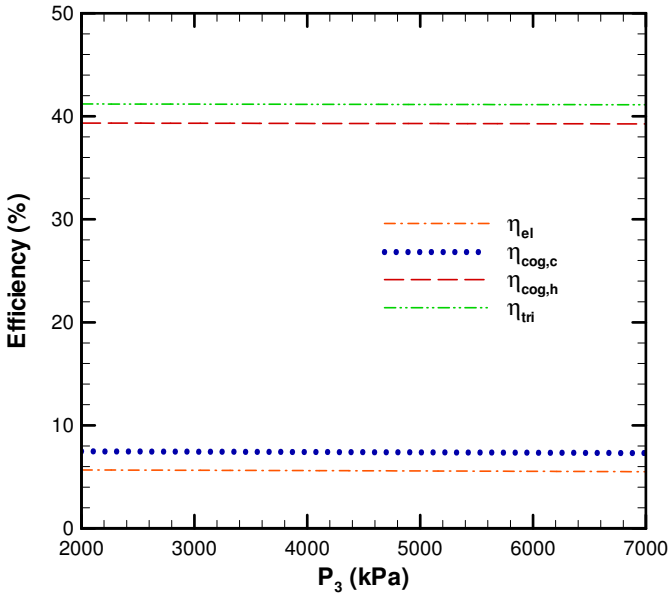

Figure 5.77 Effect of the turbine inlet pressure on the efficiency at T_1=365 K, T_{pp}=40 K, for storage mode.

storage mode is around 480 kW.

The effect of the turbine inlet pressure on the electrical to heating and cooling ratios is presented in Figures 5.79-5.81. These figures show that there is an insignificant change in the electrical to heating and cooling ratios as the turbine inlet pressure increases. This insignificant change in the ratios is attributed to the marginally change in the efficiencies as this pressure increases. The electrical to cooling ratio for the solar mode is around 4.5, for the solar and storage mode it is around 3.6, and for the storage mode it is around 3. The electrical to heating ratio for the three modes is around 0.18.

The effect of the turbine inlet pressure on the exergy efficiency is illustrated in Figures 5.82-5.84. It can be observed that the effect of this pressure is insignificant on the exergy efficiency. This insignificant change is attributed to the insignificant change in the powers and temperatures as this pressure changes. Figure 5.82 presents the solar mode. The

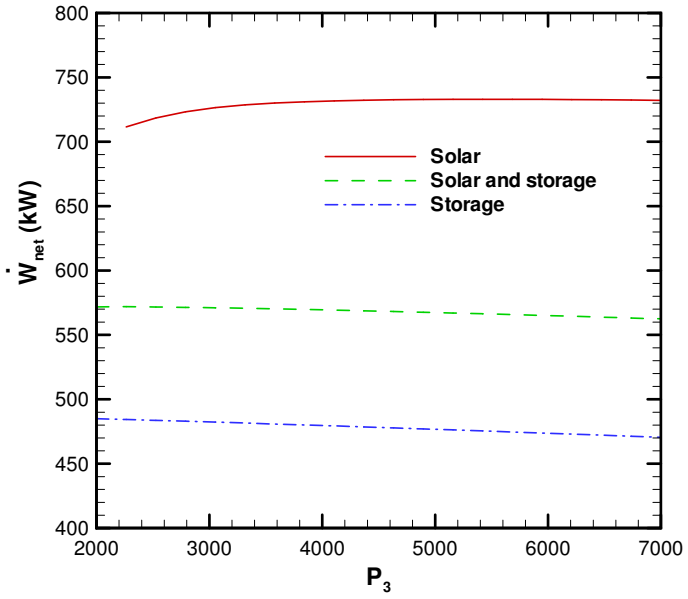

Figure 5.78 Effect of the turbine inlet pressure on the net electrical power at T_1=365 K, T_{pp}=40 K.

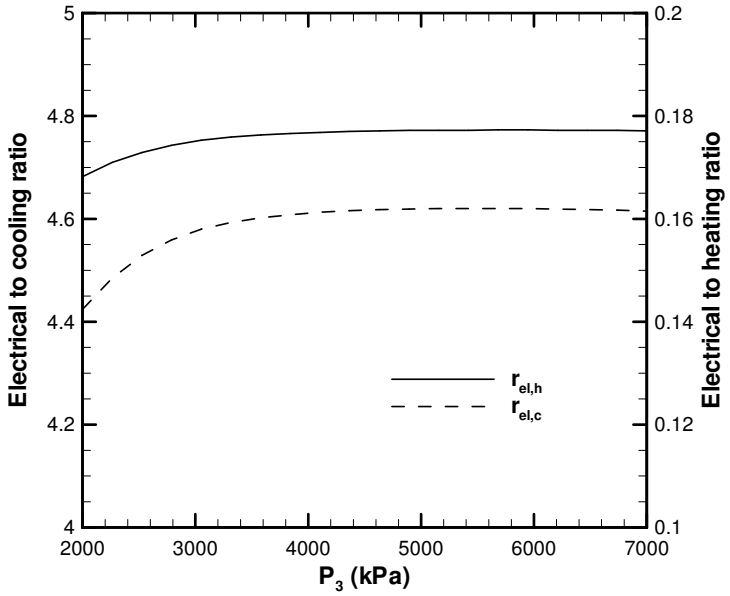

Figure 5.79 Effect of the turbine inlet pressure on the electrical to heating and cooling ratios at T_1=365 K, T_{pp}=40 K, for solar mode.

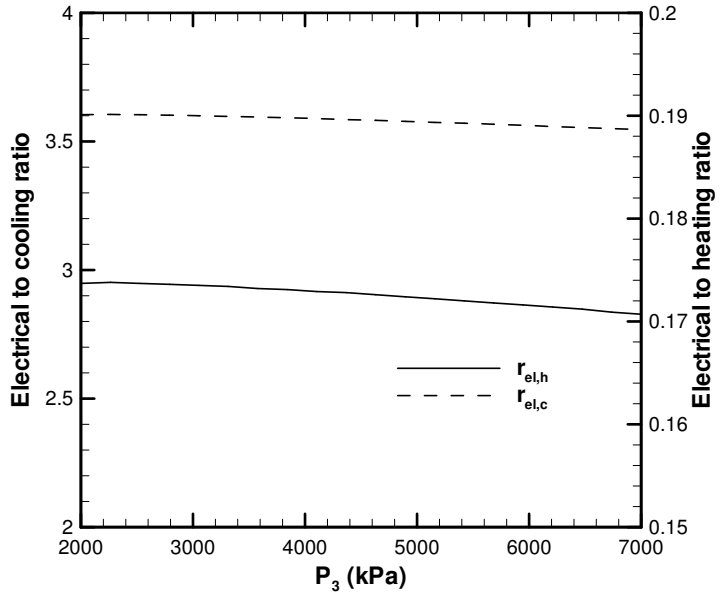

Figure 5.80 Effect of the turbine inlet pressure on the electrical to heating and cooling ratios at T_1=365 K, T_{pp}=40 K, for solar and storage mode.

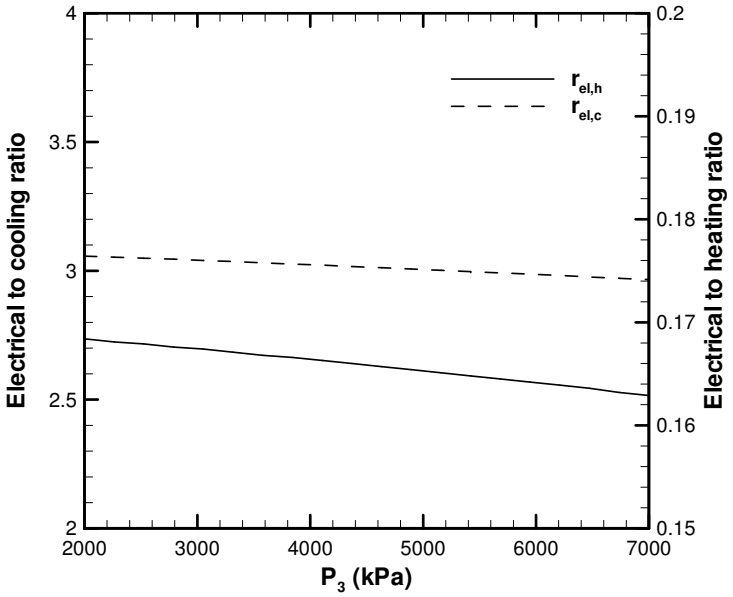

Figure 5.81 Effect of the turbine inlet pressure on the electrical to heating and cooling ratios at T_1=365 K, T_{pp}=40 K, for storage mode.

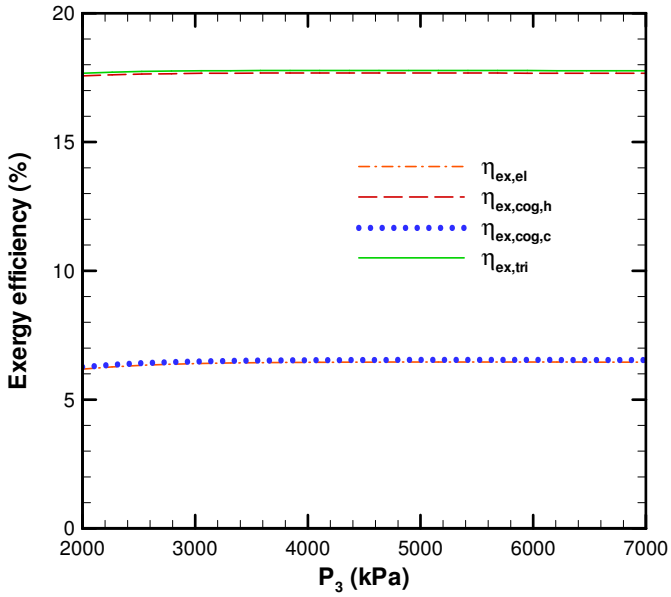

Figure 5.82 Effect of the turbine inlet pressure on the exergy efficiency at T_1=365 K, T_{pp}=40 K, for solar mode.

exergy efficiencies for the electrical, cooling cogeneration, heating cogeneration, and trigeneration are around 6%, 6.5%, 17.5%, and 18%, respectively. Figure 5.83 presents the solar and storage mode. The exergy efficiencies for the electrical, cooling cogeneration, heating cogeneration, and trigeneration are around 3%, 3.5%, 7%, and 7.5%, respectively. Figure 5.84 shows the storage mode. The exergy efficiencies for the electrical, cooling cogeneration, heating cogeneration, and trigeneration are around 2.5%, 3%, 6%, and 6.5%, respectively. It can be observed that the efficiencies for the solar mode are higher than in the other two modes. The reason for that was discussed above.

The effect of the turbine inlet pressure on the exergy destruction rate is shown in Figures 5.85-5.87. Figure 5.85 presents the solar mode. It can be noticed that effect of varying this pressure on the exergy destruction ratio is insignificant since the change in the exergy streams is negligible. The variation in the exergy destruction rate with the change in this

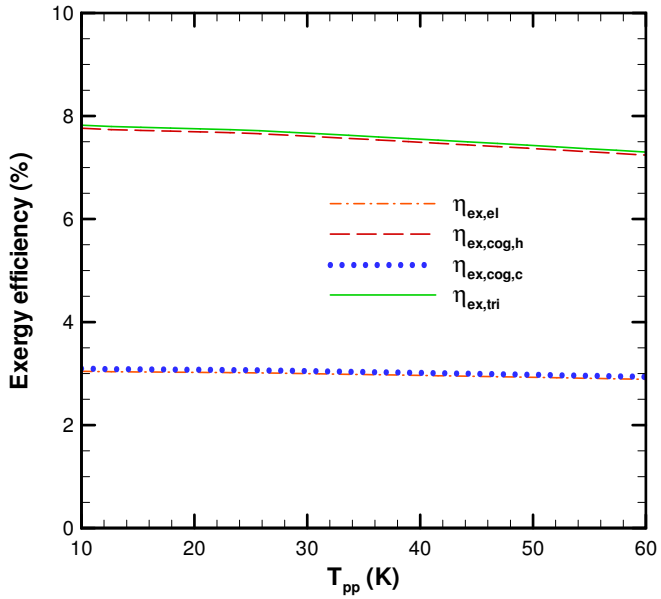

Figure 5.83 Effect of the turbine inlet pressure on the exergy efficiency at T_1=365 K, T_{pp}=40 K, for solar and storage mode.

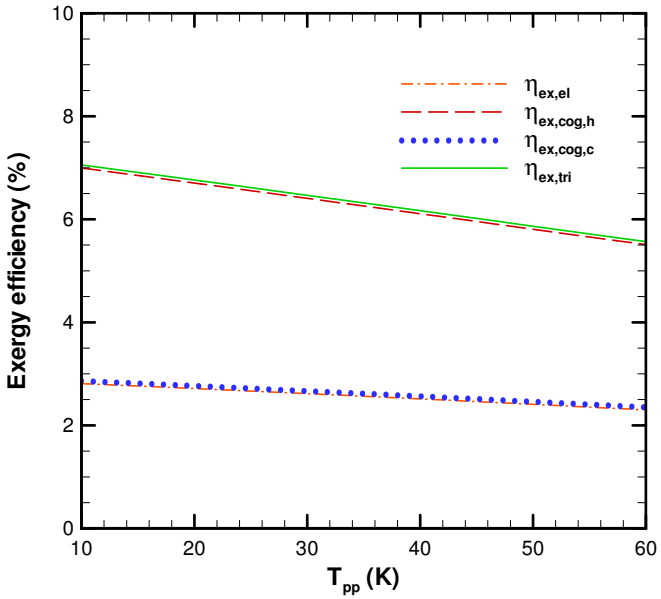

Figure 5.84 Effect of the turbine inlet pressure on the exergy efficiency at T_1=365 K, T_{pp}=40 K, for storage mode.

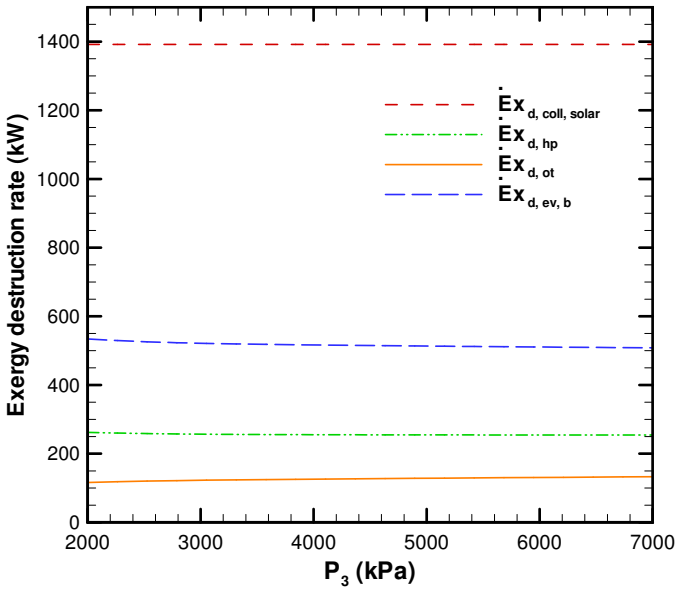

Figure 5.85 Effect of the turbine inlet pressure on the exergy destruction rate at T_1=365 K, T_{pp}=40 K, for solar mode.

pressure is within 30 kW. The destructed exergy rates of the solar collectors, evaporator-b, heating-process heat exchanger, and turbine are around 1400 kW, 520 kW, 260 kW, and 130 kW, respectively. Figure 5.86 illustrates the solar and storage mode. This figure shows that there is a considerable increase in the exergy destructed by the solar collectors for this mode, as compared to the solar mode. This increase is owing to the increase in the solar energy radiation during this mode, as mentioned above. The variation of the exergy destruction rate is within 15 kW. The exergy destruction rates of the solar collectors, evaporator-b, heating-process heat exchanger, turbine, and hot storage tank are around 4800 kW, 500 kW, 115 kW, 110 kW, and 21 kW, respectively. Figure 5.87 presents the storage mode. This figure illustrates that the change in the exergy destruction rate is within 15 kW. The exergy destruction rates of evaporator-a, heating-process heat exchanger, turbine, and hot storage tank are around 585 kW, 70 kW, 100 kW, and 30 kW, respectively.

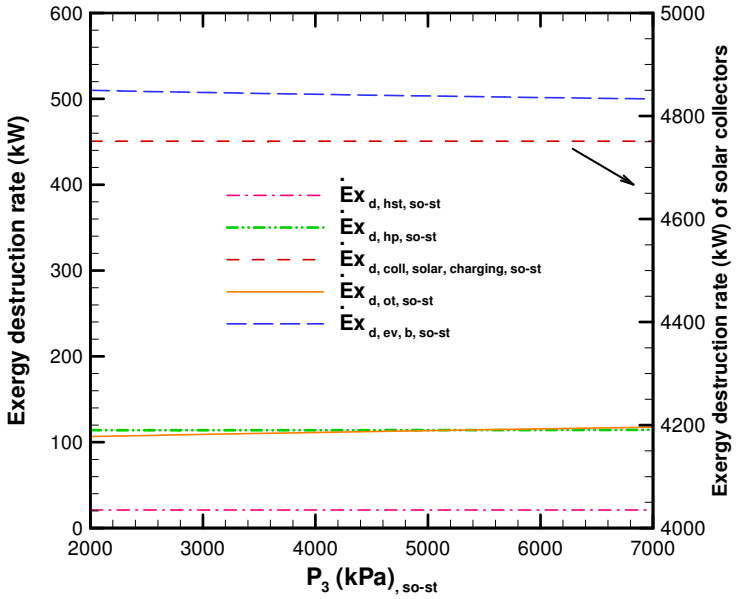

Figure 5.86 Effect of the turbine inlet pressure on the exergy destruction rate at T_1=365 K, T_{pp}=40 K, for solar and storage mode.

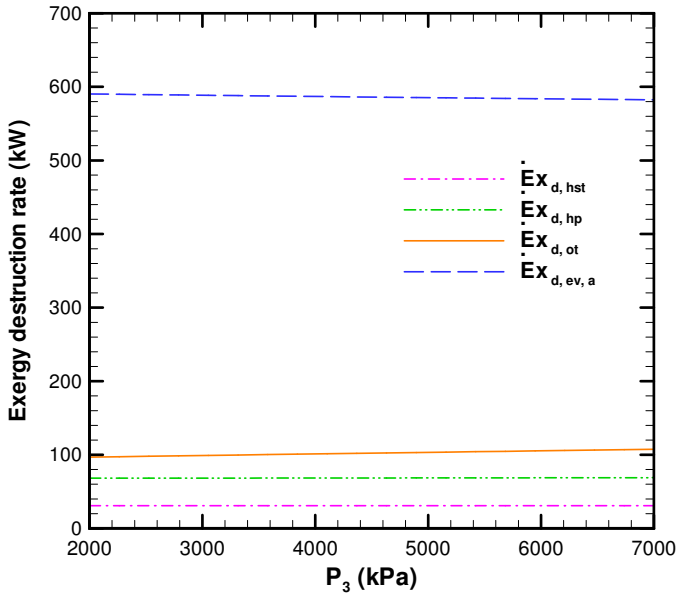

Figure 5.87 Effect of the turbine inlet pressure on the exergy destruction rate at T_1=365 K, T_{pp}=40 K, for storage mode.

5.4.4 Overall Exergy Destruction

The overall exergy destruction rate and its percentage for the solar trigeneration system is shown in Figures 5.88-5.90. The baseline values considered here are 40 K for the ORC evaporator pinch point temperature, 365 K for the pump inlet temperature, and 2,000 kPa for the turbine inlet pressure. It should be noticed that each sector in these three figures presents the exergy destruction rate value and its percentage of the total exergy destructed. Figure 5.88 illustrates the solar mode. This figure shows that the major sources of the exergy destruction are the solar collectors and evaporator-b. The solar collectors destroy 1400 kW of exergy (59%) and evaporator-b destroys 530 kW of exergy (23%). In contrast, the destructed exergy by the heating-process heat exchanger and turbine are lower. The exergy destructed exergy by the heating-process heat exchanger is 260 kW (11%) and the exergy destructed by the turbine is 115 kW (5%). The other components of the system destroy 38 kW of exergy (2%). Figure 5.89 illustrates the solar and storage mode. This figure demonstrates that most of the destructed exergy is destroyed by the solar collectors, which is around 4750 kW (86%). Conversely, the other components have less destruction of exergy. The exergy destructed by evaporator-b, turbine, heating process, and hot storage tank are 510 kW (9%), 110 kW (2%), 115 kW (2%), and 21 kW, respectively. The other components of the system destroy 42 kW (1%). Figure 5.90 illustrates the storage mode. This figure shows that during this mode the significant source of exergy destruction is evaporator-a, which destroys 590 kW of exergy (71%). The other components that have a relatively high destruction rate of exergy are the turbine (96 kW, 12%), heating process (70 kW, 8%), and hot storage tank (30 kW, 4%). The remaining components of the system destroy 42 kW (5%). The above three figures demonstrate that the most significant components that have high destruction rates are the solar collectors and the evaporators. Therefore, in designing a solar-trigeneration system, the most significant components that require careful design and selection are the solar collectors and evaporators.

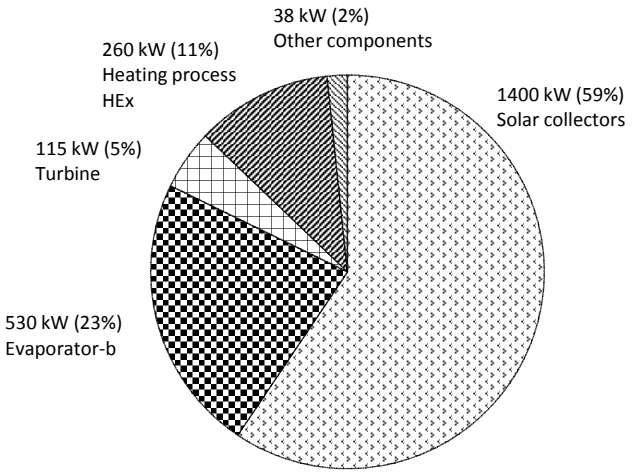

Figure 5.88 Overall exergy destruction rates and percentages for the solar mode (P_3=2000 K, T_1=365 K, and T_{pp}=40 K).

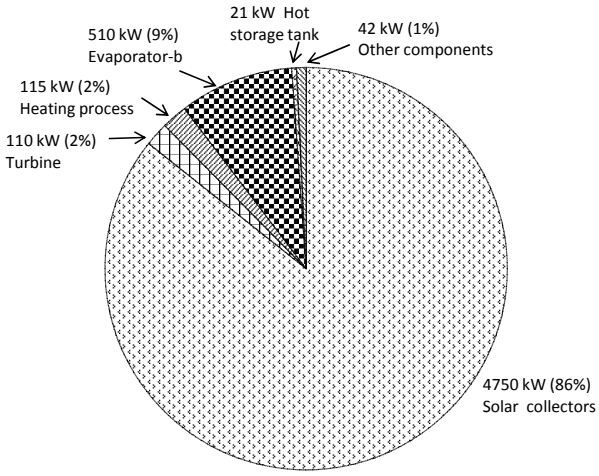

Figure 5.89 Overall exergy destruction rates and percentages for the solar and storage mode (P_3=2000 K, T_1=365 K, and T_{pp}=40 K).

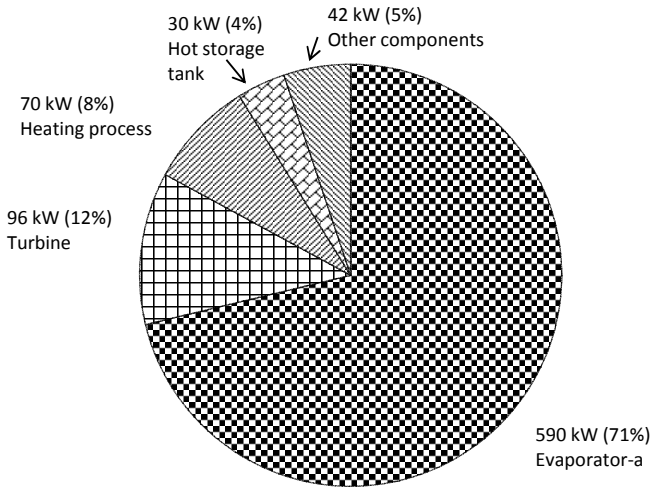

Figure 5.90 Overall exergy destruction rates and percentages for the storage mode (P_3=2000 K, T_1=365 K, and T_{pp}=40 K).

5.4.5 Summary

In this study, the thermodynamic modeling of the solar-trigeneration system considers three modes of operation: solar, solar and storage, and storage modes. The thermodynamic modeling of this system is examined by varying the ORC evaporator pinch point temperature, ORC pump inlet temperature, and turbine inlet pressure. Moreover, exergy destruction modeling is conducted under the selected baseline operating values that are taken from literature. The main findings in this study are summarized below.

- The thermodynamic analysis reveals that the solar mode has the highest energy and exergy efficiencies, and net electrical power. The solar and storage mode has lower energy and exergy efficiencies, and lower electrical power although the solar radiation is higher for this mode as compared to the solar mode. The main reason for this is that major part of the solar energy collected in the solar and storage mode is stored

in the thermal storage tank. On the other hand, the storage mode has marginally lower efficiencies and electrical power as compared to the solar and storage mode. Further increments in the efficiencies and electrical power during the solar and storage mode can be obtained by decreasing the portion of the stored energy during this mode. However, this possible reduction in this portion would result in efficiencies and electrical power reduction during the storage mode. The optimum portion of the stored energy can be obtained based on the energy demand variation during the 24 hours of operation.

- This study reveals that the maximum electrical efficiency for the solar mode is 15%, for the solar and storage mode is 7%, and for the storage mode is 6.5%. Alternatively, when trigeneration is used, the efficiency increases significantly. The maximum trigeneration efficiency for the solar mode is 94%, for the solar and storage mode is 47%, and for the storage mode is 42%.

- This study shows that the electrical to cooling ratio is sensitive to the change in the ORC pump inlet temperature. Therefore, the variation in this temperature could be used as a good control for the amount of the cooling power needed.

- The variation of turbine inlet pressure has an insignificant effect on the performance. That is, the ORC could be run on low pressure, which will result in cost savings.

- It is shown that the maximum electrical-exergy efficiency for the solar mode is 7%, for the solar and storage mode is 3.5%, and for the storage mode is 3%. In contrast, when trigeneration is used, the exergy efficiency increases noticeably. The maximum trigeneration-exergy efficiency for the solar mode is 20%, for solar and storage mode is 8%, and for the storage mode is 7%.

- The main sources of exergy destruction rate are the solar collectors and ORC evapo-

rators. Therefore, careful selection and design of these two components are essential to reduce the exergy destructed by them and, thus, increase the exergy efficiency in the system.

5.5 Thermodynamic and Thermoeconomic Comparisons of the Three Trigeneration Systems, Under Thermoeconomic Optimization

This section discusses the thermodynamic and thermoeconomic comparisons of the three trigeneration plants considered. The results of this comparison are for the thermoeconomic optimized cases.

5.5.1 Effect of the ORC Pump Inlet Temperature

The effect of the ORC pump inlet temperature variation on the efficiency, electrical power, electrical to cooling ratio, electrical to heating ratio, exergy efficiency, cost rate, and cost per exergy unit is examined in Figures 5.91-5.102. The subscripts of the parameters used in these figures are explained next. The subscript SOFC indicates the trigeneration system based on the solid oxide fuel cells. The subscript BM refers to the trigeneration system based on the biomass combustor. The subscript So indicates the trigeneration system based on the solar subsystem. The subscripts so, so-st, and st refer to the solar, solar and storage, and storage modes for the solar-trigeneration system, respectively. The subscripts el and tri indicate electrical and trigeneration, respectively.

Figure 5.91 presents the electrical efficiencies of the three systems considered. This figure demonstrates that as the ORC pump inlet temperature increases, the electrical efficiency decreases. This decrement is owing to the decrease in the temperature difference

between the maximum and minimum temperatures in the ORC. This figure illustrates that the electrical efficiency of the SOFC-trigeneration system is the highest because it has another subsystem that has high efficiency, i.e. the SOFC subsystem. The efficiency of this system drops from almost 19% at 345 K to 17% at 380 K. In contrast, the electrical efficiency of the biomass-trigeneration system drops from almost 15% at 345 K to around 11% at 380 K. On the other hand, the electrical efficiency of the solar-trigeneration system for the solar mode is close to the electrical efficiency of the biomass-trigeneration system. However, the electrical efficiencies of the solar and storage, and storage modes of the solar-trigeneration system are noticeably lower. This drop is owing to the decrease in the amount of the heat input to the ORC during these two modes. As mentioned above, during the solar and storage mode a major portion of the collected energy from the solar collectors is stored in the storage tank. Therefore, during this mode the efficiency is lower as compared to the solar mode. The electrical efficiency of the solar and storage mode drops from 7% at 345 K to 6% at 380 K. The efficiency of the storage mode drops from 6% at 345 K to 5% at 380 K.

The trigeneration efficiency is presented in Figure 5.92. This figure demonstrates that the efficiency improves significantly when trigeneration is used. This figure also shows that the biomass-trigeneration and solar mode of the solar-trigeneration system have the highest trigeneration efficiency, which is around 90%, whereas the SOFC-trigeneration system has a lower trigeneration efficiency, 76%. The reason why the SOFC-trigeneration system has a lower efficiency for trigeneration, while it has the highest electrical efficiency, is explained next. The SOFC-trigeneration system has two devices that produce electrical power, the SOFC and the electrical generator, where most of the electricity is produced by the SOFC; because of this, less energy is needed for the ORC to produce the remaining portion of the electricity as compared to the other two systems. Thus, the amount of the heat that enters the ORC is lower. As a result of the lower heat, lower waste heat is available for heating

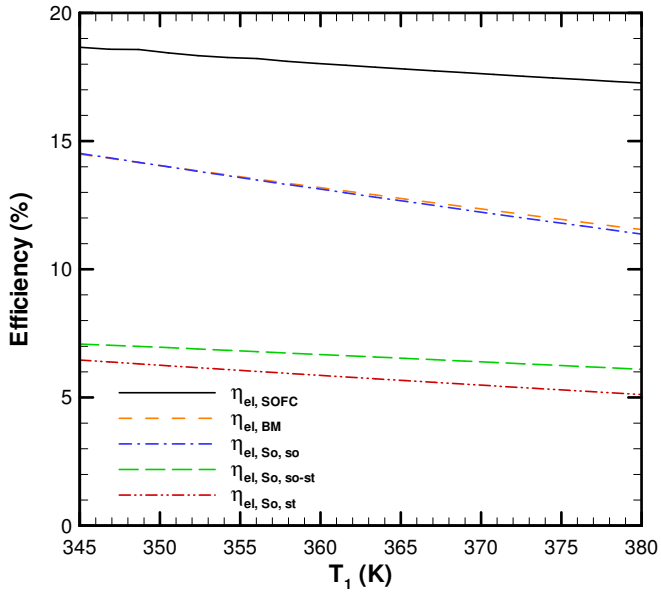

Figure 5.91 Effect of the ORC pump inlet temperature on the electrical efficiency.

and cooling. Thus the trigeneration efficiency of the SOFC is lower than the other two systems. The trigeneration efficiencies of the solar and storage, and storage modes of the solar-trigeneration system are less than that of the solar mode, since less energy is available for these two modes. The trigeneration efficiency of the solar and storage mode is around 45% and for the storage mode is around 41%.

Figure 5.93 illustrates the variation of the net electrical power as the ORC inlet temperature changes. The electrical power decreases as this temperature increases because the operating temperature range of the ORC is reduced and, thus, less power can be obtained from the turbine. It can be observed that the electrical power during the solar mode for the solar-trigeneration system is the highest. This power can be reduced by storing part of the collected energy during the operation of this mode. The electrical power in this mode changes from 830 kW at 345 K to 600 kW at 380 K. The electrical power during the solar and storage mode is 645 kW at 345 K and it decreases to 510 kW at 380 K. The electrical

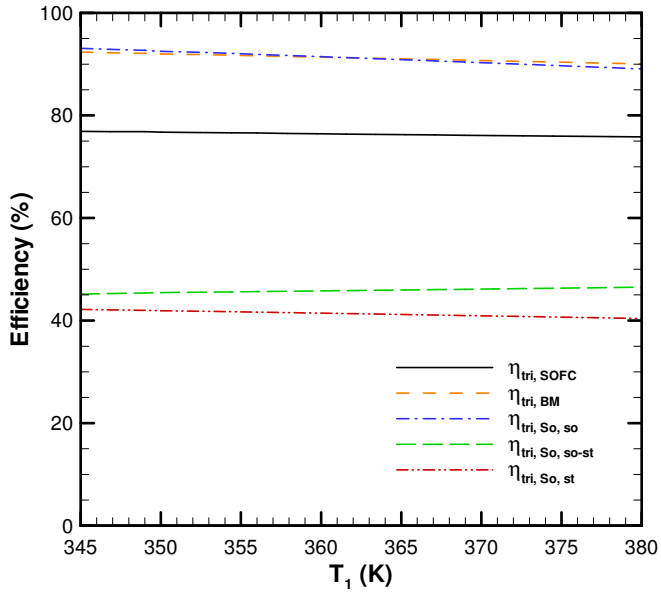

Figure 5.92 Effect of the ORC pump inlet temperature on the trigeneration efficiency.

power of the storage mode decreases from 575 kW at 345 kW to 420 kW at 380 K. Alternatively, the electrical power of the biomass-trigeneration system decreases from 640 kW at 345 kW to 440 kW at 380 K. It can be noticed that the electrical power of the SOFC-trigeneration system is less sensitive to the change in this temperature as compared to the other two systems. The reason of this reduced sensitivity is because the major part of the electrical power is produced from the SOFC subsystem. Hence, less power is produced by the ORC where the change in this temperature has a direct effect on the electrical power produced.

Figure 5.94 presents the electrical to cooling ratio of the three systems considered. This figure shows that the electrical to cooling ratio is sensitive to the change in the ORC pump inlet temperature for the three systems. The degree of sensitivity is related mainly to the sensitivity of the electrical power produced by these three systems as this temperature

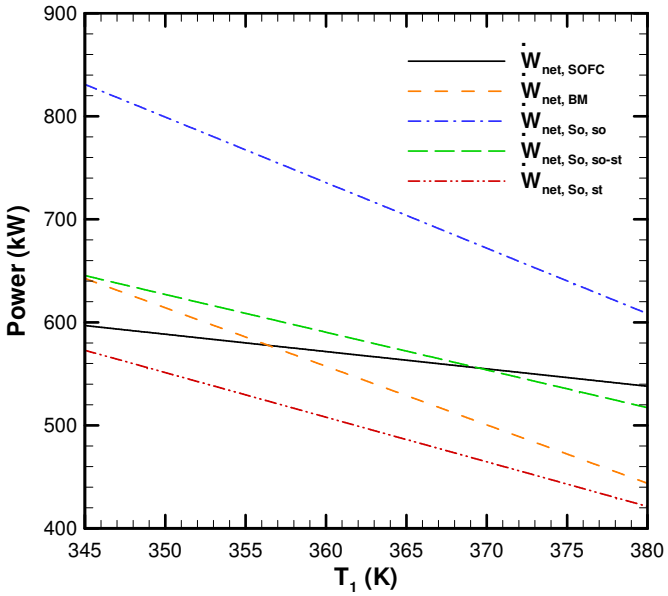

Figure 5.93 Effect of the ORC pump inlet temperature on the net electrical power.

varies. The electrical to cooling ratio of the solar mode of the solar-trigeneration system is the highest while the electrical to cooling ratio of the SOFC-trigeneration system is the lowest. For the SOFC-trigeneration system, this ratio varies from 6.3 at 345 K to 2.7 at 380 K. However, for the biomass-trigeneration system, this ratio varies from 6.7 at 345 K to 2.2 at 380 K. Alternatively, for the solar-trigeneration system, this ratio varies from 8.7 at 345 k to 3.1 at 380 for the solar mode, from 6.7 at 345 K to 2.6 at 380 K for the solar and storage mode, and from 6 at 345 K to 2.1 at 380 K for the storage mode.

Figure 5.95 shows the electrical to heating ratio of the three systems considered. This figure illustrates that as the ORC pump inlet temperature increases, this ratio decreases. This decrement is attributed to the decrease in electrical power as this temperature increases. This figure shows that this ratio is the highest for the SOFC-trigeneration system. This high ratio is obtained since most of the electrical power is produced from the SOFC subsystem for this trigeneration system. Thus, less electrical power is produced by the

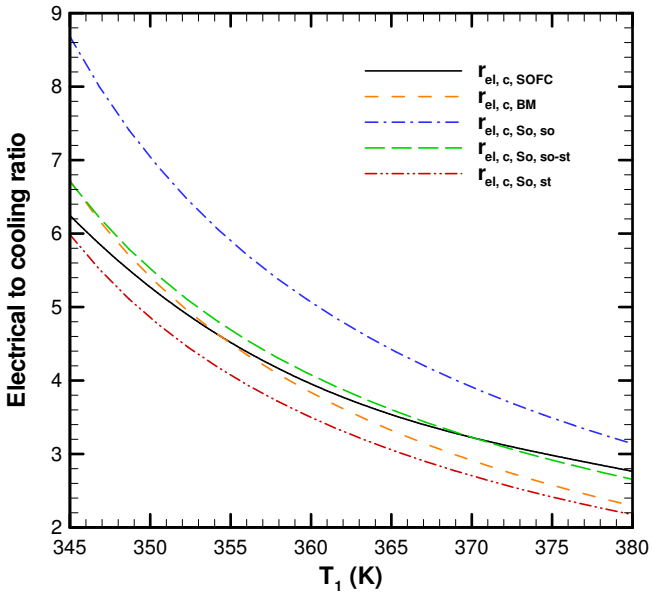

Figure 5.94 Effect of the ORC pump inlet temperature on the electrical to cooling ratio.

ORC and, hence, less heating energy is available from this system. Therefore, this ratio is the highest for the SOFC-trigeneration system. This ratio varies from 0.34 at 345 K to 0.33 at 380 K for the SOFC-trigeneration system. On the other hand, for the other cases this ratio varies from around 0.19 at 345 K to 0.16 at 380 K.

Figure 5.96 demonstrates the emissions of CO_2 in kg per MWh of electrical and trigeneration powers. This figure presents the emissions for the SOFC trigeneration and biomass trigeneration systems. This figure shows that the emissions per MWh of electrical power are significantly high. Alternatively, when trigeneration is used, the emissions per MWh of trigeneration drop significantly. This figure reveals that the emissions of CO_2 per MWh of electrical power for both systems increase as the ORC pump inlet temperature increases. This increase is attributed to the drop in the electrical efficiencies of these two systems as this temperature increases. The CO_2 emissions per MWh of electrical power from the

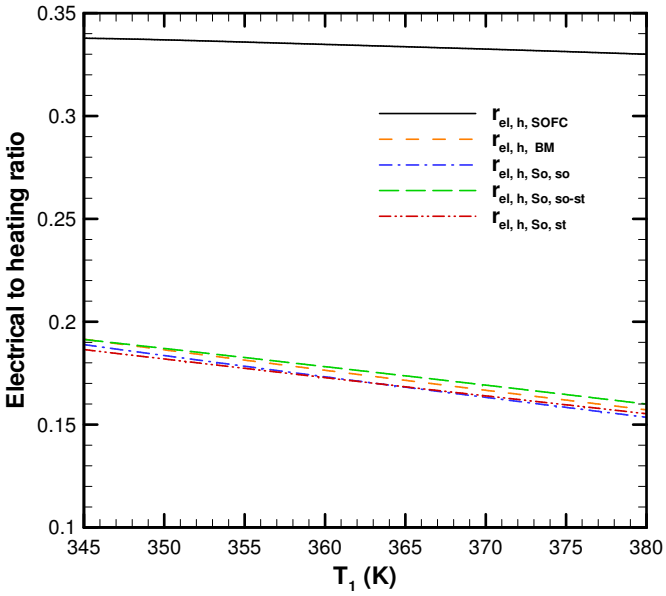

Figure 5.95 Effect of the ORC pump inlet temperature on the electrical to heating ratio.

biomass-trigeneration system increases from 2500 kg/MWh at 345 K to 3200 kg/MWh at 380 K. In contrast, the emissions for the SOFC-trigeneration system increase from 1750 kg/MWh at 345 K to 1900 kg/MWh at 380 K for the electrical power production. Alternatively, when trigeneration is used, the emissions drop significantly to around 400 kg/MWh for these two systems.

Figure 5.97 presents the electrical-exergy efficiency variation as the ORC pump inlet temperature changes. This figure illustrates that the electrical-exergy efficiency of the SOFC-system is the highest. This result is attributed to the high efficiency of the SOFC subsystem that has a contribution to the electrical power produced; unlike the other two systems where all the electrical power is produced by the electrical generator. The exergy-efficiency of the SOFC-trigeneration system varies from almost 15% at 345 K to 13.7% at 380 K. In contrast, this efficiency varies from 13% at 345 K to 10% at 380 K for the

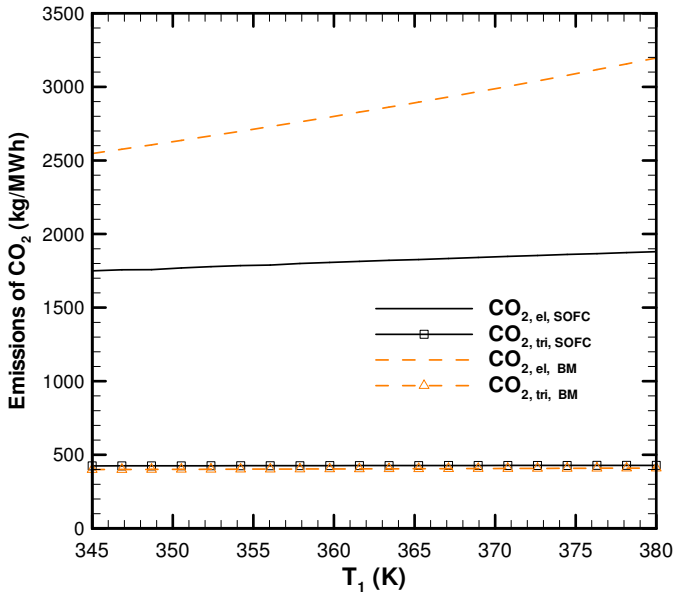

Figure 5.96 Effect of the ORC pump inlet temperature on the CO_2 emissions.

biomass-trigeneration system. Nevertheless, the electrical exergy efficiency of the solar-trigeneration system is considerably less for the solar-trigeneration system. This decrease is attributed to the large temperature difference between the sun temperature and fluid in the collectors [160]. For the solar-trigeneration system, the electrical-exergy efficiency of the solar mode decreases from 7.5 at 345 K to 5% at 380 K; the electrical-exergy efficiency of the solar and storage mode decreases from 3.5% at 345 K to 3% at 380 K; the electrical-exergy efficiency of the storage mode decreases from 3% 345 K to 2% at 380 K.

Figure 5.98 presents the trigeneration-exergy efficiency of the three systems considered. This figure shows that SOFC-trigeneration system has the highest trigeneration-exergy efficiency. This result is owing to the SOFC subsystem that has a high electrical-exergy efficiency. The trigeneration exergy efficiency of this system is around 38%. Conversely, the exergy efficiency of the biomass-trigeneration system is around 28%. For the solar-trigeneration system, the trigeneration-exergy efficiency is noticeably lower for the reason

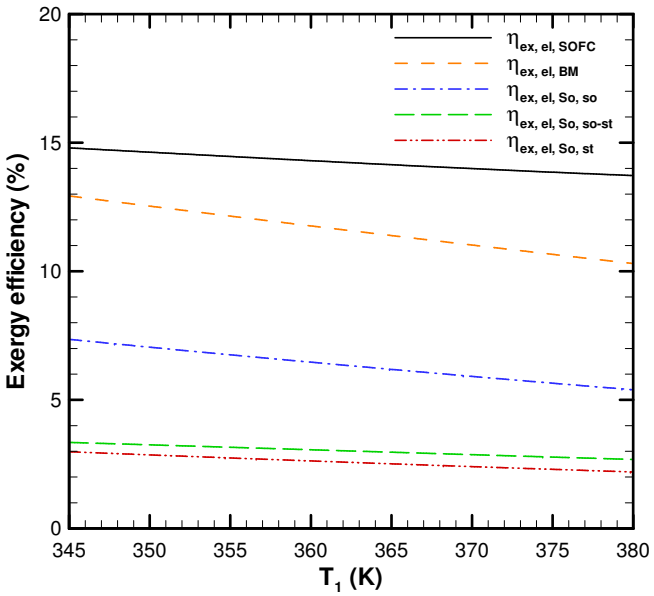

Figure 5.97 Effect of the ORC pump inlet temperature on the electrical-exergy efficiency.

mentioned above. This efficiency is around 18% for the solar mode, 8% for the solar and storage mode, and 6% for the storage mode.

Figure 5.99 presents the cost rate for the electrical production. It can be observed that the cost rates of the electrical power of all the three systems considered decrease as this temperature increases. Considering that the cost rate of the electrical product is a direct function of the electrical power produced. Consequently, as the electrical power decreases, the cost rate of the electrical product decreases. This figure shows that the cost rate of the SOFC is slightly higher than the other two systems. The reason for that is the high capital cost of the SOFC, as well as the cost of the methane and biomass wood fuels for the SOFC-trigeneration system. The cost rate of the SOFC-trigeneration system decreases from 45 $/h at 345 K to 39 $/h at 380 K. Conversely, the cost rate of the biomass-trigeneration system decreases from 45 $/h at 345 K to 30 $/h at 380 K. The cost rate of the solar-trigeneration

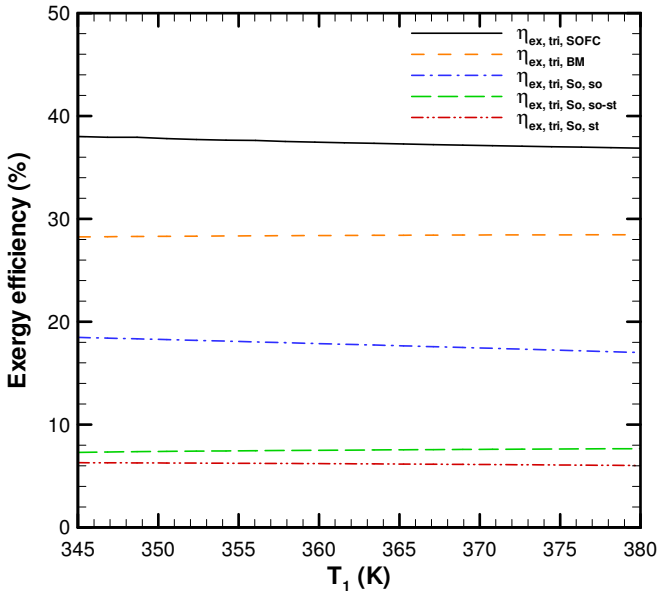

Figure 5.98 Effect of the ORC pump inlet temperature on the trigeneration-exergy efficiency.

system varies depending on the operation mode. The cost rate of the solar mode is the highest among the three modes of the solar-trigeneration system. This result is owing to the low solar radiation during this mode and, hence, the solar subsystem is operating at a lower capacity of its design capacity where it is designed to work in a higher solar radiation. The cost rate of the solar and storage mode is the lowest since the solar radiation is high and, thus, the solar subsystem is utilized more efficiently. The cost rate of the solar mode is 45 $/h at 345 k and decreases to 35 $/h at 380 K. The cost rate of the solar and storage mode is 26 $/h at 345 k and decreases to 22 $/h at 380 K. The cost rate of the storage mode is 36 $/h at 345 k and decreases to 27 $/h at 380 K.

Figure 5.100 illustrates the cost rate of the trigeneration. It can be observed that the cost rate of the trigeneration is less sensitive to the temperature change as compared to the cost rate of the electrical power. This lower sensitivity is owing to the definition of the cost rate

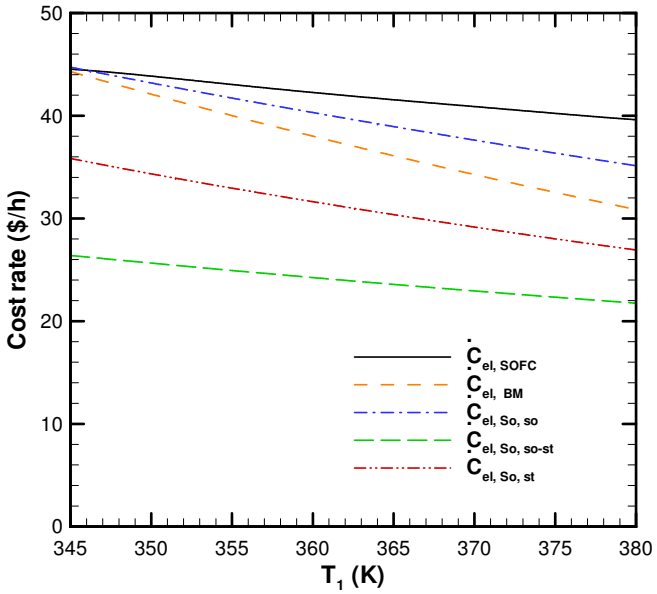

Figure 5.99 Effect of the ORC pump inlet temperature on the cost rate of the electrical power production.

which is a direct function of the products. Since the drop in the electrical power and, thus, the efficiency as this temperature increases is reflected in an increase in the waste heat, the trigeneration power is not sensitive to the change of this temperature. Therefore, the cost rate is not sensitive to the variation of this temperature. This figure reveals that the cost rate of the SOFC-trigeneration system is the highest while the cost rate of the solar mode of the solar-trigeneration system is the lowest. The reason for this behavior was discussed above. The cost rate of the SOFC-trigeneration system is around 110 $/h whereas for the biomass-trigeneration system it is around 70 $/h. The cost rates of the solar-trigeneration system are around 82 $/h for the solar mode, 44 $/h for the solar and storage mode, and 57 $/h for the storage mode.

Figure 5.101 presents the cost per exergy unit of the electrical power. It can be noticed that the electrical-product costs per exergy unit for the biomass and solar-trigeneration

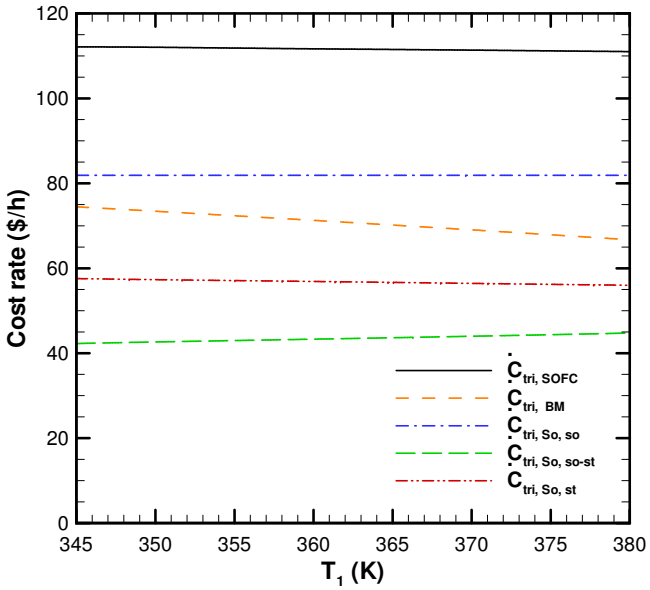

Figure 5.100 Effect of the ORC pump inlet temperature on the cost rate of the trigeneration production.

systems decrease as this temperature increases. This decrease is attributed to the decrease in the exergy efficiency. The cost per exergy unit of the biomass-trigeneration system is around 19 $/GJ. Alternatively, the costs per exergy unit of the solar-trigeneration system are around 15.5 $/GJ for the solar mode, 11.5 $/GJ for the solar and storage mode, and 17.5 $/GJ for the storage mode. Nevertheless, the cost per exergy unit of the SOFC-trigeneration system decreases marginally as this temperature increases. This decrease is owing to the design of the SOFC-trigeneration system where the major portion of the electrical power is produced by the SOFC, which is not part of the ORC. The cost per exergy unit of the SOFC-trigeneration system is around 20.5 $/GJ.

Figure 5.102 presents the trigeneration cost per exergy unit. It can be observed that the cost of the SOFC-trigeneration system is the highest while the solar-trigeneration system is the lowest. The SOFC-trigeneration system costs more since the capital cost of the SOFC

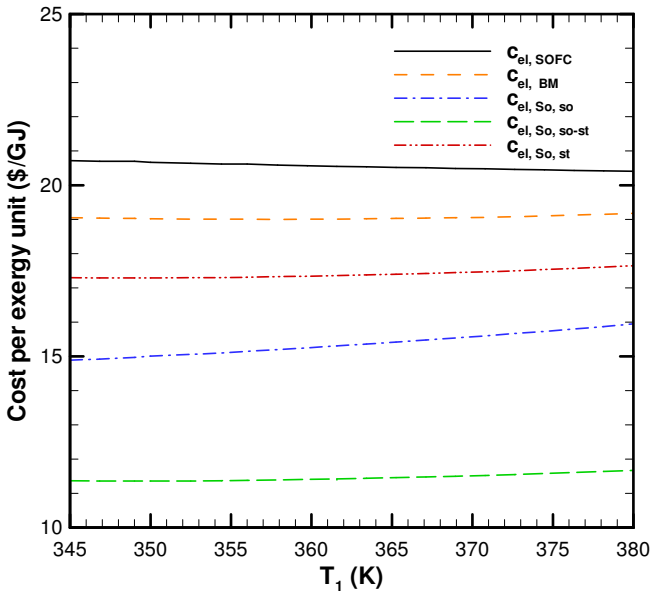

Figure 5.101 Effect of the ORC pump inlet temperature on the cost per exergy unit of the electrical power production.

subsystem is expensive, as well as the operation of this system requires both methane and biomass wood as fuel sources. Similarly, the cost of the biomass-trigeneration system is higher than the solar-trigeneration system since it requires the biomass wood fuel. It can be observed that the trigeneration costs per exergy unit of the three systems increase as the ORC inlet temperature increases. This increase is attributed to the decrease in the exergy efficiency and the trigeneration energy as this temperature increases. This figure shows that the trigeneration cost per exergy unit of the SOFC increases from 35 $/GJ at 345 K to 38 $/GJ at 380 K while the cost of the biomass-trigeneration system increases from 24 $/GJ at 345 K to 27 $/GJ at 380 K. The trigeneration cost of the solar-trigeneration system increases from 19 $/GJ at 345 K to 22 $/GJ at 380 K for the solar mode, from 14 $/GJ at 345 K to 16 $/GJ at 380 K for solar and storage mode, and from 22 $/GJ at 345 to 24 $/GJ at 380 K for the storage mode.

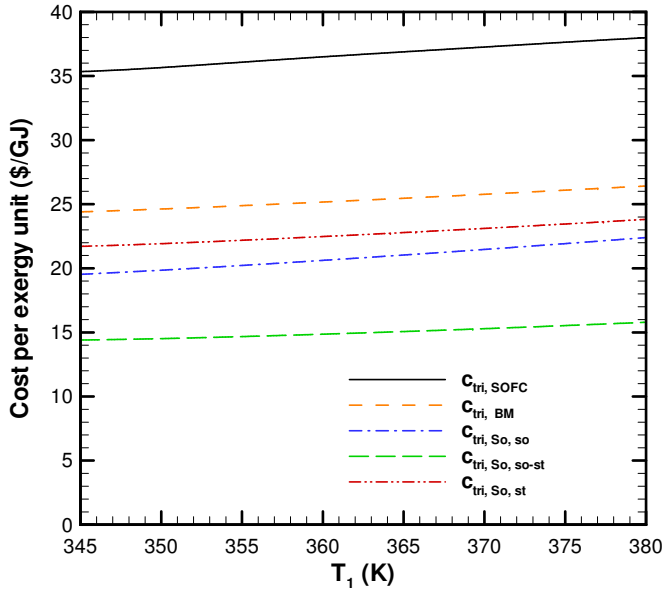

Figure 5.102 Effect of the ORC pump inlet temperature on the cost per exergy unit of the trigeneration production.

5.5.2 Effect of the Turbine Inlet Pressure

The effect of the turbine inlet pressure variation on the performance of the three systems considered is shown in Figures 5.103-5.114. Figure 5.103 presents the effect of the pressure variation on the electrical efficiency. It can be noticed that the effect of pressure variation is insignificant except for the SOFC-trigeneration system. The SOFC-trigeneration system is sensitive to the pressure variation since the size of the ORC where the power produced by the turbine and mass flow rate of the working fluid is smaller than the other two systems. Therefore, the electrical efficiency of the SOFC-trigeneration system is more sensitive to the pressure variation as compared to the other two systems. The electrical efficiency of the SOFC-trigeneration system increases from 18 % at 345 K to 19.5% at 380 K. Alternatively, the electrical efficiency of the biomass-trigeneration system is around 12.5%. On the other hand, the electrical efficiency of the solar-trigeneration system is around 13% for the solar

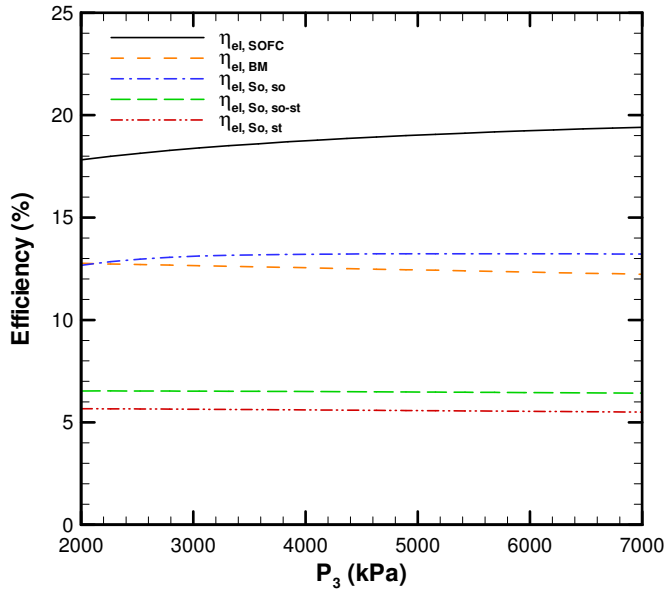

Figure 5.103 Effect of the turbine inlet pressure on the electrical efficiency.

mode, 6.5% for the solar and storage mode, and 5.5% for the storage mode.

Figure 5.104 presents the effect of the turbine inlet pressure on the trigeneration efficiency of the systems considered. It can be noticed that the effect of varying this pressure is negligible on the trigeneration efficiencies of all three systems. Therefore, these systems could be operated at low pressure, since this will result in cost savings. It is observed that the trigeneration efficiency of the SOFC-trigeneration system is lower than the biomass and solar (solar mode) systems; unlike the electrical efficiency of the SOFC which was the highest. The reason for that was discussed above. The trigeneration efficiency of the biomass-trigeneration system is approximately 90% while this efficiency is around 76% for the SOFC-trigeneration system. The trigeneration efficiencies of the solar-trigeneration system are around 90% for the solar mode, 46% for the solar and storage mode, and 41% for the storage mode.

Figure 5.105 illustrates the effect of the turbine inlet pressure variation on the net elec-

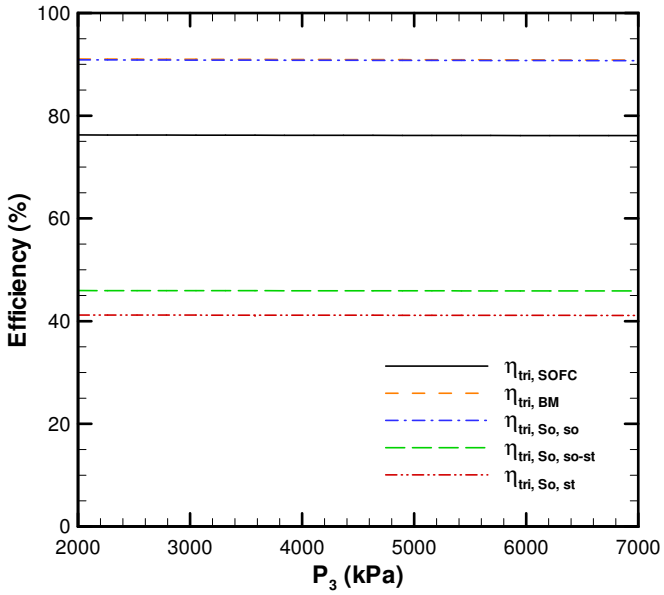

Figure 5.104 Effect of the turbine inlet pressure on the trigeneration efficiency.

trical power. This figure shows that as the pressure increases, the electrical power of the SOFC-trigeneration system increases. It increases from 560 kW at 2000 kPa to 610 kW at 7000 kPa. Nevertheless, the electrical power of the biomass-trigeneration system decreases from 530 kW at 345 kPa to 480 kW at 7000 kPa. Alternatively, the electrical power of the solar-trigeneration system increases from 700 kW at 2000 kPa to 730 kW at 7000 kPa for the solar mode. The electrical power of the solar and storage mode is around 520 kW, whereas it is around 470 kW for the storage mode.

Figure 5.106 illustrates the electrical to cooling ratio variation as the pressure varies. This figure reveals that the effect of the pressure variation on this ratio is insignificant. This electrical to cooling ratio is around 3.7 for the SOFC-trigeneration system and 3.1 for the biomass-trigeneration system. Regarding the solar-trigeneration system, this ratio is around 4.5 for the solar mode, 3.5 for the solar and storage mode, and 3 for the storage mode.

Figure 5.107 presents the effect of pressure on the electrical to heating ratio. This figure

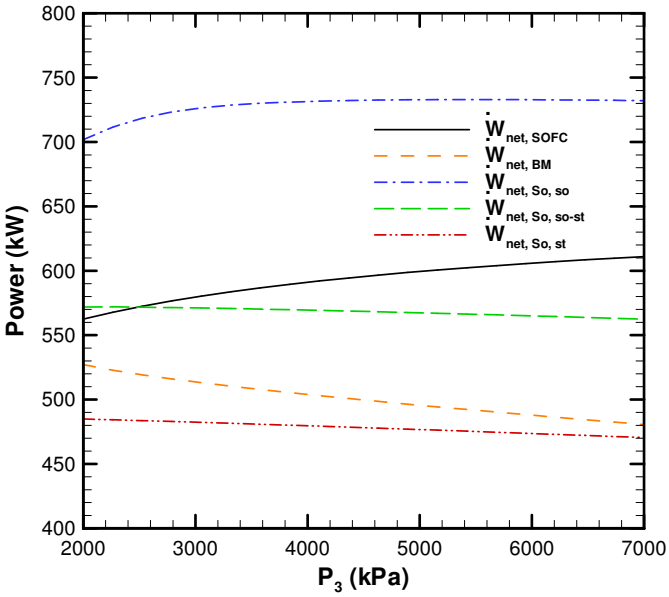

Figure 5.105 Effect of the turbine inlet pressure on the net electrical power.

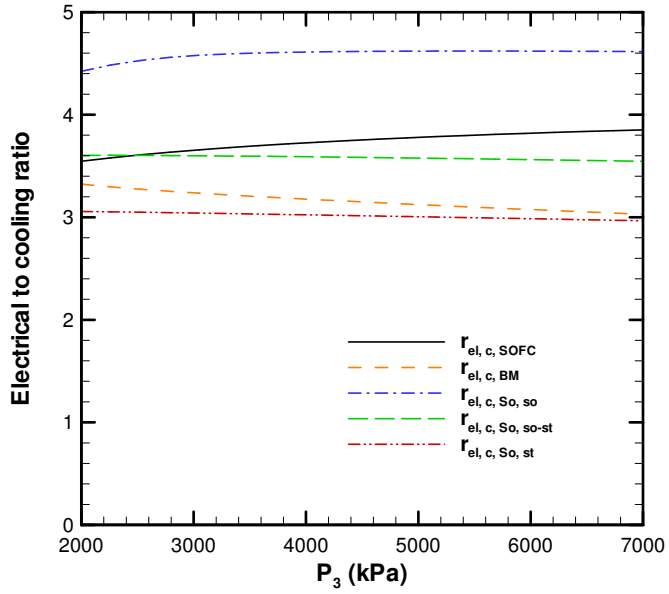

Figure 5.106 Effect of the turbine inlet pressure on the electrical to cooling ratio.

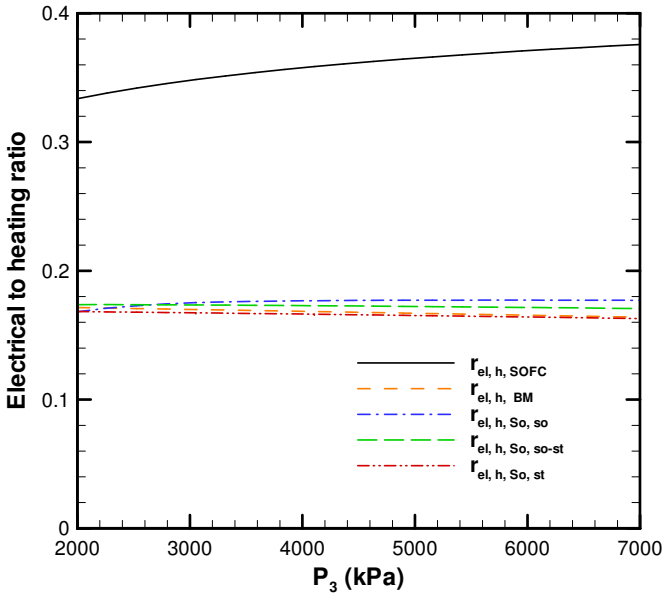

Figure 5.107 Effect of the turbine inlet pressure on the electrical to heating ratio.

shows that as the pressure increases this ratio increases noticeably only for the SOFC-trigeneration system. This increase is attributed to the relative small size of the ORC and the mass flow rate of the working fluid in the ORC, as mentioned above. This ratio increases from 0.33 at 2000 kPa to 0.38 at 7000 kPa. The electrical to heating ratio for the other two systems is around 0.18.

Figure 5.108 illustrates the effect of pressure variation on the emissions of CO_2 in kg/MWh. This figure reveals that the emission of CO_2 is insignificant to the pressure changes. This figure also shows that the emissions, when there is only electrical power production, are significantly high. However, when trigeneration is used, the emissions drop significantly. The emissions of the biomass-trigeneration system increase from 2900 kg/MWh at 2000 kPa to 3050 kg/MWh at 7000 kPa for the electrical power production. Conversely, when trigeneration is used, the emissions drop considerably to around 400 kg per MWh of trigeneration power. In contrast, the emissions for the SOFC-trigeneration

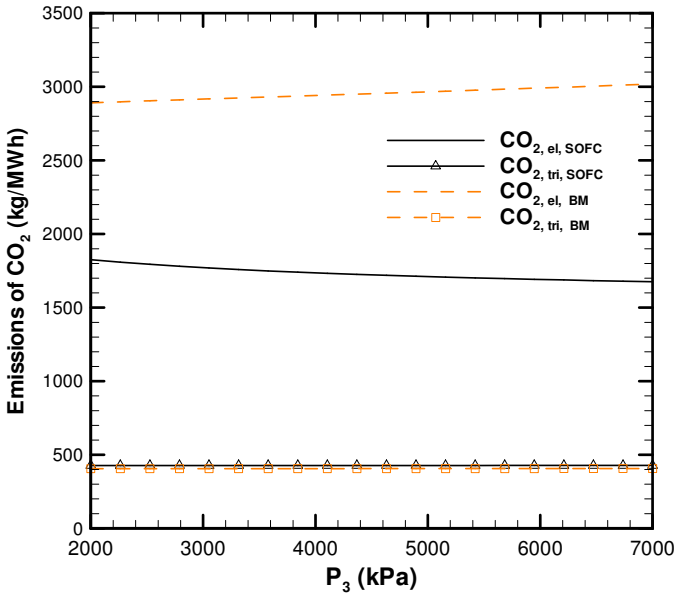

Figure 5.108 Effect of the turbine inlet pressure on the CO_2 emissions.

system are around 1700 kg/MWh while, when trigeneration is used, the emissions drop significantly to around 400 kg/MWh. Note that the emissions of the SOFC-trigeneration system are relatively high since it has an auxiliary biomass boiler to heat up the inlet fluids of the SOFC subsystem.

Figure 5.109 presents the effect of pressure variation on the electrical-exergy efficiency. This figure shows that the electrical-exergy efficiency of the SOFC-trigeneration system is the highest while for the solar-trigeneration system it is the lowest, for the reasons mentioned above. This efficiency increases as the pressure increases for the SOFC-trigeneration system. It increases from 14 % at 2000 kPa to 15.5% at 7000 kPa. In contrast, this efficiency is around 11 % for the biomass-trigeneration system. On the other hand, for the solar-trigeneration system this efficiency is approximately 6.5% for the solar mode, 3% for the solar and storage mode, and 2.5% for the storage mode.

Figure 5.110 illustrates the trigeneration-exergy efficiency variation as the turbine inlet

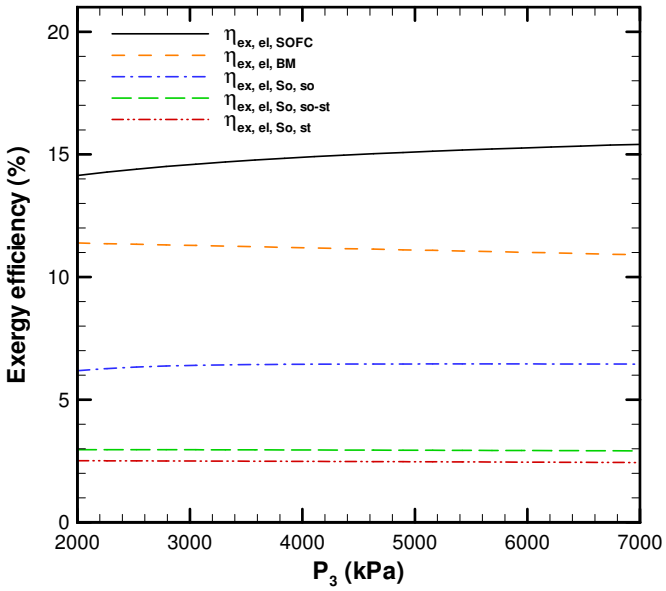

Figure 5.109 Effect of the turbine inlet pressure on the electrical-exergy efficiency.

pressure changes. This figure shows that the pressure variation has an insignificant effect on the trigeneration-exergy efficiency. The trigeneration efficiency for SOFC-trigeneration system is around 37% whereas it is around 28% for the biomass-trigeneration system. The trigeneration exergy efficiency for the solar-trigeneration system is considerably lower for the solar-trigeneration system for the reason mentioned above. This efficiency is around 17% for the solar mode, 7% for the solar and storage mode, and 6% for the storage mode.

Figure 5.111 demonstrates the effect of the turbine inlet pressure variation on the electrical-product cost rate of the three systems considered. This figure shows that the cost rates of the SOFC-trigeneration system and solar mode of the solar-trigeneration system increase as this pressure increases. This is attributed to the definition of the electrical-product cost rate where it is a direct function of the net electrical power produced. Considering that the electrical power of the SOFC-trigeneration system and the solar-trigeneration system (solar

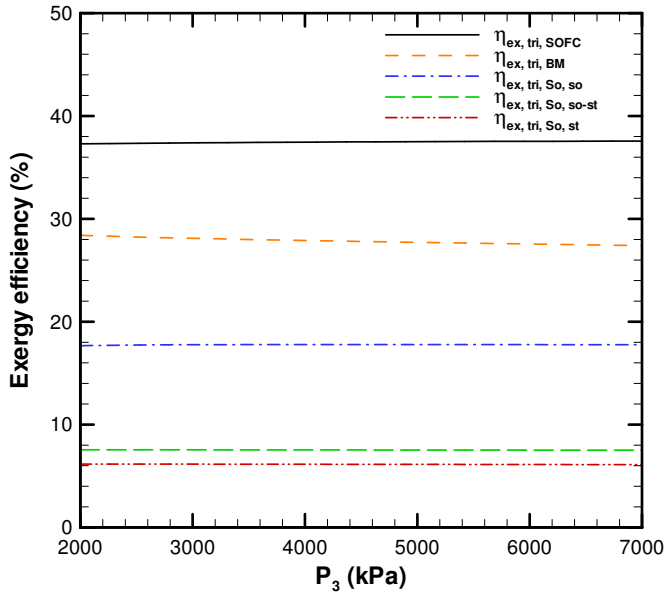

Figure 5.110 Effect of the turbine inlet pressure on the trigeneration-exergy efficiency.

mode) increase as the pressure increases, as shown in Figure 5.105, therefore, the cost rates of these two cases increase. The electrical-product cost rate of the SOFC-trigeneration system increases from 42 $/h at 2000 kPa to 46 $/h at 7000 kPa, and the electrical-product cost rate for the solar-trigeneration system (solar mode) increases from 39 $/h at 2000 kPa to 40 $/h at 7000 kPa. On the other hand, the cost rate of the electrical product of the solar-trigeneration system is almost constant for the solar and storage mode, and storage mode. It is around 24 $/h for the solar and storage mode, and around 30 $/h for the storage mode. Alternatively, the cost rate of the biomass-trigeneration system decreases from 36 $/h to 34 $/h as the pressure increases.

Figure 5.112 illustrates the trigeneration cost rate variation as the pressure changes. It is observed that the variation in the cost rate is insignificant. The trigeneration cost rate for the SOFC-trigeneration system is approximately 111 $/h and for the biomass-trigeneration

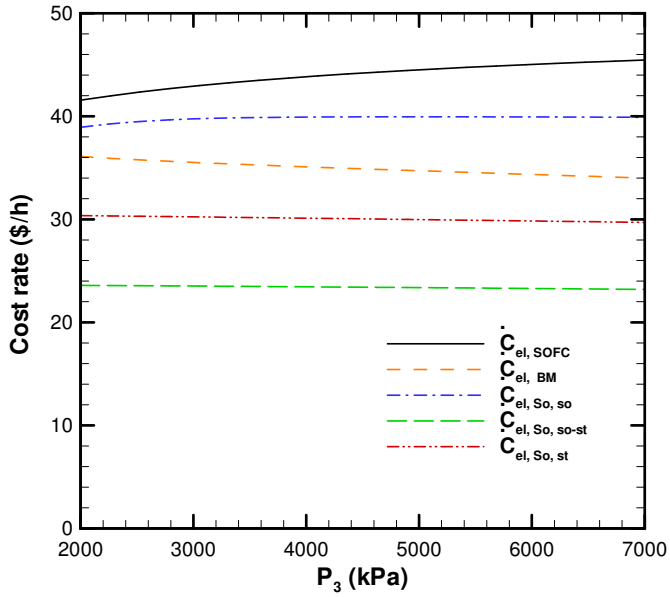

Figure 5.111 Effect of the turbine inlet pressure on the cost rate of the electrical power production.

system the cost rate is around 69 $/h. The trigeneration cost rate of the solar-trigeneration system is around 81 $/h for the solar mode, 44 $/h for the solar and storage mode, and 55 $/h for the storage mode.

Figure 5.113 shows the electrical-product cost per exergy unit variation as the pressure varies. This figure shows that the cost per exergy unit is insignificant to the pressure variation. This insensitively is attributed to the negligible effect of the pressure change on the performance of the system, as explained above. The electrical-product cost per exergy unit is around 20.5 $/GJ for the SOFC-trigeneration system and 19.5 $/GJ for the biomass-trigeneration system. Alternatively, for the solar-trigeneration system this cost is around 15.5 $/GJ for the solar mode, 11.5 $/GJ for the solar and storage mode, and 17.5 $/GJ for the storage mode.

Figure 5.114 presents the effect of pressure on the trigeneration cost per exergy unit of

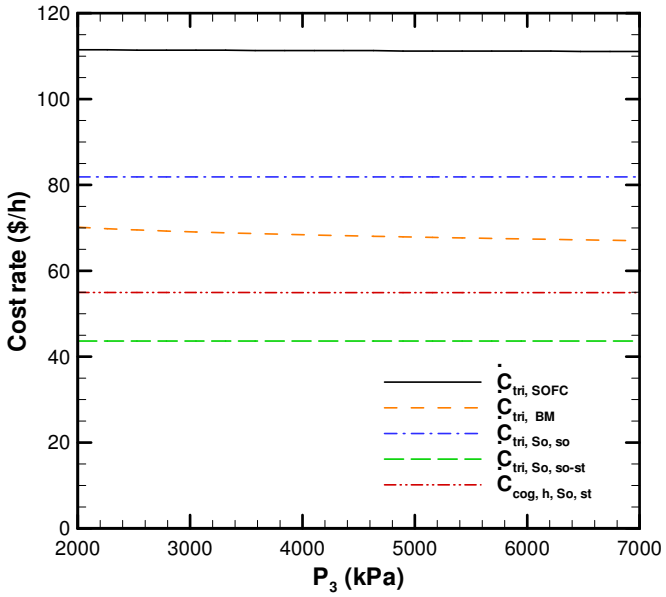

Figure 5.112 Effect of the turbine inlet pressure on the cost rate of the trigeneration production.

the three systems considered. This figure shows that the pressure variation has an insignificant effect on the trigeneration cost per exergy unit. This insignificant effect is attributed to the negligible variation of the trigeneration-exergy efficiency as this pressure varies. This figure reveals that this cost is around 37 $/GJ for the SOFC and 26 $/GJ for the biomass-trigeneration system. In contrast, for the solar-trigeneration system this cost is around 21 $/GJ for the solar mode, 15 $/GJ for the solar and storage mode, and 23 $/GJ for the storage mode.

5.5.3 Overall Exergy Rate

The total available exergy rate from the exergy source and the total overall exergy destruction rate of each system under the baseline conditions are presented in Figure 5.115. This figure reveals that the solar-trigeneration system has noticeably more available exergy rate

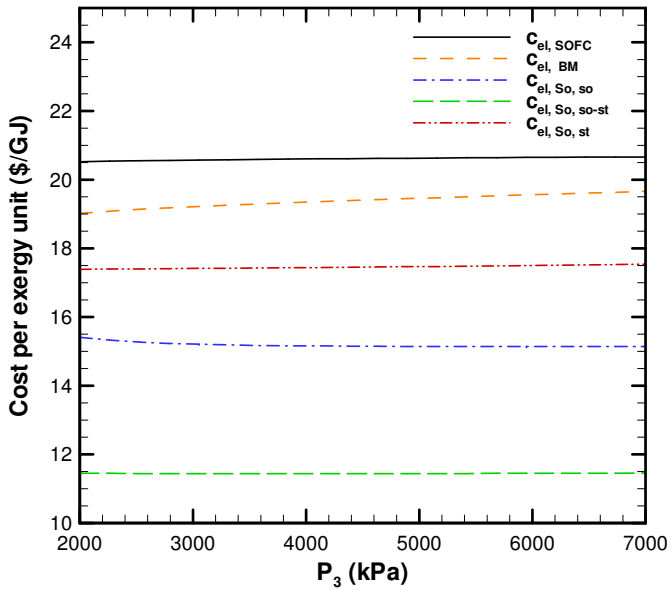

Figure 5.113 Effect of the turbine inlet pressure on the cost per exergy unit of the electrical power production.

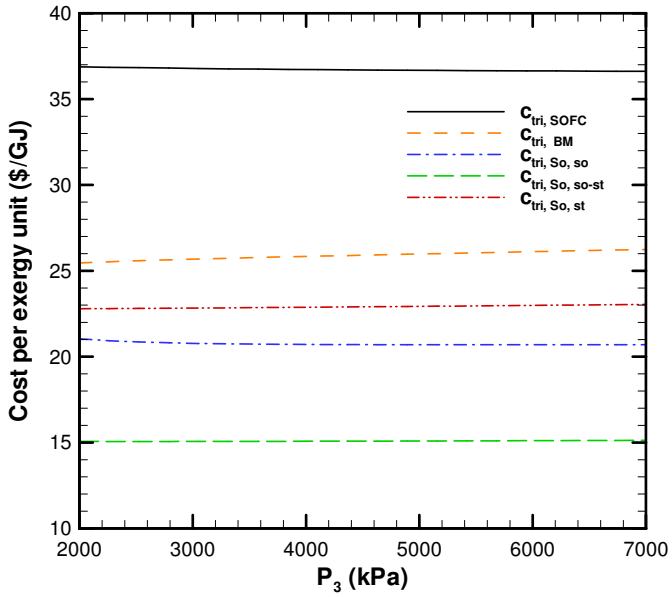

Figure 5.114 Effect of the turbine inlet pressure on the cost per exergy unit of the trigeneration production.

as compared to the other two systems. This high available exergy rate is owing to the high available exergy rate from the solar radiation that falls down on the solar collectors. The total available exergy rate for the solar and storage mode is almost 19300 kW, while for the solar mode it is around 11300 kW and for the storage mode is around 4500 kW. In contrast, the available exergy rate for the SOFC-trigeneration and biomass-trigeneration systems are around 4000 kW and 4700 kW, respectively. Moreover, this figure illustrates that the solar and storage mode of the solar-trigeneration system has the highest total exergy destruction rate. This high exergy destruction rate is attributed to the exergy destructed by the solar collectors. In this study, the net available exergy rate is defined as the total available exergy rate minus the total exergy destruction rate. In terms of the net available exergy rate, the solar-trigeneration system has the highest net available exergy rate as compared to the other two systems. Alternatively, the biomass-trigeneration system has the lowest net available exergy rate.

5.5.4 Summary

In this section, the thermodynamic and thermoeconomic results of the optimum thermoeconomic modeling of the three systems considered are presented and discussed. The three systems are SOFC, biomass, and solar-trigeneration systems. The main findings from this comparison are summarized below.

- The SOFC-trigeneration system has the highest electrical efficiency among the three systems. However, the trigeneration efficiencies of the biomass-trigeneration system and solar mode of the solar-trigeneration system are higher than the trigeneration efficiency of the SOFC-trigeneration system.

- The maximum electrical efficiency for the SOFC-trigeneration system is 19% and for the biomass-trigeneration system it is 15%. On the other hand, the maximum

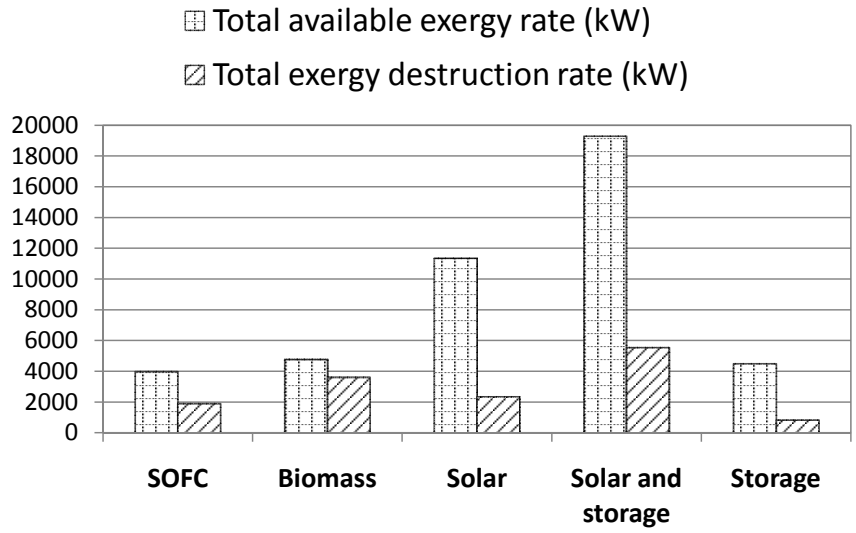

Figure 5.115 Total available exergy rate from the energy source and the total overall exergy destruction rate of each system under baseline conditions.

electrical efficiency for the solar-trigeneration system is around 15% for the solar mode, 7% for the storage and solar mode, and 6% for the storage mode.

- The efficiency increases considerably when trigeneration is used. The maximum trigeneration efficiency of the SOFC-trigeneration system is around 76% and it is around 90% for the biomass-trigeneration system. The maximum trigeneration efficiencies of the solar-trigeneration system is around 90% for the solar mode, 45% for storage and storage mode, and 41% for the storage mode.

- The electrical to cooling ratio is sensitive to the variation of the ORC pump inlet temperature. Therefore, when it is needed to increase or decrease the cooling power, it can be controlled through the variation of this temperature. This ratio is the highest and most sensitive for the solar mode, where it could vary from 8.8 to 3.1. For the

other two modes and two trigeneration systems, this ratio varies from approximately 6.5 to 2.5 as this temperature increases.

- The solar-trigeneration system has zero CO_2 emissions. Alternatively, the other two systems have significant CO_2 emissions per MWh of electrical power. When trigeneration is used, the emissions per MWh of these two systems drop significantly. The emissions per MWh of trigeneration for these two systems are reasonable, around 400 kg/MWh of trigeneration power. Regarding the SOFC-trigeneration system, the emissions are high per MWh of electricity since the hot streams at the exit of SOFC subsystem are partially used to heat the ORC. Therefore, more heat (biomass fuel) is needed from the auxiliary biomass boiler to heat the stream inlets of the SOFC and, thus, there are considerable emissions per MWh of electricity for the SOFC-trigeneration system.

- The electrical-exergy efficiency of the SOFC is the highest among the three trigeneration systems. Conversely, the electrical exergy of the solar-trigeneration system is the lowest for all of the three operating modes. Similarly, the trigeneration-exergy efficiency of the SOFC is the highest while this efficiency is the lowest for the solar-trigeneration system. The reason why the solar-trigeneration system has low exergy efficiency was discussed above. The maximum electrical-exergy efficiency for the SOFC-trigeneration system is around 15%, for the biomass-trigeneration system is approximately 13%, and for the solar-trigeneration system is around 7.5%. The maximum trigeneration-exergy efficiency for the SOFC is approximately 38%, for the biomass-trigeneration system is around 28%, and for the solar-trigeneration system is around 18%.

- The cost rate of the SOFC-trigeneration system is the highest among the three systems. The main reasons for that is the high capital cost of the SOFC subsystem, as

well as the cost of the fuel of this system.

- The cost per exergy unit of the SOFC-trigeneration system is the highest while this cost is the lowest for the solar-trigeneration system. The maximum electrical cost per exergy for the SOFC-trigeneration system is around 21 $/GJ, for the biomass-trigeneration system is approximately 19 $/GJ, and for the solar-trigeneration system is around 17.5 $/GJ. Considering the trigeneration, these costs increase. The maximum costs per exergy unit for the SOFC-trigeneration system is approximately 38 $/GJ, for the biomass-trigeneration system is 26 $/GJ, and for the solar-trigeneration system is 24 $/GJ.

- This study shows that the solar-trigeneration system has the highest net available exergy as compared to the other two systems. Hence, it has the highest potential to have the highest exergy if the solar collectors performance improve.

- It can be concluded from this study that the solar-trigeneration system is the best among the three systems. The solar-trigeneration system has the lowest cost per exergy unit and zero CO_2 emissions, as well as it is a free renewable energy source.

Chapter 6

Conclusions and Recommendations

In the present study, comprehensive thermodynamic modeling is conducted on each system. Then, a thermoeconomic optimization is carried out on each system. The results of the thermoeconomic optimization are used to compare the three systems, using thermodynamic and thermoeconomic analyses. The main objective of the current study is to assess the performance of the trigeneration systems considered. To have a better understanding, these assessments are extended to include electrical-power, cooling-cogeneration, and heating-cogeneration cases. The thermodynamic modeling includes the study of energy efficiency, exergy efficiency, net electrical power, electrical to heating ratio, and electrical to cooling ratio in the four cases. Moreover, the exergy destruction modeling is carried out to identify and quantify the sources of the irreversibilities that are associated with each component in the systems considered. In addition, this study quantifies the environmental impact of the systems considered. Furthermore, thermoeconomic optimization is carried out on each system. The optimization objective is to minimize the cost per exergy unit for trigeneration production. The main findings from this study are summarized below.

6.1 Conclusions

- This study reveals that the SOFC-trigeneration system has the highest electrical efficiency among the three systems. Nevertheless, the trigeneration efficiencies of the biomass-trigeneration system and solar mode of the solar-trigeneration system are higher than the trigeneration efficiency of the SOFC-trigeneration system. The current study shows that the maximum electrical efficiency for the SOFC-trigeneration system is 19% and for the biomass-trigeneration system is 15%. On the other hand, the maximum electrical efficiency for the solar-trigeneration system is around 15% for the solar mode, 7% for the storage and solar mode, and 6% for the storage mode. Alternatively, the efficiency increases considerably when trigeneration is used. The maximum trigeneration efficiency of the SOFC-trigeneration system is around 76%, and it is around 90% for the biomass-trigeneration system. The maximum trigeneration efficiency of the solar-trigeneration system is around 90% for the solar mode, 45% for the storage and storage mode, and 41% for the storage mode.

- It was found that the electrical to cooling ratio is sensitive to the variation of the ORC pump inlet temperature. Therefore, when the cooling power must be increased or decreased, it can be controlled through the variation of this temperature. This ratio is the highest and most sensitive during the solar mode operation where it could vary from 8.8 to 3.1. For the other two solar modes and two trigeneration systems, this ratio varies from approximately 6.5 to 2.5 as this temperature increases from 345 K to 380 K.

- The solar-trigeneration system has zero CO_2 emissions. On the other hand, the other two systems have significant CO_2 emissions per MWh of electrical power. When trigeneration is used, the emissions per MWh of these two systems significantly drop. The emissions per MWh of trigeneration for these two systems are reason-

able, around 400 kg per MWh of trigeneration power. Nevertheless, the biomass-trigeneration system is not recommended for electrical production only. Regarding the SOFC-trigeneration system, the emissions are high per MWh of electricity since the hot streams at the exit of the SOFC subsystem are partially used to heat the ORC. Hence, more heat (biomass fuel) is needed from the auxiliary biomass burner to heat the stream inlets of the SOFC and, thus, there are noticeable emissions per MWh of electricity for the SOFC-trigeneration system.

- The electrical-exergy efficiency of the SOFC-trigeneration system is the highest among the three trigeneration systems. In contrast, the electrical exergy of the solar- trigeneration system is the lowest for all the three operating modes. Similarly, the trigeneration-exergy efficiency of the SOFC is the highest while this efficiency is the lowest for the solar-trigeneration system. The reason why the solar-trigeneration system has low exergy efficiency was discussed in section 5.4. The maximum electrical-exergy efficiency for the SOFC-trigeneration system is around 15%, for the biomass-trigeneration system is around 13%, and for the solar-trigeneration system is around 7.5%. The maximum trigeneration-exergy efficiency for the SOFC is approximately 38%, for the biomass-trigeneration system is around 28% and for the solar- trigeneration system is around 18%.

- The cost rate of the SOFC-trigeneration system is the highest among the three systems. The main reasons for that are the high capital cost of the SOFC subsystem, as well as the cost of the fuel for this system. The maximum cost rate of the SOFC-trigeneration system is 45 $/h for electrical power production while it is 110 $/h for trigeneration production. For the biomass system, the maximum cost rate is 45 $/h for electrical production and it increases to 70 $/h for trigeneration production. For the solar-trigeneration system, the maximum cost rates of electrical production are

45 $/h for the solar mode, 26 $/h for the solar and storage mode, and 36 $/h for the storage mode.

- The cost per exergy unit of the SOFC-trigeneration system is the highest while this cost is the lowest for the solar-trigeneration system. The maximum electrical cost per exergy unit for the SOFC-trigeneration system is around 21 $/GJ, while for the biomass-trigeneration system it is approximately 19 $/GJ, and for the solar-trigeneration system around 17.5 $/GJ. Considering trigeneration, these costs increase. The maximum costs per exergy unit for the SOFC-trigeneration system is approximately 38 $/GJ, for the biomass-trigeneration system is 26 $/GJ, and for the solar-trigeneration system is 24 $/GJ.

- This study shows that the solar-trigeneration system has the highest net available exergy as compared to the other two systems. Hence, it has the highest potential to have the highest exergy if the solar collectors performance improve.

It can be concluded from this study that the solar-trigeneration system is the best among the three systems. This is because the solar-trigeneration system has the lowest cost per exergy unit and has zero CO_2 emissions; additionally, it is based on a free renewable energy source and does not require any fuel to buy, as compared to the other two systems.

6.2 Recommendations

The recommendations for future research are given below.

- The results of this study show that in the systems studied, the ORC evaporators always have high exergy destruction rates. Therefore, it is important to examine the exergetic performance of different ORC evaporators on the aim of finding a more

suitable ORC evaporator for each system, which is characterized by a relatively low exergy destruction rate.

- The working fluid considered in this study is n-octane. It is characterized by relatively high efficiency as compared to the other organic working fluids. While this characteristic is the main reason for selecting this working fluid, it is recommended to examine other organic fluids to explore higher efficiency operation. It is also possible to examine binary organic fluids.

- In this study, a specific pressure range was selected based on some references from the literature. The study reveals that the pressure change has an insignificant effect on the performance. However, widening the pressure range by decreasing the minimum pressure that is already considered may show a more significant effect on the performance.

- The emissions of the SOFC-trigeneration system can be reduced by, for example, using a more efficient boiler or switch the biomass fuel of the boiler to natural gas. However, by considering the carbon natural cycle, the CO_2 emissions from the biomass fuel could be considered having lesser environmental impact.

- The absorption chiller selected is a single-effect absorption chiller. Further increase in the cooling power could be achieved by using a double-effect absorption chiller. However, using a double-effect absorption chiller will reduce the heat power from the trigeneration system.

References

[1] Energy Information Administration. *International Energy Outlook 2009*. U.S.A., 2009.

[2] U.S. Environmental Protection Agency. *Inventory of U.S. Greenhouse Gas Emissions and Sinks: 1990-2007*. U.S.A., 2009.

[3] International Energy Agency. *Combined heat and power: evaluating the benefits of greater global investment*. France, 2008.

[4] T. Kerr. *Combined heating and power and emissions trading: options for policy makers*. International Energy Agency, U.S.A., 2008.

[5] C. J. Levy and K. Zernike. The blackout: hospitals; lessons learned on 9/11 help hospitals respond. *The New York Times*, 16/8/2003.

[6] E. L. Lecomte, A. W. Pang, and J. W. R. Russell. Ice storm '98. *Institute for Catastrophic Loss Reduction*, ICLR research paper series – No. 1, 1998.

[7] U.S. Environmental Protection Agency; Combined Heat and Power Partnership. *Catalog of chp technologies*. U.S.A., 2008.

[8] Gas Research Institute and National Renewable Laboratory. *Gas-fired distributed energy resource technology characterizations*. U.S.A., November 2003.

[9] Y. Timoumi, I. Tlili, and S. Ben-Nasrallah. Design and performance optimization of gpu-3 stirling engines. *Energy*, 33:1100–1114, 2008.

[10] I Urieli and D Berchowitz. *Stirling cycle engine analysis*. Adam Hilger, 1984.

[11] EDUCOGEN. *The european educational tool on cogeneration*. Second edition, December 2001.

[12] Regulatory Assistance Project. *Output-based emissions standards for distributed, www.raponline.org*. U.S.A., July 2003.

[13] X.Q. Kong, R.Z. Wang, and X.H. Huang. Energy efficiency and economic feasibility of cchp driven by stirling engine. *Energy Conversion and Management*, 45(9-10):1433 – 1442, 2004.

[14] Office of Administration U.S. Environmental Protection Agency, Energy Efficiency Resources Management In partnership with the U.S. Department of Energy, and Renewable Energy. *On-site power systems for laboratories*. Laboratories for the 21st Century, December 2003.

[15] EG, Inc G Technical Services, and U.S. Department of Energy. *Fuel cell handbook*. U.S.A., seventh edition, November 2004.

[16] ONSITE SYCOM Energy Corporation. *Review of Combined Heat and Power Technologies*. U.S.A., October 1999.

[17] Gas Research Institute. *The role of distributed generation in competitive energy markets*. U.S.A., March 1999.

[18] D. B. E. Santo. Performance evaluation of an electricity base load engine cogeneration system. *International Journal of Energy Research*, 34(9):787–799, 2010.

[19] S. Li and J.Y. Wu. Theoretical research of a silica gel-water adsorption chiller in a micro combined cooling, heating and power (cchp) system. *Applied Energy*, 86(6):958 – 67, 2009.

[20] A. S. Siddiqui, C. Marnay, R. M. Firestone, and N. Zhou. Distributed generation with heat recovery and storage. *Journal of Energy Engineering*, 133(3):181 – 210, 2007.

[21] S. Sibilio, M. Sasso, R. Possidente, and C. Roselli. Assessment of micro-cogeneration potential for domestic trigeneration. *International Journal of Environmental Technology and Management*, 7(1-2):147 – 164, 2007.

[22] Y. Wang and T. Al-Shemmeri. A theoretical and an experimental investigation of a small scale trigeneration system - a comparison between trigeneration and separate generation systems. In *American Society of Mechanical Engineers, Internal Combustion Engine Division (Publication) ICE*, volume 40, pages 41 – 46, Erie, PA, United States, 2003.

[23] L. Emho. District energy efficiency improvement with trigeneration: Basic considerations and case studies. *Energy Engineering: Journal of the Association of Energy Engineering*, 100(2):66 – 80, 2003.

[24] A. Canova, C. Cavallero, F. Freschi, L. Giaccone, M. Repetto, and M. Tartaglia. Comparative economical analysis of a small scale trigenerative plant: a case study. In *Conference Record of the 2007 IEEE Industry Applications Conference - Forty-Second IAS Annual Meeting*, pages 1456 – 9, New Orleans, LA, USA, 2007.

[25] D. Frankovic, A. Viskovic, and G. Gudac. Optimization of trigeneration plant with heating and cooling energy storages operation. In *Proceedings of the IASTED International Conference on Modeling and Simulation*, pages 84 – 88, Marina Del Rey, CA, United States, 2004.

[26] E. Cardona and A. Piacentino. A measurement methodology for monitoring a chcp pilot plant for an office building. *Energy and Buildings*, 35(9):919 – 925, 2003.

[27] Y. Huangfu, J.Y. Wu, R.Z. Wang, and Z.Z. Xia. Experimental investigation of adsorption chiller for micro-scale bchp system application. *Energy and Buildings*, 39(2):120 – 127, 2007.

[28] J.L. Miguez, S. Murillo, J. Porteiro, and L.M. Lopez. Feasibility of a new domestic chp trigeneration with heat pump: I. design and development. *Applied Thermal Engineering*, 24(10):1409 – 1419, 2004.

[29] J. Porteiro, J.L. Miguez, S. Murillo, and L.M. Lopez. Feasibility of a new domestic chp trigeneration with heat pump: ii. availability analysis. *Applied Thermal Engineering*, 24(10):1421 – 1429, 2004.

[30] L. Vasiliev. Solid sorption heat pumps for tri-generation. *Archives of Thermodynamics*, 28(3):15 – 28, 2007.

[31] J. Pospisil, J. Fiedler, Z. Skala, and M. Baksa. Comparison of cogeneration and trigeneration technology for energy supply of tertiary buildings. *WSEAS Transactions on Heat and Mass Transfer*, 1(3):262–7, 2006.

[32] G.G. Maidment and R.M. Tozer. Combined cooling heat and power in supermarkets. *Applied Thermal Engineering*, 22(6):653 – 665, 2002.

[33] G. Chicco and P. Mancarella. From cogeneration to trigeneration: Profitable alternatives in a competitive market. *IEEE Transactions on Energy Conversion*, 21(1):265 – 272, 2006.

[34] G. Chicco and P. Mancarella. Planning aspects and performance indicators for small-scale trigeneration plants. In *2005 International Conference on Future Power Systems (IEEE Cat. No.05EX1179C)*, page 6 pp, Amsterdam, Netherlands, 2005.

[35] G. Chicco and P. Mancarella. Planning evaluation and economic assessment of the electricity production from small-scale trigeneration plants. *WSEAS Transactions on Power Systems*, 1(2):393 – 400, 2006.

[36] G. Chicco and P. Mancarella. Trigeneration primary energy saving evaluation for energy planning and policy development. *Energy Policy*, 35(12):6132 – 6144, 2007.

[37] G. Temir, D. Bilge, and O. Emanet. An application of trigeneration and its economic analysis. *Energy Sources*, 26(9):857 – 867, 2004.

[38] L. Lin, Y. Wang, T. Al-Shemmeri, T. Ruxton, S. Turner, S. Zeng, J. Huang, Y. He, and X. Huang. An experimental investigation of a household size trigeneration. *Applied Thermal Engineering*, 27(2-3):576 – 585, 2007.

[39] G. Chicco and P. Mancarella. A unified model for energy and environmental performance assessment of natural gas-fueled poly-generation systems. *Energy Conversion and Management*, 49(8):2069 – 2077, 2008.

[40] J. Godefroy, R. Boukhanouf, and S. Riffat. Design, testing and mathematical modelling of a small-scale chp and cooling system (small chp-ejector trigeneration). *Applied Thermal Engineering*, 27(1):68 – 77, 2007.

[41] S. Lindmark, V. Martin, and M. Westermark. Analysis of heat-driven cooling production coupled to power generation for increased electrical yield. In *ASME, Advanced Energy Systems Division (Publication) AES*, volume 44, pages 395 – 404, ASME, Advanced Energy Systems Division (Publication) AES, Anaheim, CA, United States, 2004.

[42] H. Cho, S. D. Eksioglu, R. Luck, and L. M. Chamra. Operation of a cchp system using an optimal energy dispatch algorithm. In *American Society of Mechanical Engineers,*, pages 8pp, ASME, ES–54096, Jacksonville, Florida, USA, 2008.

[43] E. Cardona, A. Piacentino, and F. Cardona. Matching economical, energetic and environmental benefits: An analysis for hybrid chcp-heat pump systems. *Energy Conversion and Management*, 47(20):3530 – 3542, 2006.

[44] E. Cardona and A. Piacentino. Optimal design of chcp plants in the civil sector by thermoeconomics. *Applied Energy*, 84(7-8):729 – 748, 2007.

[45] E. Cardona and A. Piacentino. A new approach to exergoeconomic analysis and design of variable demand energy systems. *Energy*, 31(4):490 – 515, 2006.

[46] Y. Huangfu, J.Y. Wu, R.Z. Wang, X.Q. Kong, and B.H. Wei. Evaluation and analysis of novel micro-scale combined cooling, heating and power (mcchp) system. *Energy Conversion and Management*, 48(5):1703 – 1709, 2007.

[47] T. Tracy, J.C. Ordonez, and J.V.C. Vargas. First and second law thermodynamic analysis of a domestic scale trigeneration system. In *Proceedings of the Energy Sustainability Conference 2007, ASME*, pages 759 – 766, Long Beach, CA, United States, 2007.

[48] J. Deng, R. Wang, J. Wu, G. Han, D. Wu, and S. Li. Exergy cost analysis of a micro-trigeneration system based on the structural theory of thermoeconomics. *Energy*, 33(9):1417 – 1426, 2008.

[49] G. Temir and D. Bilge. Thermoeconomic analysis of a trigeneration system. *Applied Thermal Engineering*, 24(17-18):2689 – 2699, 2004.

[50] A. Schroeder, J. Lach, and S. Poskrobko. Production of ice water in a tri-generation centralized system. *Archives of Thermodynamics*, 28(4):41 – 62, 2007.

[51] A. Costa, J. Paris, M. Towers, and T. Browne. Economics of trigeneration in a kraft pulp mill for enhanced energy efficiency and reduced ghg emissions. *Energy*, 32(4):474 – 481, 2007.

[52] A. Rong and R. Lahdelma. An efficient linear programming model and optimization algorithm for trigeneration. *Applied Energy*, 82(1):40 – 63, 2005.

[53] A. Poredos, A. Kitanovski, and M. Tuma. The energy efficiency of chillers in a trigeneration plant. *Forschung im Ingenieurwesen/Engineering Research*, 67(1):40 – 44, 2002.

[54] M. Genrup, M. Thern, and M. Assadi. Trigeneration: Thermodynamic performance and cold expander aerodynamic design in humid air turbines. In *American Society of Mechanical Engineers, International Gas Turbine Institute, Turbo Expo (Publication) IGTI*, volume 6 A, pages 8 pp, ASME GT–38283, Atlanta, GA, United States, 2003.

[55] E. T. Calva, M. P. Nunez, and M. A. R. Toral. Thermal integration of trigeneration systems. *Applied Thermal Engineering*, 25(7 SPEC ISS):973 – 984, 2005.

[56] L. Daolin and Z. Shifei. Tri-generation (electrical power, heated and chilled water) system and their application in shanghai. In *American Society of Mechanical Engineers, Power Division (Publication) PWR*, volume 34-2, pages 265 – 270, Burlingame, CA, USA, 1999.

[57] D. Ziher and A. Poredos. Economics of a trigeneration system in a hospital. *Applied Thermal Engineering*, 26(7):680 – 687, 2006.

[58] E. Cardona, A. Piacentino, and F. Cardona. Energy saving in airports by trigeneration. part i: Assessing economic and technical potential. *Applied Thermal Engineering*, 26(14-15):1427 – 1436, 2006.

[59] T.R. Casten. District energy with trigenerated ammonia cooling. *ASHRAE Transactions*, 100(1):1136 – 1143, 1994.

[60] L. Chao-zhen, G. Jian-ming, and H. Xing-hua. Influence of energy demands ratio on the optimal facility scheme and feasibility of bchp system. *Energy and Buildings*, 40(10):1876 – 1882, 2008.

[61] J.-c. Cao and F.-q. Liu. Simulation and optimization of the performance in the air-conditioning season of a bchp system in china. *Energy and Buildings*, 40(3):185 – 192, 2008.

[62] A. Khaliq and R. Kumar. Thermodynamic performance assessment of gas turbine trigeneration system for combined heat cold and power production. *Journal of Engineering for Gas Turbines and Power, Transactions of the ASME*, 130(2), MAR 2008.

[63] A. Khaliq. Exergy analysis of gas turbine trigeneration system for combined production of power heat and refrigeration. *International Journal of Refrigeration*, 32(3):534 – 545, 2009.

[64] J.-C. Cao, F.-Q. Liu, Z.-H. Qin, S.-H. Cao, and S.-F. Zhang. Energy and exergy analysis, and thermoeconomic performance of a bchp system. *Journal of Dong Hua University (English Edition)*, 21(5):36 – 42, 2004.

[65] X. Liao and R. Radermacher. Absorption chiller crystallization control strategies for integrated cooling heating and power systems. *International Journal of Refrigeration*, 30(5):904 – 911, 2007.

[66] J. Liekens, J. Van-Bael, J. Desmedt, N. Robeyn, and P. Jannis. Results from the research on microturbine-chp-applications in flanders. In *Proceedings of the ASME Turbo Expo*, volume 1, pages 837 – 845, ASME, GT–68110, Reno-Tahoe, NV, United States, 2005.

[67] C. S. Smugeresky. An integrated combined heat and power distributed energy resource solution for modular applications. In *American Society of Mechanical Engineers, International Gas Turbine Institute, Turbo Expo (Publication) IGTI*, pages 6pp, ASME, GT–28294, Montreal, Canada, 2007.

[68] W. E. Lear, C. J. Ryu, J. F. Crittenden, A. Srinivasan, W. Ellis, D. R. Tiffany, S. A. Sherif, and P. L. Meitner. System design of a novel combined cooling, heat, power, and water microturbine combined cycle. In *American Society of Mechanical Engineers, International Gas Turbine Institute, Turbo Expo (Publication) IGTI*, pages 11pp, ASME, GT–51454, Berlin, Germany, 2008.

[69] C. Jae Ryu, A. Srinivasan, D. R. Tiffany, J. F. Crittenden, W. E. Lear, and S. S. Sherif. Dynamic modeling of a novel cooling, heat, power, and water microturbine combined cycle. In *American Society of Mechanical Engineers, Proceedings of Engergy sustainability*, pages 12pp, ASME, Energy Sustainability Proceeding, ES–54095, Florida, USA, 2008.

[70] A. A. Jalalzadeh-Azar. A parametric analysis of a grid-independent bchp system-focusing on impact of technological advancements. *ASHRAE Transactions*, 109 PART 2:69 – 78, 2003.

[71] P.D. Fairchild, S.D. Labinov, A. Zaltash, and D.T. Rizy. Experimental and theoretical study of microturbine-based bchp system. In *American Society of Mechanical Engineers, Advanced Energy Systems Division (Publication) AES*, volume 41, pages 179 – 190, New York, NY, United States, 2001.

[72] S. D. Labinov, D. T. Rizy, P. D. Fairchilid, R. C. DeVault, E. A. Vineyard, and A. Zaltash. Predictive algorithms for microturbine performance for bchp systems. *ASHRAE Transactions*, 108 PART 2:670 – 681, 2002.

[73] N. Sugiartha, S.A. Tassou, I. Chaer, and D. Marriott. Trigeneration in food retail: An energetic, economic and environmental evaluation for a supermarket application. *Applied Thermal Engineering*, 29(13):2624 – 2632, 2009.

[74] H. E. Jaaskelainen and J. S. Wallace. Operating experience with a 240 kw microturbine combined heating, cooling and power system. In *American Society of Mechanical Engineers, Energy Sustainability*, pages 12pp, ASME, ES–54314, Jacksonville, Florida, USA, 2008.

[75] S.A. Tassou, I. Chaer, N. Sugiartha, Y.-T. Ge, and D. Marriott. Application of trigeneration systems to the food retail industry. *Energy Conversion and Management*, 48(11):2988 – 95, 2007.

[76] J. C. Bruno, V. Ortega-Lopez, and A. Coronas. Integration of absorption cooling systems into micro gas turbine trigeneration systems using biogas: Case study of a sewage treatment plant. *Applied Energy*, 86(6):837 – 847, 2009.

[77] S. Campanari, Boncompagni, and E. Macchi. Microturbines and trigeneration: Optimization strategies and multiple engine configuration effects. *Journal of Engineering for Gas Turbines and Power*, 126(1):92 – 101, 2004.

[78] S. Campanari and E. Macchi. Technical and tariff scenarios effect on microturbine trigenerative applications. *Journal of Engineering for Gas Turbines and Power*, 126(3):581 – 589, 2004.

[79] H.X. Liang and Q.W. Wang. Evaluation of energy efficiency for a cchp system with available microturbine. In *American Society of Mechanical Engineers, International Gas Turbine Institute, Turbo Expo (Publication) IGTI*, pages 7pp, ASME, GT–27883, Montreal, Canada, 2007.

[80] J. Huang, C. Yue, and Z. Feng. Multi-objective optimization and performance analysis of bchp systems using genetic algorithms. In *American Society of Mechanical Engineers, International Gas Turbine Institute, Turbo Expo (Publication) IGTI*, pages 6pp, ASME, GT–91143, Brcelona, Spain, 2006.

[81] M. Medrano, J. Mauzey, V. McDonell, S. Samuelsen, and D. Boer. Theoretical analysis of a novel integrated energy system formed by a microturbine and an exhaust fired single-double effect absorpotion chiller. *International Journal of Applied Thermaodynamics*, 9(1):29–36, March 2006.

[82] I. Malico, A.P. Carvalhinho, and J. Tenreiro. Design of a trigeneration system using a high-temperature fuel cell. *International Journal of Energy Research*, 33(2):144 – 151, 2009.

[83] H. I. Henderson, B. Karambakkam, J. Boyer, and R. Staudt. An hourly building simulation model aimed at fuel cell applications. In *Proceedings of 4th International ASME Conference on Fuel Cell Science, Engineering and Technology, FUELCELL2006*, volume 2006, page 10 pp, Irvine, CA, United States, 2006.

[84] P Seifert. Rational supply of power,heat and cooling in buildings demonstrated in a hispotal in dresden. *WSEAS Transactions on Environment and Development*, (DBI Gasund Unwelttechnik GmbH, Final Technical Report, Project No. BU/0065/97), 2000.

[85] G. Bizzarri. On the size effect in pafc grid-connected plant. *Applied Thermal Engineering*, 26(10):1001 – 1007, 2006.

[86] S. Gamou, R. Yokoyama, and K. Ito. Optimal unit sizing of cogeneration systems in consideration of uncertain energy demands as continuous random variables. *Energy Conversion and Management*, 43(9-12):1349 – 61, 2002.

[87] C. Weber, M. Koyama, and S. Kraines. Co_2-emissions reduction potential and costs of a decentralized energy system for providing electricity, cooling and heating in an office-building in tokyo. *Energy*, 31(14):2705 – 2725, 2006.

[88] R. Buck and S. Friedmann. Solar-assisted small solar tower trigeneration systems. *Journal of Solar Energy Engineering, Transactions of the ASME*, 129(4):349 – 354, 2007.

[89] G. Bizzarri and G.L. Morini. New technologies for an effective energy retrofit of hospitals. *Applied Thermal Engineering*, 26(2-3):161 – 9, 2006.

[90] M. Medrano, A. Castell, G. Fontanals, C. Castellon, and L. F. Cabeza. Economics and climate change emissions analysis of a bioclimatic institutional building with trigeneration and solar support. *Applied Thermal Engineering*, 28(17-18):2227 – 2235, 2008.

[91] L. Gao, H. Wu, H. Jin, and M. Yang. System study of combined cooling, heating and power system for eco-industrial parks. *International Journal of Energy Research*, 2008(12):1107–1118, 2008.

[92] H. Li, L. Fu, K. Geng, and Y. Jiang. Energy utilization evaluation of cchp systems. *Energy and Buildings*, 38(3):253 – 7, 2006.

[93] S. Dharmadhikari, D. Pons, and F. Principaud. Contribution of stratified thermal storage to cost-effective trigeneration project. *ASHRAE Transactions*, 106 (PA):912 – 919, 2000.

[94] P. Colonna and S. Gabrielli. Industrial trigeneration using ammonia-water absorption refrigeration systems (aar). *Applied Thermal Engineering*, 23(4):381 – 396, 2003.

[95] P. Arcuri, G. Florio, and P. Fragiacomo. A mixed integer programming model for optimal design of trigeneration in a hospital complex. *Energy*, 32(8):1430 – 1447, 2007.

[96] H. Li, R. Nalim, and P.-A. Haldi. Thermal-economic optimization of a distributed multi-generation energy system - a case study of beijing. *Applied Thermal Engineering*, 26(7):709 – 719, 2006.

[97] A. Piacentino and F. Cardona. An original multi-objective criterion for the design of small-scale polygeneration systems based on realistic operating conditions. *Applied Thermal Engineering*, 28(17-18):2391 – 2404, 2008.

[98] D. Ziher and A. Poredos. Cooling power costs from a trigeneration system in a hospital. *Forschung im Ingenieurwesen/Engineering Research*, 70(2):105 – 113, 2005.

[99] A. Arteconi, C. Brandoni, and F. Polonara. Distributed generation and trigeneration: Energy saving opportunities in italian supermarket sector. *Applied Thermal Engineering*, 29(8-9):1735 – 1743, 2009.

[100] G. Chicco and P. Mancarella. Enhanced energy saving performance in composite trigeneration systems. In *Power Tech 2007*, pages 1609 – 14, Lausanne, Switzerland, 2007.

[101] J. Huang, Z. Feng, C. Yue, and L. Liu. Operation modes and economic performance study of 100kw microturbine building cooling, heating and power systems. In *American Society of Mechanical Engineers, International Gas Turbine Institute, Turbo Expo (Publication) IGTI*, pages 8pp, ASME, GT–68277, Nevada, USA, 2005.

[102] M. Meckler. Bchp design for dual phase medical complex. *Applied Thermal Engineering*, 22(5):535 – 43, 2002.

[103] F. Becchis and G. Genon. Cooling needs for a warming world? economics and governance of district cooling. *WIT Transactions on Ecology and the Environment*, 106:263 – 272, 2007.

[104] W. Wallace and W. Fuchs. Trigeneration: A new approach to coal-based cogeneration. *Annual Meeting - Technical Association of the Pulp and Paper Industry*, pages 53 – 72, 1979.

[105] E. Cardona, P. Sannino, A. Piacentino, and F. Cardona. Energy saving in airports by trigeneration. part ii: Short and long term planning for the malpensa 2000 chcp plant. *Applied Thermal Engineering*, 26(14-15):1437 – 1447, 2006.

[106] J. Hernandez-Santoyo and A. Sanchez-Cifuentes. Trigeneration: An alternative for energy savings. *Applied Energy*, 76(1-3):219 – 227, 2003.

[107] G. J. Kowalski and M. Zenouzi. Selection of distributed power-generating systems based on electric, heating, and cooling loads. *Journal of Energy Resources Technology, Transactions of the ASME*, 128(3):168 – 177, 2006.

[108] M. Burer, K. Tanaka, D. Favrat, and K. Yamada. Multi-criteria optimization of a district cogeneration plant integrating a solid oxide fuel cell-gas turbine combined cycle, heat pumps and chillers. *Energy*, 28(6):497 – 518, 2003.

[109] M. Saito, H. Yoshida, y. Iwamoto, and A. Ueda. An analysis of a micro cogeneration system composed of solid oxide fuel cell, microturbine, and $h_2o/libr$ absorption refrigerator. *Journal of Thermal Science and Technology*, 2(2):168–179, 2007.

[110] J.-J. Wang, Y.-Y. Jing, C.-F. Zhang, G.-H. Shi, and X.-T. Zhang. A fuzzy multi-criteria decision-making model for trigeneration system. *Energy Policy*, 36(10):3823 – 32, 2008.

[111] P. Mancarella and G. Chicco. Assessment of the greenhouse gas emissions from cogeneration and trigeneration systems. part ii: Analysis techniques and application cases. *Energy*, 33(3):418 – 430, 2008.

[112] G. Chicco and P. Mancarella. Assessment of the greenhouse gas emissions from cogeneration and trigeneration systems. part i: Models and indicators. *Energy*, 33(3):410 – 417, 2008.

[113] W. Bing, W. Zhiwei, L. Li, and J. Lu. Optimization of bchp schemes based on gra and ahp. In *American Society of Mechanical Engineers, Energy Sustainability*, pages 775–780, ASME, ES–36231, Long Beach, California, USA, 2007.

[114] P. J. Mago, N. Fumo, and L. M. Chamra. Performance analysis of cchp and chp systems operating following the thermal and electric load. *International Journal of Energy Research*, 33(9):852–864, 2009.

[115] A. Khaliq, R. Kumar, and I. Dincer. Performance analysis of an industrial waste heat-based trigeneration system. *International Journal of Energy Research*, 33(8):737–744, 2009.

[116] S. Plura, C. Kren, and C. Schweigler. Efficient and flexible tri-generation with two-stage absorption chiller. In *American Society of Mechanical Engineers, IMECE*, pages 189 – 197, ASME, IMECE–15900, Chicago, IL, United States, 2006.

[117] E. Cardona and A. Piacentino. A methodology for sizing a trigeneration plant in mediterranean areas. *Applied Thermal Engineering*, 23(13):1665 – 1680, 2003.

[118] G. Chicco and P. Mancarella. Characterization and planning of distributed multi-generation plants. In *Electric power generation, transmission and efficiency (editor: C. M. Lefebvre)*. Nova Science publishers, Inc, New York, pages 17-73, 2007.

[119] G. Chicco and P. Mancarella. Evaluation of multi-generation alternatives: an approach based on load transformations. In *2008 IEEE Power & Energy Society General Meeting*, page 6 pp, Pittsburgh, PA, USA, 2008.

[120] H.-M. Henning, T. Pagano, S. Mola, and E. Wiemken. Micro tri-generation system for indoor air conditioning in the mediterranean climate. *Applied Thermal Engineering*, 27(13):2188 – 94, Sept. 2007.

[121] A. Rong, R. Lahdelma, and Peter B. Luh. Lagrangian relaxation based algorithm for trigeneration planning with storages. *European Journal of Operational Research*, 188(1):240 – 257, 2008.

[122] C. Chevalier and F. Meunier. Environmental assessment of biogas co- or trigeneration units by life cycle analysis methodology. *Applied Thermal Engineering*, 25(17-18):3025 – 41, 2005.

[123] A. Piacentino and F. Cardona. On thermoeconomics of energy systems at variable load conditions: Integrated optimization of plant design and operation. *Energy Conversion and Management*, 48(8):2341 – 2355, 2007.

[124] A. Piacentino and F. Cardona. Eabot - energetic analysis as a basis for robust optimization of trigeneration systems by linear programming. *Energy Conversion and Management*, 49(11):3006 – 3016, 2008.

[125] M. A. Rosen, M. N. Le, and I. Dincer. Efficiency analysis of a cogeneration and district energy system. *Applied Thermal Engineering*, 25(1):147 – 159, 2005.

[126] F. A. Al-Sulaiman, I. Dincer, and F. Hamdullahpur. Energy analysis of a trigeneration plant based on solid oxide fuel cell and organic rankine cycle. *International Journal of Hydrogen Energy*, 35(10):5104 – 5113, 2010.

[127] F. A. Al-Sulaiman, F. Hamdullahpur, and I. Dincer. Efficiency and environmental impact assessments of a trigeneration plant using sofc and orc. In *Proceedings of the Global Conference on Global Warming*, page 11pp, Istanbul, Turkey, 2009.

[128] M. Moran and H. Shapiro. *Fundamentals of Engineering Thermodynamics*. John Wiley and Sons, Inc., fifth edition, 2004.

[129] A. Lazzarettoa and G. Tsatsaronis. Speco: A systematic and general methodology for calculating efficiencies and costs in thermal systems. *Energy*, 31:1257–1289, 2006.

[130] G. Tsatsaronis and F. Cziesta. *Thermoeconomics, In: Optimisation of Energy Systems and Processes Summer School,*. Gliwice, P., 2003.

[131] A. Ravindran, K. Radsdell, and G. Reklaitis. *Powell's Conjugate Direction Method, in: Engineering Optimization: Methods and Applications*. John Wiley & Sons, Inc., 2006.

[132] B. P. Flannery W. H. Press, S. A. Teukolsky, and W.T. Vetterling. *Numerical Recipes in Pascal*. Cambridge University Press, Ch. 10, 1989.

[133] Wolfram. *Brent's Mehtod*. http://mathworld.wolfram.com/BrentsMethod.html, 2010.

[134] S. S. Rao. *Engineering Optimization: Theory and Practice*. John Wiley & Sons, Inc., 4 edition, 2009.

[135] M. J. D. Powell. An efficient method for finding the minimum of a function of several variables without calculating derivatives. *Computer Journal*, 7:155–162, 1964.

[136] A. Bejan, G. Tsatsaronis, and M. Moran. *Thermal Design and Optimization*. John Wiley and Sons, Inc., 1996.

[137] J. C. Bruno, J. Lopez-Villada, E. Letelier, S. Romera, and A. Coronas. Modelling and optimisation of solar organic rankine cycle engines for reverse osmosis desalination. *Applied Thermal Engineering*, 28(17-18):2212 – 2226, 2008.

[138] S. Vijayaraghavan and D.Y. Goswami. Organic working fluids for a combined power and cooling cycle. *Journal of Energy Resources Technology, Transactions of the ASME*, 127(2):125 – 130, 2005.

[139] C.L. Yaws. *Chemical Properties Handbook*. McGraw-Hill, 1999.

[140] American Society of Heating Refrigerating and Air-Conditioning Engineers Inc. Chapter 1 - thermodynamics and refrigeration cycles. In *ASHRAE Handbook: Fundamentals, Inch Pound Edition*. ASHRAE, Atlanta, USA, 2005.

[141] K. E. Herold, R. Radermacher, and Klein S. A. *Absorption Chillers and Heat Pumps*. CRC press, 1996.

[142] C. Invernizzi, P. Iora, and P. Silva. Bottoming micro-rankine cycles for micro-gas turbines. *Applied Thermal Engineering*, 27(1):100 – 110, 2007.

[143] B. Saleh, G. Koglbauer, M. Wendland, and J. Fischer. Working fluids for low-temperature organic rankine cycles. *Energy*, 32(7):1210 – 1221, 2007.

[144] L. Jing, P. Gang, and J. Jie. Optimization of low temperature solar thermal electric generation with organic rankine cycle in different areas. *Applied Energy*, 87(11):3355 – 3365, 2010.

[145] Thermax Inc. *Absorpion cooling: Cogenie*. www.thermax-usa.com/index.htm, 2010.

[146] C. O. Colpan, I. Dincer, and F. Hamdullahpur. Thermodynamic modeling of direct internal reforming solid oxide fuel cells operating with syngas. *International Journal of Hydrogen Energy*, 32(7):787 – 795, 2007.

[147] U.G. Bossel. *Final Report on SOFC Data Facts and Figures*. Swiss Federal Office of Energy, 1992.

[148] J.-W. Kim, A.V. V.irkar, K.-Z. Fung, K. Mehta, and S.C. Singhal. Polarization effects in intermediate temperature, anode-supported solid oxide fuel cells. *Journal of the Electrochemical Society*, 146(1):69 – 78, 1999.

[149] S.H. Chan, C.F. Low, and O.L. Ding. Energy and exergy analysis of simple solid-oxide fuel-cell power systems. *Journal of Power Sources*, 103(2):188 – 200, 2002.

[150] G Tao, T. Armstrong, and A. Virkar. Intermediate temperature solid oxide fuel cell (it-sofc) research and development activities at msri. In *Nineteenth annual ACERC & ICES conference*, Utah, USA, 2005.

[151] P.M. Lv, Z.H. Xiong, J. Chang, C.Z. Wu, Y. Chen, and J.X. Zhu. An experimental study on biomass air-steam gasification in a fluidized bed. *Bioresource Technology*, 95(1):95 – 101, 2004.

[152] P. Basu. *Combustion and Gasification in Fluidized Beds*. CRC Press, 2006.

[153] V. Ganapathy. *Steam Plant Calculations Manual*. Marcel Dekker, 1994.

[154] J. Szargut. *Exergy Method: Technical and Ecological Applications*. WIT press, 2005.

[155] T. D. Harrison and R. A. Randall. Thermal storage experience at the msstf and plans for the future. *Thermal Energy Storage: Fourth Annual Review Meeting*, NASA CP-2125:125–130, 1980.

[156] Therminol. *Therminol-66 Heat Transfer Fluid*. www.therminol.com, 2010.

[157] S. Kalogirou. *Solar energy engineering : processes and systems*. Elsevier, 2009.

[158] J. Duffie and W. Beckman. *Solar Engineering of Thermal Processes*. John Wiley & Sons, Inc., 2006.

[159] Sloan M. Kearney D. Dudley V., Kolb G. Segs ls-2 solar collector – test results. *Report of Sandia National Laboratories*, SANDIA94-1884, 1994.

[160] R. Petela. Exergy analysis of the solar cylindrical-parabolic cooker. *Solar Energy*, 79(3):221 – 233, 2005.

[161] U. Herrmann and D. W. Kearney. Survey of thermal energy storage for parabolic trough power plants. *Journal of Solar Energy Engineering, ASME Transactions*, 124:145 –152, 2002.

[162] B. Kelly and R. L. Lessley. Investigation of commercial central receiver thermal storage and steam generator issues. In *ASME-JSES-JSME International Solar Energy Conference*, pages 611 – 616, San Francisco, CA, USA, 1994.

[163] M. Valenti. Storing solar energy in salt. *Mechanical Engineering*, 117(6):72 – 75, 1995.

[164] J. E. Pacheco and R. Gilbert. Overview of recent results of the solar two test and evaluations program, renewable and advanced energy systems for the 21st century,. In *Proc. of 1999 ASME Int. Solar Energy Conf*, Maui, HI, 1999.

[165] I. Kroizer. Design of a 13 mwel parabolic power plants at daggatt, california. In *Int. Energy Agency Workshop on the Design and Performance of Large Solar Thermal Collectors*, San Diego, Ca, USA, 1984.

[166] U. Herrmann, B. Kelly, and H. Price. Two-tank molten salt storage for parabolic trough solar power plants. *Energy*, 29(5-6):883 – 93, 2004.

[167] E. Zarza, M. E. Rojas, L. Gonzalez, J. M. Caballero, and F. Rueda. Inditep: The first pre-commercial dsg solar power plant. *Solar Energy*, 80(10):1270 – 1276, 2006.

[168] M.J. Montes, A. Abanades, J.M. Martinez-Val, and M. Valdes. Solar multiple optimization for a solar-only thermal power plant, using oil as heat transfer fluid in the parabolic trough collectors. *Solar Energy*, 83(12):2165 – 76, 2009.

[169] R.S. Means (Editor). *RS Means Mechanical Cost Data*. R.S. Means Company, 33 edition, 2010.

[170] F. Trabelsi. *GENIVAR, Constructive people Inc.*, Private communication, 2010.

[171] M. Santin, A. Traversoa, L. Magistria, and A. Massardoa. Thermoeconomic analysis of sofc-gt hybrid systems fed by liquid fuels. *Energy*, 35(2):1077–1083, 2010.

[172] L. Meyer, R. Castillo, J. Buchgeister, and G. Tsatsaronis. Application of exergoeconomic and exergoenvironmental analysis to an sofc system with an allothermal biomass gasifier. *Int. J. of Thermodynamics*, 12(4):177–186, 2009.

[173] Z.T. Lian, K.J. Chua, and S.K. Chou. A thermoeconomic analysis of biomass energy for trigeneration. *Applied Energy*, 87(2):84–95, 2010.

[174] C. O. Colpan and T. Yesin. Energetic, exergetic and thermoeconomic analysis of bilkent combined cycle cogeneration plant. *International Journal of Energy Research*, 30(11):875 – 894, 2006.

[175] O. Balli, H. Aras, and A. Hepbasli. Exergoeconomic analysis of a combined heat and power (chp) system. *International Journal of Energy Research*, 32(4):273 – 89, 2008.

[176] D. M. Paulus and G. Tsatsaronis. Auxiliary equations for the determination of specific exergy revenues. *Energy*, 31(15):3235 – 3247, 2006.

[177] E. Prabhu. Solar trough organic rankine electricity system (stores) stage 1: Power plant optimization and economics. *NREL/SR-550-39433*, 2006.

[178] Sargent & Lundy LLC Consulting Group. Assessment of parabolic trough and power tower solar technology cost and performance forecasts. *NREL/SR-550-34440*, 2003.

[179] T.-C. Hung. Waste heat recovery of organic rankine cycle using dry fluids. *Energy Conversion and Management*, 42(5):539 – 553, 2001.

[180] B. F. Tchanche, G. Papadakis, G. Lambrinos, and A. Frangoudakis. Fluid selection for a low-temperature solar organic rankine cycle. *Applied Thermal Engineering*, 29(11-12):2468 – 2476, 2009.

[181] K. W. Li and A. P. Priddy. *Power Plant System Design*. Wiley, 1985.

[182] U. Drescher and D. Brüggemann. Fluid selection for the organic rankine cycle (orc) in biomass power and heat plants. *Applied Thermal Engineering*, 27(1):223 – 228, 2007.

[183] S. B. Riffat and X. Zhao. A novel hybrid heat-pipe solar collector/chp system–part ii: theoretical and experimental investigations. *Renewable Energy*, 29(12):1965 – 1990, 2004.